FACULTY OF SCIENCE
UNIVERSITY OF COPENHAGEN

PhD thesis

Johannes Borregaard

Quantum repeaters and atomic ensembles

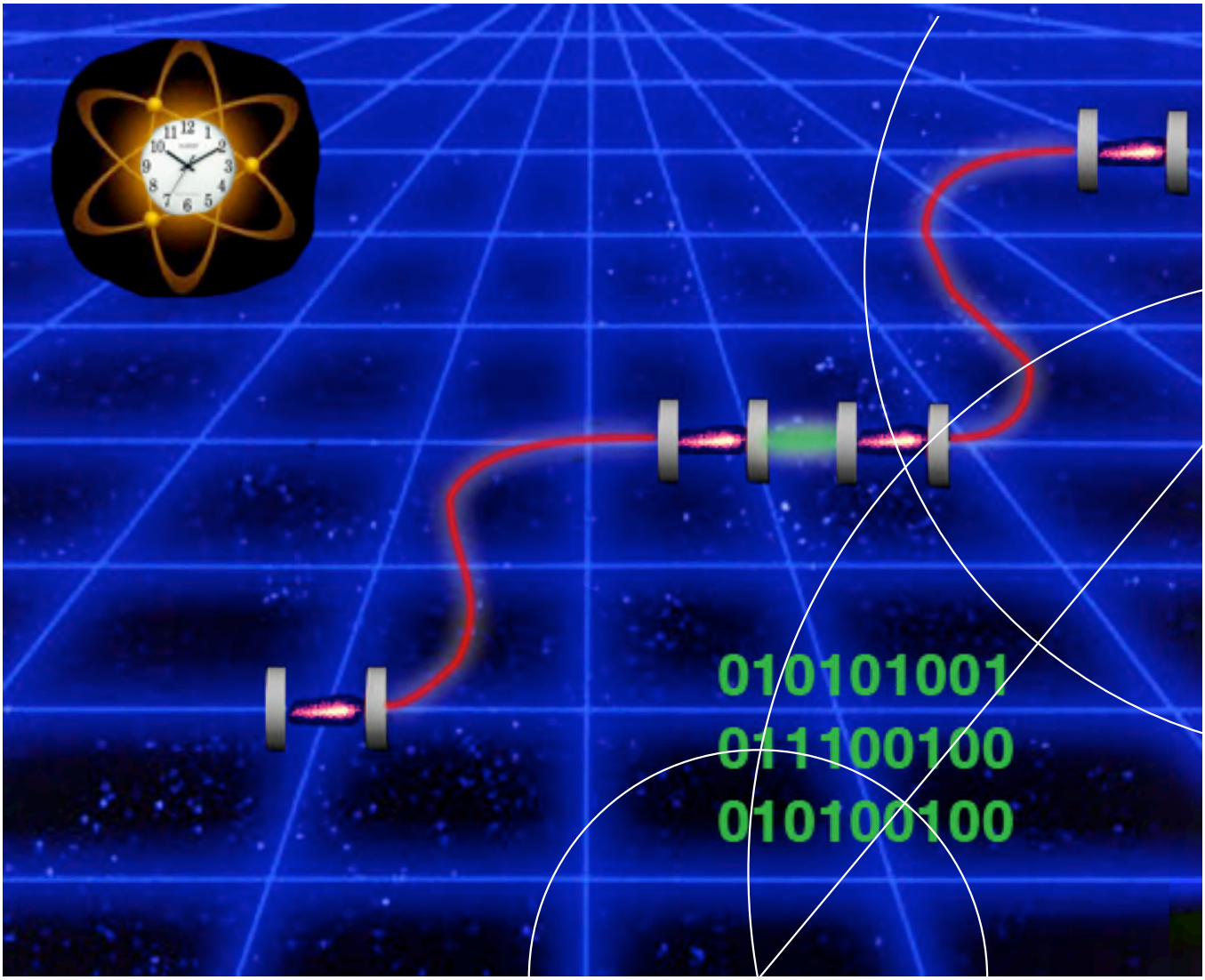

Academic advisor: Anders S. Sørensen

Submitted: 06/11/14

University of Copenhagen

PhD Thesis

Quantum repeaters and atomic ensembles

Author:
Johannes Borregaard

Supervisor:
Prof. Anders S. Sørensen

A thesis submitted in partial fulfilment of the requirements for the degree of Doctor of Philosophy

at

The Niels Bohr Institute
University of Copenhagen

November 2014

Abstract

During the last couple of decades, quantum mechanics has moved from being primarily a theory describing the behaviour of microscopical particles in advanced experiments to being the foundation of a novel technology. One of the cornerstones in this new quantum technology is the strong correlations that can exist between remote quantum systems called entanglement. These correlations are exploited to detect eavesdroppers and construct unconditionally secure communication channels, enhance the sensitivity in various metrology schemes and construct powerful quantum computers, which can solve extremely hard problems. Quantum technology is, however, still premature, which is partly due to the fragile nature of these quantum correlations to noise. Extended research is therefore taking place to find robust quantum systems and protocols, which can move quantum technology from the specialized laboratories to practical applications. In this thesis, I describe me and my collaborator's work along these lines. The first part of the thesis describes our work on optimizing a novel protocol of how to distribute entanglement over large distances for the construction of secure communication channels. We modify a previous protocol, thereby enabling fast local processing, which greatly enhances the distribution rate. We then move on to describe our work on improving the stability of atomic clocks using entanglement. Entanglement can potentially push the stability of atomic clocks to the so-called Heisenberg limit, which is the absolute upper limit of the stability allowed by the Heisenberg uncertainty relation. It has, however, been unclear whether entangled state's enhanced sensitivity to noise would prevent reaching this limit. We have developed an adaptive measurement protocol, which circumvents this problem and allows for near-Heisenberg limited stability of atomic clocks. Furthermore, we describe how the operation of a clock can be altered to gain an exponential improvement of the stability even without entanglement. In the next part of the thesis, we describe our work on a novel type of heralded quantum gates with integrated error detection, which greatly enhances the performance of the gates at the expense of a finite but possible small failure probability. Such gates may facilitate fault tolerant quantum computation or high rate entanglement distribution. In the final part of the thesis, we describe our work on room temperature quantum memories and single photon sources. We have introduced a novel concept of motional averaging, which can be used in room-temperature systems, where fluctuations due to thermal motion is an issue. In particular, we have considered a system based on microcells filled with Cs-atoms, which can facilitate efficient quantum memories and coherent single photon sources at room temperature. Finally, we describe our work on optimizing entanglement distribution protocols based on optical cavitites and single emitters. We have compared entanglement generation schemes based on single - and two-photon detection and implemented the heralded gate described above together with a similar deterministic gate in order to swap the entanglement to large distances. We have then found the combination resulting in the highest distribution rate, which is shown to outperform one of the fastest distribution protocols based on atomic ensembles.

Dansk resumé

I løbet af de sidste par årtier har kvantemekanik ændret sig fra at være en underfundig teori, der beskrev opførelsen at mikroskopiske partikler i komplicerede eksperimenter, til at være fundamentet for en helt ny teknologi. En af hjørnestenene i denne nye kvanteteknologi er de stærke korrelationer, kaldet entanglement, der kan eksistere i mellem adskilte kvantesystemer. Disse korrelationer kan udnyttes til at skabe ubetinget sikre kommunikationkanaler, forbedre sensitiviteten af præcisionsmålinger og konstruere kraftfulde kvantecomputere, der kan løse ekstremt svære problemer. Kvanteteknologien er dog stadig kun i sin spæde begyndelse, hvilket bl.a. skyldes kvantekorrelationernes skrøbelighed overfor støj. Meget forskning fokuserer derfor på at finde robuste kvantesystemer og protokoller som vil være i stand til at bringe kvanteteknologien ud af de specialiserede laboratorier og frem til praktisk anvendelse. I denne afhandling beskriver jeg mit og mine samarbejdspartneres arbejde i denne retning. Den første del af afhandlingen beskriver vores arbejde omkring optimeringen af en ny type protokol til at distribuere entanglement over store afstande. Vi har modificeret en tidligere protokol således, at de lokale operationer kan gøres hurtigt, hvilket øger distributionsraten signifikant. Herefter beskriver vi vores arbejde omkring at forbedre stabiliteten af atomare ure med entanglement. Entanglement kan potentielt set bringe stabiliteten af atomare ure til den såkaldte Heisenberg grænse, hvilket er den absolutte øvre grænse for stabiliteten tilladt af Heisenberg's usikkerhedsrelation. Der har dog været uklart, hvorvidt entanglements øgede sensitivitet overfor støj ville bringe denne grænse ud af rækkevidde. Vi har udarbejdet en protokol baseret på tilpassede målinger som undgår dette problem og tillader nær-Heisenberg begrænset stabilitet. Derudover beskriver vi, hvordan betjeningen af et atomart ur kan ændres således, at en eksponential forbedring af stabiliteten kan opnås selv uden entanglement. I den næste del af afhandlingen beskriver vi vores arbejde omkring en ny type betinget kvantegate med indbygget fejldetektering. Sådanne kvantegates kan bruges til robust kvantecomputation eller effektive entanglement distributionsprotokoller. I den sidste del af afhandlingen beskrives vores arbejde omkring kvantehukommelser og enkelt-foton kilder ved stuetemperatur. Vi har introduceret bevægelsesmidling som kan bruges i systemer, hvor fluktuationer forårsaget af termisk bevægelse er et problem. Specielt viser vi, hvordan et system baseret på mikroceller fyldt med Cs-atomer kan bruges til at lave effektive kvantehukommelser og enkeltfoton kilder ved stuetemperatur. Til sidst beskriver vi vores arbejde med at optimere entanglement distributionsprotokoller baseret på optiske kaviteter og enkelte atomer. Vi har sammenlignet forskellige skemaer til at skabe entanglement og implementeret en række kvantegates for at kunne teleportere entanglement over store afstande. Vi har derefter fundet den kombination, der giver den højeste distributionsrate som viser sig at være højere end en af de hurtigste distributionsprotokoller baseret på atomare ensembler.

Acknowledgements

This thesis concludes my three years of Ph. D study at the Niels Bohr Institute at the University of Copenhagen under the supervision of Anders S. Sørensen. The project was supported financially by the Lundbeck Foundation. The thesis describes the main body of my Ph. D. work, which was carried out in collaboration with a number of very talented researches both here and abroad. Therefore, I wish to express my sincere aknowledgement of these people.

First of all, I would like to express my thanks and gratitude towards my advisor Anders S. Sørensen. Anders' deep understanding of a vast group of different quantum mechanical systems has lead to brilliant research proposals, which I have been priviledged to be able to investigate during my Ph.D. As an advisor, Anders has not only equipped me with a set of useful tools for further research. Most importantly he has also groomed me for independent thinking and developement of ideas. Furthermore, Anders has been very generous with his time and has always been ready to discuss the obstacles that presented themselves along the way. One could not have asked for a better Ph. D. advisor.

During my Ph. D. study, I visited Mikhail D. Lukins group for six months at the Department of Physics at Harvard University. I am very grateful to Mikhail Lukin for letting me visit his group, which allowed me to interact with a number of gifted scientists including Mikhail Lukin himself, who was a great inspiration. I would in particular like to thank Peter Kómár, Eric Kessler and Jeff Thompson for fruitful discussions and collaboration.

The main part of my Ph. D. study was carried out at the Niels Bohr Insitute and I would like to thank all the people that I have had the privilege to meet here. Both my fellow members of Anders' group but also many of the members of the experimental quantum optics group of Eugene Polzik, with whom I have collaborated with.

Finally, I would like to thank my family and friends for their support and continous interest in my work. I am very grateful for the oppertunities they have given me to talk about my work and their constructive questions and comments, which followed. Especially, I would like to thank my wife Stine Mai Borregaard for her loving support throughout my entire work. Stine has always been very understanding when I ran into obstacles along the way and she has been a tremendous support for me.

Johannes Borregaard
October 2014

List of publications

Some of the main results described in this thesis has been published in the following publications

- J. Borregaard, J. B. Brask and A. S. Sørensen, "Hybrid quantum repeater protocol with fast local processing", *Phys. Rev. A* **86**, 0.12330 (2012)
- J. Borregaard and A. S. Sørensen, "Near-Heisenberg-Limited Atomic Clocks in the Presence of Decoherence", *Phys. Rev. Lett.* **111**, 090801
- J. Borregaard and A. S. Sørensen, "Efficient Atomic Clocks Operated with Several Atomic Ensembles", *Phys. Rev. Lett.* **111**, 090802

Furthermore, the thesis contains results presented in the following manuscripts aimed at publication

- J. Borregaard, P. Kómár, E. Kessler, A. S. Sørensen and M. D. Lukin, "Heralded Quantum Gates with Integrated Error Detection", *in preparation...*
- J. Borregaard, P. Kómár, E. Kessler, M. D. Lukin and A. S. Sørensen, "High rate quantum repeater based on optical cavitites", *in preparation...*
- J. Borregaard, J. M. Petersen, M. Zugenmaier, H. Shen, G. Vasilakis, K. Jensen, E. Polzik and A. S. Sørensen, "Room Temperature Quantum Memory and Scalable Single Photon Source Based on Motional Averaging", *in preparation...*

Finally, work on a general non-classicality test of quantum systems, which is not presented in this thesis, is described in the following manuscript aimed at publication

- L. Fresta, J. Borregaard and A. S. Sørensen, "Elementary test for non-classicality", *in preparation...*

Contents

List of Figures

List of Tables

Chapter 1

Introduction

A little over a hundred years ago in 1913, Niels Bohr wrote a revolutionary paper on the structure of the hydrogen atom [1]. In this paper, Bohr discretized the energy levels of the electron orbiting the nucleus. A few years before, Einstien had proposed the excitence of photons as quanta of light in order to explain the photoelectric effect [2]. The birth of quantum mechanics had begun. This new theory was fundamentally different from the deterministic nature of established physical theories referred to as classical physics. Heisenberg's famous uncertainty relations [3] reject the idea of being able to deterministically predict the bevaiour of microscopical particles, which was otherwise believed to be possible according to classical physics. As the theory developed, strange and counter-intuitive phenomenons such as entanglement referred to as "*spooky action at a distance*" by Einstein emerged. It is well known, that Einstein and Bohr had lengthy discussions trying to understand the predictions of this new theory.

Whether quantum mechanics is well understood today is a hard question to answer. Since Bohr and Einstein's discussions, the field of quantum mechanics has undergone a vast expansion and new theories and mathematical frameworks have been developed. Many predictions made by quantum mechanics have been validated in experiments and new quantum mechanical systems have been developed. It is thus clear that the physics community understands how to use quantum mechanics. The deeper philosophical understanding of quantum mechanics is, however, still a topic, which could foster lengthy discussions among physicist even today.

People have none the less got used to quantum mechanincs at a level where part of the research have moved from simply describing quantum mechanical phenomenons in nature to actually employing quantum mechanincs in the developement of new technologies. These new quantum technologies have revolutionary potentials for a broad range of fields ranging from ultra precise sensing and metrology [4, 5] over quantum computation

[6, 7] to completely secure communication channels [8, 9]. Commen to many of these technologies is that they exploit the very same counter-intuitive phenomenon, which was discussed exhaustively by Bohr and Einstein, namely entanglement. Entanglement is thus one of the strangest but at the same time one of the strongest assets of quantum mechanical systems.

Quantum computation and quantum communication are branches of quantum information theory, which in general describes how information is stored and processed in quantum systems. The holy grail of quantum computation is to construct a computer based on quantum systems, which can have a fundamentally different computational power than any classical computer. As a result, such a computer would be able to easily solve problems, which are extremely hard on a classical computer [6, 10]. At the present stage, a quantum computer is, however, not something to expect in the stores tomorrow, even though some commercial variants of a quantum computer has already been developed (at the modst cost of a couple of millions of dollars)[1]. The main problem is that information stored in quantum systems is very fragile and quickly decoheres due to the influence of the enviroment surrounding the systems. When the information is processed, there is enevitable some coupling to the enviroment and this can have a detrimental effect on the peformance of e.g. a quantum computer. Nonetheless, new computational schemes and physical systems are continously developed and proof-of-principle experiments have already demonstrated promising candidates for realizing the constituents of a quantum computer [11, 12].

A perhaps more mature technology than the quantum computer is quantum cryptography [9, 13, 14]. Because the information stored in quantum systems is so sensitive to the enviroment, it can be used to ensure the privacy of information transfer. To be specific, two parties, usually referred to as Alice and Bob, can distribute a secret key between them by encoding information in quantum systems, which are then communicated between them. Any eavesdropper, who tries to get the quantum information, will inevitably disturb the system, which can subsequently be detected by Alice and Bob. Note that in principle nothing stops the eavesdropper from getting the quantum information but Bob and Alice will always find out. They can therefore simply discard all the information that could have been compromised by the eavesdropper and use the remaining, secure information to create a secret key. The secret key can then be used to encrypt information and Alice and Bob thus have an unconditional secure communication channel. A key ingredient in quantum cryptography schemes is, once again, entanglement, which needs to be distributed between Alice and Bob without any eavesdropper being able to access the information stored in the quantum systems. This is a very demanding task since the

[1] A device referred to as a quantum computer has been developed by the company D-Wave. See http://www.dwavesys.com/

direct transmission of a quantum signal is extremely hard over large distances due to losses. Usually photons are used as information carriers and for losses present in todays optical fibers, it would take many years to transmit just a single photon over a distance of 1000km. The solution to this problem was proposed in Ref. [15] and is referred to as a quantum repeater. The quantum repeater basically divides the distance into smaller segments, where direct transmission of a quantum signal is possible. The information is then teleported between the segments until it is distributed over the entire distance. Since the first proposal in Ref. [15], there have been numerous proposals of quantum repeaters [16–19] and many promising proof-of-principle experiments [20–23] have been developed. The need of quantum cryptograhy can actually be linked with the possiblity of a quantum computer. The commonly used RSA crytography scheme relies on the assumption that it is hard to factorize large numbers into prime numbers. However, in 1994, Shor [6] showed that this problem is actually not a hard problem on a quantum computer. Quantum cryptography is thus needed to ensure secure communication if a quantum computer should appear.

During my Ph. D. study, I have been investigating various aspects of quantum technology. My primary focus point has been quantum repeaters and the various constituents of these, such as quantum memories and teleportation protocols. The goal has been to find efficient schemes, which allow for high communication rates even over large distances. In addition, I have examined how some existing experimental systems could be the building blocks in quantum technology. Finally, I have worked on atomic clocks, where I have investigated how entanglement can increase the precision of current clocks and analysed how to operate a clock efficiently.

1.1 Thesis Outline

The first part of the thesis, consisting of Chap. 2, describes some of the general concepts referred to in the remaining parts of the thesis. Some of these have already been discussed briefly in the above introduction such as entanglement and quantum repeaters. These are, however, treated in more detail in Chap. 2. Furthermore, two different kinds of physical systems, single emitters and atomic ensembles are briefly introduced as building blocks of quantum repeaters. Finally, the basic concepts behind atomic clocks are presented.

The rest of the thesis describes me and my collaboraters's work on quantum repeaters, atomic clocks, quantum gates and quantum memories. Chap. 3 describes our work on optimizing an existing hybrid repeater protocol [24], which combines single photon detection with amplitude detection of electrical fields referred to as *homodyne detection*.

We present two ways of improving this protocol. In the previous protocol, entangled single-photon states are produced and grown into superpositions of coherent states, known as two-mode cat states. The entanglement is then distributed using homodyne detection. To improve the protocol, we replace the time-consuming nonlocal growth of cat states with local growth of single-mode cat states, eliminating the need for classical communication during growth. Entanglement is generated in subsequent connection processes. Furthermore, the growth procedure is optimized. These two modification leads to a significantly better performance than the original protocol.

In Chap. 4, we describe our work on realizing near-Heisenberg limited stability of atomic clocks. The ultimate stability of atomic clocks is limited by the quantum noise of the atoms. To reduce this noise it has been suggested to use entangled atomic ensembles with reduced atomic noise. Potentially this can push the stability all the way to the limit allowed by the Heisenberg uncertainty relation, which is denoted the Heisenberg limit. In practice, however, entangled states are often more prone to decoherence, which may prevent reaching this performance. In Chap. 4, we present an adaptive measurement protocol that, in the presence of a realistic source of decoherence, enables us to get near Heisenberg limited stability of atomic clocks using entangled atoms. The protocol may thus realize the full potential of entanglement for quantum metrology despite the detrimental influence of decoherence.

We pursued the topic of atomic clocks a bit further and looked into the basic operation of a clock. Atomic clocks are typically operated by locking a local oscillator (LO) to a single atomic ensemble. In Chap. 5, we describe a scheme where the LO is locked to several atomic ensembles instead of one. This results in an exponential improvement compared to the conventional method and provides a stability of the clock scaling as $(\alpha N)^{-m/2}$, with N being the number of atoms in each of the m ensembles and α is a constant depending on the protocol being used to lock the LO.

Chap. 6 describes our work on heralded quantum gates in optical cavities. This work was inspired by the nanovavity experiment conducted in Prof. Lukin's group at Harvard [25]. We describe a scheme where an auxiliary atom heralds that a successful gate occurred. In this manner, the errors, which would have corrupted a determinsitc gate, are converted into a non-unity probability of success, and once successful, the gate will have a much higher fidelity than a similar deterministic gate. Specifically, we show how to make a heralded and near-deterministic controlled phase gate between two atoms, where the conditional error can be arbitrarily close to zero for realistic atomic systems and where the success probability approaches unity as the cooperativity of the system, C, becomes large. Furthermore, we show how to make a heralded, cavity-assisted and near-deterministic N-qubit Toffoli gate with a favorable error scaling of $1/C$.

The work desribed in Chap. 7 is also inspired by a current experimental system. The experimental quantum optics group of Prof. Polzik at NBI is currently investigating microcells filled with Cs-atoms at room temperature. In Chap. 7, we describe the concept of motional averaging to enable quantum memories and coherent single photon sources with atomic ensembles at room temperature. We show that by choosing the interaction so that atoms can cross the light beam many time and by suitable spectral filtering, we erase the "which atom" information and obtain an efficient and homogenous coupling between all atoms and the light. Single excitations can thus be created as collective spinwaves, which can later be readout to produce coherent single photons in a scalable fashion.

Finally, we describe our work on optimizing repeater structures based on single emitters in optical cavitites in Chap. 8. We make a detailed analysis of the constituents of such a quantum repeater in order to find the optimal repeater architecture for a given distance. We consider various schemes for both entanglement generation, purification and entanglement swapping and find the combination resulting in the highest secret key rate for a given quality of the cavities and number of qubits pr repeater station.

Chap. 9 is a brief summary of the results presented in Chaps. 3-8 and a small outlook based on these.

Chapter 2

General concepts

In this chapter, I will introduce some of the common concepts used troughout the thesis. These concepts will be quite general but will be put into a more specific context in the subsequent chapters. There will not be given an introduction to the fundamentels of quantum optics and, if necessary, the reader is referred to e.g. the book by Gerry and Knight [26].

2.1 Qubits and Entanglement

Two essential ingredients in quantum information theory are the concepts of qubits and entanglement. These are the key constituents in almost any aspect of information processing, where quantum systems are considered to potentially outperform classical systems.

The qubit is a quantum analog of the classical bit, which is used to express information in binary form. Any system with two orthogonal states such as "spin up" and "spin down" can be used to make the physical qubit and the two states are denoted as $|0\rangle$ and $|1\rangle$ in the computational basis. This way of handling information is very effficient for computation since it allows for decomposing complicated functions into a series of simple operations involving only one or two bits at a time. A so called *universal set of gates* is a collection of two and single qubit operations called gates, which can be used to construct any quantum computation [27]. An example of such a set is single qubit rotations and the CNOT gate. The CNOT gate is a two-qubit gate that makes the transformation

$$\begin{aligned} |0\rangle_a|0\rangle_b &\rightarrow |0\rangle_a|0\rangle_b, \qquad |0\rangle_a|1\rangle_b \rightarrow |0\rangle_a|1\rangle_b \\ |1\rangle_a|0\rangle_b &\rightarrow |1\rangle_a|1\rangle_b, \qquad |1\rangle_a|1\rangle_b \rightarrow |1\rangle_a|0\rangle_b, \end{aligned} \tag{2.1}$$

where the qubit with subscript a is referred to as the control qubit and the other is called the target qubit. In Chap. 6, we will also refer to a *Toffoli* gate and a *CZ*-gate. The Toffoli gate is a multi-qubit gate, which leaves all qubit states unchanged except the state $|11\ldots1\rangle$, which obtains a phase of π. The Cz-gate is simply the two-qubit Toffoli gate. Note that the CNOT gate and the CZ-gate are identical up to single qubit rotations and the CZ-gate can thus also be used to form a universal set.

Most often, one discriminates between *stationary* and *flying* qubits where an example of the first could be the electronic levels of an atom and an example of the latter could be the polarization states of a single photon. The crucial difference between the bit and the qubit is that the physical qubit is a quantum system, i.e it is goverened by the rules of quantum mechanics. As a result, the qubit does not always evolve according to being in either state $|0\rangle$ or $|1\rangle$ but can be in a superposition of the two. A general qubit state, $|\psi\rangle$ can thus be written as

$$|\psi\rangle = \alpha|0\rangle + \beta|1\rangle, \tag{2.2}$$

where $|\alpha|^2$ ($|\beta|^2$) is the probability of measuring the qubit in state $|0\rangle$ ($|1\rangle$) and $|\alpha|^2 + |\beta|^2 = 1$. The ability to evolve as a superposition between two orthogonal states is one of the strongest assets of using quantum systems for information processing.

Entanglement is an extenstion of the superposition principle to include more than one qubit. The joint state of two qubits is called a maximally entangled state, if it is in an equal superposition between two orthogonal states. Such a state can be written as

$$|\Psi^+\rangle = \frac{1}{\sqrt{2}}\left(|0\rangle_a|1\rangle_b + |1\rangle_a|0\rangle_b\right), \tag{2.3}$$

where $|0\rangle_a$ ($|0\rangle_b$) refers to qubit a (b) being in state 0. Imagining a continous supply of these states, we could repeatedly measure the states of the two qubits. The measurements collapse the superpositions and we would find that both qubits had a 50-50 distribution of being in state $|0\rangle$ and $|1\rangle$. Nonetheless, there would be a complete correlation between the states of the two qubits. Everytime qubit a was found in state $|0\rangle$, qubit b was measured to be in state $|1\rangle$ and vice versa. Note that this situation is independent of the distance between the two qubits. In principle, one could be on the Moon while the other was down on Earth and they would still have this correlation between them. In a way, the two qubits simultanously decide to be in opposite states upon a measurement since the state of the two qubits is in a superposition before the measurement. This sort of correlation has no classical counter part and is what allows for exotic phenomenon like teleportation with quantum systems [28]. The state in Eq. (2.3) is one of the four possible, maximally entangled two-qubit states referred to as the

Bell states. The remaning three Bell states are

$$|\Psi^-\rangle = \frac{1}{\sqrt{2}}\left(|0\rangle_a|1\rangle_b - |1\rangle_a|0\rangle_b\right), \tag{2.4}$$

$$|\Phi^\pm\rangle = \frac{1}{\sqrt{2}}\left(|0\rangle_a|0\rangle_b \pm |1\rangle_a|1\rangle_b\right), \tag{2.5}$$

Note, that entanglement can in general exist for an arbitrary number of qubits, e.g. the GHZ states, $\frac{1}{\sqrt{2}}\left(|0\rangle|0\rangle\ldots|0\rangle + |1\rangle|1\rangle\ldots|1\rangle\right)$ are examples of multi-qubit, entangled states.

2.2 Quantum Repeaters

Entanglement can be used in protocols for secret key sharing between to remote parties [9, 13]. The idea is to distribute an entangled pair between two parties, ususally referred to as Alice and Bob. This is repeated many times so that they both end up with a big collection of qubits. By measuring their qubits in different bases and sharing their measurement strategy, they can obtain a secret key to be used for encryption/decryption. The correlation contained in the qubit pairs are disturbed if any eavesdropper tries to get some information about the key by, e.g. measuring the state of a qubit before it arrives at Bob. Alice and Bob can therefore check for eavesdroppers by comparing the states of their qubits for a small subset from which they estimate the information an eavesdropper could have obtained. In this way, entanglement can be used to make unconditionally secure communication channels [13].

Distributing entanglement over a large distance is, however a challenging task because quantum information is very sensitive to noise. Entanglement can be established between to parties by sending a quantum signal, e.g. a single photon in a specific quantum state, between them. The probability to loose the photon will, however, scale exponentially with the distance if no intermediate signal processing is employed [15]. This means that the rate of entanglement distribution will decrease exponentially with the distance. In classical communication, intermediate repeater stations are therfore used to amplify and purify the signal before it is transmitted to the next station. The same architecture is necessary to transmit a quantum signal but an amplification of the signal would mean to interact with it and this adds noise that destroys the quantum information [29, 30]. In a quantum repeater, the losses are instead avoided by teleporting the entanglement from one repeater station to the next. This is called entanglement swapping [15, 16].

2.2.1 Entanglement swapping

The first step in a quantum repeater is to divide the total distribution distance, L_{tot}, into smaller segments, called elementary links, in which entanglement can be established by direct transmission of a quantum signal (see Fig. 2.1). The generation of entanglement is often probabilistic and done with flying qubits. Therefore, it is necessary to use so-called quantum memories, where the quantum information is stored as stationary qubits until there is entanglement in two neighboring links. Once entanglement has been established in two neighboring links, the entanglement is swapped by making a Bell state measurement on a qubit from each entangled pair (Fig. 2.1). A Bell state measurement is a projection of a two-qubit state onto one of the four Bell states. Note that this requires som ingenuity since a simple measurement of the individual qubit states will only descriminate between $|\Psi^{\pm}\rangle$ and $|\Phi^{\pm}\rangle$. However, one can, e.g. make use of a CNOT gate to perform the entanglement swap. Entanglement swapping can be expressed in simple mathematical terms. Assume, that two neighboring links contain the Bell states $|\Psi^{+}\rangle_{ab}$ and $|\Psi^{+}\rangle_{cd}$, where qubits a, b belongs to the first link and qubits c, d belongs to the second link. The joint state of both links is then

$$|\Psi^{+}\rangle_{ab}|\Psi^{+}\rangle_{cd} = \frac{1}{2}\left(|00\rangle_{bc}|11\rangle_{ad} + |00\rangle_{bc}|11\rangle_{ad} + |01\rangle_{bc}|10\rangle_{ad} + |10\rangle_{bc}|01\rangle_{ad}\right) \tag{2.6}$$

$$= \frac{1}{2}\left(|\Phi^{+}\rangle_{bc}|\Phi^{+}\rangle_{ad} - |\Phi^{-}\rangle_{bc}|\Phi^{-}\rangle_{ad} + |\Psi^{+}\rangle_{bc}|\Psi^{+}\rangle_{ad} - |\Psi^{-}\rangle_{bc}|\Psi^{-}\rangle_{ad}\right). \tag{2.7}$$

So far, this is only rewriting the terms of the intial state with the notation $|00\rangle_{ab} = |0\rangle_a|0\rangle_b$. Nonetheless, Eq. (8.14) illustrates that a projection of the qubits b and c onto a Bell state will leave the qubits a and d in one of the four Bell states. Thus, by performing a Bell state measurement on qubit b and c and sending the measurement result to the stations containing qubit a and d, appropriate single qubit rotations [1] can be applied to obtain the desired Bell state of qubit a and d. In summary, entanglement has been swapped to qubit a and d by means of a local Bell measurement, sending a classical signal (the measurement result) and local single qubit rotations. No quantum signal needs to be transmitted between qubit a and d and the classical signal can easily be amplified using conventional techniques. The same procedure is now repeated until entanglement has been established over the total distance. The number of swap levels, n, determines the length, L_0, of the elementary lengths, i.e. $L_0 = L_{tot}/2^n$. Fig. 2.1 shows two swap levels.

[1] A single qubit rotation would e.g. be to flip $|0\rangle \leftrightarrow |1\rangle$ of one of the qubits

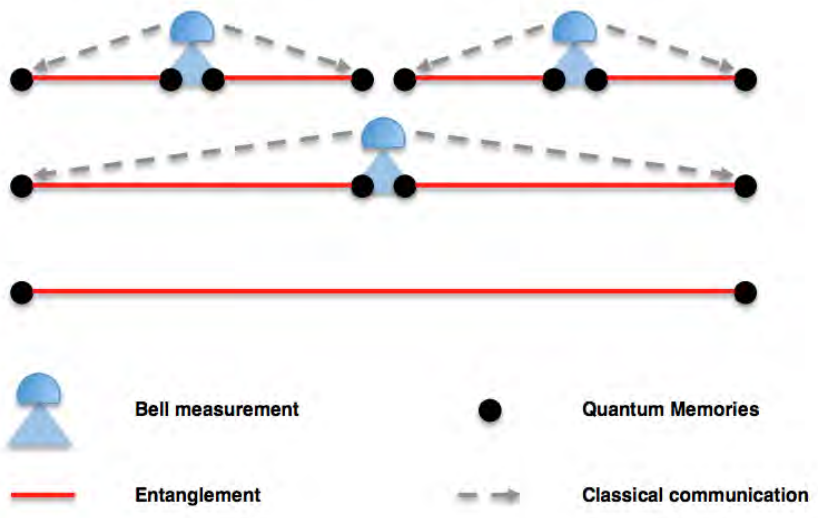

FIGURE 2.1: The total distance is divided into smaller segments, where entanglement can be established by direct transmission of a quantum signal. By performing Bell measurements, the entanglement is swapped to larger distances. The result of the measurements are communicated to the end stations so that the appropriate single qubit rotations can be applied. Note, that the repeater requires quantum memories, where the signals can be stored and processed.

2.3 Single emitters and atomic ensembles

The quantum repeater can potentially overcome the problem of losses and enable secure quantum networks. However, the constituents in a quantum repeater such as entanglement generation, quantum memories and Bell state measurements are challenging to realize. As a result, much of the work presented in this thesis, focusses on the building blocks of a quantum repeater. Generally, we have considered two kinds of quantum systems that can be used to make a repeater namely single emitters and atomic ensembles.

2.3.1 Single emitters

A single emitter could be an atom, ion or a doped diamond crystal or semiconductor material [11, 12, 31–33]. What characterizes a single emitter is that it can be described as a single object with a given internal energy structure. Single emitters can be very efficient single photon sources since they never emit more than a single photon. An atom can decay from an excited state by emitting a single photon and the reverse process, where a photon is absorbed by the atom and excites it, can also take place. In that sence, the single emitter can be considered as a quantum memory with a stationary qubit consisting of two stable ground states, which can be converted into a flying qubit

by emitting a photon as depicted in Fig. 2.2, which shows some of the hyperfine energy levels of a ^{133}Cs atom.

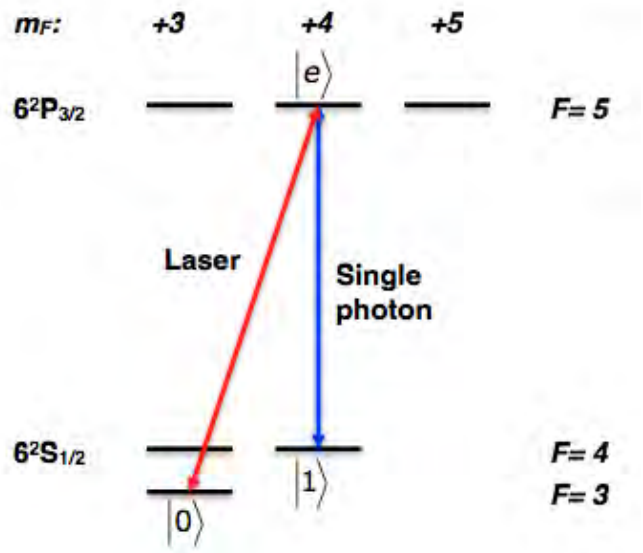

FIGURE 2.2: A ^{133}Cs atom can be used as a single emitter by exploting the hyperfine level structure. The $6^2S_{1/2}$ manifold is stable and can be used as qubit states. The atom can be brought to the excited manifold $6^2P_{3/2}$ by absorbing light with a wavelength of 852 nm. The figure shows how a control laser can be applied to drive the $|0\rangle \leftrightarrow |e\rangle$ transition. By emitting a single photon, the state can move from $|0\rangle \rightarrow |1\rangle$ and by absorbing a photon, the state can move from $|1\rangle \rightarrow |0\rangle$. In this fashion a flying qubit can be converted to a stationary qubit and vice versa. The three levels $|0\rangle, |1\rangle$, and $|e\rangle$ constitutes what is referred to as a Λ-system.

Single emitters can, however, in general emit light in any spatially direction. To use a single emitter as a quantum memory, it is therefore necessary to have an efficient method of guiding the light emission to a specific direction/mode. To this end, one can use, e.g. waveguides and optical cavities [34–38]. Waveguides and cavities confines the light to a small number of well-defined modes. Other modes are simply not allowed due to, e.g. interference effects. Placing the single emitter inside one of these constructions can solve the problem of collecting the emitted light. At the same time, the process of storing light in the emitter also benefits from this. There are several ways of obtaining a cavity to confine light. Nonetheless, a generic cavity is simply two mirrors, which reflect the light such that the intracavity fields is build up by counter-propagating electromagnetic fields, which interfere to form a standing wave between the two mirrors [26]. This standing wave has nodes and anti-nodes and by placing the single emitter in the vicinity of one of the nodes, a very strong coupling can be achieved. Recently, nanocavities realized in photonic crystals have demonstrated very strong coupling between a single atom and a light field [25, 36]. In such cavities, light is confined by changing the index of refraction for the light in a periodic manner by e.g. edging holes in a semiconductor material.

Single emitter systems have long been considered for quantum information processing because they usually offer a large degree of control. Furthermore, systems like trapped ions and atoms have demonstrated very long coherence times [11, 12, 31] allowing for extended manipulation of the quantum information before initialization of the system is necessary. Experiments with trapped ions have demonstrated many of the constituents of a quantum computer such as entanglement and two qubit gates [11, 12]. Nonetheless, these systems are hard to scale since the ions need to be kept in traps, which can only contain a limited number of qubits. A solution to this could be to move ions between different traps in the line of Ref. [12]. Other more scalable systems, which have been considered for quantum information processing, are semiconductor systems like quantum dots and NV centers [32, 33]. The coherence times of these systems are much smaller than for ions or atoms but this is not necessarily a problem as long as gates can be implemented fast enough. Long coherene times are however needed for quantum memories in a repeater. Recent experiments on quantum dots in nanophotonic waveguides have also demonstrated efficient collection of light emitted from the dots, which could realize single photon sources for quantum information processing [39].

2.3.2 Atomic ensembles

With single emitters, a cavity can be used to enhance the coupling to light. Another way of improving this coupling is to increase the number of emitters that the light can interact with. This is the basic idea behind using atomic ensembles for quantum information processing. Here, the stationary qubit is no longer the internal energy levels of a single atom but the collective state of all the atoms. Atomic ensembles can consist of billions of atoms and can thus increase the interaction with light significantly. This is often described in terms of the optical depth, which is the fraction of light being scattered or absorbed passing through a medium. The optical depth is directly proportional to the number of atoms [40].

When describing an ensemble of atoms, it is commen to refer to the collective spin of the atoms. This terminology is used because any two-level system can be thought of as the spin-1/2 system like e.g. an electron, which has either spin up or down wrt. some reference frame. Referring to the single emitter picture of ^{133}Cs depicted in Fig. 2.2 we can think of the qubit states in an ensemble of ^{133}Cs atoms to be

$$\begin{aligned} |\mathbf{0}\rangle &= |0\rangle_1|0\rangle_2\ldots|0\rangle_N \qquad (2.8)\\ &= |0_1 0_2 \ldots 0_N\rangle, \\ |\mathbf{1}\rangle &= \frac{1}{\sqrt{N}}\sum_{j=1}^{N}|0_1 0_2 \ldots 1_j \ldots 0_N\rangle \qquad (2.9) \end{aligned}$$

$|\mathbf{0}\rangle$ is the state where all atoms are in the ground state $|0\rangle$ while $|\mathbf{1}\rangle$ is the symmetric superposition of all the possible states with a single atom being in state $|1\rangle$ and all the rest being in state $|0\rangle$. This state is called a Dicke state. Another very useful picture of a collective atomic state is as a vector on a so-called Bloch sphere. To clarify the spin-1/2 analogy we let $|0\rangle = |\uparrow\rangle$ and $|1\rangle = |\downarrow\rangle$ and define the following spin operators of the j'th atom

$$\hat{S}_x^{(j)} = \frac{\hbar}{2}\left(|\uparrow\rangle_j\langle\downarrow| + |\downarrow\rangle_j\langle\uparrow|\right), \tag{2.10}$$

$$\hat{S}_y^{(j)} = \frac{i\hbar}{2}\left(|\downarrow\rangle_j\langle\uparrow| - |\uparrow\rangle_j\langle\downarrow|\right), \tag{2.11}$$

$$\hat{S}_z^{(j)} = \frac{\hbar}{2}\left(|\uparrow\rangle_j\langle\uparrow| - |\downarrow\rangle_j\langle\downarrow|\right). \tag{2.12}$$

These operators can be used to define a coordinate system with an x, y, and z axis. The spin state of the j'th atom is now a spin vector $\mathbf{S}_j = (S_x^{(j)}, S_y^{(j)}, S_z^{(j)})$ where $S_a^{(j)}$ is the coordinate from projecting on $\hat{S}_a^{(j)}$. The vector has a fixed length of 1/2 since a two level atom will always be in some spin state $|\psi\rangle = \alpha|\uparrow\rangle + \beta|\downarrow\rangle$ with $|\alpha|^2 + |\beta|^2 = 1$. The atomic spin state can therefore be depicted as a point on a sphere called a Bloch sphere (see Fig. 2.3)[2].

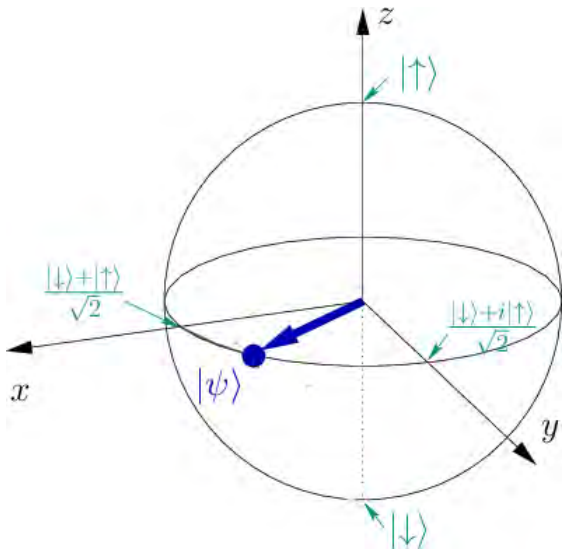

FIGURE 2.3: The state of a two level atom can be described as a vector lying on a sphere called a Bloch sphere. The axis are defined by the atomic spin operators $\hat{S}_x, \hat{S}_y$, and $\hat{S}_y$.

We can generalize the Block sphere to describe N atoms by defining collective spin operators $\hat{J}_a = \sum_{j=1}^{N} \hat{S}_a^{(j)}$ where $a = x, y, z$. The total angular momentum vector is $\mathbf{J} = \sum_{j=1}^{N} \mathbf{S}_j$ and lies on a Block sphere with radius $N/2$. Like the single atom spin

[2]The picture is a modified version of the one found at
http://nbi.ku.dk/forskningsgrupper/Kvanteoptik/english/qoptlab/research/exp-clock/bloch/

operators $\hat{S}_a$, the collective spin operators obeys the standard commutation relation

$$\left[\hat{J}_x, \hat{J}_y\right] = i\hat{J}_z. \tag{2.13}$$

The collective spin operators is a nice way of describing the total atomic spin state. For a coherent spin state with e.g. all atoms in state $|\uparrow\rangle$, we can treat $\hat{J}_z$ as a classical number, $\hat{J}_z \approx \langle \hat{J}_z \rangle = N/2$ and define new canonical position and momentum operators $\hat{X}_A = \hat{J}_x/\sqrt{\langle \hat{J}_z \rangle}$, $\hat{P}_A = \hat{J}_y/\sqrt{\langle \hat{J}_z \rangle}$ and it follows from Eq. (2.13) that they obey the standard position and momentum commutation relation. We can then define the collective annihilation operator

$$\hat{a}_A = \frac{\hat{X}_A + i\hat{P}_A}{\sqrt{2}} = \frac{1}{\sqrt{N}} \sum_{j=1}^{N} |0\rangle_j\langle 1|, \tag{2.14}$$

and it is seen that the Dicke state defined in Eq. (2.9) is now $\hat{a}_A^\dagger|\mathbf{0}\rangle$. Note that the collective operators are only a good description when all the atoms in the ensemble evolve equally. For an extensive review on atomic ensembles and light-matter interaction the reader is referred to Ref. [40].

2.4 Atomic clocks

Atomic ensembles can be used as quantum memories in quantum repeaters but they are also used in metrology experiments like atomic clocks [5, 41, 42]. Atomic clocks provide some of the mose precise measurements in physics and have applications ranging from ultra precise GPS systems to gravitational wave detectors. The underlying assumption in an atomic clock is that the atoms have well defined transition frequencies, which are constants of nature. The idea is to lock a laser to such a transition frequency resulting in an ultra stable laser. Time can then be measured by counting the laser periods.

Some of the first atomic clocks were based on atomic ensembles of ^{133}Cs atoms, which lead to a definition of the second as being 9192631770 periods of radiation corresponding to the transition between the two hyperfine levels of the ground state $6S_{1/2}$. Since then a lot of different types of atomic clocks have emerged, which have continously improved the precision and accuracy of the clocks [43–46]. So-called ion clocks use only one or a few ions to lock the laser while others, like optical clocks, use thousands of atoms held in an optical lattice. The *stability* of a clock is a measure for how well the laser is locked at a given frequency while the *precision* of a clock is how well this frequency match the atomic transition frequency. The dominant limitation of present atomic clocks is the stability and most research focus on improving this.

The fundamental operation used in atomic clocks is Ramsey spectroscopy [47]. Consider a collection of N two level atoms, where we want to measure the transition frequency ω_0 between the two levels with a laser. We describe the atoms as a spin system and prepare them in a coherent spin state with a mean spin $\langle \hat{J}_z(0) \rangle = -N/2$ and $\langle \hat{J}_x(0) \rangle = \langle \hat{J}_y(0) \rangle = 0$. We now apply a laser, hereafter referred to as the LO (Local Oscillator), with frequency ω to the atoms. In a reference frame rotating with the LO frequency, the interaction between the atoms and the laser is described by the Hamiltonian [5, 48]

$$\hat{H} = \frac{\hbar\delta}{2}\left(\hat{J}_z + 1\right) - \frac{\hbar}{2}\operatorname{Re}\{\Omega\}\,\hat{\tilde{J}}_x - \frac{\hbar}{2}\operatorname{Im}\{\Omega^*\}\,\hat{\tilde{J}}_y, \tag{2.15}$$

where Ω is the Rabi frequency of the interaction, $\delta = \omega_0 - \omega$ and $\hat{\tilde{J}}_x$ ($\hat{\tilde{J}}_y$) is the $\hat{J}_x$ ($\hat{J}_y$) spin operator in the rotating frame. Note, that we have assumed all atoms to have the same interation with the LO. The constant term in the Hamiltonian can be ignored since it only gives an overall phase to the system. Using the Bloch sphere picture with axis defined by $\hat{\tilde{J}}_x, \hat{\tilde{J}}_y$, and $\hat{J}_z$, the equations of motions in the Heisenberg picture can be written as [5, 48]

$$\frac{d}{dt}\tilde{\mathbf{J}} = \mathbf{\Omega} \times \tilde{\mathbf{J}}. \tag{2.16}$$

Here $\mathbf{\Omega} = (-\operatorname{Re}\{\Omega\}, -\operatorname{Im}\{\Omega\}, \delta)$ and $\tilde{\mathbf{J}} = \left(\tilde{J}_x, \tilde{J}_y, J_z\right)$ is the spin vetor in the rotating frame. Eq. (2.16) describes the dynamics in Ramsey spectroscopy which consists of the following steps (see also Fig. 2.4a)

1. Apply a LO pulse for a short time $t_{\pi/2} = \pi/(2\operatorname{Im}\{\Omega\})$ such that the atomic state is rotated $\pi/2$ around the y axis. This is called a $\pi/2$-pulse.

2. For a time, T, called the *interrogation time*, the detuning δ makes the atomic state rotate $\phi = \delta T$ around the z-axis.

3. Apply a final $\pi/2$ pulse, which rotates the atomic state to lie in the xy-plane and measure the atomic spins, i.e. a measurement of $\hat{J}_z(2t_{\pi/2} + T) = \hat{J}_z(t_f)$

The expression for $\langle \hat{J}_z(t_f) \rangle$ is $\langle \hat{J}_z(t_f) \rangle = \cos(\phi)\langle \hat{J}_z(0) \rangle + \sin(\phi)\langle \hat{J}_y(0) \rangle = -N/2\cos(\phi)$. Fig. 2.4b shows the Ramsey resonance curve, which results from plotting $\langle \hat{J}_z(t_f) \rangle$ against ϕ.

The measurement of $\langle \hat{J}_z(t_f) \rangle$ can provide an estimate of ϕ, which can be used to lock the frequency of laser to the atomic transition. In an atomic clock, the laser should be kept at a frequency $\omega = \omega_0 - \pi/(2T)$ such that $\phi \sim \pi/2$ since at this point, the measured signal ($\langle \hat{J}_z(t_f) \rangle$) has a maximum sensitivity to fluctuations in ϕ. All practical lasers will experience frequency fluctuations and the drifted phase can therefore be written as $\phi = \pi/2 - \delta\phi$, where $\delta\phi$ is the contribution from the frequency fluctuations. $\delta\phi$ can

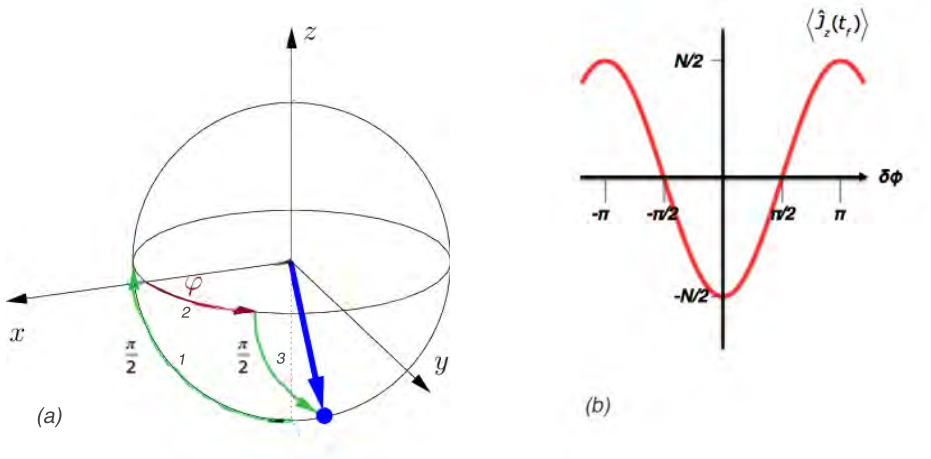

FIGURE 2.4: (a) The Ramsey sequence depicted on the Bloch sphere of the collective state and (b) sketch of the Ramsey resonance curve obtained with Ramsey spectroscopy.

be estimated from the measurement of $\langle \hat{J}_z(t_f) \rangle$ and a suitable frequency correction can be applied to the laser. Thus, the frequency fluctuations of the LO can monitored and corrected for by repeatedly doing Ramsey spectroscopy.

The stability of the clock depends on how well we can estimate $\delta\phi$. The atomic spin operator, that we measure at the end of the Ramsey sequence, is $\hat{J}_z(t) = \sin(\delta\phi)\hat{J}_z(0) + \cos(\delta\phi)\hat{J}_y(0)$, assuming that $\phi = \pi/2 - \delta\phi$. A good estimate of $\delta\phi$ is therefore

$$\delta\phi_e = \frac{\langle \hat{J}_z(t) \rangle}{\langle J_z(0) \rangle}. \tag{2.17}$$

The accuracy of the estimate is characterized by the variance $\Delta\delta\phi_e = \langle \delta\phi_e^2 \rangle^{1/2}$, where we have assumed that $\langle \delta\phi_e \rangle = 0$. For $\delta\phi \ll 1$, the dominant term of $\Delta\delta\phi_e$ is $\sim \Delta\hat{J}_y(0)/\langle \hat{J}_z(0) \rangle$, which for a coherent spin state is $\sim 1/\sqrt{N}$. This limit, where the accuracy of the phase estimate is limited by the uncertainty from the atomic measurement, is called the standard quantum limit. The standard quantum limit shows that the stability of the clock improves with the number of atoms in the clock. However, having many atoms also leads to other decoherence effects than the frequency fluctuations of the LO such as atomic dephasing. This limits the interrogation time T, which also affects the stability of a clock. The stability of a clock can be characterized by the *Allan deviation* defined as [49]

$$\sigma_\gamma(\tau) = \langle (\delta\bar{\omega}(\tau)/\omega)^2 \rangle^{1/2}, \tag{2.18}$$

where $\tau \ll T$ is the total time the clock is running and $\delta\bar{\omega}(\tau)$ is the mean frequency offset of the LO. The mean frequency offset of the LO after each Ramsey sequence is

estimated as $\bar{\omega}_e = \delta\phi_e/T$ and subsequently a correction is made to the LO to correct for this. This results in a scaling $\sim \frac{1}{\sqrt{TN}}$ of $\sigma_\gamma(\tau)$. The stability of a clock can thus be improved both by increasing the number of atoms or by increasing the interrogation time. For ion clocks, N is small but in return T is large while the opposite is, in general, the case for clocks based on atomic ensembles.

Chapter 3

Hybrid quantum repeater protocol with fast local processing

Quantum communication generally works in two regimes; the discrete and the continuous variable regime. In the discrete variable regime, information is carried by single photons and measurements rely on single photon detection (SPD). This facilitates detection and correction for loss, but the efficiency of most available single-photon detectors is low, reducing the rate of entanglement distribution. High-efficiency ($> 90\%$) SPD is possible, but requires detectors, such as superconducting transition-edge sensors, which are expensive and not widely available [50]. In the continuous variable regime, information is encoded in operators with a continuous spectrum such as the field quadratures of the electromagnetic field. These are measured using homodyne detection, which is very efficient in practice ($\sim 99\%$) but has the drawback that loss is not as easily detected as in the discrete variable regime. Recently, hybrid quantum repeater protocols, combining the two regimes, were proposed first for spin systems in cavities [19] and later for atomic ensembles [24]. The performance of the repeater protocol in Ref. [24] is comparable to the best proposed atomic-ensemble based repeaters in the discrete variable regime if these are operated using realistic SPD with limited efficiency [18, 51, 52].

In this chapter, I describe the work of me and my collaborators on two modifications to the protocol of Ref. [24]. The work has been carried out in collaboration with J. B. Brask and A. S. Sørensen and is described in Ref. [53], which is the basis of this chapter.

3.1 Introduction

The hybrid repeater protocol in Ref. [24] creates entanglement between two repeater stations in the form of single-photon superpositions $|01\rangle + |10\rangle$ ignoring normalization for simplicity. Through a probabilistic procedure, these states are then grown into states resembling

$$|\gamma(\theta,\alpha)\rangle \propto e^{i\theta}|\alpha\rangle_a|\alpha\rangle_b + e^{-i\theta}|-\alpha\rangle_a|-\alpha\rangle_b, \tag{3.1}$$

by means of local operations and classical communication. Here $|\alpha\rangle_a$ denotes a coherent state with amplitude α in mode a, and θ is a phase. We refer to states of the form in Eq. (3.1) as two-mode cat states since they are two-mode superpositions of two "classical" states $|\alpha\rangle, |-\alpha\rangle$. Because classical communication between distant stations is time consuming, the growth procedure is slow. In particular, the single-photon entanglement generation step, which has low success probability, needs to be repeated every time the growth step fails. In a related setup, a solution to this problem was suggested in Ref. [17]. To improve the communication rate, it was proposed to replace the low success, non-local entanglement generation by a rapid preparation of a suitable local states. Because local operations do not rely on communication with distant parties, they have a much higher obtainable rate. The locally generated states are more suitable for entanglement generation and can be connected with a much higher probability reducing the time spent on the slow non-local operations. We have followed a similar path and considered interchanging the first two steps of the repeater protocol in Ref. [24] such that states resembling one-mode cat states,

$$|\xi(\theta,\alpha)\rangle \propto e^{i\theta}|\alpha\rangle + e^{-i\theta}|-\alpha\rangle, \tag{3.2}$$

are first grown locally and then subsequently connected to create entanglement by means of non-local single-photon subtraction. Such a modification reduces the need for classical communication and allows a higher repetition rate to be reached. This is the main idea behind the new repeater protocol we have proposed and which is detailed below. In addition, we have optimized the cat-state growth procedure of Ref. [24], improving the rate further.

3.2 Review of previous scheme

The repeater protocol of Ref. [24] consists of three steps, (i) heralded entanglement generation based on sources of two-mode squeezed vacuum and SPD, (ii) growth of two-mode cat states from entangled single photons by means of homodyning, and (iii) entanglement swapping based on homodyning. The steps are outlined in Fig. 3.1.

In step (i) (see Fig. 3.1(i)), two sources produce two-mode squeezed vacuum states of the form

$$|00\rangle + \sqrt{p_{pair}}|11\rangle + O(p), \tag{3.3}$$

where p_{pair} is the probability to produce a photon pair. These sources can be realized using parametric downconversion crystals or ensembles of Λ-type atoms [51, 54]. One output mode from each source is read into a quantum memory while the remaining modes are sent to a balanced beam splitter positioned between the two sources. The beam-splitter outputs are measured and a single SPD click projects the two modes in the quantum memories into an entangled state $|01\rangle + |10\rangle$. The pair-production probability p_{pair} (and hence the squeezing) needs to be small to ensure that the final state does not contain more than a single photon.

In step (ii) (see Fig. 3.1(ii)), two entangled single-photon states are combined on balanced beam splitters and the $\hat{X}$ quadratures of one output mode from each beam splitter are measured (a related procedure to perform distillation of continuous-variable entanglement was shown in Ref. [55, 56]). Whenever the sum of the measurement outcomes fulfill $|x_a + x_b| \leq \Delta$, for a certain acceptance interval, Δ, the state is kept. The process can be iterated by combining two states resulting from successful growth at the previous level and repeating the procedure. In the limit of small Δ, the final output resulting from this procedure approaches a non-locally squeezed two-mode cat state of the form

$$\hat{S}_+(2)|\gamma(0, \mu_m/\sqrt{2})\rangle, \tag{3.4}$$

where $\mu_m = \sqrt{2^m + 1/2}$ and m is the number of iterations. $\hat{S}_+(2)$ denotes non-local squeezing in the variance of $\hat{X}_a + \hat{X}_b$ by a factor of two. The squeezing operator has the general form $\hat{S}(\zeta) = \exp\left(\frac{1}{2}\zeta^*\hat{a}^2 - \frac{1}{2}\zeta\hat{a}^{\dagger 2}\right)$. The acceptance interval, Δ, determines the probability for successful growth, and hence the rate, as well as the fidelity of the output state with respect to the state in Eq. (3.4). Larger Δ corresponds to higher success probability but lower fidelity. The choice of Δ thus defines a tradeoff between the rate and the fidelity. In Ref. [24], Δ was fixed to take the same value for all m.

The final step (iii) (see Fig. 3.1(iii)) is entanglement swapping where neighboring entangled segments are combined to create longer segments. Two modes, one from each entangled pair, are combined on a balanced beam splitter and the $\hat{X}$ and $\hat{P}$ quadratures of the output modes are measured. Whenever $|x| \leq \delta$, x being the outcome of the $\hat{X}$ measurement, the entanglement swapping is considered to be a success and the output state is kept. The process is iterated until entanglement is distributed over the total length, L of the repeater. This is obtained by first dividing L into 2^n segments of length $L_0 = L/2^n$ over which entanglement is created. At each swap level, every two neighbouring segments are connected, such that the entanglement distance is doubled. After

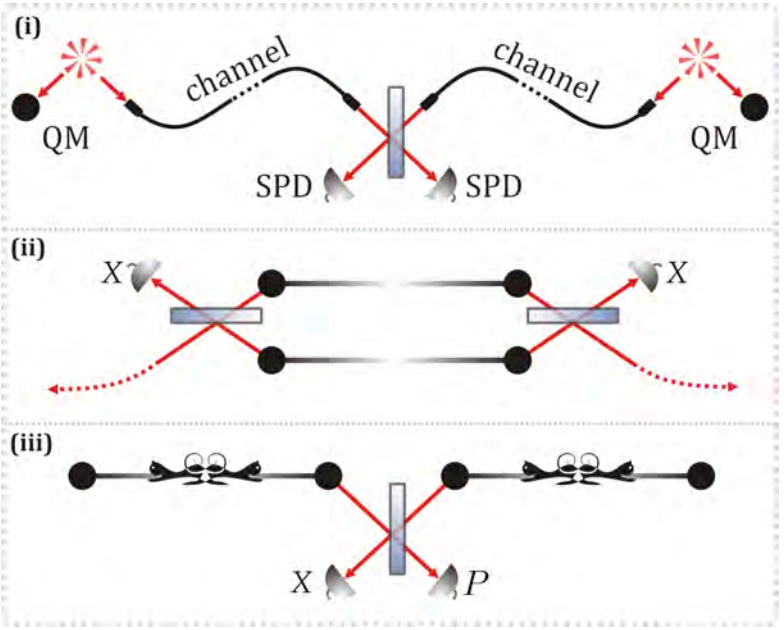

FIGURE 3.1: Steps of the protocol in Ref. [24]. **(i)** Entanglement is generated using two sources of two-mode squeezed vacuum. One mode from each source is transmitted to a balanced beam splitter and the outputs are measured. Detection of a single photon heralds entanglement between the remaining modes stored in quantum memories (QM). **(ii)** Growth of cat states. Two entangled states are combined locally on balanced beam splitters and the $\hat{X}$ quadrature is measured. Success is conditioned on the sum of the outcomes taking a value close to zero. **(iii)** Entanglement swapping. One mode from each state is combined on a balanced beam splitter and the $\hat{X}$ and $\hat{P}$ quadrature of the outputs are measured. Success is conditioned on a value of the $\hat{X}$-outcome close to zero.

n swap levels, entanglement is distributed over the entire length L. In the limit of small δ, the state produced after n swap levels approaches a locally squeezed two-mode cat state

$$|\psi_{ideal}\rangle_{ab} = \hat{S}_a(\sqrt{2})\hat{S}_b(\sqrt{2})|\gamma(\phi_n, 2^{-5/4}\mu_m)\rangle_{ab}, \tag{3.5}$$

where the phase ϕ_n depends on the $\hat{P}$-measurement outcomes from the previous levels. This state contain one ebit of entanglement and is used to quantify the performance of the repeater via the fidelity

$$F_{prev} = \langle\psi_{ideal}|\,\hat{\rho}\,|\psi_{ideal}\rangle\,, \tag{3.6}$$

where $\hat{\rho}$ is the density matrix of the final output state of the repeater. As for the growth step (ii), there is a tradeoff between fidelity and rate through the acceptance parameter δ. The upper limit to the success probability of entanglement swapping is 1/2 for the simple procedure considered here but the success probability can in principle be increased by using a more complicated procedure (see Ref. [57]).

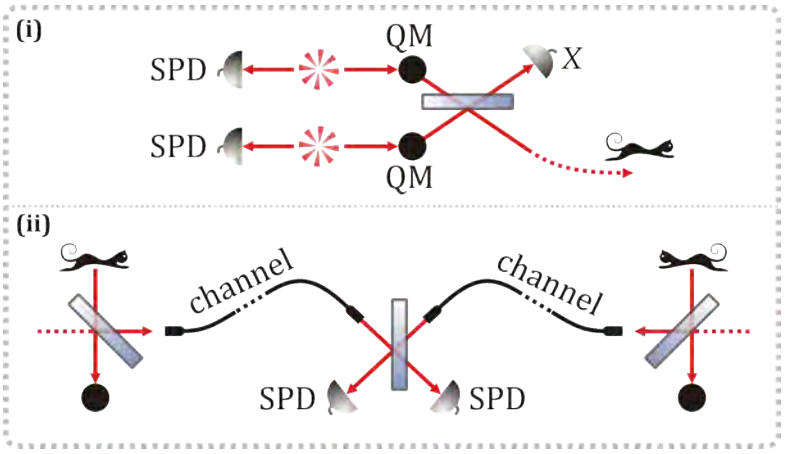

FIGURE 3.2: Steps of the modified repeater. **(i)** Local growth of cat states. The output modes from two sources of two mode squeezed vacuum states are combined on a balanced beamsplitter and the $\hat{X}$ quadrature of one of the outputs is measured conditioned on a click in both SPD-detectors. Conditioned on the measurement outcome the resulting state is kept for further processing. **(ii)** Entanglement generation from single-mode cat states. Small parts are tapped off from two input cat states at two separate locations, and the remaining parts are stored in quantum memories (black dots). The fraction tapped off is controlled by the reflectivity r of the local beam splitters. The reflected signals are transmitted to a central, balanced beam splitter, and the output ports are measured. Conditioned on a click in either of the detectors, the memories are prepared in an entangled state.

3.3 The modified scheme

To improve the rate of entanglement distribution, we have interchanged steps (i) and (ii) above, resulting in a new protocol based on local growth of single-mode cat states and subsequent non-local single-photon subtraction. The steps of the new protocol are sketched in Fig. 3.2. Entanglement swapping is performed in the same manner as in step (iii) above.

3.3.1 Growth of cat states

The first step of the modified protocol is growth of states approximating squeezed single-mode cat states

$$|\zeta_m\rangle = \hat{S}(2)\frac{1}{\sqrt{N^+_{\mu_m}}}(|\mu_m\rangle + |-\mu_m\rangle), \tag{3.7}$$

where $\hat{S}(2)$ denotes squeezing by a factor of two in the variance of the $\hat{X}$ quadrature, $|\mu_m\rangle$ is a coherent state with amplitude $\mu_m = \sqrt{2^m + 1/2}$ and $N^+_{\mu_m}$ is a normalization constant. These states can be grown by a setup very similar to step (ii) of the original protocol, as explained in Ref. [24]. The input states are single-mode, one-photon states, generated by detecting one half of a two-mode squeezed state with small pair-production

probability p_{pair}. To understand the growth procedure, we consider the ideal limit where each source produces a pure single-photon state $|1\rangle$ with corresponding wave function for the x-quadrature

$$\psi_0(x) = \frac{\sqrt{2}}{\pi^{-1/4}} e^{-\frac{1}{2}x^2} x. \tag{3.8}$$

The joint wave function before the beam splitter is $\psi_0(x)\psi_0(y)$. At the output of the balanced beam splitter, this is transformed into $\psi_0((x+y)/\sqrt{2})\psi_0((x-y)/\sqrt{2}) \propto e^{-\frac{1}{2}(x^2+y^2)}(x^2-y^2)$. Now mode y is measured and the state is kept if $y_0 \in [-\Delta, \Delta]$ where y_0 is the measurement outcome. Taking the limit $\Delta \to 0$ we find the output state $\psi_1(x) \propto e^{-\frac{1}{2}x^2}x^2$. Then the process is iterated with $\psi_1(x)$ as input. After m iterations, the output wave function becomes

$$\psi_m(x) = \Gamma\left(2+\frac{1}{2}\right)^{-\frac{1}{2}} x^{2^m} e^{-\frac{1}{2}x^2}. \tag{3.9}$$

The overlap of this state with the state in Eq. (3.7) exceeds 99% for $m \geq 2$ and approximate squeezed cat states can thus be grown this way.

As in the previous section, there will be a tradeoff between the fidelity and the rate controlled by Δ. In Ref. [24], Δ was kept fixed at the same value in every iteration but here we investigate the improvement by allowing different values of Δ for each m. To understand the possible improvement allowed by varying the interval, we first analyze how the growth procedure works. The output wave function of the growth procedure (approximately $\psi_m(x)$ for small Δ) is symmetric with two peaks; one at $x < 0$ and one at $x > 0$. Suppose that the measurement is performed in the symmetric output of the beam splitter with quadrature operator $\hat{X}_+ = \hat{X}_1 + \hat{X}_2$. In this mode the quadratures add. If the two peaks with positive x are combined, the measurement outcome will likely have a positive value. Similarly, combining the negative peaks leads to a negative outcome. These two possibilities are not desirable since the wave function in the antisymmetric mode $\hat{X}_- = \hat{X}_1 - \hat{X}_2$ essentially will be a peak around zero, because in this mode the quadratures subtract. However, when a negative and a positive peak combine, the measurement outcome will be in the vicinity of zero. Since there are two paths leading to this result, corresponding to two different states in the antisymmetric output mode, the desired cat state is generated. The acceptance interval must be chosen such that one avoids outcomes resulting from the tail of the distribution coming from the combination of two positive or two negative peaks. The closer the peaks are to each other at the input, the smaller acceptance interval is allowed. As the growth process is iterated, the peaks become more separated and larger acceptance intervals can be chosen, resulting in a higher probability of success.

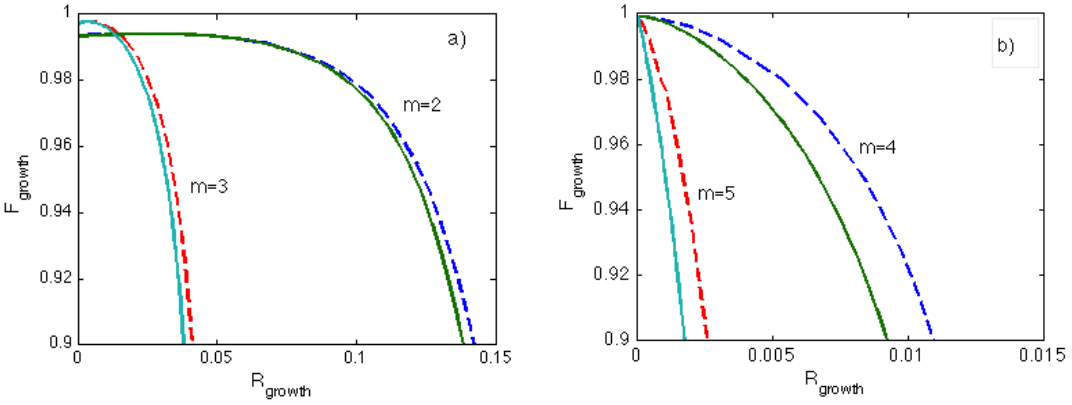

FIGURE 3.3: Optimized production rate of approximate squeezed cat states after (a) m=2,3 iterations (b) m=4,5 iterations. The dashed lines are the optimal curves and the solid curves are obtained for identical acceptance intervals in all iterations. The fidelity was calculated with the target state in Eq. (3.7) and the rate is given in units of the source repetition rate.

We have optimized the acceptance interval to achieve the highest possible probability for a fixed target fidelity

$$F_{growth} = \langle \zeta_m | \, \hat{\rho}_m \, | \zeta_m \rangle \tag{3.10}$$

of the output state $\hat{\rho}_m$ of the growth procedure. We assume perfect one-photon states at the inputs, and calculate the fidelity and rate on a grid of values for each acceptance interval, Δ_m under the constraint that $\Delta_{m+1} \geq \Delta_m$. The optimization was made using Wigner functions, since these provide a natural description of mixed continuous-variable states and make it possible to compute the average output fidelity. Details are given in App. A.1. The rate, in units of the source repetition rate is approximated by

$$R_{growth} = \left(\frac{2}{3}\right)^{m-1} P_1 P_2 \ldots P_m, \tag{3.11}$$

where P_m is the probability of successful growth in iteration m. This expression assumes that the outcomes of successful events can be stored while unsuccessful events are repeated until they succeed [18]. Note, that by assuming that successful events are stored in quantum memories, we avoid the usual exponential scaling with the number of conversion events (recall that the number of down conversions is 2^m). The result of the optimization is shown in Fig. 3.3 where we plot F_{growth} against R_{growth}. Note that the fidelity does not reach unity as $R_{growth} \to 0$ since we take the fidelity with the approximate cat state in Eq. (3.7) and not the state in the ideal limit in Eq. (3.9). The calculation was restricted to $m \leq 5$ for runtime reasons.

Fig. 3.3 shows that the growth procedure is indeed improved by allowing for different acceptance intervals in every iteration. However, the rate is not significantly improved for

a small number of iterations m. Nonetheless, Fig. 3.3 indicates that the improvement will increase with m since for larger m the peaks in the input states become more separated. For an output fidelity of 0.9 the ratio of the modified rate to the previous rate is 1.03, 1.10, 1.21, and 1.53 for $m = 2, 3, 4$, and 5 respectively. For very large m, the two peaks will be so far separated that we can choose an acceptance interval for which the success probability approaches $\frac{1}{2}$ without affecting the fidelity.

3.3.2 Connection of cat states

The second step of the new protocol is to create entanglement by connecting the single-mode cat states from the first step. The method we employ was proposed by N. Sangouard and coworkers in Ref. [52] and the setup is shown in Fig. 3.2(ii).

A small part is subtracted from each input state by means of asymmetric beam splitters with low reflectivity r. The remaining parts of the states are stored and the reflected parts are transmitted to a central station. Here, the two signals are combined on a balanced beam splitter and the two output ports are measured with photodetectors. Successful entanglement generation is conditioned on a click in exactly one of the detectors. When a click is observed in the symmetric output port of the beam splitter, the quantum memories are projected into an entangled state approximating the two-mode cat $|\gamma(0, \alpha\sqrt{1-r})\rangle$. For a click at the antisymmetric output, the state is identical up to a local phase shift. The procedure can be understood easily in the ideal case where the inputs are exact cat states $|\xi(0, \alpha)\rangle$ and $r \to 0$. In this limit, a click heralds non-local subtraction of a single photon from the joint state of the memories. The memories are thereby projected into the (unnormalized) state

$$(\hat{a} \pm \hat{b})|\xi(0, \alpha)\rangle_a |\xi(0, \alpha)\rangle_b, \tag{3.12}$$

where a, b label the output modes. Inserting the definition Eq. (3.2) and recalling that coherent states are eigenstates of the annihilation operators, we notice that the component of the wave function, where the a and b mode have the opposite (same) phase e.g. $|\alpha\rangle_a|-\alpha\rangle_b$ ($|\alpha\rangle_a|\alpha\rangle_b$), vanish by interference for the plus (minus) combination. Therefore the resulting state is

$$|\alpha\rangle_a|\pm\alpha\rangle_b - |-\alpha\rangle_a|\mp\alpha\rangle_b. \tag{3.13}$$

Comparing to Eq. Eq. 3.1, we see that up to a local phase shift this state is equal to $|\gamma(\pi/2, \alpha)\rangle$.

In practice, it is very hard to create genuine cat states. Therefore, we shall use the approximate squeezed cat states from the previous step of the repeater protocol. We now examine the behaviour of these states under entanglement generation in the ideal limit $\Delta \to 0$, in which case they are given by Eq. (3.9), and taking again the limit $r \to 0$, we find

$$\begin{aligned} |\Psi_m\rangle_{ab} &= (\hat{a} \pm \hat{b})|\psi_m\rangle_a|\psi_m\rangle_b, \\ &\propto \frac{1}{\sqrt{2}}(|0_m\rangle_a|1_m\rangle_b \pm |1_m\rangle_a|0_m\rangle_b), \end{aligned} \tag{3.14}$$

where

$$\begin{aligned} \langle x|0_m\rangle &= \langle x|\, a\, |\psi_m\rangle = \Gamma(2^m - 1/2)^{-1/2} x^{2^m-1} e^{-\frac{1}{2}x^2}, \\ \langle x|1_m\rangle &= \psi_m(x) = \Gamma(2^m + 1/2)^{-1/2} x^{2^m} e^{-\frac{1}{2}x^2}. \end{aligned} \tag{3.15}$$

Here, $|1_m\rangle$ is a superposition of even photon states and $|0_m\rangle$ is a superposition of odd photon states, and for $m \geq 2$ they resemble squeezed, even and odd, single-mode cat states respectively i.e:

$$|1_m\rangle \approx \hat{S}(2)\frac{1}{\sqrt{N^+_{\mu_m}}}(|\mu_m\rangle + |-\mu_m\rangle) \tag{3.16}$$

$$|0_m\rangle \approx \hat{S}(2)\frac{1}{\sqrt{N^-_{\tilde{\mu}_m}}}(|\tilde{\mu}_m\rangle - |-\tilde{\mu}_m\rangle) \tag{3.17}$$

where $\tilde{\mu}_m = \sqrt{2^m - 1/2}$, $\mu_m = \sqrt{2^m + 1/2}$ and $N^+_{\mu_m}, N^-_{\tilde{\mu}_m}$ are normalization constants. For $m \geq 2$ the fidelities between $|1_m\rangle, |0_m\rangle$ and the respective cat states are both $\geq 99\%$.

The state $|\Psi_m\rangle$ contains one ebit of entanglement and is obtained in the low-rate limit of small acceptance intervals during growth and small reflectance during connection. $|\Psi_m\rangle$, however, deviates from the squeezed two-mode cat state that was shown to be useful for entanglement swapping in Ref. [24]. For $m = 2$ the overlap with a locally squeezed two-mode cat state of the form used in Ref. [24]

$$\hat{S}(2)_a\hat{S}(2)_b|\gamma(0, 2^{m/2})\rangle_{ab}, \tag{3.18}$$

is 96% and for $m = 3$ it is 97%. As we will see, this discrepancy has a detrimental effect on the overall performance of the repeater. This could be avoided by unsqueezing the approximate squeezed cat states going into the entanglement connection. Such unsqueezing operations may, however, be technically demanding, and we prefer not to include them here. We therefore consider the simplest situation, where we directly connect the states generated in the first step. Alternatively, the problem could be

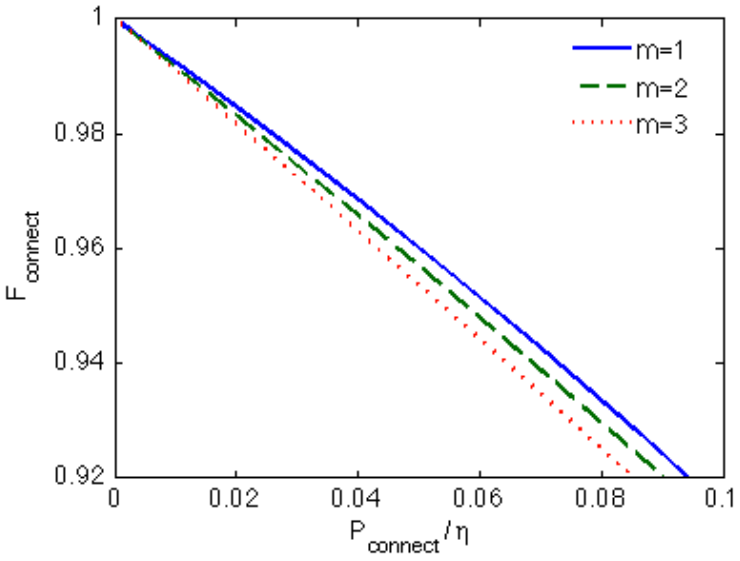

FIGURE 3.4: The fidelity of the connected state with respect to the state $|\Psi_m\rangle$ plotted against the rescaled probability of a successful connection. We have assumed the input states to be of the form in Eq. (3.9).

mitigated by increasing m. E.g. for $m \geq 5$ we get an overlap of 99% with the state in Eq. (3.18). However, going to such high m would also be very demanding in practice.

Below, we analyse the full repeater protocol, including entanglement swapping. Before proceeding, we first examine the performance of the connection step itself. We compute the output state for finite r and lossy transmission channels. Loss is modelled by fictitious beam splitters of transmittivity η, such that the probability for a photon to get lost on the way to the central station is $1 - \eta$. We assume that the photodetectors do not resolve the photon number. Details of the calculation are given in App. A.2. First, we study the output fidelity, $F_{connect}$ of the connected state with respect to $|\Psi_m\rangle$ as a function of the reflectivity, r of the first two beamsplitters. For this purpose, we simulate the connection of states of the form in Eq. (3.9) for a fixed number of iterations (m). We restrict the simulations to small r since this is the relevant regime of the repeater. This implies that the probability of a successful connection is $P_{connect} \approx P_{c,noloss}(r)\eta$ where $P_{c,noloss}(r)$ is independent of the losses in the optical fibers. The results of the simulations are shown in Fig. 3.4.

Fig. 3.4 shows that the fidelity depends linearly on $P_{connect}/\eta$ in the limit of small r. Furthermore, the rate of the connection step for a fixed distance is more or less independent of m for small r. These results can be understood by noting that the connection fails if a second photon is tapped off at the beam splitters. The probability for this to happen conditioned on at least a single photon being tapped off is $\sim P_{connect}/\eta$ regardless of m.

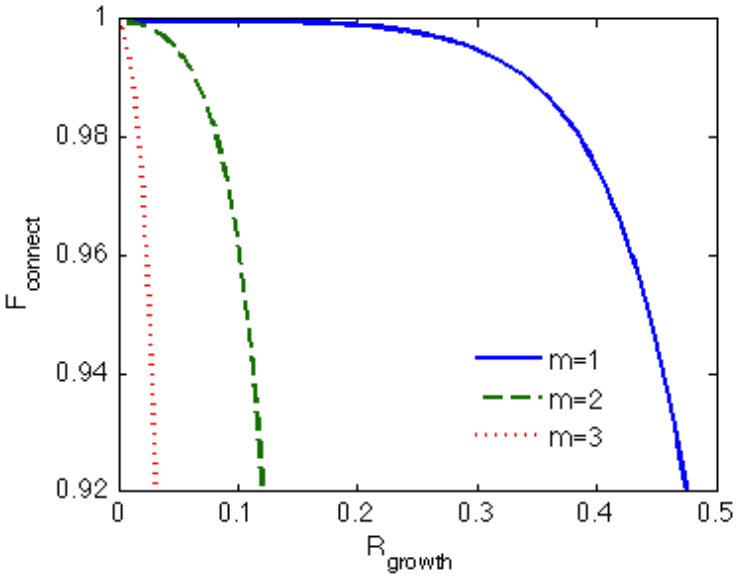

FIGURE 3.5: Influence of finite acceptance intervals in the growth on the state after connection. The fidelity of the connected state is w.r.t. the state $|\Psi_m\rangle$ and $\vec{\Delta}$ is represented through R_{growth}. Here, we have neglected losses in the optical fibers and R_{growth} is in units of the rate at which the one-photon input states for the growth can be provided.

The second parameter to consider in the connection step is the vector of acceptance intervals for the growth step, $\vec{\Delta}$, which determines the fidelity of the input states with respect to $|\psi_m\rangle$. To determine the effect of finite acceptance intervals in the growth procedure on the state after connection, we simulate the connection step for different $\vec{\Delta}$, taking the limit of $r \to 0$ and $\eta \to 0$. We take $\vec{\Delta}$ to be the vectors giving the optimal fidelity for a given rate R_{growth} in Fig. 3.3. The result of the simulations is shown in Fig. 3.5.

Fig. 3.5 shows the same kind of behavior as Fig. 3.3 taking into account that the fidelity in Fig. 3.3 is w.r.t. the squeezed one mode cat state in Eq. (3.7), i.e. as opposed to Fig. 3.3, the fidelity approaches unity. For optimizing the performance of the full repeater it is advantageous to have an analytical understanding of the entanglement generation. We have therefore fitted the graphs to functions of the form $F_{connect} = 1 - c * e^{d*R_{growth}}$. The details of the fits are shown in App. A.4 and Tab. 3.1. Fig. 3.4 and Fig. 3.5 show that the highest rate of entanglement generation is obtained for $m = 1$ but, as we will see below, we need to go to higher m for the swapping procedure to function.

3.3.3 Entanglement swapping

The final step of our altered repeater is to merge entangled segments via entanglement swapping. The method is the same as in the protocol of Ref. [24] and is illustrated in

Fig. 3.1(iii). Two modes, at the same location from two entangled pairs, are connected on a balanced beam splitter and the $\hat{X}$ and $\hat{P}$ quadratures are subsequently measured. Whether the swap attempt was successful is conditioned on the outcome of the $\hat{X}$ measurement. When swapping two states of the form Eq. (3.18), the wave functions of the states have two peaks; one at $x > 0$ and one at $x < 0$. Thus, following similar arguments as for the growth procedure, there are two paths leading to outcomes in the vicinity of zero, $|x| \leq \delta$. Measuring the plus combination, there is one from the first mode having a positive value of x combined with a negative value from the second mode and vice versa. If $x \sim 0$, the two remaining quantum memories are projected into an entangled state of the form in Eq. (3.18) with a phase determined by the outcome of the $\hat{P}$ measurement. The entangled states produced in the connection step are, however, not exactly of the ideal form in Eq. (3.18). Therefore, we need to investigate how the swapping performs with the actual states generated by our protocol. To this end, we first identify the entangled state that most closely resembles the result of swapping after ideal growth and connection by swapping states of the form in Eq. (3.14). Swapping two copies of $|\Psi_m\rangle$ using the approximations Eqs. (3.16) -(3.17) to determine how the two modes gets mixed, we find

$$\begin{aligned} |\Phi_m\rangle =& A|0_m\rangle|0_m\rangle - A^*|1_m\rangle|1_m\rangle + \\ & C|1_m\rangle|0_m\rangle + C^*|0_m\rangle|1_m\rangle, \end{aligned} \tag{3.19}$$

where the coefficients depend on the measurement outcomes of the $\hat{X}$ and $\hat{P}$ measurements in both the current and previous swap levels (see App. A.3 for details). This state contains one ebit of entanglement, and we will use it as our target state when evaluating the performance of the repeater. That is, we measure the quality of a final state $\hat{\rho}$ produced by the repeater by the fidelity

$$F(\hat{\rho}) = \langle \Phi_m | \, \hat{\rho} \, | \Phi_m \rangle \, . \tag{3.20}$$

The approximate form in Eq. (3.19) is however only obtained in the limit of large m. For finite m, even the state $|\Psi_m\rangle$, obtained in the limit of ideal growth and connection, will produce less than one ebit of entanglement. To quantify this, we examine the dependence of F on the outcome of the $\hat{P}$ measurement. This behavior is shown in Fig. 3.6 where we plot F against the $\hat{P}$-outcome for different values of m. For small values of m, there is a strong dependence. However, as m increases, the $\hat{P}$ dependence decreases because the states begin to resemble locally squeezed two mode cat states, which are insensitive to the $\hat{P}$-outcome when swapped. The probability of a successful swap is determined by the acceptance interval δ for the outcome of the $\hat{X}$-measurement and has an upper bound of 1/2, which is approached for high m as in the protocol of

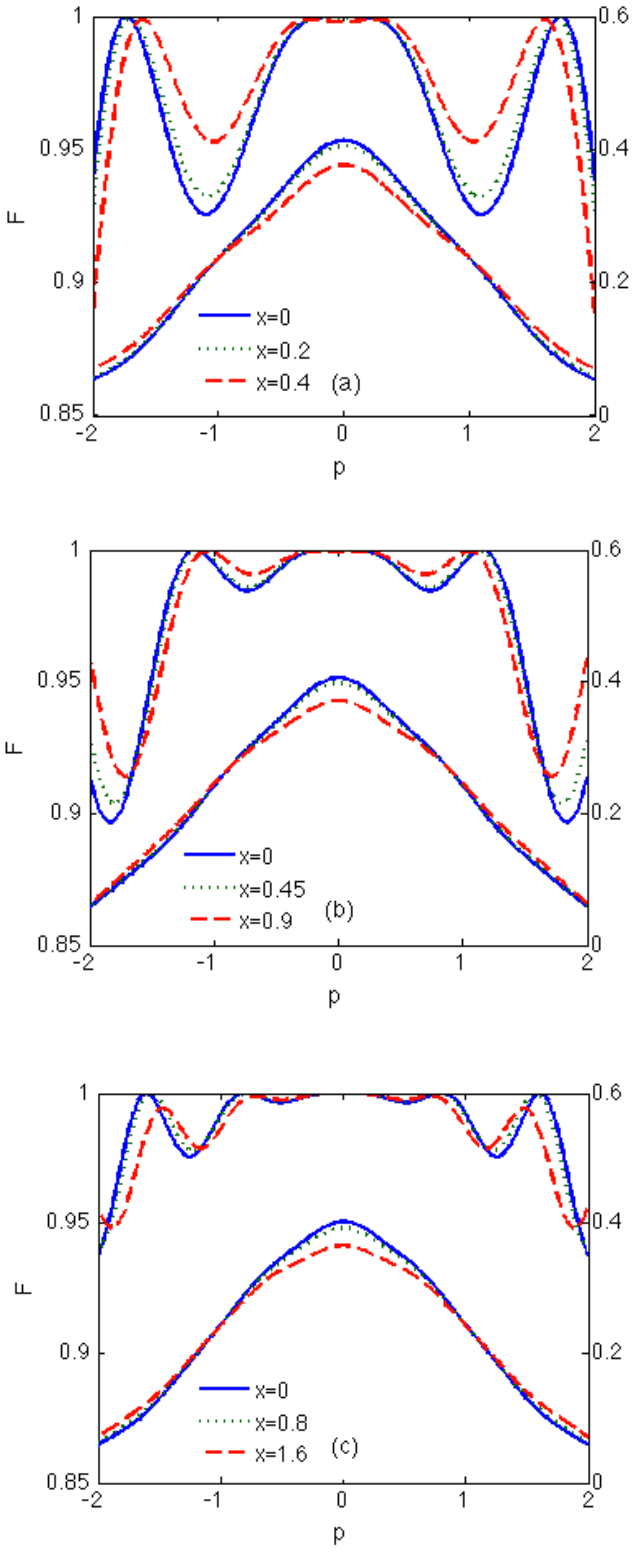

FIGURE 3.6: Upper curves (left axis): The fidelity after entanglement swapping as a function of the $\hat{P}$-outcome for (a) $m = 1$, (b) $m = 2$ and (c) $m = 3$, and various values of the $\hat{X}$-outcome. The fidelity is $F(\hat{\rho}_\Psi)$ where $\hat{\rho}_\Psi$ results from swapping two copies of $|\Psi_m\rangle$. Lower curves (right axis): The corresponding probability distributions of p for each $\hat{X}$-outcome.

Ref. [24]. Near-deterministic swapping can in principle be achieved following the method of Ref. [24] using auxiliary single-mode cat states but we will not consider this possibility here.

The strong $\hat{P}$ dependence for small m in the fidelity of the swapped state was not seen in the original hybrid repeater [24], where the the outcome of the $\hat{P}$ measurement merely resulted in an overall phase in the swapped state. As a consequence, the states produced in the connection step of the altered repeater do not swap as well as those in the original repeater for the same number of iterations m. For long distances, a large number of swap levels is needed. One therefore needs to go to higher m in the altered repeater as compared to the original repeater to reach a given output fidelity of the distributed state.

3.4 Performance

The full repeater protocol is the nested collection of the three steps described in the previous sections i.e. growth of cat states, connection, and entanglement swapping. To quantify the performance of the repeater, we use the fidelity F, as given in Eq. (3.20), and the production rate for the final entangled states. We set a target value of $F \geq 80\%$ and make a numerical optimization of the rate as a function of distance by simulating the repeater for different values of the control parameters at each step. The relevant parameters are given in Tab. 3.1. We perform a full optimization over all the parameters in Tab. 3.1, under the constraint that the final state should have a minimum fidelity $F \geq 80\%$. We do this optimization for each distance and for each value of the local repetition rate. For the simulation, we assume perfect quantum memories, perfect homodyning, and a SPD efficiency $\eta_{spd} = 50\%$. For a repeater of total length L and n swap levels, the distance between the stations is $L_0 = L/2^n$ and the transmission efficiency incurred in the entanglement generation step is $e^{-L_0/2L_{att}}$, where L_{att} is the attenuation length of the channels. The total efficiency incurred is thus $\eta = \eta_{spd}e^{-L_0/2L_{att}}$. We assume $L_{att} = 20$km corresponding to optical fibers at telecom wavelengths. The time needed for classical communication during entanglement generation is given by L_0/c, where c is the speed of light in the channels. We assume $c = 2 \cdot 10^5$km/s. The time required for local operations (measurements and memory operations) is assumed to be negligible compared to the classical communication time, such that the characteristic rates in the protocol are c/L_0 and the source rate for the two-mode squeezing sources, r_{rep}. The latter is taken to be the repetition rate of a single two mode squeezing source, i.e. the rate at which down conversion is attempted in a single crystal. The optimal

pair production probability p_{pair} is found in the numerical optimization of the rate of the repeater for a given r_{rep}. The effect of two-photon contributions in the input states is treated by perturbation in the pair-production probability p_{pair}, as in Ref. [24]. r_{rep} determines the rate of the growth, which is the first step of the protocol and thus has a large effect on the overall rate of the repeater. For runtime reasons, we have restricted the number of growth steps to $m \leq 3$ and the number of swap levels to $n \leq 4$.
For simulating both the growth and the connection step of the repeater, we use Wigner functions to obtain the average output fidelity for a given set of values of the control parameters (see App. A.1 and App. A.2). However, this is not possible when simulating the entanglement swapping since the target state depends on the outcomes of the $\hat{X}$ and $\hat{P}$ measurements. To obtain an average fidelity of the entanglement step, we therefore pick the measurement outcomes according to the probability distributions of $\hat{X}$ and $\hat{P}$ and calculate the fidelity of the resulting state. We repeat this procedure 100 times for each swap level and calculate the average output fidelity. This gives a standard deviation of the mean of the fidelity of about 1%.

When performing the numerical optimization of the rate, we calculate the fidelity of the distributed state and the rate on a grid of values for all the control parameters. The parameters affecting the performance of the repeater are summarized in Tab. 3.1. In order to pinpoint the relevant parameter regime, we use the fits listed in Tab. 3.1 to make an analytical approximation of how the fidelity depends on the different parameters. We use this approximation to optimize the rate using the method of Lagrange multipliers to find the optimal rate for a target fidelity of 80%. The resulting values of the control parameters is then used to make a grid of values for the numerical optimization around the analytical results. Finally, we pick the grid point with the highest rate where $F \geq 80\%$. The optimal rate as a function of distance is shown in Fig. 3.7 for different values of r_{rep}.

Naturally the rate of the altered repeater is very dependent on the source repetition rate. With a fast local repetition rate, cat states can be grown rapidly thus removing a time consuming step of the original repeater where this was done non-locally. Assuming an experimentally accessible repetition rate of 1MHz, the present protocol achieves a rate of ~ 0.08 pairs/min at $L = 1000$km while the rate of the previous protocol for the same distance and target fidelity is ~ 0.004 pairs/min. The altered repeater thus gives a significant increase in the rate. For $r_{rep} = 1$GHz, the task of storing the signals in quantum memories will be challenging but a rate of ~ 1.5 pairs/min would in this case be reachable within the above assumptions. The ratio of the rate of the modified to that of the original repeater decreases as a function of the distance. This is because the states produced in the modified protocol are less robust to the swapping procedure than

	Description	Effect	Fidelity-fit
p_{pair}	Pair-production probability of the sources of two-mode squeezed vacuum states.	Small $p_{pair} \to$ low production rate of input states. Large $p_{pair} \to$ large two-photon component.	$F = (1-\tau \cdot p_{pair})F_1$ $+\tau \cdot p_{pair} \cdot F_2$
$\vec{\Delta}$	Vector of acceptance intervals in the growth procedure.	Large acceptance intervals $\to$ high growth rate. Small acceptance intervals $\to$ high fidelity of the one-mode states state in (3.9).	$F = 1-\tilde{c}_{n,m}e^{\tilde{d}_{n,m}R_{growth}}$
m	Number of iterations in the growth step.	High $m \to$ low growth rate. Low $m \to$ poor swapping states.	$F = \tilde{i}_n + \tilde{j}_n \cdot m^2 + \tilde{k}_n \cdot m$
r	Reflectivity of the first two beam splitters in the connection step.	Large $r \to$ high connection rate. Small $r \to$ high fidelity with the state (3.14).	$F = 1-\tilde{a}_{n,m}(\frac{P_{connect}}{\eta})^2$ $-\tilde{b}_{n,m}\frac{P_{connect}}{\eta}$
δ	Acceptance interval in the swapping procedure.	δ determines the probability of a successful swap and the fidelity of the output state.	$F = \tilde{e}_{n,m}e^{\tilde{f}_{n,m}\delta}$ $+\tilde{g}_{n,m}e^{\tilde{h}_{n,m}\delta}, \quad m \leq 2$ $F = \tilde{e}_{n,3} + \tilde{f}_{n,3} \cdot \delta, \quad m = 3$
n	Number of swap levels.	n determines the classical communication time (L_0/c) between the stations in the elementary segments and hence the loss in the fibers during connection.	$F = 1 - \tilde{l}_m \cdot n^2$

TABLE 3.1: Parameters considered in the numerical optimization of the repeater. The last column is a functional fit of how the fidelity Eq. (3.20) depends on the parameter when the other parameters assume their ideal values i.e. $p_{pair} \to 0$, $\vec{\Delta} \to 0$, $r \to 0$, $\delta \to 0$. r is represented through $P_{connect}$ in the fit where $P_{connect}$ is the probability of a successful connection and $\vec{\Delta}$ is represented through R_{growth}. The fits for $R_{growth}, P_{connect}$ and δ are made for a specific choice of n and m. See App. A.4 for details on the matrices containing $\tilde{a}_{n,m}..\tilde{h}_{nm}$ and the vectors containing $\tilde{i}_n..\tilde{k}_n$ and $\tilde{l}_m$. The expression for the fidelity's dependence on p_{pair} is calculated by perturbation in p_{pair}. F_1 is the fidelity with pure one-photon input states for a given set of parameters and F_2 is the fidelity for the same set of parameters but with one of the input states being a two-photon state. $\tau = \frac{f_2}{4}2^{m+n+1}$, where f_2 is a factor that accounts for the different acceptance probabilities for a one-photon state and a two-photon state in the repeater.

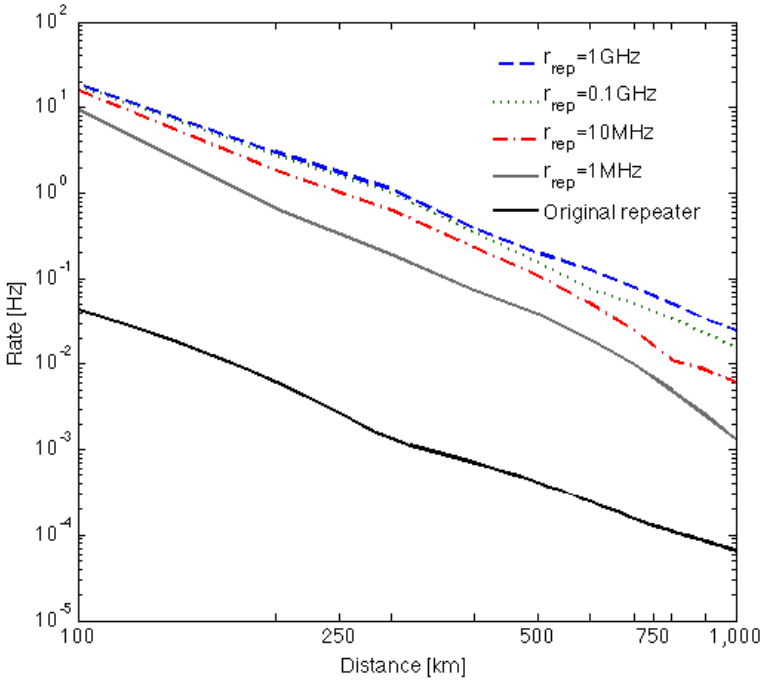

FIGURE 3.7: The optimal rates of the present and previous repeater protocols for different values of r_{rep}. The protocols are optimized over the parameters listed in Table 1, under the constraint $F \geq 80\%$. The altered repeater performs significantly better than the previous protocol even for $r_{rep} = 1$MHz.

the states produced in the original repeater. When the distance increases the number of swap levels increase, which results in a decrease of the ratio of the rates for a fixed fidelity of the distributed state.

3.5 Conclusion and discussion

We have modified the quantum repeater protocol of Ref. [24] to improve the entanglement distribution rate. By interchanging the order of entanglement generation and growth of cat states, we have made the latter a local, hence faster, process, thus increasing the rate if local operations can be done rapidly. Furthermore, we have optimized the growth protocol. For entanglement generation, we have incorporated the method for connecting cat states of Ref. [52]. We have performed a numerical simulation of our protocol, confirming that it does indeed lead to an increased rate. The final rate depends on the repetition rate of the two-mode squeezing sources at the base level of the protocol. For a moderate repetition rate of 1MHz, our protocol is 20 times faster than the repeater considered in Ref. [24], achieving a rate of $\sim$ 0.08 pairs/min over 1000km. This rate is comparable to the best proposed atomic-ensemble based repeaters for similar detection efficiencies (taking into account that we have optimized for a final fidelity of 80%) [58]. Working with discrete variables requires SPD efficiencies of $\sim$ 90%

to obtain similar rates or complicated swapping procedures [17]. Much higher source repetition rates than 1 MHz are plausible with parametric down conversion in nonlinear crystals, but compatible quantum memories operating at such high frequencies may be very difficult to implement. For quantum repeaters of this kind, the most feasible quantum memories are currently those based on atomic ensembles. The high optical depth of a dense ensemble of cold atoms enables a strong coupling even for a few photons and this can provide an increase of the bandwidth scaling as γd, with γ being the decay rate and d the optical depth. For a sufficiently high d, the bandwidth may enable high repetition rates [59]. Progress along this line was recently reported in Ref. [60], which showed memory operations with pulses of spectral bandwidth exceeding 1 GHz. The storage-and-retrieval fidelities currently achievable are far from the perfect case assumed in the present analysis [61]. The efficiency of an atomic ensemble memory can, however, in principle be made close to 100% [62]. Since the modified repeater does not operate with bigger cat states than the original repeater, we do not expect different scaling of the two when including inefficient quantum memories. Furthermore, since the modified repeater operates faster than the original repeater, the states do not need to be stored for as long a time, and the effects from decoherence will thus be smaller [63]. Thus, we expect the improvement of the present protocol over the previous protocol to persist with at least the same factor even with non-ideal memories. It would be an interesting extension of this work to include non-ideal memories in the simulations, giving a more realistic calculation of the distribution rates but this this is beyond the scope of our work.

Chapter 4

Near Heisenberg limited atomic clock

Atomic clocks provide some of the most accurate time measurements in physics. One of the main limitations to the stability of atomic clocks is the quantum noise of the atoms, which leads to the standard quantum limit (SQL), where the stability scales as $1/\sqrt{N}$ with N being the number of atoms [41, 42]. To overcome this noise, it has been suggested to use entangled states with reduced atomic noise [5, 49, 64–66]. Ultimately this may lead to a stability at the Heisenberg limit, where the resolution scales as $1/N$, and recently, the first proof-of-principle experiments have demonstrated these concepts experimentally [67–72]. In practice, however, entangled states are often more prone to decoherence, and to fully assess the advantage, it is essential to study the performance in the presence of decoherence [73]. In Ref. [49], it was proven that entanglement can be used to improve the long-term stability of atomic clocks in the presence of the dominant practical source of decoherence, but the improvement identified was rather limited.

In this chapter, I present the work of me and Anders S. Sørensen on how to obtain near Heisenberg limited atomic clocks in the presence of decoherence by combining entanglement with an adaptive measurement protocol (inspired by Ref. [74, 75]). The work has been described in Ref. [76], which is the basis of this chapter. With our adaptive measurement protocol, the entangled states are not more sensitive to the decoherence than disentangled states. As a consequence, the long term stability of the atomic clock can be improved almost to the Heisenberg limit even in the presence of decoherence.

4.1 Decoherence and spin squeezing

Many atomic clocks are operated by locking a local oscillator (LO) to an atomic transition via a feedback loop. The feedback is typically based on a measurement of the LO frequency offset $\delta\omega$ compared to the atomic transition through Ramsey spectroscopy [47]. The details of Ramsey spectroscopy was presented in Sec. 2.4 but here, we briefly state the main points. The atoms are first prepared in one of the two clock states by e.g. a laser pulse. During the Ramsey sequence, the atoms interact with the LO field. This interaction consists of three parts; first the atoms are subject to a near-resonant $\pi/2$-pulse from the LO followed by the Ramsey time T of free evolution, and finally another near-resonant $\pi/2$-pulse is applied to the atoms. During the free evolution, the LO acquires a phase $\delta\phi = \delta\omega T$ relative to the atoms. Due to the last $\pi/2$-pulses, this phase can be measured as a population difference between the two clock levels. $\delta\omega$ can thus be estimated from the measurement and used for a feedback that steers the frequency of the LO to the atomic frequency. The stability of the clock will improve with T since a longer T improves the relative sensitivity of the frequency measurement. For current atomic fountain clocks, T is limited by gravity and can hardly be varied [41]. Here, on the other hand, we consider trapped particles, where T can be increased until it is limited by the decoherence in the system [77–79]. The long term stability thus depends on the nature of the decoherence.

To take decoherence into account, Ref. [73] considered single atom dephasing. For this model, Ref. [73] showed that entanglement can not improve the stability of atomic clocks considerable (although an improvement is possible for non-Markovian noise [80, 81]). A more realistic model of the decoherence was described in Ref. [49], where the primary noise source is the frequency fluctuations of the LO [82]. In this work, a small improvement in the long term stability, scaling as $\sim N^{1/6}$, was identified for entangled atoms. Here we use the same decoherence model and disregard any decoherence of atoms, to show that entanglement and adaptive measurements may improve the performance and give near Heisenberg limited atomic clocks. Although the assumption of negligible atomic decoherence may be hard to fulfill for the highly entangled states considered here, our results highlight that there is no fundamental obstacle to reaching the Heisenberg limit. Another approach to increase the stability is to increase T [83–85]. In particular, Ref. [85] increases T through a measurement protocol highly related to ours. However that work considers a scenario where the clock is limited by technical noise so that a direct comparison with our results is not possible. Which protocol is advantageous is thus an open question, which we have not addressed.

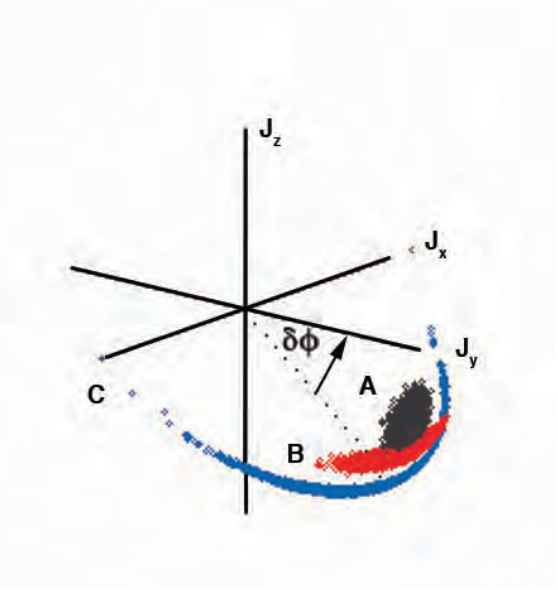

FIGURE 4.1: The atomic state just before the measurement of J_z for (A) uncorrelated atoms, (B) moderately squeezed atoms and (C) highly squeezed atoms.

4.1.1 Spin squeezing

We consider an ensemble of N two-level atoms, which we model as a collection of spin-1/2 particles with total angular momentum $\vec{J}$. The angular momentum operators $\hat{J}_{x,y,z}$ give the projections of $\vec{J}$ on the x, y and z-axis. The atoms are initially pumped to have a mean spin along the z-axis, $\langle \hat{J}_x \rangle = \langle \hat{J}_y \rangle = 0$. After the Ramsey sequence the Heisenberg evolution of $\hat{J}_x$, $\hat{J}_y$ and $\hat{J}_z$ is $\hat{J}_1(\delta\phi) = \hat{J}_x$, $\hat{J}_2(\delta\phi) = \sin(\delta\phi)\hat{J}_y - \cos(\delta\phi)\hat{J}_z$ and $\hat{J}_3(\delta\phi) = \cos(\delta\phi)\hat{J}_y + \sin(\delta\phi)\hat{J}_z$. At the end of the Ramsey sequence $\hat{J}_3$ is measured and used to estimate $\delta\phi$. The $\hat{J}_y$ term in $\hat{J}_3$ results in the so called projection noise in the phase estimate $\sim \Delta J_y / |\langle J_z \rangle|$. For uncorrelated atoms, $\Delta\hat{J}_y \Delta\hat{J}_x = \langle \hat{J}_z \rangle / 2 \approx N/4$ and the projection noise causes the stability of the clock to scale as $\sim 1/\sqrt{N}$. For a spin squeezed state [86] the variance of $\hat{J}_y$ is reduced to obtain a better phase estimate. Such a spin squeezed state is depicted in Fig. 4.1, which shows how the spin squeezed state looks like a "flat banana" on the Bloch sphere. The more we squeeze, the longer and more narrow the banana is and significant extra noise is added to the mean spin direction. For a phase estimate based on a direct measurement of $\hat{J}_3$, this gives an additional noise term $\sim \delta\phi \Delta\hat{J}_z / |\langle J_z \rangle|$. This extra noise limited the performance in Ref. [49] if strongly squeezed states were used. We avoid this problem by using an adaptive scheme with weak measurements to make a rough estimate of $\delta\phi$ and then rotate the spins of the atoms such that the mean spin is almost along the y-axis. The flat banana depicted in Fig. 4.1 will then lie in the xy-plane and this will decrease the noise from $\Delta\hat{J}_z$ in subsequent measurements (see Fig. 4.2). Having eliminated the noise from $\Delta\hat{J}_z$, we can allow strong squeezing in $\Delta\hat{J}_y$ and obtain near Heisenberg limited stability.

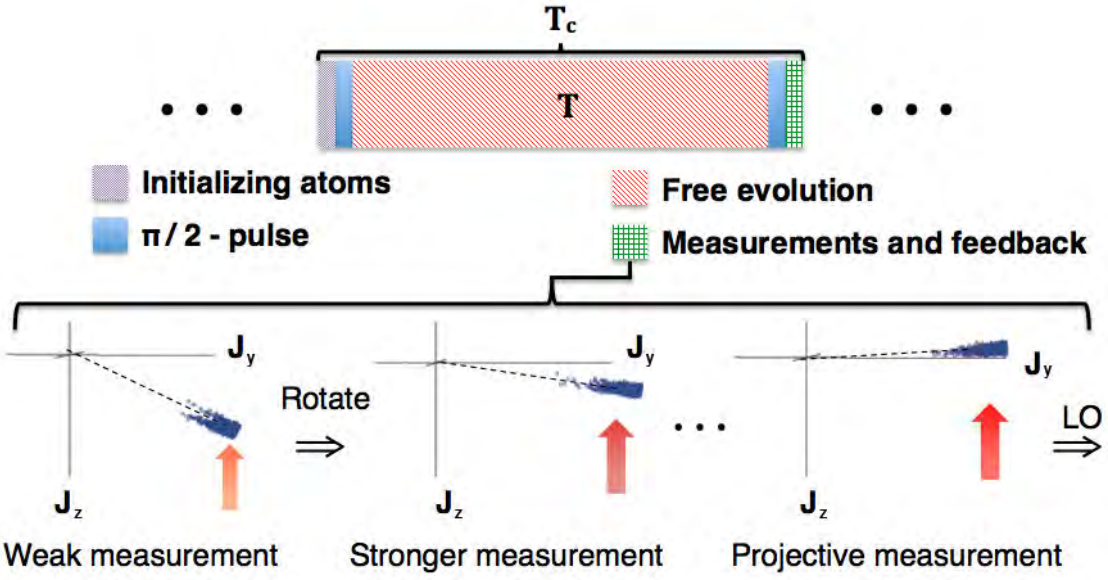

FIGURE 4.2: Operation of an atomic clock. A clock cycle of duration T_c starts with initializing the atoms and ends with the measurements and feedback on the LO. The bottom part of the figure shows the adaptive protocol consisting of a series of weak measurements with intermediate feedback. The feedback seeks to rotate the atomic state to have mean spin almost along the y-axis before the final projective measurement and subsequent feedback on the LO.

4.2 Clock operations and adaptive measurements

The operation of the clock consists of repeating the clock cycle illustrated in Fig. 4.2. The total cycle duration, T_c, will be larger than the period of free evolution, due to the time spent on preparation and measurement of the atoms, and this dead time introduces Dick noise to the stability [87]. To focus on the atomic noise we assume that the dead time is negligible ($T_c \sim T$) so that we can ignore the Dick noise. We will discuss this assumption further in sec. 4.5. We discretize time in the number of clock cycles (k) such that at time $t_k = kT$ the frequency correction $\Delta\omega(t_k) = -\alpha\delta\phi^e(t_k)/T$ is applied to the LO, where α sets the strength of the feedback loop and $\delta\phi^e(t_k)$ is the estimate of the accumulated phase $\delta\phi(t_k)$ between time t_{k-1} and t_k. The frequency offset of the LO at time t_k is then $\delta\omega(t_k) = \delta\omega_0(t_k) + \sum_{i=1}^{k}\Delta\omega(t_i)$, where $\delta\omega_0(t_k)$ is the frequency fluctuation of the unlocked LO. The mean frequency offset, after running for a period $\tau = lT$ ($l \gg 1$), is

$$\delta\bar{\omega}(\tau) = \frac{1}{l}\sum_{k=1}^{l}\frac{\delta\phi(t_k) - \delta\phi^e(t_k)}{T}, \tag{4.1}$$

resulting in the long term stability of the atomic clock,

$$\sigma_\gamma(\tau) = \langle(\delta\bar{\omega}(\tau)/\omega)^2\rangle^{1/2} \tag{4.2}$$

$$= \sqrt{\frac{1}{\tau\omega^2}}\left(\frac{1}{l}\frac{\langle(\sum_{k=1}^{l}\delta\phi(t_k)-\delta\phi^e(t_k))^2\rangle}{T}\right)^{1/2} \tag{4.3}$$

We initially assume that the phase offset of the unlocked LO $\delta\phi_0$ is due to frequency fluctuations in the LO with a white noise spectrum. Later, we will also consider the case where the fluctuations have a $1/f$ spectrum. For white noise, we have $\langle\delta\phi_0^2\rangle = \gamma T$ ($\langle\delta\phi_0\rangle = 0$), where γ is a parameter characterizing the fluctuations. We will argue below that in the limit $\alpha \ll 1$, the phases are uncorrelated such that $\sigma_\gamma(\tau) = \sqrt{\gamma/\tau\omega^2}(\langle(\delta\phi_0 - \delta\phi^e)^2\rangle/\gamma T)^{1/2}$. This expression shows that for fixed γ and τ the stability of the clock only depends on how precisely we can estimate $\delta\phi_0$.

4.2.1 Adaptive measurements

Our weak measurements is based on the strategy developed and demonstrated in Refs. [69, 70, 88, 89], where a light field dispersively interact with the spin and is subsequently measured. This is described by a Hamiltonian $H_{int} = -\chi_1\hat{J}_3\hat{X}_1$ where χ_1 is the interactions strength and $\hat{X}_1$ is the canonical position operator of the light [90–92]. The measurement results in a rotation around $\hat{J}_3$ described by the rotation matrix $\mathbf{R}_3(\hat{\Pi}_1)$, where $\hat{\Pi}_1 = \Omega_1\hat{X}_1$. $\Omega_1 = \chi_1\mu_1$ is the measurement strength and μ_1 is the measurement time. The canonical momentum operators of the light before, $\hat{P}_1$, and after, $\hat{P}_1'$, the interaction are then related by $\hat{P}_1' = \hat{P}_1 - \Omega_1\hat{J}_3$. $\hat{P}_1'$ is measured using homodyne detection [40] and the phase is estimated as $\delta\phi_1^e = \frac{-\beta_1\hat{P}_1'}{\Omega_1\langle\hat{J}_z\rangle}$ where the factor β_1 is found from minimizing $\langle(\delta\phi_0 - \delta\phi_1^e)^2\rangle$. Based on the phase estimate, we rotate the spin of the atoms around $\hat{J}_1$ in order to compensate for the extra noise added (ΔJ_z) by the spin squeezing. This is described by a rotation matrix $\mathbf{R}_1(\delta\phi_1^e)$. The process can be iterated such that after $n-1$ weak measurements, the Heisenberg evolution of the original operators $(\hat{J}_1, \hat{J}_2, \hat{J}_3)$ is:

$$\begin{pmatrix}\hat{J}_1\\ \hat{J}_2\\ \hat{J}_3\end{pmatrix}_n = \mathbf{R}_1(\delta\phi_{n-1}^e)\mathbf{R}_3(\hat{\Pi}_{n-1})...\mathbf{R}_1(\delta\phi_1^e)\mathbf{R}_3(\hat{\Pi}_1)\begin{pmatrix}\hat{J}_1\\ \hat{J}_2\\ \hat{J}_3\end{pmatrix} \tag{4.4}$$

The final measurement is assumed to be a projective measurement and the final phase estimate $\delta\phi_n^e$ is thus $\delta\phi_n^e = \frac{\beta_n\hat{J}_{3,n}}{\langle\hat{J}_z\rangle}$. The factors of β_i in the phase estimates are found by minimizing $\langle(\delta\phi_0 - \sum_{j=1}^{i}\delta\phi_j^e)^2\rangle$ with respect to β_i after each measurement. The final

estimate of $\delta\phi_0$ at the end of the measurement sequence is $\delta\phi^e = \sum_{i=1}^{n} \delta\phi_i^e$, where $\delta\phi_i^e$ is the phase estimate after the i'th measurement.

4.3 Near Heisenberg limited stability

We will now show semi-analytically that the measurement strategy contained in Eq. (4.4) allows for near Heisenberg limited stability. For simplicity, we set all $\beta_i = 1$ in our analytical calculations. Note that this choice is not ideal and the true performance of the clock will thus be better than what we estimate analytically. Later we will argue that for white noise, and in the limit of a weak feedback ($\alpha \ll 1$), we can determine the stability of the LO from looking at the the error between the estimated phase and the true phase of the LO for each Ramsey sequence independently. After j weak measurements the difference between the true phase and the estimated phase $\delta\Phi_j$ is

$$\delta\Phi_j = \delta\phi_0 - \sum_{i=1}^{j} \delta\phi_i^e = \delta\phi_0 - \sum_{i=1}^{j-1} \delta\phi_i^e - \delta\phi_j^e. \tag{4.5}$$

Using equation (4.4) to get an expression for $\delta\phi_j^e$ and the fact that $\delta\Phi_{j-1} = \delta\phi_0 - \sum_{i=1}^{j-1} \delta\phi_i^e$, we can express the phase error as

$$\delta\Phi_j \;\approx\; \delta\Phi_{j-1}(1-\hat{J}_z/\langle\hat{J}_z\rangle) - (\hat{J}_y + \delta\hat{J}_{3,j} - \hat{P}_j/\Omega_j)/\langle\hat{J}_z\rangle, \tag{4.6}$$

where we have assumed $\delta\Phi_{j-1} \ll 1$. The first term in (4.6) gives a contribution $\sim \delta\Phi_{j-1}\Delta J_z/\langle\hat{J}_z\rangle$ to $\sigma_\gamma(\tau)$ from the noise in the mean spin direction as discussed previously. Note that this term is proportional to the phase estimation error at the previous measurement stage, since it depends on how well the 'banana' in Fig. 4.1 is rotated into the xy-plane. For a useful adaptive protocol, $\delta\Phi_{j-1}$ gets smaller for growing j and the noise that enters through $\Delta\hat{J}_z$ is reduced. The last terms in Eq. (4.6) gives the noise from $\Delta\hat{J}_y$, the accumulated back action of the previous measurements ($\langle\delta J_{3,j}^2\rangle$), and the noise from the incoming light in the measurement ($\Delta\hat{P}_j^2 = \langle\hat{P}_j^2\rangle$).

The stronger a measurement is, the less noise is added through $\Delta\hat{P}_j^2/\Omega_j^2$ since the measurement is more precise. Any imprecision $\Delta\hat{P}_{i<j}^2/\Omega_{i<j}^2$ from previous measurements is contained in $\delta\Phi_{j-1}$ and is corrected for in the subsequent stages of the protocol, which estimate how well we corrected the phase in previous measurements. This means that we can initially work with weak measurements, which only give a rough estimate since later stronger measurements correct for the imprecision in the initial measurements.

The accumulated back action noise, $\delta\hat{J}_{3,j}$, originates from the disturbance caused by the measurements. The measurements add noise in $\hat{J}_1, \hat{J}_2$, which is mixed into $\hat{J}_3$ when the

atomic state is rotated to have mean spin almost along the y-axis. We will later show that the dominant term in $\delta\hat{J}_{3,j}$ is $\delta\hat{J}_{3,j} \sim \sum_{i=1}^{j-1} \delta\phi_i^e \Omega_i \hat{X}_i \hat{J}_x$. The stronger a measurement is, the more noise is added to the stability. For a useful adaptive protocol, however, $\delta\phi_i^e$ gets smaller for growing i, which means that the i'th measurement can be stronger than the previous $(i-1)$'th measurements without adding more noise to the stability.

Above we have argued that we can suppress the noise terms originating from ΔJ_z, $\Delta\hat{P}_j$, and $\delta\hat{J}_{3,j}$ using an adaptive protocol with weak initial measurements. A remaining question is how well this suppression work. We therefore consider the expressions for the different noise terms in Eq. (4.6) in more detail. To this end, we write the phase dependence of $\hat{J}_2$ and $\hat{J}_3$ explicitely, i.e. $\hat{J}_2(\theta) = \sin(\theta)\hat{J}_y - \cos(\theta)\hat{J}_z, \qquad \hat{J}_3(\theta) = \sin(\theta)\hat{J}_z + \cos(\theta)\hat{J}_y$ and expand Eq. (4.4) in an iterative way. The Heisenberg evolution of the operators after the first weak measurement and subsequent feedback is:

$$\begin{pmatrix} \hat{J}_1 \\ \hat{J}_2 \\ \hat{J}_3 \end{pmatrix}_2 = \mathbf{R}_1(\delta\phi_1^e)\mathbf{R}_3(\hat{\Pi}_1) \begin{pmatrix} \hat{J}_1 \\ \hat{J}_2(\delta\phi_0) \\ \hat{J}_3(\delta\phi_0) \end{pmatrix} \tag{4.7}$$

$$= \begin{pmatrix} \cos\hat{\Pi}_1 & -\sin\hat{\Pi}_1 & 0 \\ \cos\delta\phi_1^e \sin(\hat{\Pi}_1) & \cos(\delta\phi_1^e)\cos(\hat{\Pi}_1) & -\sin(\delta\phi_1^e) \\ \sin(\delta\phi_1^e)\sin(\hat{\Pi}_1) & \sin(\delta\phi_1^e)\cos(\hat{\Pi}_1) & \cos(\delta\phi_1^e) \end{pmatrix} \begin{pmatrix} \hat{J}_1 \\ \hat{J}_2(\delta\phi_0) \\ \hat{J}_3(\delta\phi_0) \end{pmatrix} \tag{4.8}$$

$$= \begin{pmatrix} \hat{J}_1 \\ \hat{J}_2(\delta\phi_0 - \delta\phi_1^e) \\ \hat{J}_3(\delta\phi_0 - \delta\phi_1^e) \end{pmatrix} + \begin{pmatrix} \delta\hat{J}_{1,2} \\ \delta\hat{J}_{2,2} \\ \delta\hat{J}_{3,2} \end{pmatrix} \tag{4.9}$$

where the operators

$$\delta\hat{J}_{1,2} = (\cos(\hat{\Pi}_1)-1)\hat{J}_1 - \sin(\hat{\Pi}_1)\hat{J}_2(\delta\phi_0) \tag{4.10}$$

$$\delta\hat{J}_{2,2} = \cos(\delta\phi_1^e)\sin(\hat{\Pi}_1)\hat{J}_1 + \cos(\delta\phi_1^e)(\cos(\hat{\Pi}_1)-1)\hat{J}_2(\delta\phi_0) \tag{4.11}$$

$$\delta\hat{J}_{3,2} = \sin(\delta\phi_1^e)\sin(\hat{\Pi}_1)\hat{J}_1 + \sin(\delta\phi_1^e)(\cos(\hat{\Pi}_1)-1)\hat{J}_2(\delta\phi_0) \tag{4.12}$$

describe the noise due to the back action of the measurement. Note that the back action also affects $\hat{J}_3$ even though $\hat{J}_3$ is conserved and hence unaffected during the measurement. This is because the rotation during the feedback mixes back action noise into $\hat{J}_3$.

The process is now iterated such that the Heisenberg evolution after $n-1$ weak measurements and subsequent rotations is

$$\begin{pmatrix} \hat{J}_1 \\ \hat{J}_2 \\ \hat{J}_3 \end{pmatrix}_n = \begin{pmatrix} \hat{J}_1 \\ \hat{J}_2(\delta\phi_0 - \sum_{i=1}^{n-1}\delta\phi_i^e) \\ \hat{J}_3(\delta\phi_0 - \sum_{i=1}^{n-1}\delta\phi_i^e) \end{pmatrix} + \begin{pmatrix} \delta\hat{J}_{1,n} \\ \delta\hat{J}_{2,n} \\ \delta\hat{J}_{3,n} \end{pmatrix} \tag{4.13}$$

where the iterative expressions for $\delta\hat{J}_{1,j-1}, \delta\hat{J}_{2,j-1}$ and $\delta\hat{J}_{3,j-1}$ are

$$\begin{aligned}
\delta\hat{J}_{1,j} &= (\cos(\hat{\Pi}_{j-1})-1)\hat{J}_1 - \sin(\hat{\Pi}_{j-1})\hat{J}_2\left(\delta\phi_0 - \sum_{i=1}^{j-1}\delta\phi_i^e\right) + \cos(\hat{\Pi}_{j-1})\delta\hat{J}_{1,j-1} \\
&\quad -\sin(\hat{\Pi}_{j-1})\delta\hat{J}_{2,j-1} \qquad (4.14)\\
\delta\hat{J}_{2,j} &= \cos(\delta\phi_{j-1}^e)\sin(\hat{\Pi}_{j-1})\hat{J}_1 + \cos(\delta\phi_{j-1}^e)(\cos(\hat{\Pi}_{j-1})-1)\hat{J}_2\left(\delta\phi_0 - \sum_{i=1}^{j-1}\delta\phi_i^e\right) \\
&\quad + \cos(\delta\phi_{j-1}^e)\sin(\hat{\Pi}_{j-1})\delta\hat{J}_{1,j-1} + \cos(\delta\phi_{j-1}^e)\cos(\hat{\Pi}_{j-1})\delta\hat{J}_{2,j-1} \\
&\quad -\sin(\delta\phi_{j-1}^e)\delta\hat{J}_{3,j-1} \qquad (4.15)\\
\delta\hat{J}_{3,j} &= \sin(\delta\phi_{j-1}^e)\sin(\hat{\Pi}_{j-1})\hat{J}_1 + \sin(\delta\phi_{j-1}^e)(\cos(\hat{\Pi}_{j-1})-1)\hat{J}_2\left(\delta\phi_0 - \sum_{i=1}^{j-1}\delta\phi_i^e\right) \\
&\quad + \sin(\delta\phi_{j-1}^e)\sin(\hat{\Pi}_{j-1})\delta\hat{J}_{1,j-1} + \sin(\delta\phi_{j-1}^e)\cos(\hat{\Pi}_{j-1})\delta\hat{J}_{2,j-1} \\
&\quad +\cos(\delta\phi_{j-1}^e)\delta\hat{J}_{3,j-1} \qquad (4.16)
\end{aligned}$$

with $\delta\hat{J}_{1,1} = \delta\hat{J}_{2,1} = \delta\hat{J}_{3,1} = 0$. In the final *projective* measurement, we measure $\hat{J}_{3,n}$ and obtain a phase estimate $\delta\phi_n^e = \hat{J}_{3,n}/\langle\hat{J}_z\rangle$. Our final estimate of $\delta\phi_0$ is then $\delta\phi^e = \sum_{i=1}^{n}\delta\phi_i^e$, i.e. $\delta\phi_i^e$ refers to a phase estimate during the adaptive measurement sequence while $\delta\phi^e$ is the final phase estimate at the end of the adaptive measurement sequence. The difference, $\delta\Phi_n$, between $\delta\phi^e$ and the true phase is given in Eq. (4.5) with $j = n$. Using equation (4.13), we can express $\delta\Phi_n$ using the previous phase estimation error ($\delta\Phi_{n-1}$) and the last measurement

$$\begin{aligned}
\delta\Phi_n &= \delta\Phi_{n-1} - \left(\sin(\delta\Phi_{n-1})\hat{J}_z + \cos(\delta\Phi_{n-1})\hat{J}_y + \delta\hat{J}_{3,n}\right)/\langle\hat{J}_z\rangle \qquad (4.17)\\
&\approx \delta\Phi_{n-1}(1-\hat{J}_z/\langle\hat{J}_z\rangle) - \hat{J}_y/\langle\hat{J}_z\rangle - \delta\hat{J}_{3,n}/\langle\hat{J}_z\rangle \qquad (4.18)
\end{aligned}$$

where $\delta\Phi_{n-1} = \delta\phi_0 - \sum_{i=1}^{n-1}\delta\phi_i^e$ and we have assumed $\delta\Phi_{n-1} \ll 1$ to expand the sine and cosine. As noted above, we will argue later that the stability of the LO will be given by the phase error $\langle\delta\Phi_n^2\rangle^{1/2}$ for each Ramsey sequence independently. We will therefore explore the limitations to the stability from the noise terms in $\langle\delta\Phi_n^2\rangle^{1/2}$ in this limit. Note that Eq. (4.18) is similar to Eq. (4.6) with $j = n$ except that the light noise $\hat{P}_n$ is not included. This is because the final measurement is a projective measurement and the light power is therefore assumed strong enough for this noise to be neglected.

We now analyze the various terms in $\langle\delta\Phi_n^2\rangle$ in more detail. The estimated phase in the j'th weak measurement is

$$\delta\phi_j^e = \left(\sin(\delta\Phi_{j-1})\hat{J}_z + \cos(\delta\Phi_{j-1})\hat{J}_y + \delta\hat{J}_{3,j} - \hat{P}_j/\Omega_j\right)/\langle\hat{J}_z\rangle. \qquad (4.19)$$

Using Eqs. (4.14)-(4.16) and Eqs. (4.18)-(4.19), we can express the three dominant contributions to the stability due to the noise in $\hat{J}_z$ as

$$1. \quad \langle \delta\phi_0^2 \rangle \langle (1 - \hat{J}_z/\langle \hat{J}_z \rangle)^{2n} \rangle \tag{4.20}$$

$$2. \quad 2\langle \delta\phi_0 (\sin(\delta\phi_0) - \delta\phi_0) \rangle \langle (1 - \hat{J}_z/\langle \hat{J}_z \rangle)^{2n-1} \hat{J}_z/\langle \hat{J}_z \rangle \rangle \tag{4.21}$$

$$3. \quad \langle (\sin(\delta\phi_0) - \delta\phi_0)^2 \rangle \langle (1 - \hat{J}_z/\langle \hat{J}_z \rangle)^{2n-2} \hat{J}_z^2/\langle \hat{J}_z \rangle^2 \rangle. \tag{4.22}$$

Here "dominant" refers to decreasing slowest with N.

The above expressions are independent of the atomic state but we will now focus on a specific type of states in order to treat the system in more detail. We consider spin squeezed states of the form $|\psi(\kappa)\rangle = \mathcal{N}(\kappa) \sum_m (-1)^m e^{-(m/\kappa)^2} |m\rangle$, where $|m\rangle$ are eigenstates of $\hat{J}_y$ with eigenvalue m, $\mathcal{N}(\kappa)$ is a normalization constant and the sum is from $-J$ to J where $J = N/2$ is the total angular momentum quantum number. This form gives a simple family of states characterized by a single parameter (κ), which can extrapolate between uncorrelated states, $\kappa = \sqrt{N}$, and highly squeezed states approaching the $|m = 0\rangle$ Fock state $\kappa \to 0$. It may be possible to identify more optimal states [93] but this simple form is sufficient for our present purpose. We consider the limit where $N \gg 1$ such that we can replace sums with integrals when calculating the moments of the angular momentum operators. This allows us to get analytical expressions for the moments of J_z in Eqs. (4.20)-(4.22). All these terms will decrease with growing κ since ΔJ_z decreases for growing κ, e.g., for a coherent spin state $\kappa = \sqrt{N}$ we have $\Delta J_z \sim 0$. For a fixed κ, all three terms will also decrease with a growing number of measurements n until a certain $n_{max}(\kappa)$ is reached. Since we have set all $\beta_i = 1$ in our analytical calculations, we find that for $n > n_{max}(\kappa)$ the noise will increase and $n_{max}(\kappa)$ is thus a minimum indicating that there is an optimal number of measurements. In our numerical simulations, however, we include the correct β_i's and find that increasing n above $n_{max}(\kappa)$ have no effect, i.e. there are no further noise reduction or enhancement. This is because the optimal feedback algorithm (with $\beta_i \neq 1$) knows not to react too strongly to measurements, which provide to little useful information. At $n_{max}(\kappa)$ the uncertainty in $\hat{J}_z$ prevents us from gaining information by introducing more measurements. We believe that this effect is due to the finite probability of measuring a J_z with opposite sign than $\langle \hat{J}_z \rangle$, which spoils the measurement strategy. Note that $n_{max}(\kappa)$ grows with κ since the width of $\hat{J}_z$ decreases with κ.

Of the three therm in Eqs. (4.20)-(4.22), the term in equation (4.22) is decreasing the slowest with n since this contains $(1 - \hat{J}_z/\langle \hat{J}_z \rangle)$ to the lowest power. In the following, we therefore focus on this term. In order for the performance to be nearly Heisenberg limited, we need the contribution from this term to be close to or smaller than the Heisenberg limit, and this put restrictions on the possible values of κ. To determine the

conditions for κ, we have numerically solved the equation $\langle(1-\hat{J}_z/\langle\hat{J}_z\rangle)^{2n-2}\hat{J}_z^2/\langle\hat{J}_z\rangle^2\rangle = 1/N^2$ since $1/N^2$ is the Heisenberg limit of $\langle\delta\Phi_n^2\rangle$. This condition thus determines the parameters for which the noise from ΔJ_z is comparable to the Heisenberg limit. For N in the range $N = 10^3 - 10^9$, we have found the minimum κ for which the equation is fulfilled with $n = n_{max}(\kappa)$ i.e. assuming the optimal number of measurements. The result is that κ needs to grow with increasing N to suppress the noise in J_z, but the growth can be slower than $\kappa \sim \log\sqrt{N} + 2$ if $n = n_{max} \sim 3\log N$ measurements are used. Thus, if we choose $\kappa \sim \log\sqrt{N} + 2$ and $n \sim 3\log N$ the noise terms in equation (4.20)-(4.22) will decrease as $\lesssim 1/N^2$, which is the Heisenberg limit.

We now turn to the measurement noise, which consists of two parts. One is the accumulated back action contained in $\langle\delta\hat{J}_{3,n}^2\rangle$ (see Eq. (4.18)) while the other is due to the noise in the probe light (the last term in Eq. (4.19)). For now, we consider the accumulated back action. Using Eqs. (4.14)-(4.16), we find that this is dominated by $\sum_{i=1}^{n-1}\Omega_i^2\langle\hat{X}_i^2\rangle\langle(\delta\phi_i^e\hat{J}_x/\langle\hat{J}_z\rangle)^2\rangle$ and that the dominant terms from each measurement are

$$i = 1: \qquad \frac{1}{2}\langle\sin(\delta\phi_0)^2\rangle\langle(1-\hat{J}_z/\langle\hat{J}_z\rangle)^2\hat{J}_x^2/\langle\hat{J}_z\rangle^2\rangle\Omega_1^2 \tag{4.23}$$

$$i > 1: \qquad \frac{1}{2}\langle(\sin(\delta\phi_0) - \delta\phi_0)^2\rangle\langle(1-\hat{J}_z/\langle\hat{J}_z\rangle)^{2i-2}\hat{J}_z^2\hat{J}_x^2/\langle\hat{J}_z\rangle^4\rangle\Omega_i^2 \tag{4.24}$$

where we have assumed that the probe light has vacuum statistics such that $\langle\hat{P}\rangle = \langle\hat{X}\rangle = \langle\hat{X}\hat{P}\rangle = 0$ and $\langle\hat{X}^2\rangle = \langle\hat{P}^2\rangle = 1/2$. Again, we can get analytical expressions for $\langle(1-\hat{J}_z/\langle\hat{J}_z\rangle)^2\hat{J}_x^2/\langle\hat{J}_z\rangle^2\rangle$ and $\langle(1-\hat{J}_z/\langle\hat{J}_z\rangle)^{2i-2}\hat{J}_z^2\hat{J}_x^2/\langle\hat{J}_z\rangle^4\rangle$ by using the Gaussian approximation. Motivated by the previous numerical calculations, we set $\kappa = \log\sqrt{N}+2$, $n \sim 3\log N$ and by numerically evaluating the terms for $N = 10^3 \to 10^9$ we find that for $\Omega_i = N^{-1+\frac{i}{n+1}}$ all terms will be $\lesssim 1/N^2$, i.e. at the Heisenberg limit.

We now consider the part of the measurement noise that comes from the noise in the probe light. From Eqs. (4.14)-(4.16) and Eq. (4.19), we find that the dominant terms are $\sum_{i=1}^{n-1}\langle(1-\hat{J}_z/\langle\hat{J}_z\rangle)^{2n-2i}\rangle\langle\hat{P}_i^2\rangle/(\langle\hat{J}_z\rangle^2\Omega_i^2)$. Again, by numerically evaluating the terms for $N = 10^3 \to 10^9$, we get the scaling of the terms and we find that for $\kappa = \log\sqrt{N}+2$, $n \sim 3\log N$ and $\Omega_i = N^{-1+\frac{i}{n+1}}$ all the terms will be $\lesssim 1/N^2$.

So far, we have found that we can make the noise from the measurements and from ΔJ_z be $\lesssim 1/N^2$, which is the Heisenberg limit. The limiting noise in $\langle\Phi_n^2\rangle$ is then the noise from ΔJ_y. From Eq. (4.18), we find that this has a contribution of $\langle\hat{J}_y^2\rangle/\langle\hat{J}_z\rangle^2 = \Delta\hat{J}_y^2/\langle\hat{J}_z\rangle^2$. For the states $|\psi(\kappa)\rangle$, we find that $\Delta\hat{J}_y^2/\langle\hat{J}_z\rangle^2 \sim \kappa^2/N^2$. We thus get

$$\sigma_\gamma \sim \frac{2+\log\sqrt{N}}{N\sqrt{\gamma T}}, \tag{4.25}$$

for $\kappa = \log\sqrt{N} + 2$, $n \sim 3\log N$ and $\Omega_i = N^{-1+\frac{i}{n+1}}$. Note that we are in the limit of $N \gg 1$ and that σ_γ is in units of $(\gamma/(\omega^2\tau))^{1/2}$ (see Sec. 4.2). For comparison, the Heisenberg limit for the same Ramsey time is $\sigma_\gamma = 1/(N\sqrt{\gamma T})$ in the same units. Hence, our results show that near Heisenberg limited stability can be obtained with the adaptive protocol. It is seen that for $N = 10^6$ the upper limit of the stability will differ from the Heisenberg limit by a factor of ~ 5.

4.4 Numerical optimization

To verify the semi-analytical findings in the previous section and to get the optimal stability, we numerically minimized σ_γ. We have simulated an atomic clock with a LO subject to both white and $1/f$ noise. For both types of noise, we have simulated the clock for atom numbers ranging from 100 to 10^6. For $N \leq 1000$ we simulate the full quantum evolution during the measurements by bringing the input state $|\psi(\kappa)\rangle$ trough a Ramsey sequence and mixing it with a light state, which is assumed to have vacuum statistics. We pick the measurement outcome of $\hat{P}'$ according to the corresponding probability distribution and subsequently update the state of the atoms for the next measurement etc. We denote this as 'full quantum simulation'. For $N > 1000$, we approximate the probability distributions of $\hat{J}_{x,y,z}$ with Gaussian distributions with moments calculated from $|\psi(\kappa)\rangle$ in the limit of $N \gg 1$ such that we can replace the sum over m with an integral. We denote this as 'Gaussian simulation'.

4.4.1 Final phase correction

For a fixed Ramsey time, the feedback strength (α) determines how long time the clock has to run before the LO is locked to the atoms. Since we simulate a clock running for a long but finite time there will be some remaining information from the last measurement results, which have not been fully exploited by the feedback loop. In our simulations, we therefore do an additional phase correction to the LO after the final measurement. In principle the influence of the last few measurements could also have been reduced by running the simulation for a longer time, but by doing the correction we reduce the required simulation time. To find the required phase correction and obtain an expression for the stability of the clock, we study the phase of the locked LO. At time $t_k = kT$ the phase of the LO is

$$\delta\phi(t_k) = \int_{t_{k-1}}^{t_k} \left(\delta\omega_0(t) + \sum_{i=1}^{k-1} \Delta\omega_i\right) \mathrm{d}t, \tag{4.26}$$

where $\delta\omega_0(t)$ is the frequency fluctuations of the unlocked LO and $\Delta\omega_i$ is the frequency corrections applied at time t_i. Using that $\Delta\omega_i = -\alpha\delta\phi_e(t_i)/T$ where $\delta\phi_e(t_i)$ is the estimated phase of the LO at time t_i, we can write

$$\delta\phi(t_k) = \delta\phi_0(t_k) - \alpha\sum_{i=1}^{k+1}\delta\phi_e(t_i), \tag{4.27}$$

where $\delta\phi_0(t_k) = \int_{t_{k-1}}^{t_k}\delta\omega_0(t)\mathrm{d}t$. The mean frequency offset of the LO after running for a period $\tau = lT$ ($l \gg 1$) is

$$\delta\bar{\omega}(\tau) = \frac{1}{\tau}\left(\sum_{i=1}^{l}\delta\phi(t_i) - \phi_{\text{final correct}}\right), \tag{4.28}$$

where $\phi_{\text{final correct}}$ is the phase correction that we apply after the final measurement. Combining Eqs. (4.27) and (4.28), we find that $\phi_{\text{final correct}} = \sum_{i=1}^{l}\left((1-\alpha)^{l-i}\delta\phi_e(t_i) + \sum_{j=1}^{i-1}\alpha(1-\alpha)^{l-i}\delta\phi_e(t_j)\right)$ will give the ideal performance. For this choice of $\phi_{\text{final correct}}$ the mean frequency offset becomes

$$\delta\bar{\omega}(\tau) = \frac{1}{l}\sum_{i=1}^{l}\frac{\delta\phi(t_i) - \delta\phi_e(t_i)}{T}, \tag{4.29}$$

i.e. the error is determined by the sum of the phase estimation errors. We use this expression to determine the stability of the clock, which is given by $\sigma_\gamma(\tau) = \langle(\delta\bar{\omega}(\tau)/\omega)^2\rangle^{1/2}$. Note that while the sum is over different time intervals, we cannot in general determine the stability by looking at different intervals independently since the phases are correlated for finite α or for correlated noise in the free running LO e.g. $1/f$ noise. In our analytical calculations, however, we assumed white noise and $\alpha \to 0$ so that we could ignore the correlations and consider each Ramsey sequence independently.

4.4.2 Locking of the LO

The adaptive measurement protocol and the feedback on the LO are simulated as described in Eq. (4.1) and below and the clock cycle is pictured in Fig. 4.2. The feedback effectively locks the LO to the atoms, and lowers the noise level of the LO as shown in Fig. 4.3, where the noise spectrum $S(f)$ of the LO is plotted against the frequency, f. The noise spectrum is here defined as $S(f)\delta(f+f') = \langle\delta\omega(f)\delta\omega(f')\rangle$, where $\delta\omega(f)$ is the Fourier transform of the frequency fluctuations $\delta\omega(t)$ of the LO. For a free running LO with white noise, we use $S(f) = \gamma$ while for 1/f noise, we use $S(f) = \gamma^2/f$, where γ is a parameter characterizing the fluctuations of the LO. Fig. 4.3 shows that for high frequencies, the locked LO has the noise of the free running oscillator but for low

frequencies, the LO is locked to the atoms and is limited by the atomic noise. Furthermore, Fig. 4.3 shows how squeezing improves the stability of the clock by lowering the noise level of the locked LO more than for uncorrelated atoms. While the conventional Ramsey scheme works ideally for $\kappa \sim 14$, the adaptive protocol allows for $\kappa \sim 3$ at the atom number $N = 1000$ used in the figure, and thus leads to an improved stability.

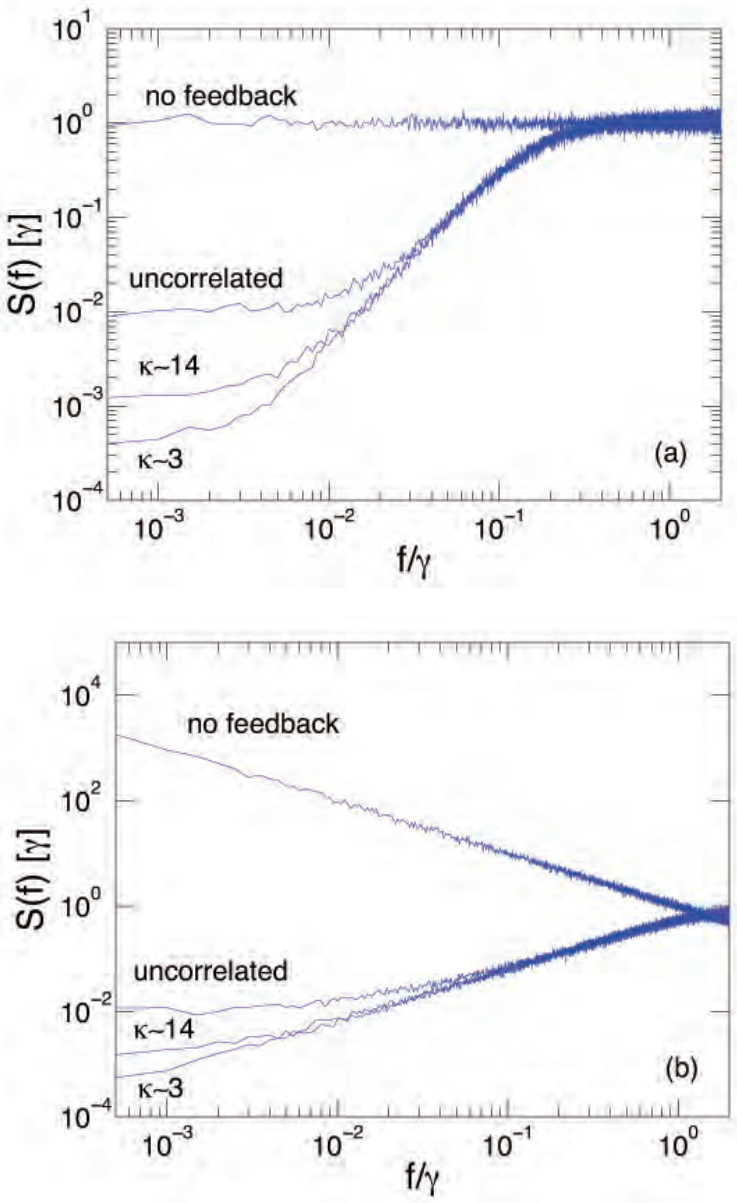

FIGURE 4.3: Noise spectrum of the slaved LO for (a) white noise and (b) $1/f$-noise. The noise spectrum is defined as $S(f)\delta(f+f') = \langle \delta\omega(f)\delta\omega(f')\rangle$ where $\delta\omega(f)$ is the Fourier transform of the frequency fluctuations $\delta\omega(t)$ of the LO. The plots show how the feedback effectively locks the LO to the atoms so that the noise in the LO becomes limited by the atomic noise for low frequencies. Furthermore, it is seen how squeezing lowers the atomic noise and hence the noise of the locked LO. The plots were made for $N = 1000$ and $\gamma T = 0.1$. Counting from above the curves show the noise spectrum for a unlocked LO, the conventional protocol with uncorrelated atoms, the conventional protocol with the optimal squeezing of $\kappa \sim 14$ and the adaptive protocol with optimal squeezing of $\kappa \sim 3$. Note that the optimal performance of the adaptive protocol is reached at higher γT and further improvement is thus possible.

4.4.3 Limit of the Ramsey time

For the model investigated here, the stability increases with the Ramsey time T, but T is limited by two types of error. For experiments or simulations running with a fixed Ramsey time, there will always be a finite probability that the feedback loop jumps to a state with a phase difference of 2π (so called *fringe hops* [65]) or that a phase jump that is large enough to spoil the measurement strategy occurs. For the adaptive scheme, this happens for phase jumps $\gtrsim \pi$ while it happens for phase jumps $\gtrsim \pi/2$ for the conventional protocol. The reason for this is that the adaptive protocol is able to distinguish whether the phase lies in the intervals $[0;\pi/2]$ or $[\pi/2;\pi]$ since they will lead to different responses when we rotate the state during the feedback. On the contrary, the conventional protocol only has a single projective measurement and cannot distinguish in which of the two intervals the phase lies. In our simulations, we see the phase jumps as an abrupt break down as we increase the width of the distribution of the acquired phase, i.e. as we increase T, since the variance is $\sigma^2 = \gamma T$ for white noise. This break down is clearly visible in Fig. 4.4. Ideally, we should include correction strategies for the errors due to large phase jumps in our simulations (e.g. running with different Ramsey times would correct for fringe hops), but for simplicity, we ignore this. This means that our simulations have a weak dependence on the number of steps we simulate, but it is shown in App. B.1 that this is only a logarithmic correction and we do not expect this to change our results significantly. Instead, we find the upper limit of γT from the simulations plotted in Fig. 4.4, where $l = 10^6$ (for $1/f$ noise we average over 100 independent runs with $l = 10^4$).

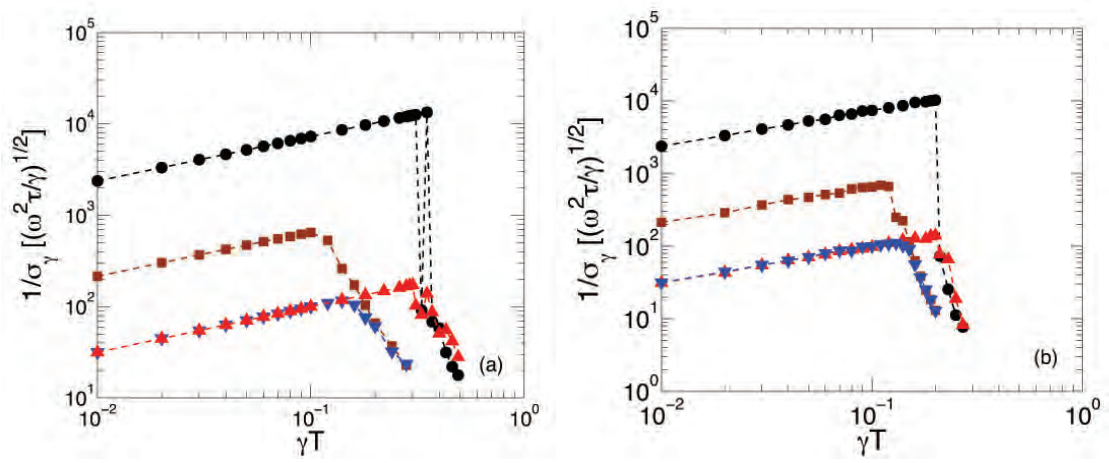

FIGURE 4.4: Stability as a function of the Ramsey time (γT) for (a) white noise and (b) $1/f$ noise in the LO. The plots were made with $N = 10^5$. ■, ▼ are the best non-linear protocol of Ref. [49] while •, ▲ are the adaptive protocol discussed in this article. The adaptive protocol allows for $\gamma T \sim 0.3$ and 0.2 for white and $1/f$ - noise respectively while the conventional protocol of Ref. [49] only allows for $\gamma T \sim 0.1$ for both white and $1/f$ noise. ▼, ▲ correspond to uncorrelated atoms while •, ■ are the ideal choices of squeezing in the adaptive and conventional protocols respectively. The probabilistic nature of the errors that limits γT is visible in (a) where the stability for the adaptive protocol jumps back and forth for $\gamma T > 0.3$ before it is definitely diminished.

We have used $\alpha = 0.1$ in our simulations and do not expect our results to change significantly for a different choice of α. As previously mentioned α determines how long time it takes for the feedback to lock the LO to the atoms (the LO is locked after a time $\sim T/\alpha$). As long as the long term stability is considered at a time $\tau \gg T/\alpha$ the LO is effectively locked to the atoms and the stability does not depend on α (as mentioned above the final phase correction also correct for the influence of the last measurements). To support this, we have repeated the simulations of Fig. 4.4b with $\alpha = 0.5, 0.8$, and 0.9. The simulations show basically the same limits to γT as seen in Fig. 4.4b and more or less identical results for the long term stability for γT below these limits, which supports the above analysis. For γT exceeding the maximal limit for the adaptive protocol, the phase jump errors diminish the stability even more than shown in Fig. 4.4b for larger α, i.e. stronger feedback. This is because the probability of a phase jump error to result in a fringe hop is greater for a stronger feedback. For the conventional protocol, we do not see this effect right above the maximal limit of γT because the probability of a phase jump error to result in a fringe hop is small. However, we expect to see the same effect if we increased γT well above the maximal limit of the conventional protocol.

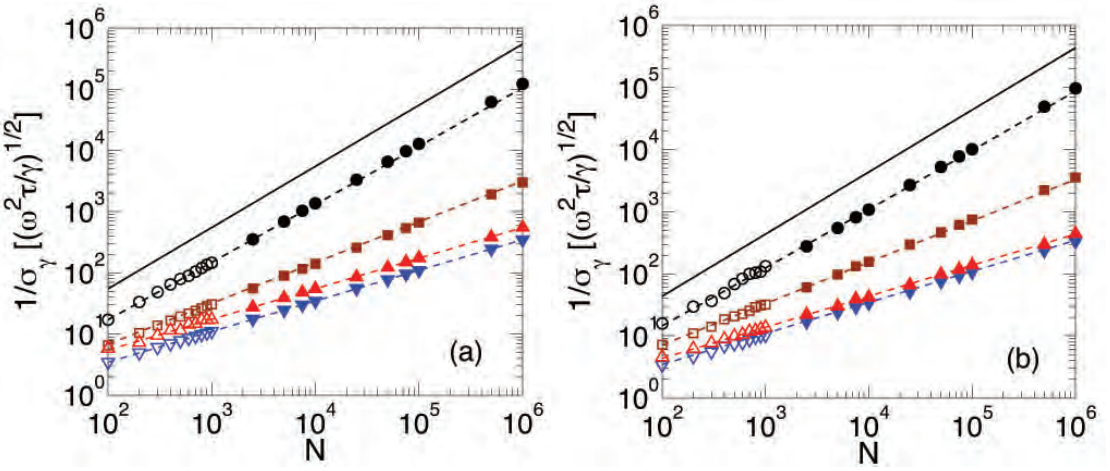

FIGURE 4.5: Optimized stability of an atomic clock for a LO subject to (a) white noise and (b) $1/f$-noise. $\circ, \square, \triangle, \triangledown$ are the full quantum simulation while $\bullet, \blacksquare, \blacktriangle, \blacktriangledown$ are the Gaussian simulation. The Gaussian simulation can be extended down to $N = 100$, which give more or less identical results to the full quantum simulation. $\circ$,$\bullet$ ($\blacktriangle$,$\triangle$) are the adaptive scheme and $\square$, $\blacksquare$ ($\triangledown$,$\blacktriangledown$) are the conventional protocol with (without) entanglement. The dotted lines are the analytical results and the solid line is the Heisenberg limit for the maximal Ramsey time $\gamma T = 0.3$ (a) and $\gamma T = 0.2$ (b).

4.4.4 Numerical minimization

We have numerically minimized $\sigma_\gamma(\tau)$ in the degree of squeezing, the number of weak measurements and the strengths of the measurements. Fig. 4.5a shows the result of the optimization for both the adaptive protocol and the conventional protocol with/without squeezing. Here we have assumed that the LO has a white noise spectrum. The adaptive protocol gives a significant improvement compared to using uncorrelated atoms resulting in near Heisenberg limited stability. The numerical calculations also agree nicely with the analytical calculations. Note that with the adaptive protocol, the Ramsey time can be as large for highly entangled states as for disentangled states and there is thus no difference in the relevant coherence time. Furthermore, because the adaptive protocol can determine phases $\lesssim \pi$, it allows longer interrogation times $\gamma T \lesssim 0.3$ than the conventional protocol $\gamma T \lesssim 0.1$, which begins to give ambiguous results for phases $\sim \pi/2$. This gives an improvement in the stability of roughly a factor 1.6 for uncorrelated atoms.

In practice, the noise of the LO is, however, more likely to have a nontrivial spectrum like $1/f$-noise. We have therefore repeated the numerical optimization with $1/f$-noise in the LO and the results are shown in Fig. 4.5b. The improvement obtained using the adaptive scheme with correlated atoms persists also for $1/f$ noise as shown in the figure. Again near-Heisenberg limited stability is obtained using the adaptive protocol. The longer Ramsey time of the adaptive scheme compared to projective measurements gives an improvement of roughly a factor 1.3 for uncorrelated atoms.

4.5 Conclusion and discussion

In conclusion, we have developed an adaptive measurement protocol, which allows operating atomic clocks near the Heisenberg limit using entangled spin squeezed ensembles of atoms. Our adaptive measurements consist of a series of weak measurements with subsequent phase estimations and feedbacks on the atomic state. The objective of the feedbacks is to rotate the atomic state such that the phase estimate after the final projective measurement, where the main information about the atomic state is extracted, is not influenced by the extra noise added to the mean spin direction, when the atoms are in a highly spin squeezed state. This allows us to fully exploit the advantage of spin squeezing and we show semi-analytically how this can be used to make the stability σ_γ of a clock near-Heisenberg limited with a small logarithmic correction. We have also performed a numerical simulation of spin squeezed clocks operated with adaptive measurement, which confirmed our semi-analytical calculations. We have done this both for a LO with white and $1/f$ noise. Our results clearly demonstrate that entanglement can be an important resource for quantum metrology. Importantly our results are obtained under realistic assumptions, where we account for the dominant source of noise in practice. We find that in this situation, we can gain nearly the full potential of entanglement estimated without accounting for decoherence. Furthermore, the adaptive protocol allows for a higher Ramsey time, which gives an improvement even for uncorrelated atoms. It should be noted that recently another approach to increase the stability of atomic clocks using GHZ states was proposed in Ref. [94]. Here the interrogation of the LO with a cascade of GHZ states allows to obtain near-Heisenberg limited stability with a logarithmic correction similar to what we have found in our protocol.

As stated in Sec. 4.2, the initialization time, the measurement time, and the time of the two $\pi/2$ pulses result in the dead time T_{dead} of the clock, where we do not monitor the fluctuations of the LO. This dead time results in the Dick noise [87], which may limit the stability of the clock. It is therefore desirable to have the ratio T/T_c as close to unity as possible, to minimize the Dick noise, but this ratio depends on the experimental setup used to realize the clock. By technical improvements in the setups being used, e.g., by decreasing the dead time and improving the LO stability, it is in principle possible to reduce the Dick noise. Ultimately the clock will then be limited by the quantum noise of the atoms, which is denoted the standard quantum limit (SQL) for uncorrelated atoms. For current optical lattice clocks, the limit of the stability is not the SQL but rather the Dick limit but a significant amount of research is put into pushing the stability towards the SQL [79, 95, 96]. Clocks based on trapped ions and atomic fountain clocks can, however, be operated with a small Dick noise and demonstrations of SQL limited clocks have been reported [41, 77, 78] (Although the fountain clock are not limited by LO

decoherence and are thus less relevant for our study). Alternatively, some clock based measurements can be performed, which circumvent the Dick noise [45, 95, 96]. The adaptive measurement protocol, that we propose, will inevitably increase the dead time of the clock compared to a clock operated with projective measurements but this increase depends only logarithmically on N since the number of weak measurement is $\sim 3 \log N$. Furthermore, we increase the Ramsey time of the clock by a factor of 3 for white noise in the LO. The ratio between the measurement time and the Ramsey time thus only increases with a factor proportional to $\log N$ where the proportionality constant is the ratio between the time of a weak measurement plus subsequent feedback and a projective measurement We therefore do not expect our scheme to significantly enhance the Dick effect compared to a conventional Ramsey clock operated with projective measurements.

Chapter 5

Efficient atomic clocks operated with several atomic ensembles

As mentioned in Sec. 4.1, the stability of an atomic clock can also be enhanced by increasing the Ramsey time T, resulting in an improvement scaling as $1/\sqrt{T}$ [44, 82, 97]. For clocks with trapped atoms, where there are no other limitations, T becomes limited only by the decoherence in the system. As previously described, this decoherence in practice often originates from the frequency fluctuations of the local oscillator (LO) used to drive the atomic clock transition [82]. Hence, the stability can be increased by simply devising methods to increase the Ramsey period by stabilizing the LO [85].

In this chapter, I present the work of me and Anders S. Sørensen on a scheme where the frequency of the LO is locked to the atomic transition using several ensembles of atoms. This procedure allows increasing the Ramsey period each time another ensemble is used. As a result, we find that the stability of the clock can increase exponentially with the number of ensembles. The work has been described in Ref. [84], which is the basis of this chapter. It should be noted that independently from and simultaneously with our work, T. Rosenband and D. R. Leibrandt worked out essentially the same scheme [83]. Taking the different figures of merit into account, they arrived at results consistent with ours.

5.1 Introduction

Fig. 5.1 illustrates the idea behind the scheme. The feedback of the first ensemble locks the frequency of the LO thus reducing the noise to the atomic noise. Having reduced the noise in the LO, the second ensemble can be operated with a longer Ramsey time.

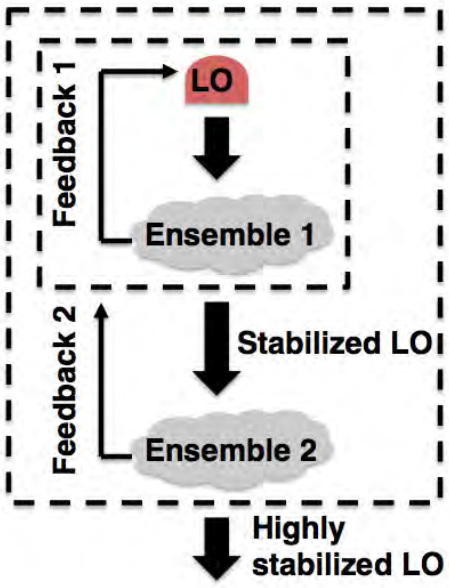

FIGURE 5.1: Illustration of locking the LO using several ensembles. The feedback of the first ensemble stabilizes the LO such that the second ensemble can be operated with a longer Ramsey time. The feedback from the second ensemble then further stabilizes the LO.

Through a second feedback, the noise of the LO can be further reduced as shown in the simulation in Fig. 5.2 (details are given later). The procedure can be extended to any number of ensembles and for uncorrelated atoms, the stability of the LO will scale as $\sqrt{\gamma}(\gamma T_1 N)^{-m/2}$, where m is the number of ensembles (each containing N atoms), γ is a parameter characterizing the frequency fluctuations of the unlocked LO, and T_1 is the Ramsey time of the first ensemble. Hence, the scheme can provide an exponential improvement in the stability with the total number of atoms. In order for the clock to be stable, we need $\gamma T_1 \ll 1$ and hence the protocol requires a minimum number of atoms to improve the performance. With the conventional Ramsey protocol, we find that the scheme works for a minimum ensemble size of 20 atoms. To further optimize the performance of the scheme, we have studied an adaptive measurement protocol for estimating the LO frequency offset, which extends the applicability of the scheme down to ensembles with only 4 (7) atoms for white ($1/f$) noise in the LO. A related procedure, involving multiple measurements on a single ensemble, was proposed in Ref. [85]. By using multiple ensembles, our procedure avoids disturbances from the measurements affecting later measurements.

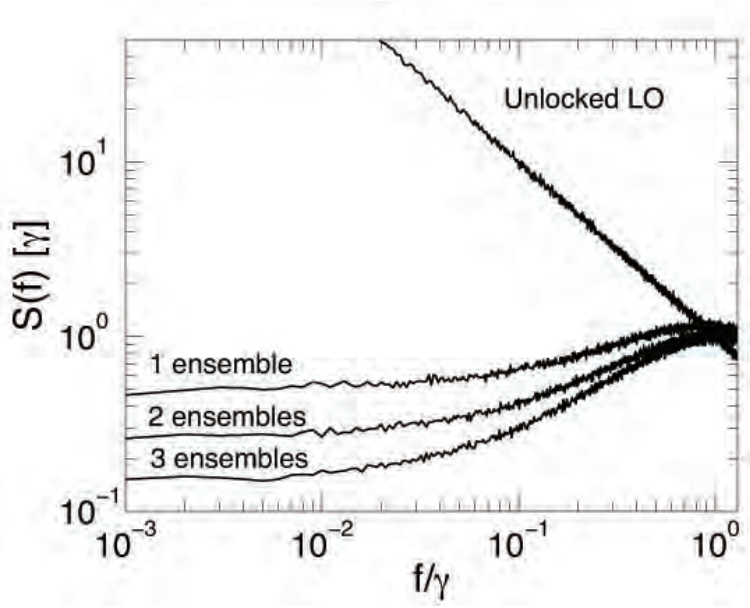

FIGURE 5.2: Numerical simulation of the frequency noise spectrum $S(f)$ of the LO when locked to between 1 and 3 ensembles. The data was simulated as described in Sec. 5.3 for $N = 20$ and $T_1 = 0.1/\gamma$ for the conventional Ramsey scheme. The first feedback lowers the noise of the LO and whitens the spectrum even though the unlocked LO was assumed to be subject to $1/f$ noise. The second and third feedbacks further lowers the noise of LO by a constant factor.

5.2 Locking of the LO

We assume that the LO is locked to the atomic transition using Ramsey spectroscopy. Similar to the approach described in Sec. 4.1.1, we model an ensemble of N atoms as a collection of spin-1/2 particles with total angular momentum $\vec{J}$. We define the angular momentum operators $\hat{J}_x$, $\hat{J}_y$ and $\hat{J}_z$ in the usual way and initially, the atoms are pumped to have $\langle\vec{J}\rangle$ along the z-direction, $\langle\hat{J}_x\rangle = \langle\hat{J}_y\rangle = 0$. The Heisenberg evolution of $\hat{J}_z$ after the Ramsey sequence is $\hat{J}_3 = \cos(\delta\phi)\hat{J}_y + \sin(\delta\phi)\hat{J}_z$ where $\delta\phi = \delta\omega T$ is the acquired phase of the LO relative to the atoms. At the end of the Ramsey sequence $\hat{J}_3$ is measured and used to make an estimate $\delta\phi^e = -\arcsin(2\hat{J}_3/N)$ of $\delta\phi$. The feedback loop then steers the frequency of the LO towards the atomic transition by applying a frequency correction of $\Delta\omega = -\alpha\delta\phi^e/T$ to the LO where α sets the strength of the feedback loop. As in Chap. 4, we assume a negligible Dick noise [87].

We now consider an atomic clock with two atomic ensembles operated with different Ramsey times and show how this can improve the stability of the clock. These considerations can then easily be extended to several ensembles. Note that we assume the intrinsic linewidth of the atoms to be negligible such that the atomic linewidth is only limited by the Ramsey time. The first ensemble is operated with Ramsey time T_1 and we assume that the second ensemble is operated with Ramsey time $T_2 = nT_1$ where n

is an integer. We can make two discrete time scales describing ensemble one and two respectively. Ensemble one is measured at $t_k = kT_1$ and ensemble two is measured at $t_s = sT_2 = s \cdot nT_1$. The frequency offset of the LO between time t_{k-1} and t_k is then

$$\delta\omega(t) = \delta\omega_0(t) + \Delta\omega_1(t_{k-1}) + \Delta\omega_2(t_{s-1}), \tag{5.1}$$

where $\delta\omega_0(t)$ is the frequency fluctuation of the unlocked LO, $\Delta\omega_1(t_{k-1})$ is the sum of the frequency corrections applied up to time t_{k-1} from the first ensemble and $\Delta\omega_2(t_{s-1})$ is the sum of the frequency corrections applied up to time t_{s-1} from the second ensemble ($t_{s-1} \leq t_{k-1}$). The feedback loops are described by the equations

$$\Delta\omega_1(t_{k-1}) = \Delta\omega_1(t_{k-2}) - \alpha\delta\phi^{e_1}(t_{k-1})/T_1 \tag{5.2}$$

$$\Delta\omega_2(t_{s-1}) = \Delta\omega_2(t_{s-2}) - \alpha\delta\phi^{e_2}(t_{s-1})/T_2, \tag{5.3}$$

where $\delta\phi^{e_1}(t_{k-1})$ and $\delta\phi^{e_2}(t_{s-1})$ are the estimated phases from the first and second ensemble at times t_{k-1} and t_{s-1} respectively. Using Eq. (5.1), we can write the phase of the LO relative to the atoms of the second ensemble at time t_s as

$$\delta\phi_2(t_s) = \int_0^{T_2} \mathrm{d}t' \delta\omega(t_s - t') = \Delta\phi_{s-1} + \delta\tilde{\phi}(t_s), \tag{5.4}$$

where $\Delta\phi_{s-1} = \int_0^{T_2} \Delta\omega_2(t_{s-1})\mathrm{d}t'$ is the accumulated phase due to the feedback of the second ensemble and

$$\delta\tilde{\phi}(t_s) = \int_0^{T_2} \mathrm{d}t' \delta\tilde{\omega}(t_s - t') = \int_0^{T_2} \mathrm{d}t' \delta\omega_0(t_s - t') + \Delta\omega_1(t_s - t') \tag{5.5}$$

is the accumulated phase due to the frequency oscillations of the LO when locked by the feedback of the first ensemble. For now, we assume that $T_2 \gg T_1$ such that the feedback of the first ensemble has stabilized the LO but later we will relax this assumption. From Eqs. (5.3)-(5.4), we then derive the difference equation

$$\delta\phi_2(t_s) - \delta\phi_2(t_{s-1}) = \delta\tilde{\phi}(t_s) - \delta\tilde{\phi}(t_{s-1}) - \alpha\delta\phi^{e_2}(t_{s-1}). \tag{5.6}$$

From this expression, we see that the evolution of the second phase $\delta\phi_2$ is essentially driven by the noise of the stabilized LO from the first step $\delta\tilde{\phi}$ but is stabilized by the second feedback loop described by $\alpha\delta\phi^{e_2}$.

To solve Eq. (5.6), we need to characterize the width of the noise of the stabilized LO from the first stage, $\langle\delta\tilde{\phi}^2\rangle = \int_0^{T_2}\mathrm{d}t \int_0^{T_2}\mathrm{d}t' \langle\delta\tilde{\omega}(t)\delta\tilde{\omega}(t')\rangle$. From Eq. (5.2) and (5.5), we can derive a difference equation for $\delta\tilde{\phi}(t_k) = \int_0^{T_1} \delta\tilde{\omega}(t_k - t')\mathrm{d}t'$, which is the acquired phase of the LO relative to the first ensemble between time t_{k-1} and t_k (we can neglect the

feedback from the second ensemble since $T_2 \gg T_1$),

$$\delta\tilde{\phi}(t_k) - \delta\tilde{\phi}(t_{k-1}) = \delta\phi_0(t_k) - \delta\phi_0(t_{k-1}) - \alpha\delta\phi^{e_1}(t_{k-1}). \tag{5.7}$$

Here $\delta\phi_0(t_k) = \int_0^{T_1} \delta\omega_0(t_k - t')\mathrm{d}t'$ is the phase of the unlocked LO. In comparison to Eq. (5.6), we see that the evolution of the phase $\delta\tilde{\phi}$ is driven by the noise of the unlocked LO but is stabilized by the first feedback loop described by $\alpha\delta\phi^{e_1}$. To solve this equation, we follow the lines of Ref. [98], where the locking of the LO to a single ensemble is described. First, we derive a differential equation from Eq. (5.7) in the limit $N \gg 1$, treating $\hat{J}_x, \hat{J}_y$, and $\hat{J}_z$ as Gaussian variables and considering, for now, a LO subject to white noise. Assuming that the atoms start out in a coherent spin state, we can solve this equation to obtain

$$\langle\delta\tilde{\phi}^2\rangle = T_2/NT_1 = \tilde{\gamma}T_2, \tag{5.8}$$

where we have defined the parameter $\tilde{\gamma} = 1/NT_1$, which characterizes the noise of the stabilized LO. This noise is effectively white for both white and $1/f$ noise in the unlocked LO (Fig. 5.2 and Ref. [98]). The second ensemble thus sees an effective white noise in the LO with $\tilde{\gamma} = 1/(T_1 N)$.

We now return to Eq. (5.6). Writing $\delta\phi_2(t) \sim \delta\omega(t)T_2$, the stability of the clock after running for a time $\tau \gg T_2$ is

$$\sigma_\gamma(\tau) = \frac{1}{\omega\tau T_2}\left(\int_0^\tau \mathrm{d}t \int_0^\tau \mathrm{d}t' \langle\delta\phi_2(t)\delta\phi_2(t')\rangle\right)^{\frac{1}{2}}, \tag{5.9}$$

where ω is the frequency of the atomic transition. Following similar arguments as before, we can derive and solve a differential equation from Eq. (5.6) to obtain an expresion for $\langle\delta\phi_2(t)\delta\phi_2(t')\rangle$. Inserting this into Eq. (5.9) and taking the limit of $\tau \gg T_2$ results in

$$\sigma_\gamma(\tau) = \frac{1}{\omega}\sqrt{\frac{1}{\tau N T_2}}. \tag{5.10}$$

Eq. (5.10) describes how the stability improves with T_2 and N. The longest T_2, we can allow, is determined by how well the LO is stabilized by the first ensemble as contained in $\tilde{\gamma}$ and we parameterize it by $T_{2,max} = \beta_2/\tilde{\gamma}$. In a similar fashion, we assume that $T_{1,max} = \beta_1/\gamma$ for the first ensemble. With these parameterizations, we can express the stability as

$$\sigma_\gamma(\tau) = \frac{1}{\omega}\sqrt{\frac{\gamma}{\tau N^2 \beta_1 \beta_2}} = \frac{1}{\omega}\sqrt{\frac{\gamma\beta_1/\beta_2}{\tau(N\gamma T_{1,max})^2}}. \tag{5.11}$$

With white noise in the unlocked LO, we can pick $\beta_1 = \beta_2$. As previously noted the noise of the LO will also be approximately white with $\tilde{\gamma} \sim 1/NT_1$ after locking it to the first ensemble also for other types of noise, e.g. $1/f$ noise. In that case, it is

desirable to have $\beta_2 \neq \beta_1$ but we still expect β_1/β_2 to be of order unity. Eq. (5.11) shows that by locking the LO to two ensembles of uncorrelated atoms the stability can be significantly improved. If $N\gamma T_1 \gg 1$ the stability obtained from Eq. (5.11) is much better than the single ensemble result in Eq. (5.10) (with $T_2 \to T_1$). The arguments leading to Eq. (5.11) can be generalized in a straight forward way to show that if the LO is locked to m ensembles each containing N atoms, the stability of the clock is $\sigma_\gamma(\tau) = \sqrt{(\beta_1/\beta)^{(m-1)}\gamma/(\omega^2\tau)}(N\gamma T_{1,max})^{-m/2}$ (since the noise of the LO is white after locking it to the first ensemble we use $\beta = \beta_2 = \ldots = \beta_m$). By continuing the procedure, we thus improve the stability exponentially!

5.3 Numerical simulation I: Conventional Ramsey

For the analytical calculations in the previous chapter, we have assumed $N \gg 1$. To investigate the performance for smaller N, we simulate an atomic clock locked to between 1 and 4 atomic ensembles each with atom numbers from $N = 20$ to $N = 100$. From the simulations, we can generalize to the case where the LO is locked to m ensembles. We simulate the full quantum evolution of the atomic state through the Ramsey sequences and subsequent measurements and implement the feedback on the LO similar to the description in Eq. (5.1) and above. The assumption of $T_2 \gg T_1$ can be relaxed by applying a phase correction in the measurement (see App. C.1). Note that we also include a final phase correction in our simulations in order to decrease the necessary simulation time as described in App. C.1.

The number of atoms required in each ensemble to increase the Ramsey time by a factor a at each level is set by the white noise level of the stabilized LO. Using Eq. (5.8) and remembering that β parameterize the maximal Ramsey time for white noise, we have that $T_2/NT_1 = \tilde{\gamma}T_2 = \beta$. Assuming $T_2 = aT_1$, we find that $N \sim a/\beta$ atoms are required in each ensemble to increase the Ramsey time by a factor of a at each level. The minimum number of atoms required for our protocol to work is thus obtained by setting $a = 2$.

To determine β, we need to investigate the errors that limit the Ramsey time T for a LO subject to white noise characterized by γ. This was already done in Sec. 4.4.3 for $N \gg 1$ using a Gaussian approximation for the probability distributions of $\hat{J}_{x,y,z}$. We can effectively use the same procedure to find the limit of T in our setup as described in App. C.2. We find that Ramsey spectroscopy with projective measurements only allows for $\beta \sim 0.1$ and thus $N_{min} = 20$. We find the same limit of $\beta_1 \sim 0.1$ for a LO subject to $1/f$ noise (see App.C.2). Note that our results have a weak (logarithmic) dependence on the number of steps that we simulate as described in App. B.1.

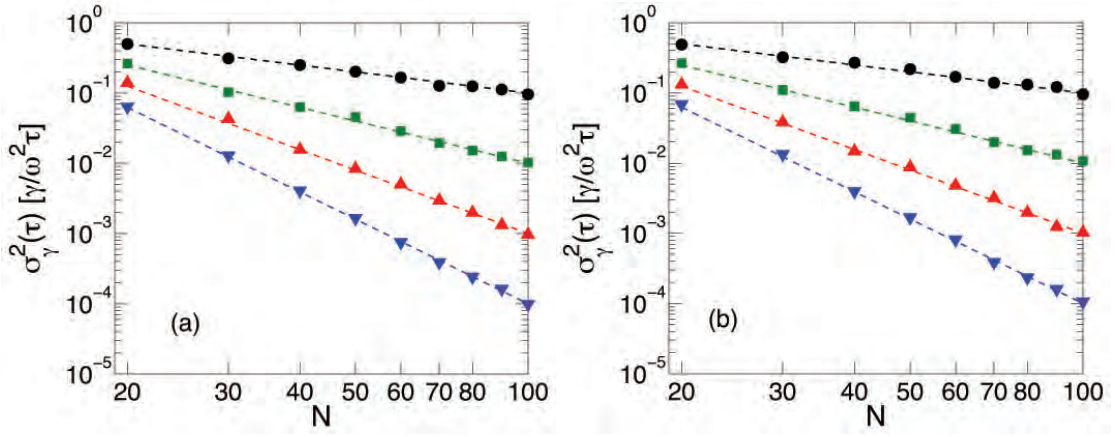

FIGURE 5.3: The stability of atomic clocks for a LO subject to (a) white noise and (b) $1/f$-noise. •, ■, ▲, and ▼ is the stability of a clock with the LO locked to 1,2,3, and 4 ensembles containing N atoms each. The clocks were simulated with $\beta = \beta_1 = 0.1$ and $T_j = nT_{j-1}$. Counting from the left (low N) the points are for integers n from 2 to 10. The dashed lines are the analytical calculations.

We have simulated clocks with an unlocked LO subject to both white and $1/f$ noise with the constraint $\beta = \beta_1 = 0.1$. In Fig. 5.3, the stability of the clocks are plotted against the ensemble size N. Fig. 5.3 confirms that the scheme works down to atom numbers of $N = 20$, where we gain a factor of $\sim 2^{m-1}$ in $\sigma_\gamma^2(\tau)$ by locking the LO to m ensembles for both white and $1/f$ noise. Furthermore, the numerical results are seen to agree nicely with the analytical calculations. We obtain practically the same long term stability for $1/f$ noise as for white noise since the first feedback whitens the noise for small frequencies (cf. Fig. 5.2). We have used a feedback strength of $\alpha = 0.01$ for white noise and $\alpha = 0.5$ for $1/f$ noise in the LO in our simulations. The strong feedback strength of $\alpha = 0.5$ is only used for the first ensemble for $1/f$ noise since the noise seen by the other ensembles is white for which a weaker feedback strength is desirable (see App. C.2).

5.4 Adaptive measurements

The conventional Ramsey protocol considered so far has a lower limit of $N_{min} = 20$ in order for our protocol to work. This limit is due to the inability of the conventional protocol to effectively resolve phases larger than $\pi/2$. The adaptive protocol described in Sec. 4.2.1, however, effectively resolves phases $\lesssim \pi$. In App. C.2, we show that this protocol enables us to extend the Ramsey time to $\beta \sim 0.3$ for white noise and to $\beta_1 \sim 0.2$ for a LO subject to $1/f$ noise. However, the type of weak measurements used in this protocol is hard to implement for ensembles with few atoms. We have therefore modified the protocol such that individual atoms are read out one at a time and a

Bayesian procedure similar to that of Ref. [74, 75] is used for the phase estimation and atomic feedback. We perform intermediate feedbacks during the measurements to rotate the atomic state to be almost in phase with the LO. Due to the rotations, the protocol can resolve phases $\lesssim \pi$ as the previous protocol.

We will now describe the details of the modified protocol. At the end of the Ramsey sequence, i.e. after the second $\pi/2$ pulse, an atom can either be detected in a spin up state, $s = 0$, or a spin down state, $s = 1$. The probability of measuring $s = 0, 1$ depends on the acquired phase $\delta\phi$ of the LO relative to the atoms during the free evolution in the following way

$$P(s|\delta\phi) = s\cos\left(\pi/4 - \delta\phi/2\right)^2 + (1-s)\sin\left(\pi/4 - \delta\phi/2\right)^2. \tag{5.12}$$

According to Baye's theorem, we can write the probability density of $\delta\phi$, conditioned on the measurement result, as

$$P(\delta\phi|s) = \frac{P(s|\delta\phi)P(\delta\phi)}{P(s)}, \tag{5.13}$$

where $P(s) = \int P(\delta\phi)P(s|\delta\phi)\mathrm{d}(\delta\phi)$ is the total probability of measuring s and $P(\delta\phi)$ is the a priori probability distribution of $\delta\phi$, which is determined from characterizing the frequency fluctuations of the LO. We choose a Gaussian distribution with zero mean and variance γT as the a priori distribution. This a priori distribution is exact for a LO subject to white noise but a better a priori distribution could possibly be found for $1/f$ noise. We will, however, use this a priori distribution in both cases, which results in our modified protocol not being as effective for $1/f$ noise as for white noise in the LO. Note that this inaccuracy in our a priori distribution only introduce a less ideal performance in our phase estimate. In our numerical simulations, we retain the full information about the phase evolution so that our suboptimal assumption about the a priori distribution only degrade the performance of the scheme. We estimate the phase based on the measurement as

$$\delta\phi^e = \int \delta\phi P(\delta\phi|s)\mathrm{d}(\delta\phi). \tag{5.14}$$

We then apply a feedback to the remaining atoms, which in the Block sphere picture rotates them by an angle $\delta\phi^e$ around the $\hat{J}_x$ axis, i.e. the feedback tries to bring them into phase with the LO. Generalizing this procedure to a measurement record $S_m =$

$s_1 s_2 \ldots s_i \ldots s_m$, where the measurement result of the i'th atom is s_i, we obtain

$$P(S_m|\delta\phi, \sum_{k=1}^{n_m} \delta\phi_k^e) = \prod_i^m \left[s_i \cos\left(\pi/4 - \delta\phi/2 + \sum_{k=1}^{n_i} \delta\phi_k^e/2\right)^2 + (1-s_i)\sin\left(\pi/4 - \delta\phi/2 + \sum_{k=1}^{n_i} \delta\phi_k^e/2\right)^2 \right], \quad (5.15)$$

where $P(S_m|\delta\phi, \sum_{k=1}^{n_m} \delta\phi_k^e)$ is the probability of obtaining the measurement record S_m conditioned on a drifted phase $\delta\phi$ with a total feedback of $\sum_{k=1}^{n_m} \delta\phi_k^e$ applied during the measurements ($\sum_{k=1}^{n_i} \delta\phi_k^e$ is the feedback experienced by the $i'th$ atom before it is read out). Note that in general $n_i \neq i-1$, i.e. we might read out more than one atom before we do a phase estimate and a subsequent feedback on the remaining atoms. In our simulations, we group the measurements such that we perform ~ 4 feedbacks in total as in the protocol of Ref. [76] for uncorrelated atoms. The final phase estimate $\delta\phi_{n_m+1}^e$, after having readout m atoms, is

$$\delta\phi_{n_m+1}^e = \frac{\int (\delta\phi - \sum_{k=1}^{n_m} \delta\phi_k^e) P(S_m|\delta\phi, \sum_{k=1}^{n_m} \delta\phi_k^e) P(\delta\phi) \mathrm{d}(\delta\phi)}{\int P(S_m|\delta\phi, \sum_{k=1}^{n_m} \delta\phi_k^e) P(\delta\phi) \mathrm{d}(\delta\phi)}, \quad (5.16)$$

where we have used Baye's theorem as described above. All the phase estimates and the feedbacks are performed after the final $\pi/2$ pulse in the Ramsey sequence. Thus, the final estimate of the drifted phase is $\delta\phi_e = \sum_{k=1}^{n_m+1} \delta\phi_k^e$, i.e. the sum of the rotations performed during the measurements and the final phase estimate.

5.5 Numerical simulation II: Adaptive measurements

With the modified adaptive measurement strategy, we simulate clocks locked to between 1 and 4 ensembles for atom numbers from $N = 4$ to 34 with an unlocked LO subject to both white and $1/f$ noise with the constraint $\beta = 0.3$ and $\beta_1 = 0.2$. The upper limits of the Ramsey time were found as described in App. C.2 using the adaptive protocol descibed in Chap. 4 since this simplified the numerics and the Baysian protocol is assumed to lead to similar results. In Fig. 5.4, the stability of the clocks is plotted against the ensemble size N. Fig. 5.4 shows that the adaptive measurement protocol works and allows us to extend the applicability of the scheme of locking to several ensembles down to ensemble sizes of $N = 4$ (7) for white ($1/f$) noise, where we gain a factor of $\sim 2^{m-1}$ in $\sigma_\gamma^2(\tau)$ by locking the LO to m ensembles. We have used the same feedback strengths of $\alpha = 0.01$ for white noise and $\alpha = 0.5$ for $1/f$ noise as in the simulations of the conventional measurements. The minimal number of atoms is higher for $1/f$ noise due to the shorter required Ramsey time for the first ensemble

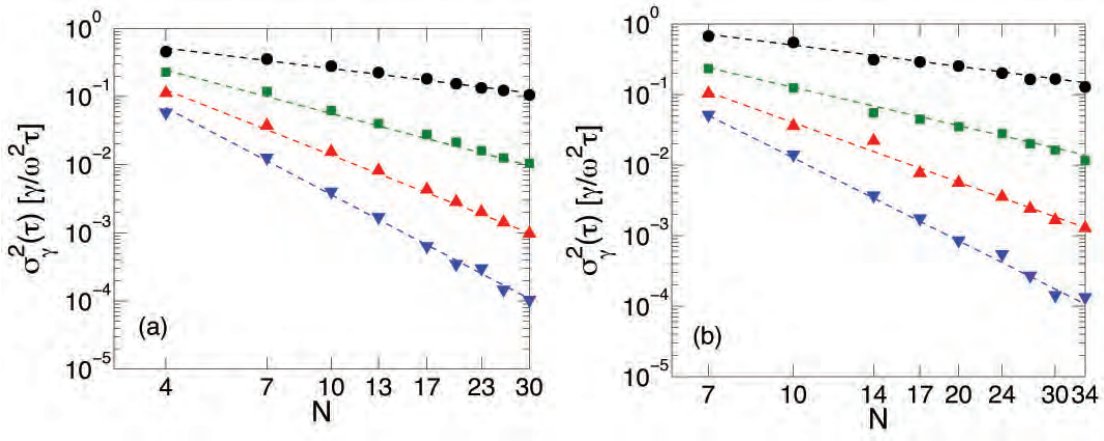

FIGURE 5.4: The stability of atomic clocks with adaptive measurements for a LO subject to (a) white noise and (b) $1/f$-noise. •, ■, ▲, and ▼ is the stability of a clock with the LO locked to 1,2,3, and 4 ensembles of N atoms each. The adaptive protocol allows for $\beta_1 = 0.3$ (a) and $\beta_1 = 0.2$ (b). The clocks were simulated with $T_j = nT_{j-1}$ and counting from the left (low N) the points are for integers n from 2 to 10. The dashed lines are fits of the simulated data.

($\beta_1 \sim 0.2$) and the incomplete characterization of the a priori probability distribution in the Bayesian approach (see Sec. 5.4). The adaptive protocol is therefore not as effective as for white noise, where we have a better understanding of the a priori distribution. It should be noted, however, that in principle it is only in the first ensemble that we need more atoms than for white noise since the feedback of the first ensemble whitens the noise. The adaptive protocol is thus more effective for the subsequent ensembles. We estimated the minimum number of atoms required for the scheme to work to be $N_{min} \sim 2/\beta$, which would give $N_{min} \sim 7$ for $\beta = 0.3$. In this estimate of N_{min}, we assumed that the adaptive protocol leads to a stability at the SQL. This is only true for large N and there are corrections to this for small N. From our simulations, we find that with the modified adaptive protocol, and white noise in the unlocked LO, the feedback of the first ensemble stabilizes the LO to a white noise floor below $1/NT_{1,max}$, i.e. better than what we expect from the SQL. As a result, we can extend the applicability of the protocol to atom number $N = 4$ as shown in Fig. 5.4a.

5.6 Conclusion and discussion

In conclusion, we have demonstrated a scheme for locking the LO in an atomic clock to m ensembles of N atoms each. We have shown how the locking of the LO to one ensemble increases the stability of the LO such that a second ensemble can be interrogated with a longer Ramsey time. As a result, the second ensemble can be used to further increase the stability of the LO. This scheme can be etended to locking the LO to m ensembles

fo which the stability of the clock will scale as $\sqrt{\gamma}(\gamma T_1 N)^{-m/2}$ where T_1 is the Ramsey time of the first ensemble. Our scheme thus provide an exponential improvement in the stability with the number of atoms. This was shown analytically in the limit of $N \gg 1$ and by simulation in the limit of small N. For the conventional Ramsey protocol, our scheme is applicable down to ensemble sizes of $N = 20$ atoms but using a Baysian measurement protocol, it is possible to push this limit. From our simulations, we found that the scheme could be applied down to ensemble sizes of $N = 4(7)$ for white $(1/f)$ noise in the LO. This makes the scheme relevant for atomic clocks with trapped ions, which are typically constructed with only a few ions [44].

One could think of combining this scheme with the spin squeezed states considered in Chap. 4 in order to improve the stability of clocks even further. In the limit of large N, where the adaptive protocol considered in Sec. 4.2.1 can be employed instead of the Bayesian protocol, we would expect the spin squeezing to improve the phase estimations such that the stability of a clock locked to m ensembles would scale as $\sim \sqrt{\gamma}(\gamma T_1 N^2)^{-m/2}$ up to a logarithmic correction in N. It is, however, not straightforward how spin squeezing should be combined with the Baysian measurement strategy used for small N since we are effectively reading out single atoms at a time. It might be necessary to employ another measurement strategy or consider other correlated atomic states in this limit in order to benefit from entangling the atoms.

Both the adaptive measurement strategy described in Chap. 4 and the Baysian strategy described in this chapter only consider the phase estimation after a single Ramsey sequence, i.e. each run of the clock is considered independently from the others. As a result neither one exploits the combined information from several runs. One can therefore think of a more optimal measurement strategy, which also uses the information from previous runs to optimize the measurement strategy/interrogation time in the next run in line with the protocol of Ref.[99].

Chapter 6

Heralded quantum gate

For the construction of functional quantum computers, one of the main challenges is to make gates of sufficiently high quality so that the remaining errors can be suppressed by error correction codes, which makes the computation fault tolerant [100]. On the other hand, long distance quantum communication is envisioned to be enabled by the construction of quantum repeaters, which combine probabilistic entanglement generation over short distances with (probabilistic) entanglement swaps for creating long distance entanglement [16]. For these protocols, the probabilistic nature of the entanglement generation is of less importance, but it is essential that high quality entanglement is achieved conditioned on a heralding measurement. Experimentally, such high fidelity entanglement is often much easier to implement and may be realised in situations, where it would be impossible to perform any quantum operations deterministically.

In this chapter, I present the work of me and and my collaborators on introducing a similar concept to gate operations and developing heralded quantum gates in optical cavities with integrated error detection. In the resulting gates, the infidelity, which would be present for deterministic gates, is converted into a failure probability, which is heralded by an auxiliary atom. Once successful the resulting gate can have an arbitrarily small error. The work was done in collaboration with Peter Kómár, Eric Kessler, Anders S. Sørensen and Mikhail D. Lukin and is described in Ref. [101], which is the basis of this chapter.

6.1 Introduction

Optical cavities are ideal for efficient conversion between the stationary gate qubits and flying qubits in the form of photons, which is a fundamental building block of quantum

networks [31, 102, 103]. Gates can, in principle, also be implemented in optical cavities [104], but the experimental requirements for doing this are very challenging due to the detrimental effect of spontaneous emission and cavity loss. The essential parameter quantifying this is the cooperativity of the atom-cavity system, C, and it can be argued that deterministic gates have a poor error scaling of $1 - F \propto 1/\sqrt{C}$, where F is the fidelity of the gate [105, 106]. To circumvent this limitation, we introduce heralded quantum gates with integrated error detection. As a result of the error detection, the gates exhibit high fidelities when successful. We propose a two-qubit gate where the heralded fidelity of the gate can be arbitrarily close to unity. Furthermore, we present a scheme for an N qubit Toffoli gate where the heralded fidelity have a more favourable scaling of $1 - F \propto 1/C$, than the cooresponding deterministic gate. This comes at the cost of a non-unity but possibly large success probability P_s scaling as $1 - P_s \propto 1/\sqrt{C}$.

The basic idea behind our scheme is to have a combination of qubit atoms and a heralding auxiliary atom in the same cavity. One of the atomic qubit states, e.g. state $|1\rangle$, couples to the cavity mode while $|0\rangle$ is completely uncoupled (see Fig. 6.1a). Such a system has previously been considered for quantum information processing in several papers, e.g. Refs. [36, 106–110]. If any of the qubit atoms is in state $|1\rangle$, the cavity resonance is shifted compared to the bare cavity mode, which can be exploited to make a gate between two or more qubits by reflecting single photons off the cavity [107]. The efficiency of such schemes, however, is limited by photon losses, inefficent detectors and non-ideal single photon sources [36, 110]. We circumvent these problems by introducing an auxiliary atom in the cavity to serve as both an intra-cavity photon source and a detector. The final heralding measurement on the atom can then be performed very efficiently as opposed to previous heralded gates in optical cavities, which relied on the null detection of photons leaving the cavity [111–113]. The auxiliary atom is considered to have two ground states $|g\rangle, |f\rangle$, which can be coupled through an excited state $|E\rangle$ (see Fig. 6.1a). We assume the $|E\rangle \leftrightarrow |f\rangle$ transition to be energetically close to the cavity frequency and to be a closed transition, so that we need to drive the $|g\rangle \rightarrow |E\rangle$ transisiton, e.g with a two-photon process (see below). The gate can be understood through the phase evolution imposed on the atoms. By weakly driving the $|g\rangle \leftrightarrow |E\rangle$ transition off-resonance, an AC stark shift is normally introduced on the level $|g\rangle$. If all the qubit atoms are in state $|0\rangle$ we are, however, driving a resonant, cavity-assisted Raman transition between $|g\rangle$ and $|f\rangle$, which does not give an AC stark shift. If, however, at least one qubit atom is in state $|1\rangle$, it changes the cavity resonance, and the AC stark shift persists. All states but the completely uncoupled qubit state $|00...0\rangle$ will thus acquire a phase, the magnitude of which depends on the length of the driving pulse. With an appropriate pulse length and simple single qubit rotations, we can use this to realize a general N-qubit Toffoli gate or a control-phase (CZ) gate.

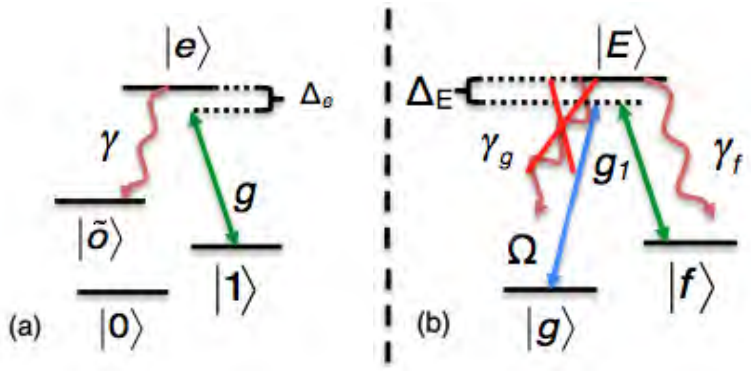

FIGURE 6.1: (a) Level structure of the qubit atoms. Only state $|1\rangle$ couples to the cavity and we assume that the excited level decays to some level $|\tilde{o}\rangle$, possible identical to $|f\rangle$ or $|0\rangle$. (b) Level structure of the auxiliary atom and the transitions driven by the weak laser (Ω) and the cavity (g_f). We assume that $|E\rangle \leftrightarrow |f\rangle$ is a closed transition, i.e. $\gamma_g = 0$.

Gate	Origin of error	Error
CZ-gate	$\gamma_g = 0$	0
	$\gamma_g > 0$	$\sim \frac{\gamma_g}{\gamma\sqrt{C}}$
Toffoli	$\Gamma_i \neq \Gamma_j$	$\lesssim \frac{1}{C}$
	$\gamma_g > 0$	$\sim \frac{\gamma_g}{\gamma\sqrt{C}}$

TABLE 6.1: The errors of the N-qubit Toffoli gate and the CZ-gate. Note that the branching fraction γ_g/γ can be made arbitrarily small using a far detuned two-photon driving as explained in the Sec. 6.3. Γ_i is the rate of detectable errors for the qubit state with i qubits in state $|1\rangle$.

Naively, the gates will be limited by errors originating from cavity decay and spontaneous emission from the atoms, which carry away information about the qubit state. These errors are, however, detectable since the level structure of the auxiliary atom is such that it will be trapped in state $|f\rangle$ if either a cavity excitation or an atomic excitation is lost. Conditioning on detecting the auxiliary atom in state $|g\rangle$ at the end of the gate thus rules out the possibility of any dissipative quantum jumps having occurred during the gate. As a result, the conditional fidelity of the gate is greatly enhanced at the modest cost of a finite but potentially low failure probability.

6.2 Gate dynamics

We now go through the details of the gates and derive the success probabilities, gate times and gate errors (see Tab. 8.1). The Hamiltonian in a proper rotating frame is (see

Fig. 6.1)

$$\hat{H} = \hat{H}_e + \hat{V} + \hat{V}^\dagger, \tag{6.1}$$

$$\hat{H}_e = \Delta_E|E\rangle\langle E| + g_f(\hat{a}|E\rangle\langle f| + H.c) + \sum_k \Delta_e|e\rangle_k\langle e| + g(\hat{a}|e\rangle_k\langle 1| + H.c), \tag{6.2}$$

$$\hat{V} = \frac{\Omega}{2}|E\rangle\langle g|, \tag{6.3}$$

where we have assumed for simplicty that all couplings (g, Ω) are real and k labels the qubit atoms ($\hbar = 1$). We have defined $\Delta_E = \omega_E - \omega_g - \omega_L$, and $\Delta_e = \omega_e - \omega_g - \omega_L + \omega_f - \omega_1$ where ω_L is the laser frequency and otherwise ω_x is the frequency associated with level x. The dissipation in the system is assumed to be described by Lindblad operators such that $\hat{L}_0 = \sqrt{\kappa}\hat{a}$ describes the cavity decay with decay rate κ, $\hat{L}_g = \sqrt{\gamma_g}|g\rangle\langle E_2|, \hat{L}_f = \sqrt{\gamma_f}|f\rangle\langle E|$ describe the decay of the auxiliary atom, and $\hat{L}_k = \sqrt{\gamma}|\tilde{o}\rangle_i\langle e|$ describes the decay of the qubit atoms ($k = 1, 2 \ldots N$) to some arbitrary ground state $|\tilde{o}\rangle$. The nature of $|\tilde{o}\rangle$ is not important for the dynamics of the gates and it may, or may not, coincide with $|0\rangle$ or $|1\rangle$. For the sake of generality, we have included a decay from $|E\rangle \to |g\rangle$ with decay rate γ_0 in order to show the effect of such a decay but, as previously mentioned, we will for now assume that $\gamma_0 = 0$.

We assume a weak laser field justifying for a perturbative treatment of $\hat{V}$ as described in Ref. [114]. The dynamics of the system is then governed by an effective master equation of the form

$$\dot{\rho} = i\left[\rho, \hat{H}_{eff}\right] + \sum_x \hat{L}_x^{eff}\rho(\hat{L}_x^{eff})^\dagger - \frac{1}{2}\left((\hat{L}_x^{eff})^\dagger\hat{L}_x^{eff}\rho + \rho(\hat{L}_x^{eff})^\dagger\hat{L}_x^{eff}\right), \tag{6.4}$$

where ρ is the density matrix of the system, $\hat{H}_{eff}$ is an effective Hamiltonian, and L_x^{eff} are effective Lindblad operators with $x = 0, g, f, k$. The effective operators are found from

$$\hat{H}_{eff} = -\frac{1}{2}\hat{V}^\dagger\left(\hat{H}_{NH}^{-1} + (\hat{H}_{NH}^{-1})^\dagger\right)\hat{V} \tag{6.5}$$

$$\hat{L}_x^{eff} = \hat{L}_x\hat{H}_{NH}^{-1}\hat{V}, \tag{6.6}$$

where

$$\hat{H}_{NH} = \hat{H}_e - \frac{i}{2}\sum_x \hat{L}_x^\dagger\hat{L}_x, \tag{6.7}$$

is the no-jump Hamiltonian. The Hilbert space of the effective operators can be described in the basis of $\{|g\rangle, |f\rangle\}$ of the auxiliary atom and the states $\{|0\rangle, |1\rangle, |\tilde{o}\rangle\}$ of the qubit atoms. To ease the notation, we define the projection operators $\hat{P}_n$, which projects on

to the states with n qubits in state $|1\rangle$. From Eq. (6.5) and (6.6) we find that

$$\begin{aligned}
\hat{H}_{eff} &= \sum_{n=0}^{N} \frac{-\Omega^2}{4\gamma} \mathrm{Re}\left\{ \frac{i\tilde{\Delta}_e/2 + nC}{\tilde{\Delta}_e(i\tilde{\Delta}_E/2 + C_f) + \tilde{\Delta}_E nC} \right\} |g\rangle\langle g| \otimes \hat{P}_n \\
&= \sum_{n=0}^{N} \Delta_n |g\rangle\langle g| \otimes \hat{P}_n \qquad (6.8) \\
\hat{L}_0^{eff} &= \sum_{n=0}^{N} \frac{1}{2\sqrt{\gamma}} \frac{\sqrt{C_f}\tilde{\Delta}_e\Omega}{\tilde{\Delta}_e(i\tilde{\Delta}_E/2 + C_f) + n\tilde{\Delta}_E C} |f\rangle\langle g| \otimes \hat{P}_n \\
&= \sum_{n=0}^{N} r_{0,n}^{eff} |g\rangle\langle f| \otimes \hat{P}_n \qquad (6.9) \\
\hat{L}_g^{eff} &= \sum_{n=0}^{N} \frac{1}{2} \frac{(i\tilde{\Delta}_e/2 + nC)\Omega}{\tilde{\Delta}_e(i\tilde{\Delta}_E/2 + C_f) + n\tilde{\Delta}_E C} \frac{\sqrt{\gamma_g}}{\gamma} |g\rangle\langle g| \otimes \hat{P}_n \\
&= \sum_{n=0}^{N} r_{g,n}^{eff} |g\rangle\langle g| \otimes \hat{P}_n \qquad (6.10) \\
\hat{L}_f^{eff} &= \sum_{n=0}^{N} \frac{1}{2} \frac{(i\tilde{\Delta}_e/2 + nC)\Omega}{\tilde{\Delta}_e(i\tilde{\Delta}_E/2 + C_f) + n\tilde{\Delta}_E C} \frac{\sqrt{\gamma_f}}{\gamma} |f\rangle\langle g| \otimes \hat{P}_n \\
&= \sum_{n=0}^{N} r_{f,n}^{eff} |f\rangle\langle g| \otimes \hat{P}_n \qquad (6.11) \\
\hat{L}_k^{eff} &= \sum_{n=1}^{N} -\frac{1}{2\sqrt{\gamma}} \frac{\sqrt{C_f}\sqrt{C}\Omega}{\tilde{\Delta}_e(i\tilde{\Delta}_E/2 + C_f) + n\tilde{\Delta}_E C} |f\rangle\langle g| \otimes |\tilde{o}\rangle_k\langle 1| \otimes \hat{P}_n \\
&= \sum_{n=1}^{N} r_n^{eff} |f\rangle\langle g| \otimes |\tilde{o}\rangle_k\langle 1| \otimes \hat{P}_n, \qquad (6.12)
\end{aligned}$$

where we have defined the cooperativities $C_{(f)} = g_{(f)}^2/\gamma\kappa$ for the qubit (auxiliary) atoms and the complex detunings $\tilde{\Delta}_E\gamma = \Delta_E - i\gamma_f/2$ and $\tilde{\Delta}_e\gamma = \Delta_e - i\gamma/2$. Note that we have defined the parameters $r_{0,n}^{eff}, r_{g,n}^{eff}, r_{f,n}^{eff}$ and r_n^{eff} in Eqs. (6.9)-(6.12) to characterize the decays described by the Lindblad operators. In the perturbative description, we have adiabatically eliminated the coupled excited states of the atoms and the cavity, which leads to an energy shift of the ground states (see Eq. (6.8)) but otherwise conserves them since the Hamiltonian in Eq. (6.1) cannot connect different unexcited states without decay. We parameterize the difference between the auxiliary atom and the qubit atoms by $C_f = \alpha C$ and $\gamma_f = \beta\gamma$ to easier treat the limit of $C \gg 1$ that we are interested in for future calculations.

The effective Hamiltonian given in Eq.(6.8) describes the basic mechanism of the gates. In the limit of $C \gg 1$ the energy shift for $n = 0$ becomes very small $\Delta_0 \sim \Delta_E\Omega^2/(16\gamma C^2)$, i.e. the resonant Raman transition surpresses the AC stark shift as assumed in the description of the gates in Sec. 6.1. On the contrary, for $n > 0$, the C in the nominator

of Δ_n shows how the coupling of the qubit atoms shifts the Raman transition out of resonance and as a result the AC stark shift $\sim \Omega^2/\Delta_E$ persists.

6.2.1 Success probability and fidelity

Eqs. (6.9)-(6.12) show that the effect of all Lindblad operators, except $\hat{L}_g^{eff}$, is that the state of the auxiliary atom is left in state $|f\rangle$. All these decays are thus detectable by measuring the state of the auxiliary atom at the end of the gate. For a heralded gate, where we condition on measuring the auxiliary atom in state $|g\rangle$ at the end of the gate, these detectable decays therefore do not effect the fidelity of the gate but only the success probability. The rate Γ_n of the detectable decays for a state with n qubits in state $|1\rangle$ is $\Gamma_n = \left|r_{0,n}^{eff}\right|^2 + \left|r_{f,n}^{eff}\right|^2 + \left|r_n^{eff}\right|^2$ and assuming an initial qubit state described by density matrix ρ_{qubit}, the success probability of the gates is

$$P_{success} = \sum_{n=0}^{N} \mathrm{Tr}\left\{e^{-\Gamma_n t_{gate}} \rho_{qubit} \hat{P}_n\right\}, \tag{6.13}$$

where t_{gate} is the gate time and $\mathrm{Tr}\{\ldots\}$ denotes the trace.

Having removed the detrimental effect of the detectable errors by heralding on a measurement of the auxiliary atom, the fidelity of the gates will be determined by more subtle, undetectable errors (see below). We define the fidelity, F of the gate as

$$F = \frac{1}{P_{success}} \langle\psi|\langle g|\tilde{\rho}_{qubit}|g\rangle|\psi\rangle, \tag{6.14}$$

where we have assumed that the ideal qubit state after the gate is a pure state $|\psi\rangle$ and $\tilde{\rho}_{qubit}$ is the actual density matrix of the qubits and the auxiliary atom after the gate operation.

6.2.2 N-qubit Toffoli gate

The dynamics described by $\hat{H}_{eff}$ can be used to implement a Toffoli gate. Putting the qubit atoms on resonance ($\Delta_e = 0$) and having $\Delta_E \propto \gamma\sqrt{C}$ gives energy shifts $\Delta_{n>0} \propto \Omega^2/(4\gamma\sqrt{C})$ while $\Delta_0 \sim \mathcal{O}(C^{-3/2})$ since the resonant Raman transition suppresses the AC stark shift such that $|00...0\rangle$ is the only state, which remains unshifted. Provided there is no decay, we can thus choose a gate time of $t_T \sim 4\pi\sqrt{C}\gamma/\Omega^2$ to make a Toffoli gate. By conditioning on measuring the auxiliary atom in state $|g\rangle$ at the end of the gate, the fidelity becomes limited by the undetectable errors listed below.

- The energy shifts of the coupled qubit states are all $\Delta_{n>0} \propto \Omega^2/(4\gamma\sqrt{C})$ in the limit $C \gg 1$. However, to higher order in C we find corrections on the order $\mathcal{O}(C^{-3/2})$ to the energy shifts, which depend on the number of qubits that couples. The gate time of the Toffoli gate is $t_T \sim 4\pi\sqrt{C}\gamma/\Omega^2$ and, as we will argue below, $\Omega \sim \gamma$. As a result, the higher order corrections give uneven phase shifts on the order of $\mathcal{O}(C^{-1})$ for the coupled qubit states at the end of the gate. This leads to a phase error in the fidelity of $\mathcal{O}(C^{-2})$.

- The difference between the rates of detectable errors (Γ_n) for different qubit states changes the relative weight of the qubit states during the gate. This error wil be $\mathcal{O}(C^{-1})$ as shown below.

- For $\gamma_g > 0$ the undetectable decay from $|E\rangle \rightarrow |g\rangle$ in the auxiliary atom will destroy the coherence between the qubit states. We find that this error will be $\sim \frac{\gamma_g}{\gamma\sqrt{C}}$. For now we will assume that $\gamma_g = 0$ and thus ignore this error since we will show that we can suppress the branching fraction γ_g/γ arbitrary close to zero by having a two photon driving.

Assuming that $\gamma_g = 0$, the dominating source of error error, limiting the performance of the Toffoli gate, is thus the difference between the rates of the detectable errors for the qubit states. To characterize the gate, we consider two cases namely the worst case and average fidelity. First, we analyse the worst case scenario. We tune Δ_E such that $\Gamma_0 = \Gamma_1$ and the largest difference between the detectable errors is between the completely uncoupled state and the state with all qubit atoms in state $|1\rangle$. The worst case scenario is then realized by the initial state $|0\rangle^{\otimes N} + |1\rangle^{\otimes N}$ because these states experience the largest difference between the number of coupled and uncoupled qubits. For the worst case fidelity and success probability we find

$$F_{worst} \sim 1 - \frac{\pi(\alpha - 2\alpha N + \alpha N^2)}{16(\alpha+\beta)N^2}\frac{1}{C} \tag{6.15}$$

$$P_{success,worst} \sim 1 - \frac{(\alpha + \alpha N + 2\beta N)\pi}{2\sqrt{\alpha}\sqrt{\alpha+\beta N}}\frac{1}{\sqrt{C}}. \tag{6.16}$$

It is seen that both quantities only depend weakly on the number of qubits N when $N \gg 1$, assuming that $\alpha \sim \beta \sim 1$. Futhermore, it is seen that the error of the gate scales as $1/C$ while the succes probability increases as $\sqrt{C}$. The gate is thus near-deterministic for large cooperativities.

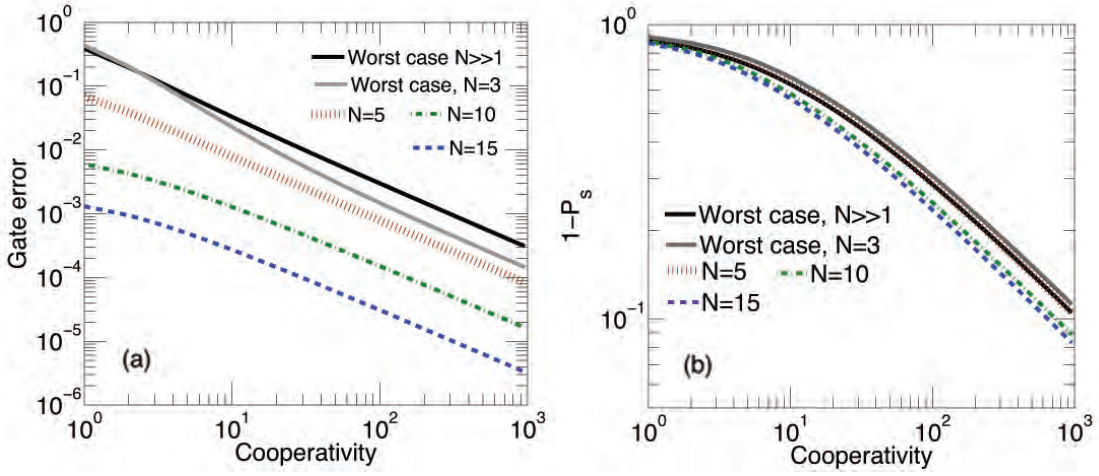

FIGURE 6.2: (a) Gate error of the Toffoli for different initial states plotted against the cooperativity. We have plotted the average error for $N = 5, 10$, and 15 and the worst case error for $N = 3$ and in the limit $N \gg 1$. Note that the average error decreases as N increases. We have fixed Δ_E such that $\Gamma_0 = \Gamma_1$ and have assumed that $\alpha = \beta = 1$. The worst case error is more or less independent of N. (b) The success probability (P_s) plotted against the cooperativity. We have used the same assumptions as in (a). P_s only have a weak dependence on N. Note that the line for $N = 5$ coincides with the worst case probability for $N \gg 1$.

To get an approximation to the average fidelity, we consider an input state $(|0\rangle + |1\rangle)^{\otimes N}$ with the same parameters as for the worst case scenario. In this case, we find

$$F_{av} \sim 1 - k(N)\frac{\alpha\pi^2}{\alpha+\beta}\frac{1}{C} \tag{6.17}$$

$$P_{success,av} \sim 1 - \left(\frac{\pi}{\sqrt{\alpha}\sqrt{\alpha+\beta}N} + d(N)\right)\frac{1}{\sqrt{C}}, \tag{6.18}$$

where $k(N), d(N)$ are scaling factors which depend on the number of qubits N. It is seen that the average fidelity and success probability have the same C dependence as in the worst case scenario. We calculate $k(N)$ and $d(N)$ numerically for $N = 1 - 100$ using the perturbation theory and find that that they both decrease slowly with N (see Fig. 6.2). The worst case and average fidelities and success probabilities are shown in Fig. 6.2 for different number of qubits, N. As N increases, we obtain higher average fidelity whereas the probability and worst case error are almost independent of N.

6.2.3 CZ-gate

So far, we have shown that we can make a heralded, near-deterministic N-qubit Toffoli gate with an error scaling as $\propto 1/C$, which is due to different rates of decay for different qubit states. In the special case of only two qubits, the Toffoli gate is referred to as a CZ-gate, and in this case, we can improve the gate to have an arbitrarily small error

by combining it with single qubit rotations. Making the single qubit transformations $|0\rangle \rightarrow e^{-i\Delta_0 t/2}|0\rangle$ and $|1\rangle \rightarrow e^{-i(\Delta_1-\Delta_0)t/2}|0\rangle$, at the end of a driving pulse of length $t_{CZ} = |\pi/(\Delta_2 - 2\Delta_1 + \Delta_0)|$, ensures the right phase evolution and gives an ideal CZ-gate, provided we can eliminate the detrimental effect of having different decay rates. For the general Toffoli gate discussed above, we needed $\Delta_E = 0$ to ensure the correct phase evolution, but by combining the CZ-gate with single qubit rotations, we can relax this assumption and ensure that $\Gamma_0 = \Gamma_1 = \Gamma_2$ by choosing

$$\Delta_E = \frac{\gamma}{2}\sqrt{\beta}\sqrt{4\alpha C + \beta} \tag{6.19}$$

$$\Delta_e = \frac{\alpha C \gamma^2}{2\Delta_E}. \tag{6.20}$$

We can thereby completely remove all dissipative errors from the CZ-gate, i.e. we have a gate with a conditional error limited only by non-adiabatic effects, that can in principle be made arbitrarily small by, e.g. reducing the driving strength. The success probability is

$$P_{success} \simeq 1 - \pi\frac{8\beta^2 + 6\beta\alpha + \alpha^2}{8\beta^{3/2}\sqrt{\alpha}}\frac{1}{\sqrt{C}}, \tag{6.21}$$

which approaches 1 as C increases. The gate is thus near-deterministic for high cooperativities (see Fig. 6.3a).

6.2.4 Gate time I: Simple scheme

The gate time of the Toffoli gate is $t_T \sim 4\pi\sqrt{C}\gamma/\Omega^2$ and for the CZ-gate, we have

$$t_{CZ} \simeq \frac{\gamma\pi\sqrt{\alpha}(\alpha + 2\beta)(\alpha + 4\beta)}{2\beta^{3/2}\Omega^2}\sqrt{C}, \tag{6.22}$$

for $C \gg 1$. Since $t_{CZ} > t_T$ we focus on t_{CZ}. The gate time is set by the strength (Ω) of the driving pulse, i.e., stronger driving gives shorter gate time. On the other hand, we need a weak drive to suppress non-adiabatic effects and to ensure the validity of our perturbative treatment. A necessary criterion for our pertubation theory to be valid is that the energy shifts Δ_n (see Eq. (6.8)) are small compared to the driving, i.e. $\Delta_n^2/\Omega^2 \ll 1$. From Eq. (6.8), we find that $\Delta_n^2/\Omega^2 \sim \Omega^2/(16\Delta_E^2)$ to leading order in the cooperativity C and this criterion is therefore met for $\Omega \ll 4\Delta_E$.

However, there is another criterion that we need to meet in order for our perturbation theory to be valid. In order not to drive the system strongly between $|g\rangle|0$ photon in cavity$\rangle \leftrightarrow |f\rangle|1$ photon in cavity$\rangle$, we need the effective driving (Ω_{eff}) of this process to be weak compared to the decay (κ) of the cavity photon. We find that we need $\Omega_{eff}/\kappa \sim$

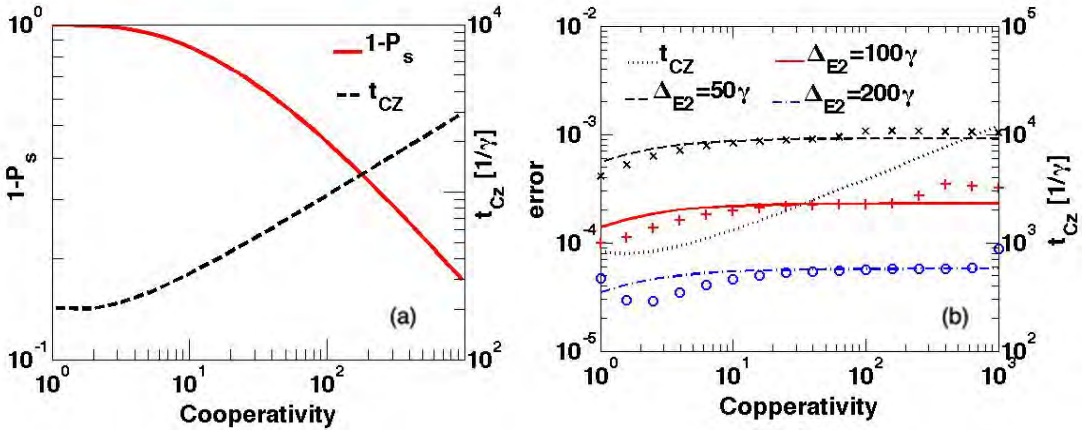

FIGURE 6.3: (a) Failure probability ($1-P_s$ - left axis) and gate time (t_{CZ} -right axis) as a function of the cooperativity (C) for the CZ gate. The gate time is in units of the inverse linewidth $1/\gamma$ of the qubit atoms. Both quantities increases as $\sqrt{C}$ and we thus have a near deterministic gate for large C. (b) Gate error (left axis) and gate time (right axis) as a function of the cooperativity for the two-photon-driven CZ-gate. We have assumed that $\Omega_{MW} = 4\gamma C^{1/4}$. The gate error is plotted for $\Delta_{E2}/\gamma = 50, 100$ and 200 showing how the error decreases as $\gamma^2\Delta_{E2}^2$. The gate time increases as $\sqrt{C}$ and is plotted in units of the inverse linewidth $(1/\gamma)$ of the qubit atoms. We have assumed $\Omega \sim \Delta_{E2}/(8C^{1/4})$. Solid lines are analytical results and symbols are numerical simulations (see App. D).

$\frac{\Omega\sqrt{C}}{\Delta_E}\sqrt{\frac{\gamma}{\kappa}} \ll 1$ in order for this to be satisfied. The different criterions for the validity of the perturbation theory are summarized in Table 6.2.

Adiabaticity criterions
$\Omega/(4\Delta_E) \ll 1$
$\frac{\Omega\sqrt{C}}{\Delta_E}\sqrt{\frac{\gamma}{\kappa}} \ll 1$

TABLE 6.2: The criterions for our perturbation theory to be valid.

Assuming that $\kappa \gg \gamma$ such that the second criterion in Table 6.2 is fulfilled, we find that we can have $\Omega \sim \gamma/2$ and keep the expression for the first criterion $\lesssim 1\%$. For this driving strength, the gate time is $\propto \sqrt{C}$ as shown in Fig. 6.3a. For cooperativities $C \lesssim 1000$ this gives a gate time $\lesssim 100$ μs for typical atomic decay rates.

6.3 Two-photon driving

So far, we have assumed a model where there is no decay from $|E\rangle \to |g\rangle$. In real atoms there will, however, always be some decay $|E\rangle \to |g\rangle$ with a decay constant $\gamma_g > 0$. The result of such an undetectable decay is that both the CZ-gate and the Toffoli gate will have an error $\sim \gamma_g/(\gamma\sqrt{C})$, which could dominate the total infidelity. To make this

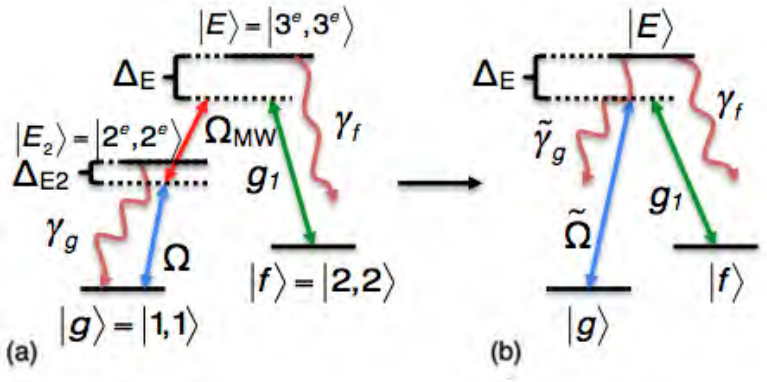

FIGURE 6.4: (a) Level structure of the auxiliary atom and the transitions driven by a weak laser (Ω), a microwave field (Ω_{MW}) and the cavity (g_f). We assume that $|E\rangle \leftrightarrow |f\rangle$ is a closed transition and for simplicity, we also assume that $|E_2\rangle \leftrightarrow |g\rangle$ is a closed transition but this is not a necessity. Here $|r^{(e)}, r^{(e)}\rangle$ with $r = 1, 2, 3$ refers to how the atom may be realized in the $(5^2P_{3/2})$ states $|F^{(e)} = r, m^{(e)} = r\rangle$ $5^2S_{1/2}$ of Rb^{87}. (b) Effective three level atom realized by mapping the two-photon drive to give an effective decay rate $\tilde{\gamma}_g$ and an effective drive $\tilde{\Omega}$.

error small, it is thus essential to suppress the branching ratio γ_g/γ. Below we show how one can suppress the branching ratio to an arbitrary level by driving the $|g\rangle \rightarrow |E\rangle$ transition with a two photon process. As a result, we realize a CZ gate with an error arbitrary close to zero and a Toffoli gate with an error scaling as $1/C$ even for a realistic atomic system.

A more realistic level structure of the auxiliary atom is shown in Fig. 6.4, where we still assume $|E\rangle \leftrightarrow |f\rangle$ to be a closed transition. For simplicity we also assume $|E_2\rangle \leftrightarrow |g\rangle$ to be a closed transition but this is not a necessity. Such a level structure could e.g. be realized in ^{87}Rb as shown in Fig. 6.4. We assume that a microwave field couples the two excited states such that we can have a two photon transition from $|g\rangle \rightarrow |E\rangle$. The Hamiltonian in a proper rotating frame is

$$\hat{H} = \hat{H}_e + \hat{V} + \hat{V}^\dagger, \tag{6.23}$$

$$\begin{aligned}\hat{H}_e = {} & \Delta_E|E\rangle\langle E| + \Delta_{E2}|E_2\rangle\langle E_2| + g_f(\hat{a}|E\rangle\langle f| + H.c) \\ & + \frac{\Omega_{MW}}{2}(|E\rangle\langle E_2| + H.c.) \\ & + \sum_k \Delta_e|e\rangle_k\langle e| + g(\hat{a}|e\rangle_k\langle 1| + H.c.),\end{aligned} \tag{6.24}$$

$$\hat{V} = \frac{\Omega}{2}|E\rangle\langle g|, \tag{6.25}$$

where we have now defined $\Delta_E = \omega_E - \omega_g - \omega_L - \omega_{MW}$, $\Delta_{E2} = \omega_{E2} - \omega_g - \omega_L$ and $\Delta_e = \omega_e - \omega_g - \omega_L - \omega_{MW} + \omega_f - \omega_1$. Here ω_L is the frequency of the laser, ω_{MW} is the frequency of the microwave field and otherwise ω_x is the frequency associated with level x. We assume that the frequency of the cavity is $\omega_c = \omega_L + \omega_{MW} + \omega_g - \omega_f$

such that the three-photon Raman transition from $|g\rangle \to |f\rangle$ is resonant. The Lindblad operators describing the system are the same as described below Eq. (6.1) except that now $\hat{L}_g = \sqrt{\gamma_g}|g\rangle\langle E_2|$. Assuming a weak drive Ω, we can follow the same recipe as before to find the following effective operators describing the dynamics of the system.

$$\begin{aligned}
\hat{H}^{(2)}_{eff} &= \sum_{n=0}^{N} \frac{\Omega^2}{4\gamma} \mathrm{Re}\left\{ \frac{-\tilde{\Delta}_e(i\tilde{\Delta}_E/2+C_f)-n\tilde{\Delta}_E C}{\tilde{\Delta}_{E2}\tilde{\Delta}_e(i\tilde{\Delta}_E/2+C_f)+n\tilde{\Delta}_E\tilde{\Delta}_{E2}C-i\tilde{\Delta}_e\tilde{\Omega}^2_{MW}/8-n\tilde{\Omega}^2_{MW}C/4} \right\} \\
&\quad \times|g\rangle\langle g| \otimes \hat{P}_n \\
&= \sum_{n=0}^{N} \Delta^{(2)}_n |g\rangle\langle g| \otimes \hat{P}_n \qquad (6.26) \\
\hat{L}^{eff(2)}_0 &= \sum_{n=0}^{N} \frac{-1}{4\sqrt{\gamma}} \frac{\sqrt{C_f}\tilde{\Delta}_e\Omega\tilde{\Omega}_{MW}}{\tilde{\Delta}_{E2}\tilde{\Delta}_e(i\tilde{\Delta}_E/2+C_f)+n\tilde{\Delta}_{E2}\tilde{\Delta}_E C-i\tilde{\Delta}_e\tilde{\Omega}^2_{MW}/8-n\tilde{\Omega}^2_{MW}C/4} \\
&\quad \times|f\rangle\langle g| \otimes \hat{P}_n \\
&= \sum_{n=0}^{N} r^{eff(2)}_{0,n} |f\rangle\langle g| \otimes \hat{P}_n \qquad (6.27) \\
\hat{L}^{eff(2)}_g &= \sum_{n=0}^{N} \frac{\Omega}{2} \frac{\tilde{\Delta}_e(i\tilde{\Delta}_E/2+C_f)+n\tilde{\Delta}_E C}{\tilde{\Delta}_{E2}\tilde{\Delta}_e(i\tilde{\Delta}_E/2+C_f)+n\tilde{\Delta}_{E2}\tilde{\Delta}_E C-i\tilde{\Delta}_e\tilde{\Omega}^2_{MW}/8-n\tilde{\Omega}^2_{MW}C/4} \frac{\sqrt{\gamma_g}}{\gamma} \\
&\quad \times|g\rangle\langle g| \otimes \hat{P}_n \\
&= \sum_{n=0}^{N} r^{eff(2)}_{g,n} |g\rangle\langle g| \otimes \hat{P}_n \qquad (6.28) \\
\hat{L}^{eff(2)}_f &= \sum_{n=0}^{N} -\frac{\Omega}{4} \frac{(i\tilde{\Delta}_e/2+nC)\tilde{\Omega}_{MW}}{\tilde{\Delta}_{E2}\tilde{\Delta}_e(i\tilde{\Delta}_E/2+C_f)+n\tilde{\Delta}_{E2}\tilde{\Delta}_E C-i\tilde{\Delta}_e\tilde{\Omega}^2_{MW}/8-n\tilde{\Omega}^2_{MW}C/4} \frac{\sqrt{\gamma_f}}{\gamma} \\
&\quad \times|f\rangle\langle g| \otimes \hat{P}_n \\
&= \sum_{n=0}^{N} r^{eff(2)}_{f,n} |f\rangle\langle g| \otimes \hat{P}_n \qquad (6.29) \\
\hat{L}^{eff(2)}_k &= \sum_{n=0}^{N-1} \frac{1}{4\sqrt{\gamma}} \frac{\sqrt{C_f}\sqrt{C}\tilde{\Omega}_{MW}\Omega}{\tilde{\Delta}_{E2}\tilde{\Delta}_e(i\tilde{\Delta}_E/2+C_f)+n\tilde{\Delta}_{E2}\tilde{\Delta}_E C-i\tilde{\Delta}_e\tilde{\Omega}^2_{MW}/8-n\tilde{\Omega}^2_{MW}C/4} \\
&\quad \times|f\rangle\langle g| \otimes |\tilde{o}\rangle_k\langle 1| \otimes \hat{P}_n \\
&= \sum_{n=0}^{N-1} r^{eff(2)}_{n} |f\rangle\langle g| \otimes |\tilde{o}\rangle_k\langle 1| \otimes \hat{P}_n, \qquad (6.30)
\end{aligned}$$

where we have defined the complex detuning $\tilde{\Delta}_{E2}\gamma = \Delta_{E2} - i\gamma_g/2$ and the parameters $r^{eff(2)}_{0,n}, r^{eff(2)}_{g,n}, r^{eff(2)}_{f,n}$ and $r^{eff(2)}_{n}$ to characterize the decay described by the Lindblad operators.

We are interested in the limit of large detuning, Δ_{E2} and large cooperativity, C. In this limit, we find that the dynamics of the system can be mapped to a simple three level

atom with effective driving $\tilde{\Omega} \sim \Omega\Omega_{MW}/\Delta_{E2}$ and an effective decay $\tilde{\gamma}_g \sim \gamma_g\Omega_{MW}^2/\Delta_{E2}^2$ as shown in Fig. 6.4. In principle, the effective operator $\hat{L}_0^{eff(2)}$ leads to an effective decay rate of $\tilde{\gamma} \sim \gamma_g\Omega^2/\Delta_{E2}^2$ to lowest order in C but we find that this first order term do not destroy the coherence between the qubit states since it is independent of n. There is, therefore, no detrimental effect of these scattering events and the performance of the gate behaves as if there is an effective decay rate of $\tilde{\gamma}_g \sim \gamma_g\Omega_{MW}^2/\Delta_{E2}^2$. Note that we also have an AC stark shift imposed on the level $|g\rangle$ by the laser characterized by Ω. This will give an overall phase to the system $\sim \Omega^2/(4\Delta_{E2})t$ which we can neglect since it does not influence the gates. Since we can do the mapping to the simple three level atom, we find similar results for the performance of the gates for the two-photon scheme as for the simple three level scheme only with effective decay $\tilde{\gamma}_g$ and drive $\tilde{\Omega}$ given by the two-photon process. Note, however, that we now assume $\gamma_g > 0$, which introduces an undetectable error as previously mentioned. We find that this introduces an error in the fidelity of both gates of roughly

$$\sim \frac{(\alpha^2 - 4\alpha\beta - 6\beta^2)\pi^2}{128\beta^2}\frac{\gamma_g^4}{\gamma^4\Delta_{E2}^4} + \frac{(\alpha^2 + 4\alpha\beta + 6\beta^2)\pi}{16\sqrt{\alpha\beta}(\alpha+2\beta)(\alpha+5\beta))}\frac{\gamma_g\Omega_{MW}^2}{\gamma\Delta_{E2}^2}\frac{1}{\sqrt{C}}. \quad (6.31)$$

Nonetheless, this error can be suppressed arbitrarily much be increasing Δ_{E2}, which enable us to have a heralded CZ-gate with arbitrarily small error in a realistic atomic setup using the two-photon drive. The error of the CZ-gate for different Δ_{E2} is shown in Fig. 6.3b assuming an initial state of $(|0\rangle + |1\rangle)^{\otimes 2}$. Note that in order to prevent an increasing scattering probability of level $|E2\rangle$ we need $\Omega_{MW} \propto C^{1/4}$ as described in the next section. The success probability and time of the gates are the same as before with $\Omega \to \tilde{\Omega} \sim \frac{\Omega_{MW}\Omega}{2\Delta_{E2}}$.

6.3.1 Gate time II: Two-photon driving

In order to find out how strongly we can drive the two photon transition, we make similar considerations about the validity of our perturbation as for the simple scheme. From Eq. (6.26)) we find that $(\Delta_n^{(2)})^2/\Omega^2 \sim \Omega^2/(16\Delta_{E2}^2)$, to leading order in C and we thus need $\Omega \ll 4\Delta_{E2}$. In order not to have strong driving between $|g\rangle|0$ photon in cavity$\rangle \leftrightarrow |f\rangle|1$ photon in cavity$\rangle$, we need $\frac{\Omega\Omega_{MW}\sqrt{C}}{\Delta_{E2}\Delta_E}\sqrt{\frac{\gamma}{\kappa}} \ll 1$.

Finally, we need to consider the scattering of photons from the level $|E2\rangle$. If the number of scattering events, n_{scat} is large compared to $\Omega^2/(4\Delta_{E2}^2)$, the perturbation theory is not valid even though the other criterions are met. We find that $n_{scat} \sim \frac{12\sqrt{C}\gamma^2}{\Omega_{MW}^2}$ for the CZ-gate and we thus need to have $\frac{3\sqrt{C}\gamma^2\Omega^2}{\Delta_E^2\Omega_{MW}^2} \ll 1$

The different criterions for the validity of the perturbation theory are summarized in Table 6.3.

Adiabaticity criterions
$\Omega/(4\Delta_{E2}) \ll 1$
$\frac{\Omega\Omega_{MW}\sqrt{C}}{\Delta_{E2}\Delta_E}\sqrt{\frac{\gamma}{\kappa}} \ll 1$
$\frac{3\sqrt{C}\gamma^2\Omega^2}{\Delta_E^2\Omega_{MW}^2} \ll 1$

TABLE 6.3: The criterions for our perturbation theory to be valid.

Assuming again that $\kappa \gg \gamma$ such that the second criterion is met, we find from Table 6.2 that we can meet the two remaining criterions using $\Omega \sim \Delta_{E2}/(4C^{1/4})$ and $\Omega_{MW} \sim 4\gamma C^{1/4}$ for the two-photon process. For these driving strengths, all the expressions in Table 6.2 are $\lesssim 1\%$. These driving strengths result in a gate time $\propto \sqrt{C}$ as shown in Fig. 6.3b.

A candidate for realizing the gate is described in Ref. [25] where single Rb atoms are placed in a nanocavity using an optical tweezer. This system is expected to reach cooperativities of several thousands. Having a detuning of $\Delta_{E2} = 50\gamma$ and a cooperativity of $C \sim 100$ would enable a heralded CZ gate with $\sim 50\%$ success probability and a heralded error $\sim 10^{-3}$ in ~ 120 μs time.

6.4 Additional errors

There are some additional errors in a realistic atomic setup that we have not treated in detail so far. Here we estimate the dominant errors and determine under which conditions, they can be sufficiently suppressed such that they do not limit the performance of the gates. We assume a realistic atomic setup where ^{87}Rb atoms are used both for the auxiliary atom and the qubit atoms. In the ^{87}Rb atoms, we assume that $|g\rangle = |1,1\rangle, |f\rangle = |2,2\rangle$ and $|E_2\rangle = |2^e, 2^e\rangle, |E\rangle = |3^e, 3^e\rangle$ where $|r^{(e)}, r^{(e)}\rangle$ with $r = 1,2,3$ refers to state $|F^{(e)} = r, m^{(e)} = r\rangle$ in $5^2S_{1/2}$ ($5^2P_{3/2}$). In this case, we estimate that the dominant errors are:

- In our perturbative theory, we have assumed that the laser field (Ω) only couple $|g\rangle \to |E2\rangle$ in the auxiliary atom. However, for a large detuning Δ_{E2} it may also couple $|f\rangle \to |E\rangle$, which could lead to an undetectable error where the auxiliary atom is pumped back to $|E2\rangle$ from, which it decays to $|g\rangle$. This error is, however, suppressed by the large frequency separation, Δ_g of $|g\rangle$ and $|f\rangle$, which is $\Delta_g \sim 1000\gamma$ for ^{87} Rb. We estimate the error using effective operators to find the decay

rate back to $|g\rangle$, assuming that the auxiliary atom starts in $|E2\rangle$ and treating the drive Ω as a perturbation while neglecting the cavity coupling. This is valid as long as $\Delta_g \gg \Delta_E$, which is fulfilled for $C \lesssim 10000$ since $\Delta_E \sim \sqrt{C}$. The error increases with Δ_{E2} but even for $\Delta_{E2} \approx 400\gamma$ we find that for $\Omega_{MW} = 4\gamma C^{1/4}$, $\Omega = \Delta_{E2}/(8C^{1/4})$ the error is $\lesssim 10^{-4}$.

- The microwave might also couple the ground states $|0\rangle - |1\rangle$ of the qubit atoms and the ground states $|g\rangle - |f\rangle$ of the auxiliary atom. The coupling of $|0\rangle - |1\rangle$ means that the qubit atoms also couple to the cavity even though they are in state $|0\rangle$. We estimate the error from this to be on the order of $\Omega_{MW}^2/(\Delta_g - (\Delta_{E2} - \Delta_E + \Delta_{2\to3}))^2$ where $\Delta_{2\to3}$ is the splitting between $|E_2\rangle$ and $|E\rangle$. For ^{87}Rb, $\Delta_{2\to3} \approx 44\gamma$. Below we argue that we need $\Delta_E < 0$ and as a result $\Delta_{E2} > 0$. Since $\Delta_E \approx -\sqrt{C}\gamma$ this error will increase slowly with cooperativity but it is surpressed by Δ_g. For $\Omega_{MW} = 4\gamma C^{1/4}$, we find that the error is $\lesssim 10^{-4}$ for $C \lesssim 1000$ even for $\Delta_{E2} \approx 400\gamma$. The errors from the coupling of the states $|g\rangle - |f\rangle$ in the auxiliary atom will likewise be surpressed by the large energy splitting Δ_g. These errors can also be further surpressed by decreasing Ω_{MW} at the cost of a larger gate time.

The above errors can be highly suppressed using e.g.^{88}Sr, ^{138}Ba$^+$ or ^{40}Ca$^+$ instead of ^{87}Rb. For these atoms, the ground states can be encoded in the S_0 and P_0 manifoldes for ^{88}Sr and the $S_{1/2}$ and $D_{3/5}$ manifolds for ^{138}Ba$^+$ and ^{40}Ca$^+$, which have separations at optical frequencies between the stable states.

A final error that we will consider is that the transition $|E\rangle \leftrightarrow |f\rangle$ will not be completely closed if the cavity is linearly polarized. This will, e.g. be the case for the system in Ref. [25]. Such a cavity also couples $|f\rangle$ to the states $|1^e, 1^e\rangle, |2^e, 1^e\rangle$ and $|3^e, 1^e\rangle$. From $|1^e, 1^e\rangle$ and $|2^e, 1^e\rangle$ there might be an undetectable decay back to $|g\rangle$, which will introduce an error $\propto 1/\sqrt{C}$ in the gates. The probability of an undetectable decay from these states should be compared to the probability of the detectable decays where the cavity photon is scattered of the qubit atoms instead. For ^{87}Rb, we estimate this error by compairing the strengths of the effective couplings from $|f\rangle$ to $|1^e, 1^e\rangle$ and $|2^e, 1^e\rangle$ with a subsequent decay to $|g\rangle$ with the strength of the effective coupling from $|1\rangle$ to $|e\rangle$ in the qubit atoms with a subsequent decay back to $|1\rangle$. The latter process has a detuning of Δ_E while the first two are additional detuned by the energy gaps between $|3^e, 3^e\rangle$ and $|1^e, 1^e\rangle$ and $|3^e, 3^e\rangle$ and $|2^e, 1^e\rangle$ respectively, assuming that $\Delta_E < 0$. We find that since $|\Delta_E|$ grows as $\sqrt{C}$ the error increases from $\sim 5 \cdot 10^{-5}$ at $C = 1$ to a maximum value of $\sim 2 \cdot 10^{-3}$ for $C \sim 3000$ for which Δ_E is comparable to the extra detunings of the $|1^e, 1^e\rangle$ and $|2^e, 1^e\rangle$ transitions compared to the $|e\rangle$ transition. For $C > 3000$ the error decreases as $1/\sqrt{C}$. Note that this error could be removed by making a 4 photon drive from $|g\rangle$ to $|E\rangle$ by letting $|g\rangle = |1, -1\rangle$. Another approach is to consider other atoms

such as $^{40}Ca^{+}$, with more favorable levelstructures. The state $|g\rangle$ could be encoded in the $3^2D_{5/2}$ subspace while the state $|f\rangle$ could be encoded in the $4^2S_{1/2}$ subspace and similarly for the qubit states $|0\rangle$ and $|1\rangle$. In such a setup, we will have separations of optical frequencies between the qubit states and we can remove the decay from the excited state back to $|g\rangle$ by, e.g. driving from $3^2D_{5/2}$ to $4^2P_{1/2}$ through $3^2D_{3/2}$.

6.5 Conclusion and discussion

In conclusion, we have demonstrated the concept of heralded quantum gates where the fidelity is greatly enhanced at the expense of a finite but possible small failure probability. The gates are implemented in optical cavities and use an auxiliary atom to detect errors from spontaneous emission and cavity decay. We have demonstrated an N qubit Toffoli gate with an error scaling as $1/C$ and a failure probability decreasing as $1/\sqrt{C}$, which performance is not degraded as N increases. Furthermore, we have shown that in the special case where $N = 2$, we can completely remove all errors from the gate and thus realize a CZ-gate with perfect fidelity. Together with single qubit rotations, this gate could e.g. enable high fidelity entanglement swapping in quantum repeaters, which can greatly enhance the communication rate (see Chap. 8). Finally, we have considered the CZ-gate in a specific setup where ^{87}Rb atoms are used for both qubit atoms and the auxiliary atom. We showed how a two-photon driving can be used to sufficiently surpress the errors of the gate resulting in a highly efficient CZ gate. Such a gate could be realized with the nanocavity system described in Ref. [25].

Our gates have a built in error detection process, which removes the necessity of extracting the error by the more complicated process of entanglement purification or quantum error correction. Even though the gates are designed for the specific case of optical cavities, which is particularly relevant for quantum communication, similar advantages can be realised in other systems, where certain errors could be heralded and thus alleviate the daunting requirements of fault tolerant computation. The concept of heralded gates could thus be an interesting path to realize not only quantum communication but also quantum computation with more modest requirements for the experimental systems.

In order to confirm our results from perturbation theory, we have numerically integrated the full Master equation, defined by the Hamiltonian in Eq. (6.1) and the Lindblad operators, $\hat{L}_0, \hat{L}_g, \hat{L}_f, \hat{L}_i$ $(i = 1, 2)$. This work was primarily done be Peter Kómár and it is described in App. D. We find that the numerical calculations confirm our analytical results obtained from the perturbation theory. The same caluclations were performed by Peter Kómár for the situation with the two-photon drive described by the Hamiltonian in Eq. (6.23) (see App. D). Once again the numerics agree with the analytical results.

Chapter 7

Room temperature single photon sources and quantum memories

A major challenge in the construction of reliable quantum technology is to have simple and coherent quantum systems to function as qubits. Single photons are ideal information carriers for quantum communication. Nonetheless the information needs to be stored as stationary qubits in a quantum memory in order to process the information. Ensembles of cold atoms have previously been considered for qantum memories since the large number of atoms enables a strong and coherent light-atom interaction [59, 115–117]. But cold atoms require extended cooling apparatus, which makes the scalability of such systems a great challenge. Room temperature atoms allow for a range of operations with continuous quantum variables [40] for scalable architectures [16] but the efficiency of such systems is limited by the incoherent atomic motion.

In this chapter, I describe the work of me and my collaborators on quantum memories and single photon sources based on room temperature microcells. The work has been done in collaboration with Jonas M. Petersen, Michael Zugenmaier, Heng Shen, Georgios Vasilakis, Kasper Jensen, Eugene S. Polzik and Anders S. Sørensen and is described in Ref. [118], which is the basis of this chapter. As opposed to previous ensemble based experiments, which typically rely on performing operations sufficiently fast that the atoms remain inside the laser beams, we employ motional averaging, where atoms move in and out of the beam several times during the interaction while maintaining the phase information for much longer times. This conceptually new approach thus alleviates the detrimental effects of atomic motion for room temperature ensembles. To be specific, we describe the concept and idea behind motional averaging in the context of an experimental realisation currently being investigated in the laboratory. Nonetheless,

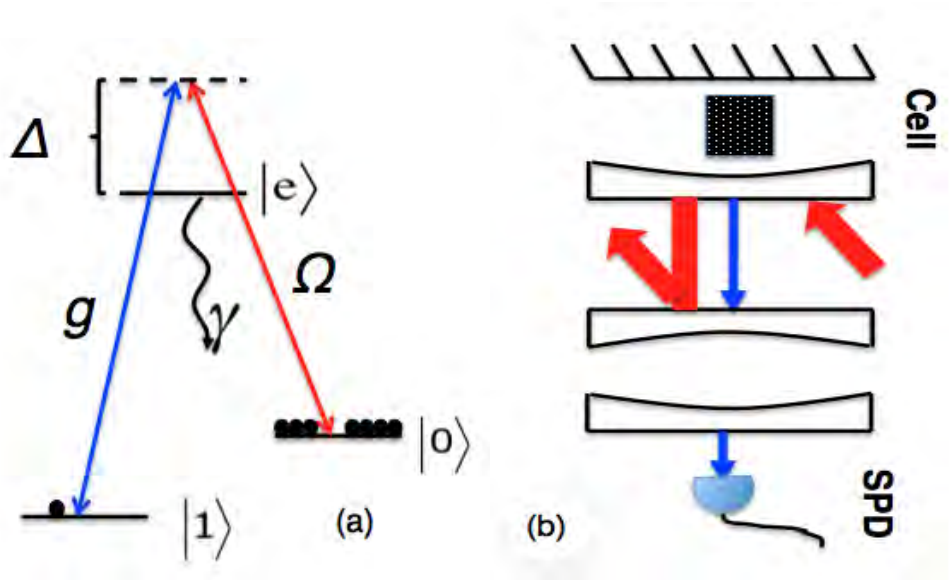

FIGURE 7.1: Sketch of (a) the atomic levels structure and (b) the experimental setup. (a) We assume that all atoms are initially pumped to state $|0\rangle$. The transition $|0\rangle \rightarrow |e\rangle$ is then driven by a weak laser field (Ω) while the cavity mode couples $|e\rangle$ and $|1\rangle$. (b) The atomic ensemble is kept in a small cell inside a single sided cavity with limited finesse. The single cavity photon (thin arrows) is coupled from the cell-cavity into a high finesse cavity, which separates it from the calssical field (broad arrows) and averages over the atomic motion.

the ideas leading to the motional averaging are generally applicable and may be used also in other systems where fluctuations of the coupling strength is an issue.

7.1 Introduction

We consider a setup, where an ensemble of Λ-atoms are kept in a small cell coated with an alkene coating to preserve the spin coherence during wall collisions [119] as depicted in Fig. 7.1. Such cells enable atomic coherence times of ~ 8 ms, making them suitable as quantum memories. The ensemble is kept at room temperature of ~ 300K and, to increase the interaction with the light, the cell is placed inside a single sided optical cavity, which we shall refer to as the *cell*-cavity. The cell-cavity is considered to have a modest finesse due to the losses possibly introduced by placing the cell inside. The light leaving the cell-cavity is therefore coupled into another high finesse cavity, which we shall refer to as the *filter*-cavity. The purpose of this cavity is two-fold as we describe below.

Initially, the atoms are all pumped to the state $|0\rangle$. We want to create a single collective excitation in the ensemble thereby producing the symmetric Dicke state $|\psi_D\rangle =$

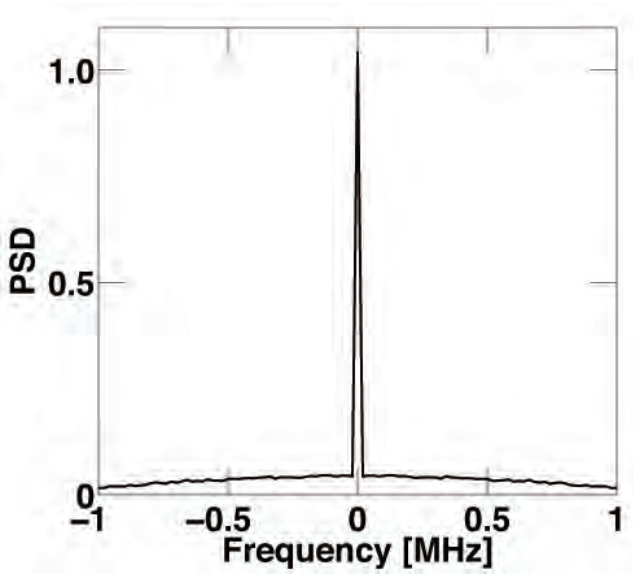

FIGURE 7.2: Simulated mean power spectral density (PSD) for a 0.05 ms long light pulse interacting with the atoms. The broad feature originates from the short time correlations of atoms interacting with the light while the sharp peak is the uncorrelated interaction of the atoms at points well seperated in time. Note that the width ($\sim 1/t_{pulse}$) and height of the sharp peak is determined by the length t_{pulse} of the light pulse, assuming that t_{pulse} is much smaller than the coherence time of the atoms.

$\hat{S}_{dicke}|00\ldots0\rangle$ where $\hat{S}_{dicke} = \frac{1}{\sqrt{N}}\sum_j |1\rangle_j\langle 0|$ and N is the number of atoms in the ensemble. We refer to this as the write process. To obtain the single excitation, we drive the $|0\rangle \rightarrow |e\rangle$ with a far-detuned laser pulse such that the Doppler broadening of the atomic levels can be neglected (see below) and sufficiently weak that multiple excitations can be neglected. We condition on detectecting the single photon emitted in a Raman transition from $|0\rangle \rightarrow |1\rangle$, which we refer to as the quantum photon. Opon detection, we project the atomic state into the symmetric Dicke state, if all the atoms have had the same interaction with the light, i.e. if the amplitude of different atoms to have emitted the photon is equal. In a realistic setup, the laser beam does not fill the entire cell and only atoms that are in the beam at any given time will thus contribute to the cavity field. Since the atoms are at room temperature, they will, however, continously move in and out of the beam and we exploit this to make a motional averaging of the atomic interaction with the light. If the interaction time is long enough to allow the atoms to move in and out of the beam several times, they will on average have had the same interaction with the light and a detection of a cavity photon will to a good approximation project the atomic state to a Dicke state. Since the cell-cavity have a limited finesse, it may in practice not have a sufficiently narrow line width to allow this averaging. We therefore introduce a second filter cavity. As we shall see, the output from the cell cavity consist of a spectrally narrow coherent beam and a broad incoherent contribution (see Fig. 7.2). By selecting out the coherent part, the filter cavity thus effectively increases the interaction time and allows the motional averaging. The filter-cavity will also help

separate the quantum photon from the classical drive by having a small frequency difference between the classical drive and single photon such that only one frequency is substained in the filter-cavity while both are substained in the cell-cavity. After a successful creation of an excitation in the ensemble, the state can be kept until readout. In the readout process, a long classical pulse is applied to the $|1\rangle \rightarrow |e\rangle$ transition such that the single excitation is convert into a photon on the $|e\rangle \rightarrow |0\rangle$ transition (g and Ω are interchanged in Fig. 7.1a). The long readout pulse serves the same purpose as the filtering cavity in the write process.

The quality of our system when considered as a part of a repeater scheme, like the DLCZ protocol [16], is characterized by both the efficiency of the write and readout processes and the quality of the single photons being readout. We first go through the details of the setup shown in Fig. 7.1b to derive the efficiency of the write and readout processes and later discuss the quality of the single photons.

7.2 Write process

The interaction between the atoms and the light in the write process is described by the Hamiltonian

$$\hat{H}_{write} = \sum_{j=1}^{N} -\Delta\hat{\sigma}_{ee}^{(j)} - \left(\frac{\Omega_j(t)}{2}\hat{\sigma}_{e0}^{(j)} + g_j(t)\hat{a}_{cell}\hat{\sigma}_{e1}^{(j)} + H.c.\right), \tag{7.1}$$

where we have defined the detuning $\Delta = \omega_L - \omega_e + \omega_0$ where ω_L is the frequency of the driving laser and ω_e (ω_0) is the frequency associated with level $|e\rangle$ ($|0\rangle$). The cell-cavity field is described by the annihilation operator $\hat{a}_{cell}$ and we have defined the atomic operators $\sigma_{xy}^{(j)} = |x\rangle_j\langle y|$ for the j'th atom. From this Hamiltonian, we obtain the equations of motion

$$\frac{d\hat{a}_{cell}}{dt} = -\frac{\kappa_1}{2}\hat{a}_{cell} + i\sum_{j=1}^{N} g_j^*(t)\hat{\sigma}_{1e}^{(j)} + \hat{F}_{\kappa_1} \tag{7.2}$$

$$\frac{d\hat{\sigma}_{1e}^{(j)}}{dt} = -\left(\frac{\gamma}{2} - i\Delta\right)\hat{\sigma}_{1e}^{(j)} - ig_j(t)\hat{a}_{cell}(\hat{\sigma}_{ee}^{(j)} - \hat{\sigma}_{11}^{(j)}) - i\frac{\Omega_j(t)}{2}\hat{\sigma}_{10}^{(j)} + \hat{F}_{1e}^{(j)} \tag{7.3}$$

$$\frac{d\hat{\sigma}_{10}^{(j)}}{dt} = -ig_j^*(t)\hat{a}_{cell}\hat{\sigma}_{e0}^{(j)} + i\frac{\Omega_j^*(t)}{2}\hat{\sigma}_{1e}^{(j)}, \tag{7.4}$$

where we have included the cavity decay with a rate κ_1 and the spontaneous emission of the atoms with a rate γ. Associated with these decays, are corresponding Langevin noise operators $\hat{F}_{\kappa_1}$ for the cavity decay and $\hat{F}_{1e}^{(j)}$ for the atomic decay [120]. Note that we have neglected dephasing of the atoms, e.g. due to collisions. We assume that all

the atoms are initially in the ground state $|0\rangle$ and that the interaction with the light is a small perturbation to the system. We can therefore assume that $\hat{\sigma}_{ee}^{(j)} - \hat{\sigma}_{11}^{(j)} \approx 0$ and ignore the noise operators since they never give rise to clicks in the detector (see Fig. 7.1b). Furthermore, we assume that $\hat{\sigma}_{10}(t)$ is slowly varying so that we can treat it as almost contant in time. We can then formally integrate Eqs. (7.2) and (7.3) to obtain

$$\hat{a}_{cell}(t') = -\frac{1}{2}\sum_{j=1}^{N}\int_0^{t'} \mathrm{d}t'' \int_0^{t''} \mathrm{d}t''' e^{-\kappa_1/2(t'-t'')} e^{-(\gamma/2-i\Delta)(t''-t''')} g_j(t'')\Omega_j(t''')\hat{\sigma}_{10}^{(j)}. \quad (7.5)$$

To find the field at the detector, we need to propagate the field through the filter-cavity, which is assumed to have a decay rate of κ_2. The input/output relations for the filter-cavity are

$$\frac{d\hat{a}_{filter}}{dt} = -\frac{\kappa_2}{2}\hat{a}_{filter} + \sqrt{\kappa_2\kappa_1/2}\hat{a}_{cell} \quad (7.6)$$

$$\hat{a} = \sqrt{\kappa_2/2}\hat{a}_{filter} \quad (7.7)$$

where κ_2 is the decay rate of the filter cavity, $\hat{a}_{filter}$ describes the field inside the filter-cavity and $\hat{a}$ describes the field outside the filter cavity, i.e. at the detector. We neglect any input noise from the cavity decay since it never gives a click in our detector and we have also neglected intra-cavity losses. Formally integrating Eq. (7.6) and using Eq. (7.7) gives

$$\hat{a} = -\frac{\kappa_2\sqrt{\kappa_1}}{4}\sum_{j=1}^{N}\theta_j(t)\hat{\sigma}_{10}^{(j)}, \quad (7.8)$$

where

$$\theta_j(t) = \int_0^t dt' \int_0^{t'} dt'' \int_0^{t''} \mathrm{d}t''' e^{-\kappa_2(t-t')/2} e^{-\kappa_1(t'-t'')/2} e^{-(\gamma/2-i\Delta)(t''-t''')} g_j(t'')\Omega_j(t'''). \quad (7.9)$$

We condition the write in on the measurement of a quantum photon at the detector. We therefore define the write efficiency η_{write} as the conditional overlap between the actual atomic state, $|\psi_a(t)\rangle$, upon detection of a quantum photon at time t, and the Dicke state $|\psi_D\rangle$. η_{write} is thus

$$\eta_{write} = \frac{\langle\psi_D|\int_0^{t_{int}} p(t)|\psi_a(t)\rangle\langle\psi_a(t)|\mathrm{d}t|\psi_D\rangle}{\int_0^{t_{int}} p(t)\mathrm{d}t}, \quad (7.10)$$

where $p(t)$ is the probability density of detecting the photon at time t. Inserting Eq. (7.8) into Eq. (7.10) and treating the interaction as a perturbation to the atomic state we

obtain [121]

$$\eta_{write} = \frac{\int_0^{t_{int}} |\langle\theta_j(t)\rangle_e|^2\, dt}{\int_0^{t_{int}} \langle|\theta_j(t)|^2\rangle_e dt} \frac{N-1}{N} + \frac{1}{N} \approx \frac{\int_0^{t_{int}} |\langle\theta_j(t)\rangle_e|^2\, dt}{\int_0^{t_{int}} \langle|\theta_j(t)|^2\rangle_e dt}. \tag{7.11}$$

Here we have defined the ensemble average $\langle\ldots\rangle_e = \frac{1}{N}\sum_j^N \langle\ldots\rangle$ and assumed $N \gg 1$ in the last step. We first focus on the expression in Eq. (7.9) for $\theta_j(t)$ in order to derive a simple expression for η_{write}. To perform the integration over t''' we assume that the couplings can be expressed as

$$\Omega_j(t''') = \Omega_{xy}^{(j)}(t'') \sin(k_c(z_j(0) + v_z^{(j)}(0)t''')) \tag{7.12}$$

$$g_j(t'') = g_{xy}(t'') \sin(k_q(z_j(t'')), \tag{7.13}$$

where k_c (k_q) is the wavenumber of the classical (quantum) field and $z_j(t)$ ($v_z^{(j)}(t)$) is the z components of the position (velocity) of the j'th atom at time t. The cavity field is thus assumed to be a standing wave along the z-direction and both modes are assumed to have a node at the center of the cell at $z = 0$. This geometry ensures an ideal overlap between the two modes. Note that an ideal overlap could also be obtained by assuming antinodes at $z = 0$. The xy-dependence of $\Omega_j(t''')$ ($\Omega_{xy}^{(j)}(t''')$) is assumed to be constant for the integration over t''', i.e. on a time scale of $1/\Delta$ (we assume that $\Delta \gg \gamma$). For atoms at room temperature, we need $\Delta \sim 1$ GHz in order to be detuned far from the Doppler broadening of the atomic levels, which gives a time scale of ~ 1 ns. The average velocity of room temperature atoms is ~ 200 m/s and the atoms will thus only move ~ 0.1 μm on this timescale, which is small compared to the transverse size of the beam, which is several μm. It is thus justified to assume that $\Omega_{xy}^{(j)}(t''')$ is constant for the intergration over t'''. The z dependence of the coupling, however, vary rapidly due to the standing wave in the cavity and cannot be assumed to be constant. Nonetheless, the velocity of the atom can be assumed to be constant since a change in the velocity requires a collision with the cell walls. We perform the integration over t''' by adiabatic elliminating the decay of the atoms since we are far detuned. As a result, we find that

$$\theta_j(t) = \frac{-1}{4} \int_0^t dt' \int_0^{t'} dt'' e^{-\kappa_2/2(t-t')} e^{-\kappa_1/2(t'-t'')} g_{xy}^{(j)}(t'') \Omega_{xy}^{(j)}(t'') \times \left(\frac{e^{-i(k_c-k_q)z_j(t'')} - e^{-i(k_c+k_q)z_j(t'')}}{-\gamma/2 + i(\Delta + k_c v_z^{(j)}(t''))} + \frac{e^{i(k_c-k_q)z_j(t'')} - e^{i(k_c+k_q)z_j(t'')}}{-\gamma/2 + i(\Delta - k_c v_z^{(j)}(t''))} \right). \tag{7.14}$$

To find the efficiency, we wish to obtain an expression for $\langle\theta_j(t)\rangle$ (see Eq. (7.11)). To this end, we assume that the spatial distribution of the atoms is uniform and that the velocity distribution of the atoms follows the Maxwell-Boltzmann distribution with temperature T. Both distributions are assumed to be independent of time. We also assume that

$k_c \sim k_q = k$ and that $kL_z \gg 1$ such that $\langle e^{\pm 2ikz}\rangle \approx 0$. Here $2L_z$ is the length of the cell in the beam direction. The xy-dependence of the couplings are assumed to have the same Gaussian form such that

$$\Omega_{xy}^{(j)}(t) = \Omega e^{\frac{-x_j^2(t)-y_j^2(t)}{w^2}} \tag{7.15}$$

$$g_{xy}^{(j)}(t) = g e^{\frac{-x_j^2(t)-y_j^2(t)}{w^2}}, \tag{7.16}$$

where w is the waist of the beam and x_j (y_j) is the x (y) component of the position of the j'th atom. With these assumptions we obtain

$$\begin{aligned}
\langle\theta_j(t)\rangle_e &= -\frac{1}{4}\int_0^t dt' \int_0^{t'} dt'' e^{-\kappa_2/2(t-t')} e^{-\kappa_1/2(t'-t'')} \langle g_{xy}(t'')\Omega_{xy}(t'')\rangle \\
&\quad \times \left\langle \frac{1-e^{-2ikz_j(t'')}}{-\gamma/2 + i(\Delta + kv_z^{(j)}(t''))} + \frac{1-e^{2ikz_j(t'')}}{-\gamma/2 + i(\Delta - kv_z^{(j)}(t''))} \right\rangle_e \qquad (7.17) \\
&= \frac{\pi^{3/2} g\Omega}{16\Gamma_d} \mathbf{w}\left[(\Delta + i\gamma/2)/\Gamma_d\right] \frac{w^2}{L^2} \int_0^t \mathrm{d}t' \int_0^{t'} \mathrm{d}t'' e^{-\kappa_2/2(t-t')} e^{-\kappa_1/2(t'-t'')} \qquad (7.18) \\
&= \frac{\pi^{3/2} g\Omega}{4\Gamma_d} \mathbf{w}\left[(\Delta + i\gamma/2)/\Gamma_d\right] \frac{w^2}{L^2} \frac{1}{\kappa_1\kappa_2}, \qquad (7.19)
\end{aligned}$$

where we have assumed that $e^{-(\kappa_1/2)t} \approx e^{-(\kappa_2/2)t} \approx 0$ in going from Eq. (7.18) to (7.19). Furthermore, we have assumed that the cell dimensions ($x \times y \times z$) are $2L \times 2L \times 2L_z$ and that $\mathrm{erf}\left(\sqrt{2}L/w\right)^2 \approx 1$ meaning that we ignore any small portion of the beam, which is outside the cell. $\mathbf{w}[\ldots]$ is the Faddeeva function defined as $\mathbf{w}[z] = e^{-z^2}(1 - \mathrm{erf}(-iz))$ and $\Gamma_d = \sqrt{2k_bT/mk}$ is the Doppler width of the atomic levels at temperature T where m is the atomic mass and k_b is the Boltzmann constant.

Having obtained an expresion for $\langle\theta_j(t)\rangle$, we now focus on $\langle|\theta_j(t)|^2\rangle$. It follows from Eq.(7.14) that

$$\begin{aligned}
\langle|\theta_j(t)|^2\rangle_e &= \frac{1}{16}\int_0^t dt_1' \int_0^{t_1'} dt_1'' \int_0^t dt_2' \int_0^{t_2'} dt_2'' e^{-\kappa_2/2(t-t_1')} e^{-\kappa_1/2(t_1'-t_1'')} e^{-\kappa_2/2(t-t_2')} e^{-\kappa_1/2(t_2'-t_2'')} \\
&\quad \times \langle XY_j^*(t_1'')XY_j(t_2'')Z_j^*(t_1'')Z_j(t_2'')\rangle_e, \qquad (7.20)
\end{aligned}$$

where we have defined

$$XY_j(t) = g_{xy}^{(j)}(t)\Omega_{xy}^{(j)}(t) \tag{7.21}$$

$$Z_j(t) = \frac{1-e^{-2ikz_j(t)}}{-\gamma/2 + i(\Delta + kv_z^{(j)}(t))} + \frac{1-e^{2ikz_j(t)}}{-\gamma/2 + i(\Delta - kv_z^{(j)}(t))}. \tag{7.22}$$

To proceed we write $Z_j(t) = \langle Z\rangle + \delta Z_j(t)$ and $XY_j(t) = \langle XY\rangle + \delta XY_j(t)$, i.e. we assume that the terms consist of large average parts ($\langle Z\rangle, \langle XY\rangle$) and small time-dependent perturbations ($\delta Z_j(t), \delta XY_j(t)$). To second order in the perturbations, we get the single

atom correlation terms $\langle \delta Z_j^*(t_1'')\delta Z_j(t_2'')\rangle$ and $\langle \delta XY_j^*(t_1'')\delta XY_j(t_2'')\rangle$. These terms represent the correlations between the atomic positions at different times. After several collisions with the walls, the atoms loose all memory of their initial position and velocity, and hence for large $|t_1 - t_2|$, the correlations are only through the mean values and all the fluctuations disappear. From now on, we neglect the terms $\propto e^{2ikz_j}$ in Eq. (7.22) since these average to zero very fast. For simplicity, we assume the decay of the correlations to be exponential such that we can write

$$\langle \delta Z_j^*(t_1'')\delta Z_j(t_2'')\rangle = \left(\langle |Z_j|^2\rangle - |\langle Z_j\rangle|^2\right) e^{-\Gamma|t_1''-t_2''|} \tag{7.23}$$

$$\langle \delta XY_j^*(t_1'')\delta XY_j(t_2'')\rangle = \left(\langle |XY_j|^2\rangle - |\langle XY_j\rangle|^2\right) e^{-\Gamma|t_1''-t_2''|}, \tag{7.24}$$

where Γ is the decay rate of the correlations. We will later justify this assumption by simulating the correlations for a box of non-interacting atoms (see Sec. 7.2.1). In the simulations, we find good agreement with an exponential model with decay rate $\Gamma = \alpha v_{thermal}/w$, where $v_{thermal}$ is the average thermal velocity of the atoms and α is a numerical constant on the order of unity. Γ is thus given by the average transient time of the atoms through the beam. Employing the exponential decay model, we evaluate the averages, with similar assumptions as before, and arrive at the following expression for $\langle |\theta_j(t)|^2\rangle$ after performing the integrals and assuming that $e^{-(\kappa_1/2)t} \approx e^{-(\kappa_2/2)t} \approx 0$

$$\begin{aligned}\langle |\theta_j(t)|^2\rangle &= |\langle \theta_j(t)\rangle_e|^2 \left(1 - \frac{\kappa_1^2\kappa_2^2 A(\kappa_1,\kappa_2,\Gamma)}{8}\right) + \frac{|g|^2\,|\Omega|^2\,A(\kappa_1,\kappa_2,\Gamma)}{4} \\ &\times\left(\frac{\pi^{5/2}}{128\Gamma_d}\frac{w^4}{L^4}\left(\frac{\mathrm{Re}\left\{\mathbf{w}\left[(\Delta+i\gamma/2)/\Gamma_d\right]\right\}}{\gamma/2} + \frac{\mathrm{Im}\left\{\mathbf{w}\left[(\Delta+i\gamma/2)/\Gamma_d\right]\right\}}{\Delta}\right)\right. \\ &\left. + \frac{\pi^2}{16\Gamma_d^2}\left|w\left[(\Delta+i\gamma/2)/\Gamma_d\right]\right|^2\frac{w^2}{L^2}\right),\end{aligned} \tag{7.25}$$

where we have defined

$$A(\kappa_1,\kappa_2,\Gamma) = \frac{16(2\Gamma+\kappa_1+\kappa_2)}{\kappa_1\kappa_2(2\Gamma+\kappa_1)(2\Gamma+\kappa_2)(\kappa_1+\kappa_2)}. \tag{7.26}$$

Using Eqs. (7.19) and (7.25) we can directly evaluate the write efficency from Eq. (7.11). In the limit of $\kappa_1 \gg (\Gamma, \kappa_2)$ and $\Delta \gg \Gamma_d \gg \gamma$, the expression for η_{write} reduces to

$$\eta_{write} \approx \frac{1}{1 + \frac{\kappa_2}{2\Gamma+\kappa_2}\left(\frac{4L^2}{\pi w^2} - 1\right)}, \tag{7.27}$$

Note, we have assumed that the Gaussian xy dependence of the couplings have a waist of $w < L$. Eq. (7.27) shows that $\eta_{write} \to 1$ as $\kappa_2/\Gamma \to 0$, i.e. the write efficency improves with the length of the effective interaction time. This is the motional averaging of the

atomic interaction with the light. Note that Eq. (7.27) also shows how the efficiency improves as the ratio between the beam area and the cell area $\pi w^2/L^2$ increases.

7.2.1 Numerical simulation I: Write

To justify our assumption of an exponential decay of the correlations appearing in $\langle|\theta_j(t)|\rangle^2$, and to qualitatively characterize the readout efficency, we perform a numerical simulation of a gas of non-interacting atoms in a cell. We have based the simulation on the microcells filled with Cs-atoms, which are currently being considered for future proof-of-principle experiments in the laboratory. These cells have dimensions of 300 μm $\times$ 300 μm $\times$ 1 cm. The cells have been placed inside a cavity with a linewidth of $\kappa_1 \approx 2\pi \cdot 46$ MHz and both the field from the quantum photon and the classical drive are assumed to have approximately a cylindrical shape with a waist of 55 μm. The modest beam waist ensures that we can neglect losses from the walls of the cell. An approximate Λ atom can be realized in the hyperfine states of Cs with state $|0\rangle = |F = 4, m_F = 4\rangle$ and state $|1\rangle = |F = 3, m_F = 3\rangle$ in the $6^2S_{1/2}$ manifold. The Doppler width of the atomic levels, at a temperature of $T = 293$ K, is $\Gamma_d \sim 2\pi \cdot 225$ MHz and we assume to be detuned $\Delta \sim 4\Gamma_d$ from the excited level such that the Doppler broadening is negligible.

The starting point of our simulations is Eq. (7.20) but we do not make the assumption of $k_c \approx k_q \approx k$, as in our analytical calculations, since we have the $2\pi \cdot 9.2$ GHz splitting between the ground states, which corresponds to $k_q - k_c = \Delta_k \approx 193$ m^{-1}. As a result, the expression for $Z_j(t)$ is

$$Z_j(t) = \frac{e^{i(\Delta_k)z_j(t)} - e^{-i(k_c+k_q)z_j(t)}}{-\gamma/2 + i(\Delta + k_c v_z^{(j)}(t))} + \frac{e^{-i(\Delta_k)z_j(t)} - e^{i(k_c+k_q)z_j(t)}}{-\gamma/2 + i(\Delta - k_c v_z^{(j)}(t))}, \tag{7.28}$$

which reduces to Eq. (7.22) for $\Delta_k = 0$. The extra terms $\propto e^{\pm i\Delta_k z_j}$ will approximately result in a factor of

$$c_{\Delta k} = \frac{\langle \cos(\Delta_k z_j)\rangle^2}{\langle \cos(\Delta_k z_j)^2\rangle} \tag{7.29}$$

multiplying the analytical expression for the write efficency, which was obtained assuming $\Delta_k = 0$. Fig. 7.3 shows how $c_{\Delta k}$ depends on the length of the cell assuming that the atoms are equally distributed in the entire cell. It is seen from Fig. 7.3 that as long as the length of the cell is $2L_z \lesssim 1$ cm then $c_{\Delta k} \gtrsim 0.97$ for $\Delta_k \approx 193$ m^{-1} and hence the frequency difference between the quantum and classical fields does not significantly degrade the write efficiency. In all our numerical simulations, we, however, keep the terms $\propto e^{\pm i\Delta k z_j}$ for completeness.

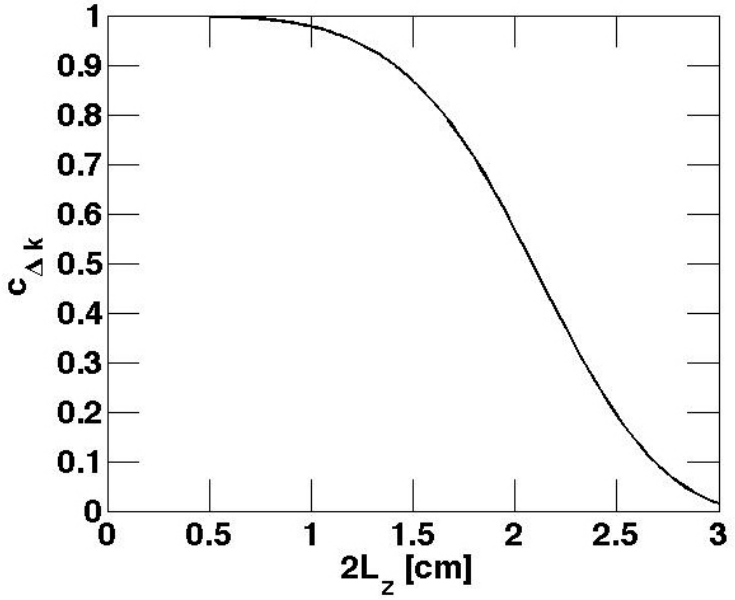

FIGURE 7.3: $c_{\Delta k}$ plotted against the length $2L_z$ of the cell for $\Delta_k \approx 193$ m^{-1} corresponding to the $2\pi \cdot 9.2$ GHz splitting between the hyperfine ground states of ^{133}Cs. The atoms are assumed to be evenly distributed in the cell. $c_{\Delta k} \gtrsim 0.97$ for $2L_z \lesssim 1$ cm.

The correlations appearing in $\langle XY_j^*(t_1'')XY_j(t_2'')Z_j^*(t_1'')Z_j(t_2'')\rangle_e$ (see Eq. (7.20)) depend on $|t_1'' - t_2''|$ and we therefore introduce the shorthand notation $\langle XY_j^*(t_1'')XY_j(t_2'')Z_j^*(t_1'')Z_j(t_2'')\rangle_e = \langle XY, Z\rangle_e(t_1''-t_2'')$. We change to the variables $u = t_1''+t_2''$ and $s = t_1''-t_2''$ and by changing the order of integration, we can perform the integrals over t, t_1', t_2' and u. To obtain the write efficency η_{write}, we need to perform an additional integration over t (see Eq. (7.11)). We are therefore left with

$$\int_0^{t_{int}} \langle|\theta(t)|^2\rangle_e dt = \int_0^{t_{int}} h(t_{int}, \kappa_1, \kappa_2, s)\langle XY, Z\rangle_e(s)ds, \tag{7.30}$$

where $h(t_{int}, \kappa_1, \kappa_2, s)$ is a function of u obtained by performing the integrals over t, t_1', t_2' and u. We can evaluate the integral over u numerically by simulating the correlations $\langle XY, Z\rangle_e(s)$. Since the atoms do not interact with each other, we independently simulate the motion of $N = 5000$ atoms through the cell and evaluate the correlations of atoms at points separated in time by s and then average over many realizations. The atoms are assumed to be evenly distributed in the cell and their velocity distribution is assumed to follow a Maxwell Boltzmann distribution at temperature $T = 293$ K. We assume that the atoms are rethermalized completely after every collision with the walls of the cell but qualitatively similar results are obtained for a balistic model without thermalization. For the ballistic model, the Z_j parts of the couplings in principle do not average down and Eq. (7.23) is no longer strictly valid. In principle, this could lead to effects not averaged away by using narrow filter cavitites. However, we are far detuned compared

to the Doppler width of the atoms and the cavity fields are standing waves, which can be viewed as the superposition of two counter propagating waves. As a result, the effect of the velocity fluctuations of the atoms cancel and the fluctuations in the Z_j terms are greatly suppressed. This is in contrast to what happens in ensemble based schemes with a laser coming from one side where Doppler effects do not go away by working far of resonance [120]. We therefore obtain similar results for the ballistic model as for the model with complete thermalization. The result of a simulation with thermalization is seen in Fig. 7.5a, which shows how the correlations decay as a function of s such that for $s \to \infty$, we have $\langle XY, Z\rangle_e(s) \to |\langle XY\rangle_e|^2 \, |\langle Z\rangle_e|^2$. This enables us to introduce a maximal cutoff, s_{max}, in the numerical integral appearing in Eq. (7.30), above which, the correlations have effectively vanished. As a result, we can semianalytically evaluate η_{write} for an arbitrary pulse length t_{int} without additional numerical difficulty. Note that Fig. 7.5a also shows that the exponential model of the decay of the correlations assumed in our analytical calculations is a good approximation.

The result of our semianalytical calculation of the write efficiency is shown in Fig. 7.4. Here, the write efficiency is plotted against the linewidth of the filter cavity.

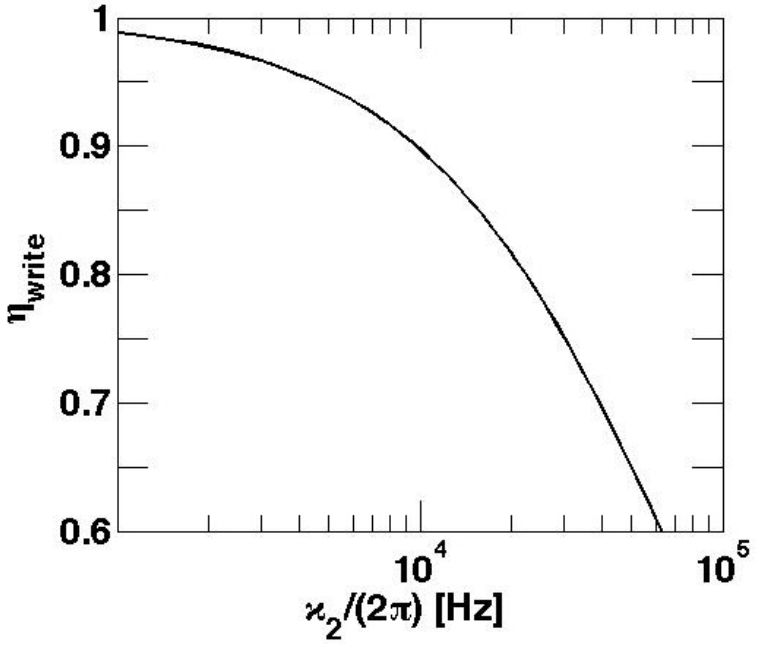

FIGURE 7.4: Write efficency plotted against the linewidth of the filter cavity. We have simulated a Cs cell with $L = 150$ μm and $w = 55$ μm corresponding to the experimental cells considered for future proof-of-principle experiments. We have assumed a detuning of $\Delta \sim 2\pi \cdot 900$ MHz, a pulse length of $t_{int} = 10/\kappa_2$ and that the cell cavity has $\kappa_1 = 2\pi \cdot 46$ MHz. Furthermore, we have assumed a perfect detection efficiency and that the filter cavity removes all classical photons.

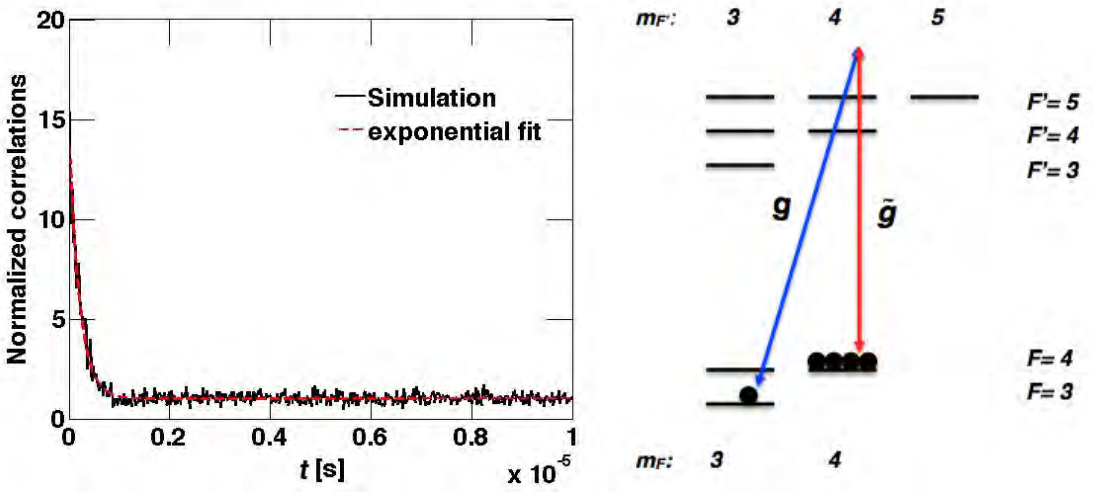

FIGURE 7.5: (a) Simulation of the correlations $\langle XY_j^*(0)XY_j(t)Z_j^*(0)Z_j(t)\rangle_e$. The correlations are normalized to be unity for $t \to \infty$ where there are no correlations and $\langle XY_j^*(0)XY_j(t)Z_j^*(0)Z_j(t)\rangle_e \to |\langle XY\rangle_e|^2 \, |\langle Z\rangle_e|^2$. The data from the simulation have been fitted with an exponential model validating our assumption of an exponential decay of the correlations. The fit gives a decay rate of $\Gamma = 2\pi \cdot 0.75$ MHz corresponding to $\Gamma \sim 1.3 v_{thermal}/w$. (b) Sketch of the $6^2S_{1/2}$ and $6^2P_{3/2}$ hyperfine levels in ^{133}Cs. A Λ-atom is realized with $|0\rangle = |F = 4, m_F = 4\rangle$, $|1\rangle = |F = 3, m_F = 3\rangle$ as ground states in $6^2S_{1/2}$ and $|e\rangle = |F' = 4, m_{F'=4}\rangle$ as the excited level in $6^2P_{3/2}$. To characterize the optical depth, we assume that $g = 0$.

It is seen that we reach $\eta_{write} \sim 90\%$ for $\kappa_2 \sim 2\pi \cdot 10$ kHz, which translates into a write time of $t \approx 140$ μs.

7.3 Number of photons

As mentioned in Sec. 7.1, the purpose of the filter cavity is both to increase the averaging time and to filter the quantum photon from the classical photons. We will now estimate the number of classical photons, which needs to be filtered from the single quantum photon. In order to do this, we need to characterize the ensemble and therefore introduce the optical depth.

To obtain an expression for the optical depth, we assume that we are working with the previously mentioned Cs-cells. The relevant level structure is shown in Fig. 7.5b. Note that with this field configuration, the cell-cavity in principle also mediate the transition $|F = 4, m_F = 4\rangle \to |F = 4, m_F = 3\rangle$ in the write setup but this transition is suppressed by the $2\pi \cdot 9.2$ GHz splitting between the ground states, which makes the corresponding photon non-resonant with the subsequent filter-cavity. This transition will, therefore, never give a click in the detector. Since the interaction is only a perturbation to the system, we can therefore neglect this transition in our numerical simulations. All atoms

in the ensemble are initially pumped to the ground state $|0\rangle = |F = 4, m_F = 4\rangle$ and, in order to characterize the optical depth, we assume $g = 0$ such that the cavity field only couples $|0\rangle \rightarrow |e_1\rangle$ and $|0\rangle \rightarrow |e_2\rangle$ with coupling constants $\tilde{g}_1$ and $\tilde{g}_2$. Here $|e_1\rangle = |F' = 4, m_{F'} = 4\rangle$ and $|e_2\rangle = |F' = 5, m_{F'} = 4\rangle$ (see Fig. 7.5b).

The equations of motion for the cavity field, $\hat{a}_{cav}$, and the relevant atomic operators in a suitable rotating frame are

$$\dot{\hat{a}}_{cav} = -(\kappa/2)\hat{a}_{cav} + i\sum_{j=1}^{N}\left[\tilde{g}_1^{(j)}(t)\hat{\sigma}_{e_10}^{(j)} + \tilde{g}_2^{(j)}(t)\hat{\sigma}_{e_20}^{j}\right] \tag{7.31}$$

$$\dot{\hat{\sigma}}_{e_10}^{(j)} = -(\gamma_1/2 - i\Delta_1)\hat{\sigma}_{e_10}^{(j)} + i\tilde{g}_1^{(j)}(t)\hat{a}_{cav} \tag{7.32}$$

$$\dot{\hat{\sigma}}_{e_20}^{(j)} = -(\gamma_2/2 - i\Delta_2)\hat{\sigma}_{e_20}^{(j)} + i\tilde{g}_2^{(j)}(t)\hat{a}_{cav}, \tag{7.33}$$

where $\sigma_{e_l0}^{(j)} = |e_l\rangle_j\langle 0|$ $(l = 1, 2)$ and we have assumed that $\sigma_{e_le_l}^{(j)} - \sigma_{00}^{(j)} \approx -1$. For simplicity, we have assumed the couplings $(\tilde{g})$ to be real. $\Delta_1 = \omega_1 - \omega_{cav}$ $(\Delta_2 = \omega_2 - \omega_{cav})$ is the detuning of $|e_1\rangle$ $(|e_1\rangle)$, while γ_1 (γ_2) is the corresponding decay rate. Here ω_1 (ω_2) is the frequency associated with the atomic level and ω_{cav} is the frequency of the cavity field. Formally integrating Eqs. (7.32)-(7.33), assuming that $\sigma_{e_10}^{(j)} = \sigma_{e_20}^{(j)} = 0$ at time $t = 0$, and inserting the resulting expression for $\sigma_{e_10}^{(j)}$ and $\sigma_{e_20}^{(j)}$ into Eq. (7.31) gives

$$\begin{aligned}\dot{\hat{a}}_{cav} = -(\kappa/2)\hat{a}_{cav} - \sum_{j=1}^{N}\Bigg[&\tilde{g}_1^{(j)}(t)\int_0^t e^{-(\gamma_1 - i\Delta_1)(t-t')}\tilde{g}_1^{(j)}(t)\hat{a}_{cav}(t')\mathrm{d}t' \\ &+\tilde{g}_2^{(j)}(t')\int_0^t e^{-(\gamma_2 - i\Delta_2)(t-t')}\tilde{g}_2^{(j)}(t')\hat{a}_{cav}(t')\mathrm{d}t'\Bigg],\end{aligned} \tag{7.34}$$

where we have explicitely written the time dependence of $\hat{a}_{cav}$ inside the integrals. We evaluate the integrals in Eq. (7.34) assuming that we can treat $\hat{a}_{cav}(t')$ as a constant in time and move it outside the integrals. Furthermore we write the couplings $\tilde{g}_l^{(j)}(t') = \tilde{g}_{l,xy}^{(j)}(t)\sin(k(z_j(0) + v_z^{(j)}(0)t'))$ similar to the procedure described in Eq. (7.12) and below. Note that k is the wavenumber associated with the cavity field while $z_j(0)$ $(v_z^{(j)})$ is the z-part of the position (velocity) of the j'th atom. After evaluating the integrals, we obtain

$$\dot{\hat{a}}_{cav} = -(\kappa/2)\hat{a}_{cav} + \frac{\hat{a}_{cav}}{4}\sum_{j=1}^{N}\left[\left|\tilde{g}_{1,xy}^{(j)}(t)\right|^2 Z_j(\Delta_1, \gamma_1, k) + \left|\tilde{g}_{2,xy}^{(j)}(t)\right|^2 Z_j(\Delta_2, \gamma_2, k)\right], \tag{7.35}$$

where we have adiabatically elliminated the decay of the atoms and have rewritten $Z_j(t)$ defined in Eq. (7.22) to

$$Z_j(\Delta, \gamma, k) = \frac{e^{2ikz_j(t)} - 1}{\gamma/2 + i(kv_j(0) - \Delta)} - \frac{1 - e^{-2ikz_j(t)}}{\gamma/2 - i(kv_j(0) + \Delta)}, \tag{7.36}$$

such that γ, Δ, and k become variable parameters. We now perform an ensemble average of Eq. (7.35) assuming that the atoms are evenly distributed in the cell and that their velocity distribution follows a Maxwell Boltzmann distribution, as previously considered. Furthermore, we assume that the xy-dependece of the couplings are Gaussians similar to Eq. (7.15) and that we are detuned far from the Doppler width of the atoms. This results in

$$\dot{\hat{a}}_{cav} = -(\kappa/2)\hat{a}_{cell} - \frac{\hat{a}_{cell}N}{4}\left[\frac{|\tilde{g}_1|^2\gamma_1}{\gamma_1^2/4+\Delta_1^2} + \frac{|\tilde{g}_2|^2\gamma_2}{\gamma_2^2/4+\Delta_2^2}\right]\frac{\pi}{8}\frac{w^2}{L^2} + i[\ldots], \tag{7.37}$$

where the imaginary part is contained in $[\ldots]$. The second term in Eq. (7.37) is identified as the single pass optical depth $\tilde{d}$ divided by the cavity round trip time τ, where $\exp(\tilde{d})$ is the attenuation of the field of the light after passing through the ensemble. Since $\tilde{d}$ depends on e.g., the detuning, it is, however, a direct characterisation of the ensemble. Instead, we characterise the ensemble by d, the hypothetical optical depth, which would be obtained for resonant fields in the absence of doppler broadening and hyperfine interaction, i.e., Eg. (7.37) with $\Delta_1 = \Delta_2 = 0$. Furthermore, we assume that $\gamma_1 = \gamma_2 = \gamma$ such that the optical depth is

$$d = \frac{N\tau}{\gamma}\left(|\tilde{g}_1|^2 + |\tilde{g}_2|^2\right)\alpha_{xy} \tag{7.38}$$

where we have defined the factor $\alpha_{xy} = \frac{\pi}{8}\frac{w^2}{L^2}$. Note that Eq. (7.38) can be rewritten to the following well known formula for the optical depth [122]

$$d = 6\pi\frac{N}{(2L)^2}\tilde{\lambda}^2\left(\frac{\gamma_1+\gamma_2}{\gamma}\right), \tag{7.39}$$

where $2L$ is the transverse size of the cell, $\tilde{\lambda} = \lambda/2\pi$ is the rescaled wavelength of the light, and γ_s is the spontaneous decay rate of level e_s back to $|0\rangle$ (s=1,2). The optical depth can also be related to the Faraday rotation angle, θ_F, which is typically measured in experiments and used to estimate the number of atoms, N in the ensemble [40, 123]. For ^{133}Cs, the relation between θ_F and N is [123]

$$N = \left|\frac{32\pi L^2\theta_F\Delta_2}{a_1(\Delta_2)\gamma\lambda^2}\right| \tag{7.40}$$

where $a_1(\Delta_2)$ is the vector polarizability given by

$$a_1(\Delta_2) = \frac{1}{120}\left(-\frac{35}{1-\Delta_{3'5'}/\Delta_2} - \frac{21}{1-\Delta_{4'5'}/\Delta_2} + 176\right), \tag{7.41}$$

with $\Delta_{x'5'}$ denoting the hyperfine splitting between level $F' = x$ and $F' = 5$. Combining Eq. (7.39) and Eq. (7.40) gives the following relation between d and θ_F

$$d = \left| \frac{12\Delta_2\theta_F}{a_1(\Delta_2)} \frac{\gamma_1 + \gamma_2}{\gamma^2} \right| \tag{7.42}$$

For the cells considered for future proof-of-principle experiments, the Faraday rotation angle has been measured to be 4.4° for a detuning of $\Delta = 2\pi \cdot 850$ MHz. This translates into an optical depth of $d \approx 84$.

Having defined the optical depth, we can now estimate the number of classical photons that need to be filtered from the quantum photon. The field at the detector (see Fig. 7.1b) is described by the operator $\hat{a}$ in Eq. (7.8). Assuming a write pulse of length t_{int}, we write the average number of quantum photons, N_{quant} at the detector as

$$N_{quant} = \langle \hat{a}^\dagger \hat{a} \cdot t_{int} \rangle = \frac{1}{16} \kappa_2^2 \kappa_1 N \langle |\theta_j|^2 \rangle_e, \tag{7.43}$$

where we have used that $\langle |\theta_j|^2 \rangle_e$ is independent of time as shown in Eq. (7.25). Note that $\langle |\theta_j|^2 \rangle_e \propto |g|^2 |\Omega|^2$ and we estimate the number of classical photons contained in the write pulse as $N_{clas} \sim |\Omega|^2 t_{int} \kappa_1 / (4 |\tilde{g}|^2) = |\Omega|^2 t_{int} \kappa_1 / (4\beta |g|^2)$, where $\beta = |\mu_\Omega|^2 / |\mu_g|^2$ is the ratio between the Clebsh-Gordan coefficients (μ) of the transitions characterized by $\tilde{g}$ and g (see Fig. 7.5b). From Eq. (7.43), we then get

$$N_{clas} \sim \frac{N_{quant}}{N} \frac{4}{|g|^4 \langle |\theta|^2 \rangle \beta \kappa_2^2}. \tag{7.44}$$

The number of classical photons that needs to be filtered is then estimated by settting $N_{quant} = 1$. Using Eqs. (7.38)-(7.39), we can express N_{clas} in terms of the optical depth and the finesse of the cell-cavity, defined as $\mathcal{F} = 2\pi/(\tau\kappa_1)$, where τ is the cavity roundtrip time. Furthermore, we assume that $\langle |\theta_j|^2 \rangle_e \approx |\langle \theta_j \rangle_e|^2$ such that the number of classical photons can be estimated as

$$N_{clas} \sim \frac{8\pi\beta_2^2 L^2 \Delta^2}{3\beta\tilde{\lambda}^2 \gamma(\gamma_1 + \gamma_2)} \frac{1}{d\mathcal{F}^2}, \tag{7.45}$$

where we have expanded the espression for $|\langle \theta_j \rangle|^2$ in the limit of large detuning. $\beta = \frac{|\mu_{g1}|^2 + |\mu_{g2}|^2}{|\mu_g|^2}$ is the ratio between the Clebsh-Gordon coefficents of the transitions characterized by $\tilde{g}_1, \tilde{g}_2$ and g in Fig. 7.5b. For the experimental Cs-cells and a detuning of $\Delta = 2\pi \cdot 898$ MHz, we find that $N_{clas} \sim \frac{7.4 \cdot 10^{11}}{d\mathcal{F}^2}$. With $d = 84$ and $\mathcal{F} = 100$ this gives $N_{class} = 9 \cdot 10^5$. Since the quantum and classical field differ both in polarisation and frequency this level of filtering is expected to be easily obtained using both polarization filtering and the filter-cavity.

7.4 Readout

In this section, we go through the details of the readout process. As it was the case in the analytical treatment of the write process, we will, for now, assume that the atoms are perfect Λ-atoms. We will later include the complex level structure of ^{133}Cs in a numerical treatment of the readout efficiency. The interaction between the atoms and the light is described by the Hamiltonian

$$\hat{H}_{read} = -\sum_{j=1}^{N} \Delta \hat{\sigma}_{ee}^{(j)} + \left(\frac{\Omega_j(t)}{2} \hat{\sigma}_{e1}^{(j)} + g_j(t) \hat{a}_{cell} \hat{\sigma}_{e0}^{(j)} + H.c. \right), \tag{7.46}$$

which is identical to $\hat{H}_{write}$ if $g_j(t)$ and $\Omega_j(t)$ are interchanged (see Eq. (7.1)). Including spontaneous emission and cavity decay, as in the write process, we obtain the equations of motion for the cavity field, $\hat{a}_{cell}$, and the atomic operators $\hat{\sigma}_{0e}^{j}$ and $\hat{\sigma}_{01}^{j}$

$$\frac{d\hat{a}_{cell}}{dt} = -\frac{\kappa_1}{2}\hat{a} + i\sum_{j=1}^{N} g_j^*(t)\hat{\sigma}_{0e}^{(j)} \tag{7.47}$$

$$\frac{d\hat{\sigma}_{0e}^{(j)}}{dt} = -\left(\frac{\gamma}{2} - i\Delta\right)\hat{\sigma}_{0e}^{(j)} + i g_j(t)\hat{a}_{cell} + i\frac{\Omega_j(t)}{2}\hat{\sigma}_{01}^{(j)} \tag{7.48}$$

$$\frac{d\hat{\sigma}_{01}^{(j)}}{dt} = i\frac{\Omega_j^*(t)}{2}\hat{\sigma}_{0e}^{(j)}, \tag{7.49}$$

where we have assumed that $\hat{\sigma}_{ee}^{(j)} - \hat{\sigma}_{00}^{(j)} \approx -\mathbb{1}$ and that the dynamics of $\hat{\sigma}_{10}^{(j)}$ are governed by the classical drive (Ω). Furthermore, we have neglected the noise operators associated with spontaneous and cavity decay, as in the write process. We can formally integrate Eq. (7.48), assuming the xy-dependence of the couplings to be constant for the integration while the z-dependent parts are of the form $\sin(k(z_j(0) + v_z^{(j)}(0)t))$, as in the write process. Note, that the z-part of the couplings are sinusoidal due to the standing wave in the cavity. Futhermore, we need to integrate over the motion in the z-direction since the coupling changes rapidly with z while the xy-dependent parts vary relatively slowly with x and y due to the broad Gaussian profile of the beams compared to the wavelength. The integration gives a set of coupled equations

$$\frac{d\hat{a}_{cell}}{dt} = \mathcal{A}(t)\hat{a}_{cell} + \sum_{j=1}^{N} \mathcal{B}_j(t)\hat{\sigma}_{01}^{(j)} \tag{7.50}$$

$$\frac{d\hat{\sigma}_{01}^{(j)}}{dt} = \mathcal{B}_j(t)\hat{a}_{cell} + \mathcal{C}_j(t)\hat{\sigma}_{01}^{(j)}, \tag{7.51}$$

where

$$\mathcal{A}(t) = \frac{-\kappa_1}{2} + \frac{1}{4}\sum_{j=1}^{N}\left|g_{xy}^{(j)}(t)\right|^2\left(\frac{e^{2ikz_j(t)}-1}{\gamma/2 - i(\Delta - kv_z^{(j)}(t))} - \frac{1-e^{-2ikz_j(t)}}{\gamma/2 - i(\Delta + kv_z^{(j)}(t))}\right) \quad (7.52)$$

$$\mathcal{B}_j(t) = \frac{1}{8}g_{xy}^{(j)}(t)\Omega_{xy}^{(j)}(t)\left(\frac{e^{2ikz_j(t)}-1}{\gamma/2 - i(\Delta - kv_z^{(j)}(t))} - \frac{1-e^{-2ikz_j(t)}}{\gamma/2 - i(\Delta + kv_z^{(j)}(t))}\right) \quad (7.53)$$

$$\mathcal{C}_j(t) = \frac{1}{16}\left|\Omega_{xy}^{(j)}(t)\right|^2\left(\frac{e^{2ikz_j(t)}-1}{\gamma/2 - i(\Delta - kv_z^{(j)}(t))} - \frac{1-e^{-2ikz_j(t)}}{\gamma/2 - i(\Delta + kv_z^{(j)}(t))}\right). \quad (7.54)$$

We have assumed that $k_c \approx k_q \approx k$ and for simplicy we have also assumed the couplings (g, Ω) to be real. We now write

$$\mathcal{A}(t) = \langle\mathcal{A}(t)\rangle_e + \delta\mathcal{A}(t) = \bar{\mathcal{A}} + \delta\mathcal{A}(t) \quad (7.55)$$

$$\mathcal{B}_j(t) = \langle\mathcal{B}_j(t)\rangle_e + \delta\mathcal{B}_j(t) = \bar{\mathcal{B}} + \delta\mathcal{B}_j(t) \quad (7.56)$$

$$\mathcal{C}_j(t) = \langle\mathcal{C}_j(t)\rangle_e + \delta\mathcal{C}_j(t) = \bar{\mathcal{C}} + \delta\mathcal{C}_j(t), \quad (7.57)$$

and assume that the couplings consist of large, average and time-independent parts $(\bar{\mathcal{A}}, \bar{\mathcal{B}}, \bar{\mathcal{C}})$ and small, time-dependent perturbations $(\delta\mathcal{A}(t), \delta\mathcal{B}_j(t), \delta\mathcal{C}_j(t))$. Furhermore, we define

$$\hat{S}_l = \frac{1}{\sqrt{N}}\sum_{j=1}^{N} e^{2i\pi(j-1)l/N}\hat{\sigma}_{01}^{(j)} \quad (7.58)$$

$$\mathcal{B}'_l(t) = \frac{1}{\sqrt{N}}\sum_{j=1}^{N} e^{2i\pi(j-1)l/N}\mathcal{B}_j(t) \quad (7.59)$$

$$\mathcal{C}_{l,l'}(t) = \sum_{j=1}^{N} e^{2i\pi(j-1)(l-l')/N}\mathcal{C}_j(t), \quad (7.60)$$

which allows us to transform the system of equations described by Eqs. (7.50)-(7.51) into

$$\frac{\mathrm{d}\mathbf{x}(t)}{\mathrm{d}t} = (\mathbf{M}_0 + \delta\mathbf{M}(t))\mathbf{x}(t), \quad (7.61)$$

where $\mathbf{x} = \left(\hat{a}_{cell}, \hat{S}_0, \hat{S}_1 \ldots \hat{S}_{N-1}\right)$ and

$$\mathbf{M}_0 = \begin{pmatrix} A & \sqrt{N}\bar{\mathcal{B}} & 0 & 0 & \ldots & 0 \\ \sqrt{N}\bar{\mathcal{B}} & \bar{\mathcal{C}} & 0 & 0 & \ldots & 0 \\ 0 & 0 & \bar{\mathcal{C}} & 0 & \ldots & 0 \\ \vdots & \vdots & \vdots & \ddots & & \vdots \\ \vdots & \vdots & \vdots & & \ddots & \vdots \\ 0 & 0 & 0 & \ldots & \ldots & \bar{\mathcal{C}} \end{pmatrix}, \tag{7.62}$$

$$\delta\mathbf{M}(t) = \begin{pmatrix} \delta\mathcal{A}(t) & \mathcal{B}_0'(t) & \mathcal{B}_{-1}'(t) & \mathcal{B}_{-2}'(t) & \ldots & \mathcal{B}_{1-N}'(t) \\ \mathcal{B}_0'(t) & \mathcal{C}_{0,0}(t) & \mathcal{C}_{0,1}(t) & \mathcal{C}_{0,2}(t) & \ldots & \mathcal{C}_{0,N-1}(t) \\ \mathcal{B}_1'(t) & \mathcal{C}_{1,0}(t) & \mathcal{C}_{1,1}(t) & \mathcal{C}_{1,2}(t) & \ldots & \mathcal{C}_{1,N-1}(t) \\ \vdots & \vdots & \vdots & \ddots & & \vdots \\ \vdots & \vdots & \vdots & & \ddots & \vdots \\ \mathcal{B}_{N-1}'(t) & \mathcal{C}_{N-1,0}(t) & \mathcal{C}_{N-1,1}(t) & \ldots & \ldots & \mathcal{C}_{N-1,N-1}(t) \end{pmatrix}. \tag{7.63}$$

With this transformation, we thus keep the mean values in $\mathbf{M}_0$, which describes the strongly coupled symmetric mode $\hat{S}_0$ and the cavity mode $\hat{a}_{cell}$ as well as an overall damping. All fluctuations, on the other hand, are contained in $\delta\mathbf{M}(t)$, which we will treat perturbatively. Assuming that the initial state of the atoms before readout is the symmetric Dicke state, we have that $\hat{S}_{l\neq 0} = 0$ and we find that, to second order in $\delta\mathbf{M}(t)$, the cavity field can be expressed as $\hat{a}_{cell} \sim \hat{a}_{cell}^{(0)} + \hat{a}_{cell}^{(2)}$. Here we have omitted the first order term, which originates from the fluctuations in $\delta\mathcal{A}(t)$ and $\mathcal{B}_0'$ since we find that they are surpressed by a factor of at least $d\mathcal{F}/N$ compared to the other terms where d is the optical depth defined in Eq. (7.38) and $\mathcal{F}$ is the finesse of the cell-cavity. The readout efficency is $\eta_{read} = \int_0^{t_{read}} dt\kappa_1 \hat{a}_{cell}^\dagger \hat{a}_{cell}$, which to second order is

$$\eta_{read} \approx \kappa_1 \int_0^{t_{read}} dt(\hat{a}_{cell}^{(0)}(t))^\dagger \hat{a}_{cell}^{(0)} + 2\kappa_1 \mathrm{Real}\left(\int_0^{t_{read}} dt(\hat{a}_{cell}^{(0)}(t))^\dagger \hat{a}_{cell}^{(2)}\right) \tag{7.64}$$

$$\approx \eta_{read,0} + \eta_{read,2} \tag{7.65}$$

Including only the mean value terms we find that

$$\begin{aligned} \eta_{read} &\approx \eta_{read,0} = \kappa_1 \int_0^{t_{read}} dt(\hat{a}_{cell}^{(0)}(t))^\dagger \hat{a}_{cell}^{(0)} \\ &\approx \kappa_1 \int_0^{t_{read}} dt \frac{N\left|\bar{\mathcal{B}}\right|^2}{|\mathcal{D}|} e^{\mathrm{Real}(\bar{\mathcal{A}}+\bar{\mathcal{C}})t} \left(e^{\frac{1}{2}\sqrt{\mathcal{D}}t} - e^{-\frac{1}{2}\sqrt{\mathcal{D}}t}\right)\left(e^{\frac{1}{2}\sqrt{\mathcal{D}}^* t} - e^{-\frac{1}{2}\sqrt{\mathcal{D}}^* t}\right), \end{aligned} \tag{7.66}$$

where $\mathcal{D} = (\bar{\mathcal{C}} - \bar{\mathcal{A}})^2 + 4N\bar{\mathcal{B}}^2$. In the limit of weak driving Ω and consequently a long readout pulse Eq. (7.66) reduces to

$$\eta_{read,0} \approx \frac{1}{\frac{\pi}{d\mathcal{F}} + 1}. \tag{7.67}$$

$\eta_{read,0}$ is the upper limit of the readout efficiency reached for a weak drive Ω and a long readout pulse. Eq. (7.67) is equivalent to the result for cold atomic ensembles [120] and represents the long time limit of perfect motional averaging where the efficency improves with optical depth and finesse of the system. Note that we define the readout rate from Eq. (7.66) as $\Gamma_{read} \approx \text{Real}(\bar{\mathcal{A}} + \mathcal{C} + \sqrt{\mathcal{D}})$.

For the second order term $\eta_{read,2}$ we find

$$\begin{aligned}
\eta_{read,2} \;=\; & 2\kappa_1 \text{Real}\Bigg(\int_0^{t_{int}} dt \int_0^t dt' \int_0^{t'} dt'' \frac{\sqrt{N}\bar{\mathcal{B}}^*}{2\,|\mathcal{D}|} e^{\text{Real}(\bar{\mathcal{A}}+\bar{\mathcal{C}})t} \left(e^{\frac{1}{2}\sqrt{\mathcal{D}}^* t} - e^{-\frac{1}{2}\sqrt{\mathcal{D}}^* t} \right) e^{\bar{\mathcal{C}}(t'-t'')} \\
& \times e^{-\frac{1}{2}(\bar{\mathcal{A}}+\bar{\mathcal{C}})(t'-t'')} \left(e^{\frac{1}{2}\sqrt{D}t} \left(e^{\frac{-1}{2}\sqrt{D}(t'-t'')} - e^{\frac{-1}{2}\sqrt{D}(t'+t'')} \right) \right. \\
& \left(\left[\left(\bar{\mathcal{A}} - \bar{\mathcal{C}} + \sqrt{\mathcal{D}} \right) N \langle \delta\mathcal{B}_j(t') \delta\mathcal{B}_j(t'') \rangle_e + 2\bar{\mathcal{B}} N \langle \delta\mathcal{C}_j(t') \delta\mathcal{B}_j(t'') \rangle_e \right] \frac{\sqrt{N}\bar{\mathcal{B}}}{\sqrt{\mathcal{D}}} \right) \\
& + e^{\frac{1}{2}\sqrt{D}(t+t''-t')} \left(\left[\left(\bar{\mathcal{A}} - \bar{\mathcal{C}} + \sqrt{\mathcal{D}} \right) N \langle \delta\mathcal{B}_j(t') \delta\mathcal{C}_j(t'') \rangle_e \right. \right. \\
& \left. \left. + 2\bar{\mathcal{B}} \sqrt{N} \langle \delta\mathcal{C}_j(t') \delta\mathcal{C}_j(t'') \rangle_e \right] \frac{\bar{\mathcal{A}} - \bar{\mathcal{C}} + \sqrt{\mathcal{D}}}{2\sqrt{\mathcal{D}}} \right) \\
& + e^{\frac{1}{2}\sqrt{D}(t-t''-t')} \left(\left[\left(\bar{\mathcal{A}} - \bar{\mathcal{C}} + \sqrt{\mathcal{D}} \right) N \langle \delta\mathcal{B}_j(t') \delta\mathcal{C}_j(t'') \rangle_e \right. \right. \\
& \left. \left. + 2\bar{\mathcal{B}} \sqrt{N} \langle \delta\mathcal{C}_j(t') \delta\mathcal{C}_j(t'') \rangle_e \right] \frac{-\bar{\mathcal{A}} + \bar{\mathcal{C}} + \sqrt{\mathcal{D}}}{2\sqrt{\mathcal{D}}} \right) \\
& + e^{-\frac{1}{2}\sqrt{D}t} \left(e^{\frac{1}{2}\sqrt{D}(t'-t'')} - e^{\frac{1}{2}\sqrt{D}(t'+t'')} \right) \\
& \times \left(\left[\left(\bar{\mathcal{A}} - \bar{\mathcal{C}} - \sqrt{\mathcal{D}} \right) N \langle \delta\mathcal{B}_j(t') \delta\mathcal{B}_j(t'') \rangle_e + 2\bar{\mathcal{B}} N \langle \delta\mathcal{C}_j(t') \delta\mathcal{B}_j(t'') \rangle_e \right] \frac{\sqrt{N}\bar{\mathcal{B}}}{\sqrt{\mathcal{D}}} \right) \\
& + e^{\frac{1}{2}\sqrt{D}(t'+t''-t)} \left(\left[\left(\bar{\mathcal{A}} - \bar{\mathcal{C}} - \sqrt{\mathcal{D}} \right) N \langle \delta\mathcal{B}_j(t') \delta\mathcal{C}_j(t'') \rangle_e \right. \right. \\
& \left. \left. + 2\bar{\mathcal{B}} \sqrt{N} \langle \delta\mathcal{C}_j(t') \delta\mathcal{C}_j(t'') \rangle_e \right] \frac{\bar{\mathcal{A}} - \bar{\mathcal{C}} - \sqrt{\mathcal{D}}}{2\sqrt{\mathcal{D}}} \right) \\
& + e^{\frac{1}{2}\sqrt{D}(t'-t''-t)} \left(\left[\left(\bar{\mathcal{A}} - \bar{\mathcal{C}} - \sqrt{\mathcal{D}} \right) N \langle \delta\mathcal{B}_j(t') \delta\mathcal{C}_j(t'') \rangle_e \right. \right. \\
& \left. \left. \left. \left. + 2\bar{\mathcal{B}} \sqrt{N} \langle \delta\mathcal{C}_j(t') \delta\mathcal{C}_j(t'') \rangle_e \right] \frac{-\bar{\mathcal{A}} + \bar{\mathcal{C}} - \sqrt{\mathcal{D}}}{2\sqrt{\mathcal{D}}} \right) \right) \right) .
\end{aligned} \tag{7.68}$$

Here we have once again neglected the contributions from the fluctuations contained in $\delta\mathcal{A}(t)$ and $\mathcal{B}_0$ since they are surpressed by a factor of at least $d\mathcal{F}/N$ compared to the terms above. In deriving Eq. (7.68), we have used that $\hat{a}^{(2)}_{cell}$ consists of sums of the form

$$\frac{1}{N}\sum_{l=1}^{N-1}\sum_{j=1}^{N}\sum_{j'=0}^{N-1} e^{-2i\pi/N(j-j')l}\delta X_j(t')\delta X_{j'}(t''), \tag{7.69}$$

where X_j could e.g. denote $\mathcal{B}_j$. For $\eta_{read,2}$, we calculate $\langle\hat{a}^{(0)}_{cell}\hat{a}^{(2)}_{cell}\rangle$ and the average of Eq. (7.69) is $\approx N\langle\delta X_j(t')\delta X_j(t'')\rangle_e$ since $\langle\delta X_j(t')\delta X_{j'}(t'')\rangle = 0$ by construction if $j \neq j'$ and we have assumed that $N-1 \approx N$. All correlations appearing in Eq. (7.68) are thus single atom correlations and the index j is kept to indicate this. The correlations contained in $\eta_{read,2}$ can be treated analytically in a similar fashion as the correlations in $\langle|\theta_j(t)|^2\rangle$ for the write process but we have, however, treated the correlations numerically by simulating the previously mentioned Cs-cells.

7.4.1 Numerical simulation II: Readout

The simulations are performed in the same way as for the write process. An extra difficulty is, however, that we need to consider the coupling between the light fields and the extra levels in ^{133}Cs. We assume that the readout process has the level structure shown in Fig. 7.6.

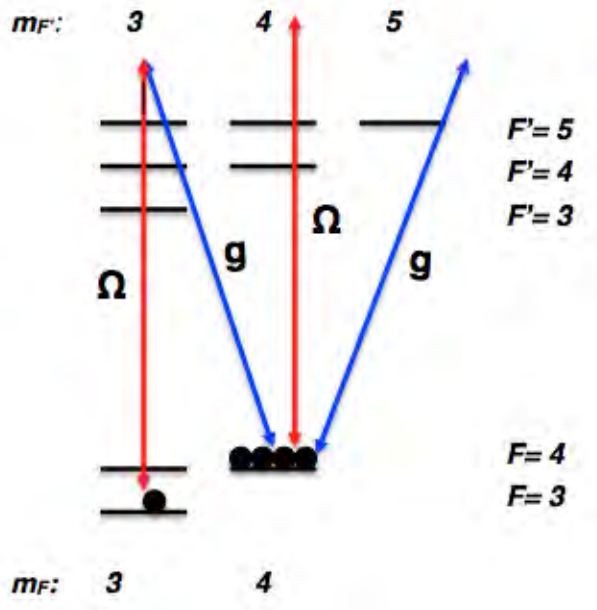

FIGURE 7.6: Schematic view of the readout realized in the hyperfine levels of $6^2S_{1/2}$ and $6^2P_{3/2}$ in ^{133}Cs. We imagine the single exitation to be stored in state $|F = 3, m_F = 3\rangle$ while the macroscopically populated state is $|F = 4, m_F = 4\rangle$. Note that the classical drive also couples $|F = 4, m_F = 4\rangle$ to $|F' = 4, m_{F'} = 4\rangle$ and $|F' = 5, m_{F'} = 4\rangle$, which can pump atoms out of the ground state. These couplings are however sufficiently surpressed by the large splitting of $2\pi \cdot 9.2$ GHz between the ground states.

The couplings to the extra levels result in extra coupling terms in the expressions for $\mathcal{A}, \mathcal{B}_j$ and $\mathcal{C}_j$, which we include, but the expression for $\eta_{read,2}$ is still the same as given in Eq. (7.68). Note, however, that a cavity detuning of the quantum field (appearing in the expression for $\mathcal{A}$) is needed to compensate the phases resulting from some of these additional couplings (see App. E). The starting point of our numerical simulations is therefore Eq. (7.68), where we can change the order of integration and introduce the variables $u = t' + t''$ and $s = t' - t''$ since the correlations only depend on the time difference $|t' - t''|$. Performing the integrals over t and u analytically, allows us to write

$$\begin{aligned}\eta_{read,2} \;=\; & \int_0^{t_{int}} (h_1(t_{int}, s)\langle \delta\mathcal{B}, \delta\mathcal{B}\rangle_e(s) + h_2(t_{int}, s)\langle \delta\mathcal{B}, \delta\mathcal{C}\rangle_e(s) \\ & + h_3(t_{int}, s)\langle \delta\mathcal{C}, \delta\mathcal{B}\rangle_e(s) + h_4(t_{int}, s)\langle \delta\mathcal{C}, \delta\mathcal{C}\rangle_e(s))ds, \end{aligned} \tag{7.70}$$

where $h_1(t_{int}, s), h_2(t_{int}, s), h_3(t_{int}, s)$ and $h_4(t_{int}, s)$ are functions of s and t_{int}, which are obtained from the integration over t and u. We have once again introduced the short notation for the correlations $\langle \delta\mathcal{B}_j(t')\delta\mathcal{C}_j(t'')\rangle_e = \langle \delta\mathcal{B}, \delta\mathcal{C}\rangle_e(s)$. Note that $\langle \delta\mathcal{B}, \delta\mathcal{C}\rangle_e(s) \to 0$ for $s \to \infty$ similar to the situation in the write process, i.e. the coupling of an atom at time t is uncorrelated from its initial coupling if t is large. We can therefore introduce a cutoff s_{max} in the integral in Eq. (7.70) such that we can evaluate $\eta_{read,2}$ for an arbitrary length of the readout pulse t_{int} without additional numerical difficulty. We then

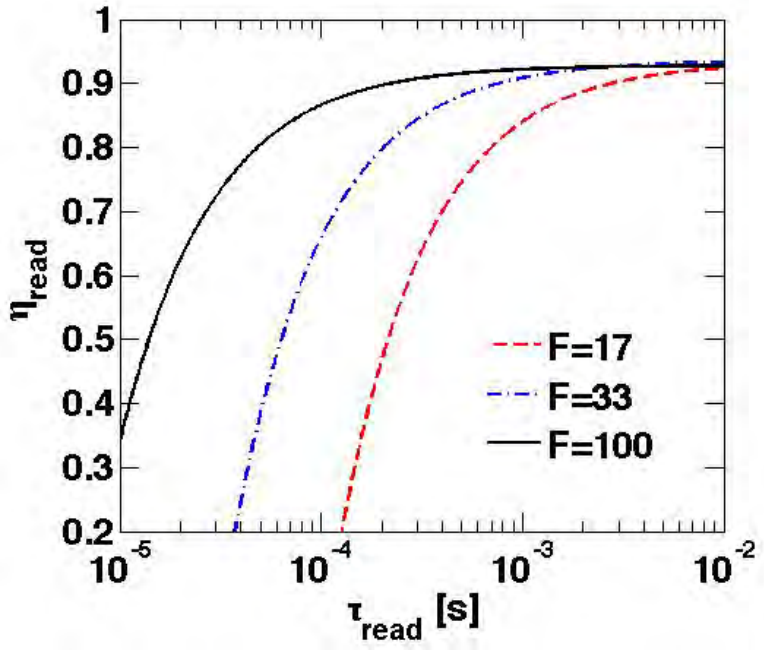

FIGURE 7.7: Read out efficiency plotted against the readout time τ_{read} for different values of the finesse (F). The efficency was simulated for the same Cs cells as the write efficiency and we have assumed that $\tau_{read} = 3/\Gamma_{read}$ where Γ_{read} is the readout rate. The optical depth was assumed to 84 which corresponds to measurements.

numerically evaluate $\eta_{read,2}$ from Eq. (7.70) by simulating the decay of the correlations similar to the simulation of the write process. From the numerical simulation, we find that the term $\langle \delta\mathcal{C}_j \delta\mathcal{C}_j \rangle_e$ dominates $\eta_{read,2}$. This term describes loss of the excitation due to spontaneous emission to modes not confined by the cavity. Fig. 7.7 shows the readout efficency for different values of the finesse plotted against the readout time $\tau_{read} = 3/\Gamma_{read}$ where Γ_{read} is the readout rate, which is proportional to the classical drive. The Cs-cells used have a measured optical depth around 84, which means that for a finesse of 100 we can obtain $\eta_{read} \approx 90\%$ for a readout time of $t \approx 183$ μs.

7.5 DLCZ repeater

So far, we have demonstrated how motional averaging enables efficient write and read processes at room temperature. The necessary time of the write and readout processes can be kept well below the reported coherence times of such systems enabeling an efficient quantum memory. We will now consider, some of the errors that limit the performance of the system when being a part of a DLCZ protocol [16].

The write efficency η_{write} as defined in Eq. (7.10) can also be viewed as the conditional fidelity of the atomic state with the symmetric Dicke state following a click in the detector. In the entanglement setup of a DLCZ repeater, two ensembles are driven weakly

and any emitted quantum photons are send to a central balanced beam splitter and subsequently detected. If the excitation probability is small, the detection of a photon, to good approximation, heralds a Bell-type state between the two ensembles, where the single excitation is shared between them. In such a setup, the write efficency would translate into an error in the fidelity of the entangled state. However, a write efficiency of 90% means that the atomic state basically contains a mixture of 10% vacuum, which can never subsequently produce a photon upon readout. The entanglement swap in a DLCZ repeater relies on reading out the stored excitation and the vacuum part would therefore not result in a detection event. Hence the error from the writing is converted into a total efficency of $\eta_{write}\eta_{read}$. Inefficient motional averaging in the write process thus degrades the efficiency but not the fidelity. The same argument applies if a single ensemble is simply used as a single photon source.

In order to create a single excitation in the write process, we have assumed that the ensemble is driven weakly. There is, however, always a finite probability of creating multiple excitations in the ensemble during the write process, which can introduce an error in the fidelity of the entanglement setup in a DLCZ repeater. Multiple excitations would also creates multiple quantum photons, which could in principle be discriminated from the situation with a single quantum photon using perfect number resolving detectors and assuming that no photons were lost between the cavity and the detectors. However, assuming number resolving detectors, but finite detection probability, η_{detect}, the multiple excitations will introduce an error of $\sim 2(1-\eta_{detect})\alpha$ where $\alpha \propto \int_0^{t_{int}} \langle|\theta_j(t)|^2\rangle$ is the excitation probability. This error can be made arbitrarily small by simply decreasing α, i.e. decreasing the strength of the classical drive. This will, however, also increase average number of times, the entangling process needs to be repeated until successful and hence decrease the rate of entanglement creation.

There are a number of errors, which cannot simply be described as an inefficiency. The photons being read out from two ensembles should be coherent, i.e. they should be indistinguishable. Any incoherence will e.g. translate into an error in the average fidelity in a DLCZ protocol. During the readout process, the excitation may not be readout collectively but rather as a single atom readout. As a result, the photon will have a random phase depending on which atom was readout, which degrades the coherence when using the ensemble as a single photon source. We characterize the error from this process by considering a Hong-Ou-Mandel experiment [124]. We assume, that we have successfully stored two single excitations in two ensembles. The excitations are readout simultaneously and combined on a balanced beam splitter. Each output port of the beamsplitter are detected with a single photon detector. If indistinguishable photons are incident on the beam splitter, they will bunch together and only one of the output detectors will give a click. If, however, they are distinguishable there is a

50 % probability that both detectors clicks. Letting $\hat{a}$ ($\hat{b}$) characterize the photon from ensemble one (two) we can write the probability of a click in both detectors as

$$\begin{aligned}\epsilon_c &= \frac{1}{2\eta_{read}^2}\int_0^\infty dt\int_0^\infty dt'\Big\langle(\hat{a}(t))^\dagger(\hat{b}(t'))^\dagger\hat{b}(t')\hat{a}(t)+(\hat{a}(t'))^\dagger(\hat{b}(t))^\dagger\hat{b}(t)\hat{a}(t')\\ &\quad-(\hat{a}(t))^\dagger(\hat{b}(t'))^\dagger\hat{b}(t)\hat{a}(t')-(\hat{a}(t'))^\dagger(\hat{b}(t))^\dagger\hat{b}(t')\hat{a}(t)\Big\rangle,\end{aligned}\tag{7.71}$$

where the factor of $1/(2\eta_{read}^2)$ ensures correct normalization (η_{read} is the total readout efficiency) such that for perfectly coherent photons $\epsilon_c = 0$ while for completely distinguishable photons $\epsilon_c = 1$. From our pertubative calculation of the redout efficiency, we have, $\hat{a} \sim \hat{a}_0 + \hat{a}_2$ and $\hat{b} \sim \hat{b}_0 + \hat{b}_2$ to second order, assuming that single symmetric excitations were stored in both ensembles. Inserting these expressions into Eq. (7.71) gives, to second order in $\hat{a}_2$ and $\hat{b}_2$,

$$\begin{aligned}\epsilon_c^{(2)} &= \frac{1}{\eta_{read}^2}\int_0^\infty dt\int_0^\infty dt'\Big\langle 2(\hat{a}_2(t))^\dagger(\hat{b}_0(t'))^\dagger\hat{b}_0(t')\hat{a}_2(t)+(\hat{a}_2(t'))^\dagger(\hat{b}_0(t))^\dagger\hat{b}_2(t)\hat{a}_0(t')\\ &\quad-2(\hat{a}_2(t))^\dagger(\hat{b}_0(t'))^\dagger\hat{b}_2(t)\hat{a}_0(t')-(\hat{a}_2(t'))^\dagger(\hat{b}_0(t))^\dagger\hat{b}_0(t')\hat{a}_2(t)\Big\rangle,\end{aligned}\tag{7.72}$$

where we have used that e.g. $\langle(\hat{a}_2(t))^\dagger(\hat{b}_0(t'))^\dagger\hat{b}_0(t')\hat{a}_2(t)\rangle = \langle(\hat{a}_0(t'))^\dagger(\hat{b}_2(t))^\dagger\hat{b}_2(t)\hat{a}_0(t')\rangle$ since the two setups are identical. The expression for $\hat{a}_0$ ($\hat{b}_0$) and $\hat{a}_2$ ($\hat{b}_2$) are found from Eqs. (7.66)-(7.68). Note, that while $\eta_{read,2}$ contains two-point correlations of the form $\langle\delta\mathcal{B}_j(t)\delta\mathcal{B}_j(t')\rangle$, we find that these cancel in Eq. (7.72) and we are left with four-point correlations of the form $\langle\delta\mathcal{B}_j(t)\delta\mathcal{B}_j(t')\delta\mathcal{B}_j(t'')\delta\mathcal{B}_j(t''')\rangle$. These are suppressed by a factor of $1/N$ compared to the two-point correlations and since $N \gg 1$ ($N \sim 10^7$ in the Cs-cells we consider), the error from $\epsilon_c^{(2)}$ can be neglected compared to e.g. the error from assymetric excitations discussed below.

Another source of incoherence originates from inefficent optical pumping and scattering of atoms through spontaneous emission during the write process. Both of these processes results in excitations being stored in assymmetric modes described by the operators $\hat{S}_{l\neq 0}$ (see Eq. (7.58)), which upon readout can degrade the coherence of the photons. The contribution to the single photon field from these assymetric modes can be found from our perturbative treatment of $\hat{a}_{cell}$ in the readout process. Letting p_{pump} denote the probability of an atom being in the wrong state, this translates into an average excitation of the asymmetric mode of p_{pump}. We find that the assymetric modes gives a

first order contribution of

$$\begin{aligned}\hat{a}_1(t) &= \sqrt{\kappa_1 p_{pump}}\int_0^t dt' \frac{e^{\frac{1}{2}(\mathcal{A}+\bar{\mathcal{C}})(t-t')}}{2\sqrt{\mathcal{D}}} e^{\bar{\mathcal{C}}t'} \frac{1}{\sqrt{N}} \sum_{l=1}^{N-1}\sum_{j=1}^{N} e^{-2i\pi(j-1)l}\Big(\\ &\left(e^{\frac{1}{2}\sqrt{\mathcal{D}}(t-t')} - e^{-\frac{1}{2}\sqrt{\mathcal{D}}(t-t')}\right)\left(\left(\mathcal{A}-\bar{\mathcal{C}}\right)\delta\mathcal{B}_j(t') + 2\bar{\mathcal{B}}\delta\mathcal{C}_j(t')\right)\hat{S}_l \\ &+ \left(e^{\frac{1}{2}\sqrt{\mathcal{D}}(t-t')} + e^{-\frac{1}{2}\sqrt{\mathcal{D}}(t-t')}\right)\sqrt{\mathcal{D}}\delta\mathcal{B}_j(t')\hat{S}_l\Big). \end{aligned} \tag{7.73}$$

where κ_1 is the decay rate of the cavity. Employing the Hong-Ou-Mandel analysis described above, we find that the resulting incoherence to lowest order is

$$\begin{aligned}\epsilon_c^{(1)} &= \frac{1}{\eta_{read}^2}\int_0^\infty dt \int_0^\infty dt' \Big\langle 2(\hat{a}_1(t))^\dagger(\hat{b}_0(t'))^\dagger\hat{b}_0(t')\hat{a}_1(t) \\ &\quad -(\hat{a}_1(t'))^\dagger(\hat{b}_0(t))^\dagger\hat{b}_0(t')\hat{a}_1(t)\Big\rangle. \end{aligned} \tag{7.74}$$

We can numerically evaluate the correlations contained in Eq. (7.74) in a similar fashion as for the correlations in $\eta_{read,2}$, i.e. we simulate the experimental Cs-cells. We find that the second term in Eq. (7.74) can be neglected since the readout rate of the assymetric excitation described by $\hat{a}_1$ is much smaller than the readout rate of the symmetric excitation described by $\hat{a}_0$. The numerical simulation of $\epsilon_c^{(1)}$ is shown in Fig. 7.8 where we have assumed a readout time of $\tau_{read} = 3/\Gamma_{read}$ where Γ_{read} is the readout rate of the symmetric excitation. The choice of readout time is made such that most of the coherent photons are being being readout while only a small part of the incoherent photons are being readout since the readout rate of incoherent photons is much smaller than the readout rate for coherent photons.

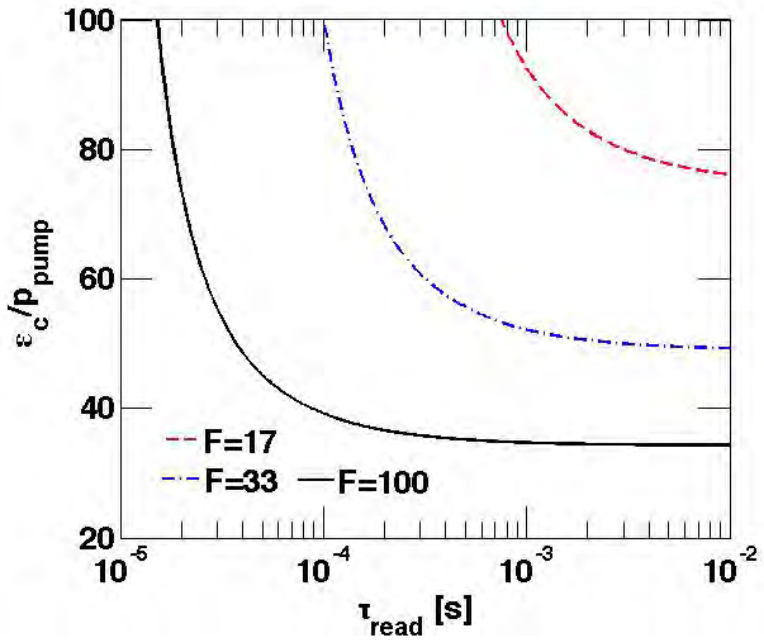

FIGURE 7.8: $\epsilon_c^{(1)}$ plotted against the readout time defined as $\tau_{read} = 3/\Gamma_{read}$ where Γ_{read} is the readout rate of the symmetric excitation. The optical depth was assumed to be 84, as measured. F in the figure is the finesse of the cell-cavity. Note that the readout rate of the assymetric excitation is much slower than Γ_{read} and $\epsilon_c^{(1)}$ will thus increase (decrease) if $\tau_{read}\Gamma_{read}$ increases (decreases).

Increasing the readout time to e.g. $4/\Gamma_{read}$ will increase $\epsilon_c^{(1)}$ since we will read out more of the assymetric excitation. In a similar fashion $\epsilon_c^{(1)}$ will decrease if we have a smaller readout time. The increase in ϵ_c/p_{pump} seen in Fig. 7.8 for small readout time is because η_{read} decreases (see Fig. 7.7). It is seen that for a finesse of $\mathcal{F} = 100$ and a readout time of ≈ 180 μs for which $\eta_{read} \approx 90\%$, we have an error of $\epsilon_c^{(1)} \approx 35 p_{pump}$. Assuming that $p_{pump} = 0.03\%$ we would thus get an error of $\approx 1\%$.

7.6 Conclusion and discussion

In conclusion, we have introduced the concept of motional averaging, which can be used to make efficient and scalable single photon sources and quantum memories based on atomic ensembles at room temperature. We have demonstrated the concept in a specific setup, where the atomic ensemble is kept in a small cell inside a cavity and shown how both write and read efficiencies above 90% can be achieved for a realistic experimental system based on Cs-atoms.

To fully exploit the effect of motional averaging, the length of the write and readout pulses need to be long enough for all atoms to have interacted equally with the light. Thus the necessary write and readut times depend strongly on the fraction of the atoms

inside the beams. If this fraction is increased, higher efficiencies can be obtained in shorter times. The size of the beams are limited by the experimental details of the setup such as losses from the cell walls. For the current experimental parameters considered in this work, the fraction of atoms inside the beam was only 10%. Improving this by a factor of two will greatly increase the performance compared to what is shown in Figs. 7.4 and 7.7.

The main limitations to the quality of the photons being readout from the ensemble are the probability of multiple excitations, which can be suppressed with efficient detection, and inefficient optical pumping. Inefficient optical pumping results in asymmetric excitations of the ensemble, which will give an error during readout since they can lead to 'false' clicks. Note that increasing the fraction of atoms in the beam also decreases the effect of inefficient optical pumping. For a fraction of 10% we found an error of $\approx 37 p_{pump}$ for an optical depth of 84 and a finesse of 100. Increasing the fraction to 20% the error would decrease to $\approx 17 p_{pump}$ for the same optical depth and finesse.

The scalable property of the room temperature system considered here makes it a candidate to realize a DLCZ-like repeater protocol with spatial multiplexing. As shown in Ref. [18] spatial multiplexing can greatly enhance the rate of entanglement distribution and decrease the necessary memory time. Other applications of the system could be in photonic quantum simulators [125, 126]. Such simulators require the creation of several photons, which can be realized using the room temperature ensembles. The excitations are simply kept in their ensembles until the apropriate number of excitations is reached. Subsequently, the excitations are readout to produce the photons for the simulation. To fully characterize the performance of the room temperature systems in these setups it would be necessary to include the effect of limited memory time, which we have not treated in our work.

Chapter 8

Optimization of repeater structures based on optical cavitites

a

Much effort has been devoted to the construction of quantum repeaters based on atomic ensembles, where the large number of atoms can, in principle, enables highly efficient quantum memories [17]. However the contruction of a practical quantum repeater remains a great challenge with the limited efficiencies demonstrated in current experiments [18, 40].

Recently, single emitter systems such as NV-centers and trapped ions have been considered for quantum repeaters [127, 128]. Such systems have long been considered for quantum computation due to the high level of control and their advantageous coherence properties [11, 12]. The long coherence times demonstrated with e.g. trapped ions make them desirable as quantum memories but in the primary step of a repeater, entanglement needs to be created non-locally between two memories. This requires efficient transfer of information from the quantum memories into light modes such as single photons. To this end, the emitter can be placed inside a cavity, which can greatly enhance the coupling to the light [31, 103]. The cavity can, however, also increase the experimental difficulty of performing the subsequent step of entanglement swapping in a repeater due to the detrimental effect of cavity loss and spontaneous emission from the single emitter. The parameter characterizing this, is the cooperativity C of the emitter-cavity system. While high fidelity logic operations such as the CNOT gate have been demonstrated without cavities [11, 129, 130], it can be argued that transferring these techniques to

a cavity system will make the gate fidelity, F, have a poor scaling of $1 - F \sim 1/\sqrt{C}$ [105, 106]. It is thus very demanding to integrate these techniques in a cavity based quantum repeater to realize entanglement swapping. It has been suggested to employ entanglement purification after each swap operation to boost the entanglement but this often requires a large number of resources or time consuming sequential generation of purification pairs [14, 131–133]. Alternatively it has also been suggested to physically move the emitters out of the cavities to perform the swap operation, which requires excellent experimental control and complex apparatus [128].

In this chapter, I describe the work of me and my collaborators on cavity based quantum repeaters without intermediate entanglement purification. The work was done in collaboration with Peter Kómár, Eric Kessler, Mikhail D. Lukin and Anders S. Sørensen and is described in Ref. [134], which is the basis of this chapter. Without intermediate entanglement purification, it is necessary to increase the performance of of the gates from the detrimental $1/\sqrt{C}$ scaling in order to have long distance distribution of entanglement. To this end, we have considered the deterministic CNOT gate suggested in Ref. [106], implemeted with the entanglement scheme of Ref. [109] and the heralded CZ-gate described in Chap. 6. Note that a CZ-gate is identical to a CNOT gate up to single qubit rotations and we will therefore refer to the heralded gate as a CNOT gate. The deterministic gate has a more favorable scaling of the fidelity as $1 - F \sim 1/C$ while the heralded gate has perfect conditional fidelity at the expense of a finite failure probability. Because of the efficient entanglement swapping obtainable with these gates, it is possible to distribute entanglement over a large distances without intermediate purification, which greatly simplifies the experimental requirements for realizing the repeater and enhances the rate of entanglement distribution. Furthermore, we investigate two different entanglement generation schemes, namely one that relies on single-photon detection, similar to Ref. [135], and one that uses two-photon detection, similar to Ref. [136]. We determine under which conditions one is favorable over the other in terms of achiving the highest secret key rate (see below). We include initial purification in the repeater but consider only scenarios with 2 or 4 qubits pr. repeater station. Finally, we optimize the general repeater architecture to obtain the highest secret key rate over a given distance. The essential parameter characterizing the performance of the repeater, is the cooperativity C of the emitter-cavity systems and we perform the opmization for a range of cooperativites allowing us to find the optimal repeater structure for a given cooperativity.

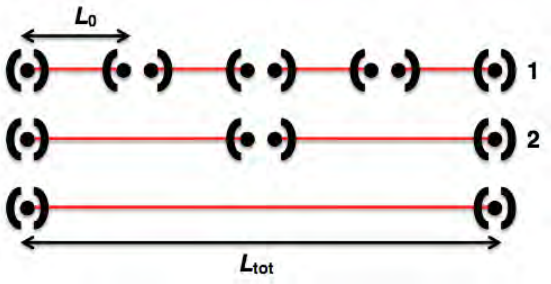

FIGURE 8.1: The general architecture of a quantum repeater. The total distance, over which entanglement should be distributed, is divided into elementary links of length L_0 connected by repeater stations pictured as cavitites containing single emitters. After creating entanglement in the elementary links the entanglement is swapped to larger distances by combining the elementary links. The numbers on the figure referes to the swap level of the repeater. The total number of swap levels is 2 for this depicted setup.

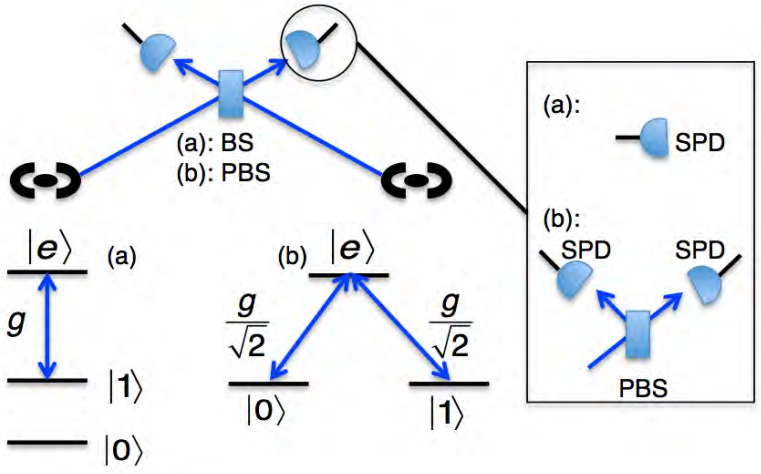

FIGURE 8.2: Entanglement generation in the elementary links. (a) is the situation of the single-photon detection scheme and (b) is the two-photon detection scheme. Both schemes use a central station with either (a) a single balanced beam splitter (BS) and two single-photon detectors or (b) three polarizing beam splitters (PBS) and four single-photon detectors. The relevant level structure of the emitters are also shown. g denotes the cavity coupling. For the two-photon scheme the levels $|0\rangle$ and $|1\rangle$ are assumed to have equal couplling of $g/\sqrt{2}$ to the excited state $|e\rangle$.

8.1 Entanglement generation

The first step in a quantum repeater is to create non-local entanglement in the elementary links (see Fig. 8.1). To this end, it has been suggested to use single photon detection (SPD) and beam splitters to entangle two emitters. In general, the different proposals rely on either single-photon detection [135, 137] or two-photon detection [136].

In a single-photon detection scheme, we assume that the two emitters are initially prepared in a state (see Fig. 8.2)

$$(1-\epsilon^2)|00\rangle + \epsilon^2|ee\rangle + \epsilon\sqrt{1-\epsilon^2}\,(|0e\rangle + |e0\rangle) \tag{8.1}$$

by a weak excitation pulse such that the excitation probability is ϵ^2. An emitter can go from state $|e\rangle$ to state $|1\rangle$ by emitting a cavity photon. The emitted photons are readout from the cavities and combined on a balanced beam splitter (BBS) on a central station between the two cavities. If losses are neglected, the detection of a single photon after the BBS will project the state of the emitters into the Bell state $|\Psi^+\rangle = \frac{1}{\sqrt{2}}(|01\rangle + |10\rangle)$ up to a single qubit rotation. Assuming that the decay rate of the cavity, κ, is much larger than the cavity coupling, g, the probability P_{phot} of an emitter to go from $|e\rangle$ to $|1\rangle$, by creating a cavity photon during a time interval $[0;T]$, is

$$P_{phot} = \frac{4C}{1+4C}\left(1 - e^{-\gamma(1+4C)T}\right), \tag{8.2}$$

where we have defined the cooperativity $C = g^2/\kappa\gamma$, where γ is the spontaneous emission rate of the emitters. Including various losses, the total probability of a single click at the detectors is $P_{1click} = 2\eta P_{phot}\epsilon^2(1-\epsilon^2) + (2\eta - \eta^2)P_{phot}^2\epsilon^4$, where η is the total detection probability including inefficent outcoupling of the cavity light, imperfect detectors and losses in the transmission fibers. The second term is the probability of emitting two cavity photons but only getting a single click. Note that we have not assumed number-resolving detectors. The probability, to have a single click and have created the state $|\Psi^+\rangle$, is $P_{correct} = 2\eta P_{phot}\epsilon^2(1-\epsilon^2)$. The average, heralded fidelity following a single click is thus $F_1 = P_{correct}/P_{1click}$. To lowest order in ϵ, we have that $1 - F_1 \sim (1-\eta/2)P_{phot}\epsilon^2$ while the success probability is $P_{1click} \sim 2\eta P_{phot}\epsilon^2$. There is thus a tradeoff between the success probability and the fidelity.

The situation in a two-photon detection scheme is also shown in Fig. 8.2. Both emitters are initailly prepared in the excited state $|e\rangle$ by a strong excitation pulse and the cavity is assumed to couple both $|e\rangle \to |1\rangle$ and $|e\rangle \to |0\rangle$ with equal coupling strength $g/\sqrt{2}$. The two transitions are, however, assumed to produce photons with different polarizations such that the emission of a cavity photon creates an entangled state between the photon and the emitter of the form $\frac{1}{\sqrt{2}}(|0\rangle|1_1\rangle_L + |1\rangle|1_2\rangle_L)$ where $|1_1\rangle_L$ ($|1_2\rangle_L$) is the single photon state with polarization 1 (2). The probability of one of the emitters to create a cavity photon of either polarization is P_{phot} (see Eq. (8.2)) under similar assumptions as for the single-photon detection scheme. The photons are readout from the cavities and combined on a central polarizing beam splitter (PBS) such that if two photons of the same polarizations are incident on the PBS, we always get a photon in each output port, while photons of different polarization always end up in the same output port. Both output ports are then send to a second set of polarizing beam splitters and both output ports of these are finally measured with single photon detectors. A click in a detector in each arm heralds the creation of the Bell state $|\Psi^+\rangle$ between the emitters up to a local qubit rotation. Note, that neglecting dark counts of the detectors, the heralded fidelity

Scheme	Fidelity	Probability
Single-photon	$F \sim 1-(1-\eta)P_{phot}\epsilon^2$	$P_{click} \sim 2\eta P_{phot}\epsilon^2$
two-photon	$F \sim 1$	$P_{2click} = \frac{1}{2}\eta^2 P_{phot}^2$

TABLE 8.1: The characteristics of the schemes of entanglement generation that we consider. η is the total detection efficiency of a cavity photon including inefficient outcoupling, fiber losses and inefficent SPD. ϵ^2 is the excitation probability in the single-photon detection scheme and P_{phot} is the probability of an emitter to emit a cavity photon from the excited state $|e\rangle$ (see Fig. 8.2).

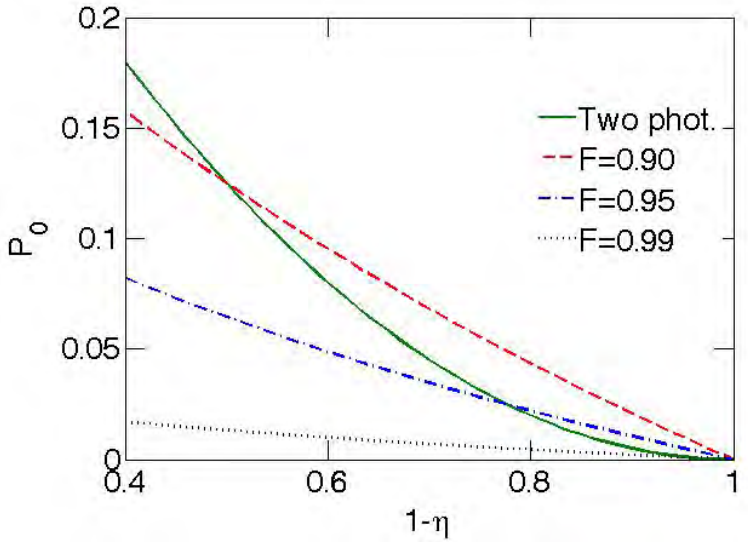

FIGURE 8.3: The success probability, P_0 for the one-photon and two-photon scheme plotted against $1-\eta$ where η is the total detection efficiency. The fidelity of the two-photon scheme is 1 while the rate of the one-photon scheme is plotted for final fidelities $F \geq 0.9$, $F \geq 0.95$ and $F \geq 0.99$. For the one-photon scheme $P_0 = P_{1click}$ and for the two-photon scheme $P_0 = P_{2click}$. Note that we have neglected dark counts.

is unity. The success probability of the scheme is, however, $P_{2click} = \frac{1}{2}\eta^2 P_{phot}^2$, which decreases rapidly with the detection efficiency.

The fidelities and success probabilities of the single-photon and two-photon schemes are summarized in Table 8.1 and illustrated in Fig. 8.3

Fig. 8.3 shows that if the detection efficency η is large, the two-photon scheme will be desirable since it will have both a high success probability and a high fidelity. However, if η is small, the single-photon scheme might be desirable since it has a relatively high succes probability. η is, among other things, determined by the losses of the fiber transmission. We write the transmission efficiency as $\eta_f = e^{-L_0/2L_{att}}$, where L_0 is the length of the elementary links of the repeater and L_{att} is the fiber attenuation length. Which entanglement generation scheme that are advantageous thus depends on the length of the elementary links, which is set by the number of swap levels and the total distance to distribute entanglement over. Note that due to the possible high succes probability but

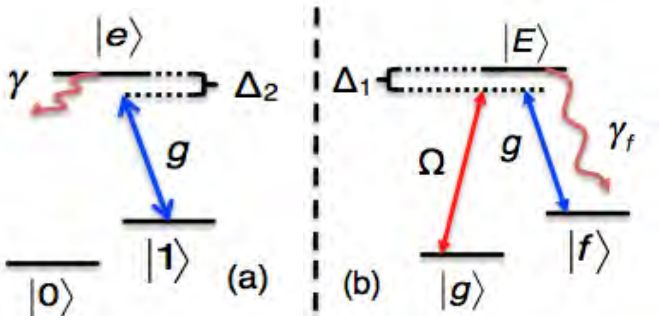

FIGURE 8.4: (a) Level structure of the qubit atoms where only state $|1\rangle$ couples to the cavity. (b) Level structure of the auxiliary atom and the transitions driven by the weak laser (Ω) and the cavity (g). We assume that $|E\rangle \leftrightarrow |f\rangle$ is a closed transition.

limited fidelity of the single-photon scheme, it might be desirable to combine this with entanglement purification to increase the final fidelity. We have therefore also considered the possibility of initial entanglement purification in the repeater.

8.2 CNOT gates

The basic operation of entanglement purification and our entanglement swapping is a CNOT gate. As previously mentioned, we consider two CNOT schemes. The first scheme we consider is the heralded CNOT gate described in Chap. 6. We will refer to this gate scheme as *gate 1*. Though the scheme was considered in particular for trapped atoms in nanocavitites, it can easily by generalized to any set of emitters, which have the appropriate level structures (see Fig. 8.4). By tuning the detunings Δ_1 and Δ_2 (see Fig. 8.4) correctly the conditional fidelity of the gate is unity while the success probability scales as $1 - P_g \sim 6/\sqrt{C}$ as described in Chap. 6. The gate time will increase with the cooperativity as $t_{gate,1} \sim 100\sqrt{C}/\gamma$. We assume that the atomic detection of the auxiliary atom is 100% efficient.

The second CNOT gate we consider is the determinstic gate proposed in Ref. [106] but realized with the entanglement generation scheme of Ref. [109]. We will refer to this gate as *gate 2*. This gate does not require an auxiliary atom but rather two auxiliary levels in the qubit atoms as shown in Fig. 8.5a. The quantum information is stored in the horizontal/qubit degree of freedom (subscripts 0 and 1) and the vertical/level degree of freedom (denoted g and f) is used to make an entanglement assisted CNOT gate between the atoms. Separating the qubit degree of freedom from the level degree of freedom, the ideal gate makes the transformation

$$|q1\rangle|q2\rangle \otimes |gg\rangle \rightarrow |q1\rangle|q2\rangle \otimes \frac{1}{\sqrt{2}}\left(|gf\rangle + |fg\rangle\right), \tag{8.3}$$

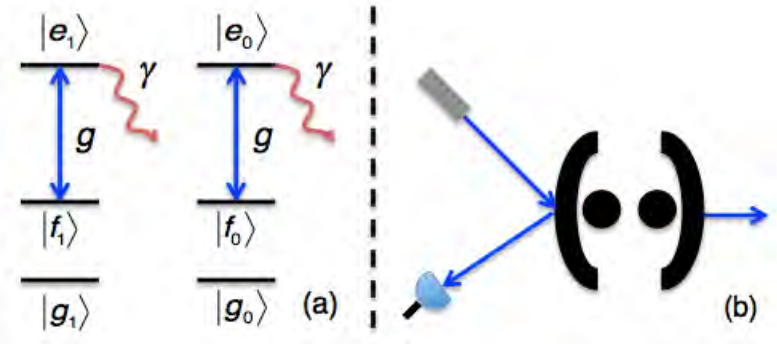

FIGURE 8.5: (a) Level structure of the qubit atoms. The levels $|r_0\rangle$ and $|r_1\rangle$ where $r = g, f$ or e are assumed to be degenerate such that the quantum information is incoded in the horizontal degrees of freedom. (b) The setup to create entanglement between the level states $|g\rangle, |f\rangle$ of the atoms. Weak coherent light is shined on the cavity and any reflected light is measured with a SPD.

where $|g\rangle, |f\rangle$ denote the vertical states and $|q1\rangle$ ($|q2\rangle$) is the qubit state of the first (second) qubit, which could be entangled with atoms at neighboring repeater stations. The entanglement between the levels can be used to make a CNOT gate, if the levels of the atoms can be measured non-destructively, i.e. without revealing any information about the qubit state as described in Ref. [106]. Both the transformation shown in Eq. (8.3) and the non-destructive measurements can be obtained by shining a weak coherent pulse on a two-sided cavity and detecting any reflected light (see Fig. 8.5b). If the light is resonant with the empty cavity mode, photons will only be reflected if one or both atoms are in the f-level. This results from the atom-cavity coupling shifting the cavity resonance from the empty cavity frequency. Note that an equivivalent setup is measuring the phase of the reflected light from a single sided cavity. Ideally single photons are used but we assume the more realistic scenario, where the light is a weak coherent pulse. We assume that the coherent light is continously shined on the cavity such that at most one photon is in the cavity at all times. A single-photon detector continously monitors if any photons are reflected from the cavity and the coherent light is blocked if a click is recorded before n_{max} photons on average have been shined on the cavity. If no click was recorded during this time, both atoms are interpreted as being in the g levels. The entangling scheme is then

1. Both atoms are initially prepared in the superposition $|g\rangle + |f\rangle$ by a e.g. a $\pi/2$-pulse.

2. Coherent light is shined on the cavity. if a click is recorded before on average n_{max} photons have been shined on the cavity, the levels of the atoms are flipped ($|g\rangle \leftrightarrow |f\rangle$). If no click is recorded, the atoms are interpreted as being in $|gg\rangle$ and the procedure is repeated from step 1.

Gate	Fidelity	Probability
1	$F = 1$	$P_g \sim 1 - 6/\sqrt{C}$
2	$F \sim 1 - 1/(\eta_d C)$	$P_g = 1$
3	$F \sim 1 - 3/\sqrt{C}$	$P_g = 1$

TABLE 8.2: The characteristics of the three gates considered for the repeater. C is the cooperativity of the atom-cavity system and η_d is the single photon detection efficiency in gate 2

3. Conditioned on the first click, another coherent light pulse is shined on the cavity after the levels of the atoms have been flipped. If a click is recorded before $n = n_{max} - n_1$ photons on average have been shined on the cavity, the entangling scheme is considered to be a success. Here n_1 is the average number of photons that had been shined on the cavity before the first click. If no click is recorded, the atoms are interpreted to be in $|gg\rangle$ and the procedure is repeated from step 1.

As seen above the entangling scheme is repeated until successful such that the operation is determinsitic. As described in Ref. [106] a series of non-destructive measurements of the atoms together with single qubit rotations are required to make the CNOT operation after the entanglement has been created. The non-destructive measurements can be performed using the same technique of monitoring reflected light as in the entangling scheme and we assume that we can effectively tune the couplings to the cavity such that possibly only a single atom couples. Spontaneous emission from the atoms will limit the fidelity of the gate to $1 - F \sim 1/(\eta_d C)$, where η_d is the detection efficency and $C = g^2/\kappa\gamma$ is the cooperativity. The time of the gate is limited by the time of the single qubit rotations and the coherent pulses. We assume that this gives a gate time on the order of 10 μs.

We also consider the naive approach, where the setup of gate 1 is used to make a deterministic gate by simply ignoring the heralding condition. This is to characterize the situation where a no-cavity gate scheme is directly transferred to a cavity setup. We will refer to this gate as *gate 3*. For such a gate, we find that the gate fidelity will scale as $1 - F \sim 3/\sqrt{(C)}$ and the time of the gate will be $t_{gate} \sim 50\sqrt{C}/\gamma$.

The characteristics of the three gates we consider are summarized in Table 8.2 and illustrated in Fig. 8.6

It is clear, that a repater based on gate 3 will never be advantageous but we consider it for comparison. The heralded gate has a finite probability, which decreases the rate of the repeater but in return, the gate has perfect heralded fidelity. This might increase the number of possible swap levels, which can increase the rate of the entanglement generation step and thus the total rate of the repeater. The deterministic gate works

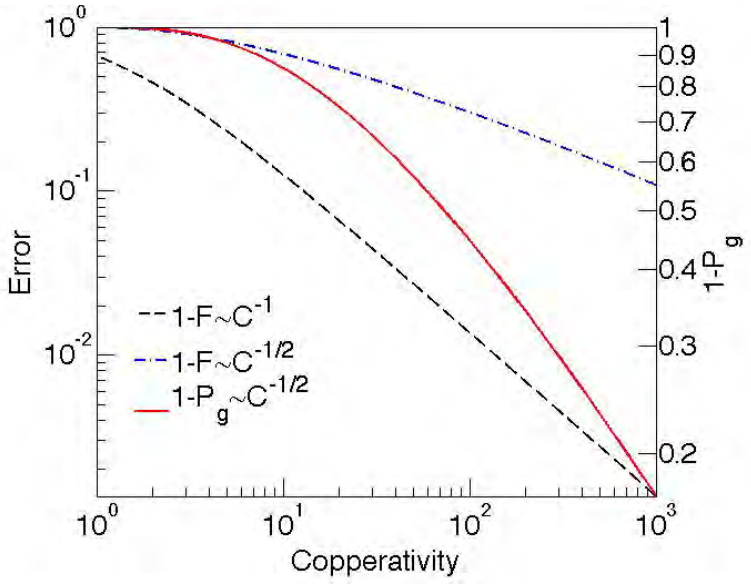

FIGURE 8.6: Characteristics of the three gates described in the text. Gate 2 (black, dashed line) and gate 3 (blue, dashed/dot line) are both deterministic and the errors (left axis) of the gates are plotted against the cooperativity. The error is defined as $1 - F$ where F is the fidelity of the gate. Gate 1 has conditional fidelity 1 but a finite failure probability $1 - P_g$ (right axis).

every time but with non-perfect fidelity, which will limit the number of possible swap levels in the repeater.

8.3 Repeater software

As previosuly mentioned, we include the possibility of combining the single-photon scheme with initial purification in the repeater. We will, however, only consider two scenarious. First, we assume that each repeater station only contains two qubits and initial purification can therefore not take place. Second, we assume that each repeater station contains 4 qubits, which makes initial purification possible. The modest number of qubits is considered to reflect what is obtainable with realistic resources. The extra qubits could also be used to simply enhance the rate of entanglement generation by increasing the number of tries pr. entanglement generation attempt. Note that we will assume the latter approach to be the case for repeaters based on the two-photon scheme.

We make a detailed analysis of the various errors that limit the fidelity for both the single-photon and the two-photon detection schemes including dark counts of the detectors (see App. F for details). As a result, we find that the purification protocol of Ref. [14] effectively corrects for the errors in the single-photon scheme and we assume that this is used for the initial purification. This protocol relies on a CNOT operation, which we assume is made with one of the three gates described in Sec. 8.2. In the purification

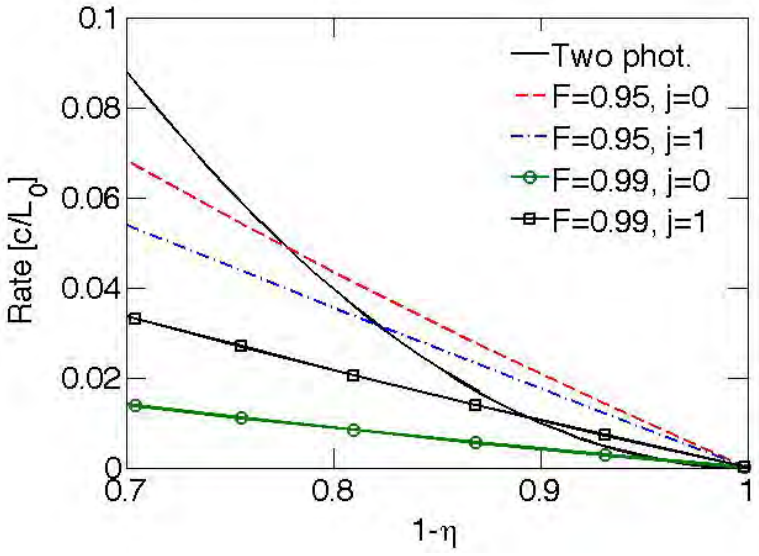

FIGURE 8.7: Rate of entangelment generation for the two-photon scheme and the one-photon scheme with target fidelity $F \geq 0.95$ and $F \geq 0.99$ with/without purification. The rate is plotted against $1 - \eta$ where η is the total detection efficiency. We have neglected dark counts and assumed that the CNOT gate is deterministic and have perfect fidelity. The rate has been estimated as described in Sec. 8.4. Furthermore we have assumed that each repeater station contains 4 qubits, which are either used for purification or to increase the rate of the entanglement generation.

scheme, two parties are assumed to share two entangled states. They each perform a CNOT operation on their qubits and subsequently measure the state of the target qubits of the CNOTs. If they obtain the same measurement outcome, they keep the control pair and otherwise they discard it. The purification can either be done in a cascaded manner where two pairs with the same fidelity are always combined or in a pumping scheme, where the fidelity of a single pair is pumped by combining it with pairs of lower fidelity. We will assume that a pumping scheme is used since this requires less qubits pr. repeater station.

The effect of combining the single-photon scheme with initial purification is shown in Fig. 8.7, where the purification is asssumed to be performed with a deterministic gate with perfect fidelity. If high fidelity pairs are desired for e.g. a repeater with many swap levels, entanglement purification can increase the rate of the entanglement generation.

We also consider the optimal use of repeater stations. For $2^n + 1$ repeater stations, one can either use all stations in a single repeater with n swap levels or one can construct a number of parallel repeaters with less swap levels. Increasing the number of swap levels, decreases the fiber losses in the elementary links and thus increases the rate of entanglement generation. If, however, the length of the elementary links is already small, such that e.g. imperfect SPD detection dominates the rate, then increasing the number of swap levels does not lead to any improvement. It would instead be advantageous

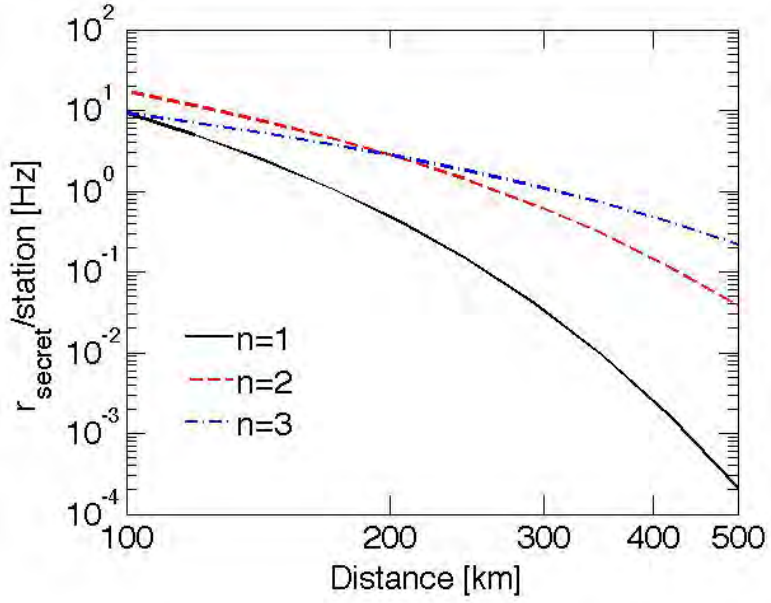

FIGURE 8.8: Secret key rate pr repeater station (r_{secret}/station) plotted against the distribution distance for a repeater with $n = 1, 2$ and 3 swap levels. The secret key rate was calculated as described in Sec. 8.5 with the assumptions summarized in Table 8.3. The repeaters were assumed to use the two-photon scheme with gate 2 and a cooperativity of 100.

to use the extra repeater stations to make another repeater with less swap levels. To treat this in our analysis of the repeater, we consider the distribution rate pr repeater station instead of simply the distribution rate. Fig. 8.8 shows how the optimal number of swap level changes with distance while considering the rate pr. repeater station. Note that Fig. 8.8 shows the so-called secret key rate pr station plotted against the distance. The secret key rate is basically the distribution rate times a secret key fraction, which depends on the fidelity of the distributed pair. We will describe this in more detail in section Sec. 8.5.

In most repeater schemes, the qubits in a repeater station are assumed to be operated more or less simultaneously with half of the qubits being used to each side such that entanglement attempts in all the elementary links are done simultaneously. We refer to this as a *parallel* repeater. We, however, also consider another sequential way of operating the qubits, where all qubits in a station are first used to make entanglement in one elementary link. After this has been obtained, all but one qubit are then used to make entanglement in the other neighboring link. This is referred to as a *sequential* repeater. The advantage of the sequential repeater is that the rate of the lowest level in the repeater, the entanglement generation, is increased. This comes at the cost of a waiting time between entanglement attempts in neighboring links. Fig. 8.9 shows that whether the sequential repeater has higher secret key rate than a parallel repeater depends on the number of qubits pr repeater station.

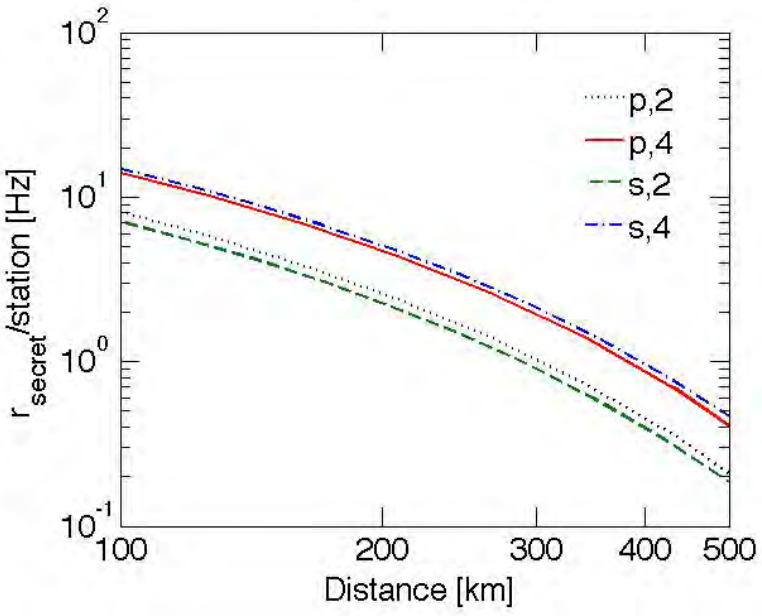

FIGURE 8.9: Secret key rate pr repeater station (r_{secret}/station) plotted against the distribution distance (Distance) for a parallel repeater with 2 (4) qubits pr station (p,2 (4)) and a sequential repeater with 2 (4) qubits pr station (s,2 (4)). The secret key rate was calculated as described in Sec. 8.5 with the assumptions summarized in Table 8.3. Both repeaters were assumed to use the two-photon scheme with gate 2 and a cooperativity of 100. Both repeaters were assumed to have 3 swap levels.

8.4 Rate analysis

We wil now analyse the rate of entanglement distribution for the different repeater softwares considered in the previous sections. The total rate of the repeater are set by the average time of entanglement creation, initial purification and entanglement swapping. Assuming that entanglement generation has a success probability P_0, we estimate the average time $\tau_{pair,l;m}$ it takes to generate l entangled pairs in one elementary link using m qubits, which can be operated in parallel, as

$$\tau_{pair,l;m} = \mathcal{Z}_{l;m}(P_0)(L_0/c + \tau_{local}). \tag{8.4}$$

Here c is the speed of light in the fibers and τ_{local} is the time of local operations such as initialization of the qubits. The factor $\mathcal{Z}_{l;m}(P_0)$ can be thought of as the average number of coin tosses needed to get at least l tails if each toss is performed with m coins simultaneously, and the probability of tail is P_0 for each coin [138]. It is furthermore assumed that coins showing tail after a toss are kept and only the coins showing head are tossed again until l tails are obtained. In the repeater context, the coins are entanglement generation attempts and tail is successful entanglement generation. The time it takes per "toss" is $L_0/c + \tau_{local}$. The expressions for $Z_{l;m}(P_0)$ is given in App. F.3.

After creating a number of entangled pairs in an elementary link of the repeater, they may be combined to create a purified pair of higher fidelity. As previously mentioned, we assume an entanglement pumping scheme since this requirs less resources than e.g. a cascading scheme. Let $P_{pur}(F_0, F_0)$ denote the success probability of the purification operation, which depends on the fidelity of the two initial pairs (F_0) and the fidelity of the CNOT gate used in the purification operation. Note that P_{pur} also contains the success probability of the CNOT gate used in the purification. We estimate the average time τ_{pur1}, it takes to make one purified pair from two intial pairs of fidelity F_0, using m qubits in parallel in the entanglement generation step, as

$$\tau_{pur,1} = \frac{\tau_{pair,2;m} + \tau_{pur}}{P_{pur}(F_0, F_0)}, \tag{8.5}$$

where $\tau_{pur} \sim L_0/c + \tau_c$ is the time of the purification operation. Here τ_c is the time of the CNOT operation and L_0/c is the communication time between the two repeater stations sharing the entangled pairs. To further pump the entanglement of the purified pair, a new entangled pair is subsequently created using $m-1$ qubits operated in parallel. The average time it takes to make j rounds of purification is thus estimated as

$$\tau_{pur,j} = \frac{\tau_{pur,j-1} + \tau_{pair,1:m-1}}{P_{pur}(F_{j-1}, F_0)}, \tag{8.6}$$

with $\tau_{pur,0} = \tau_{pair,2;m}$. Here F_{j-1} is the fidelity of the purified pair after $j-1$ purifications.

The total rate of a repeater, consisting both of purification and entanglement swapping, depends on the specific repeater software. We will first consider the case of both a parallel and sequential repeater operated with deterministic gates and afterwards the same situations with probabilistic gates.

8.4.1 Deterministic gates

For a parallel repeater with n swap levels and deterministic gates, we first estimate the average time it takes to generate 2^n purified pairs, i.e. a purified pair in each elementary link. We assume that each pair is purified j times such that the time to generate one purified pair is

$$\begin{aligned} \tau_{pur,j} \quad = \quad & \frac{\mathcal{Z}_{2;m}(P_0)(L_0/c + \tau_{local})}{P_{pur}(F_0, F_0) \cdots P_{pur}(F_{j-1}, F_0)} \\ & + \sum_{i=0}^{j-1} \frac{\tau_{pur}}{P_{pur}(F_i, F_0) \cdots P_{pur}(F_{j-1}, F_0)} \\ & + \sum_{i=1}^{j-1} \frac{\mathcal{Z}_{1;m-1}(P_0)(L_0/c + \tau_{local})}{P_{pur}(F_i, F_0) \cdots P_{pur}(F_{j-1}, F_0)}, \end{aligned} \tag{8.7}$$

where we have solved the recurrence in Eq. (8.6). We now wish to estimate the total time, $\tau_{link,2^n}$ it takes to make a purified in every elementary link, i.e. the time it takes to make 2^n pairs. A lower limit of $\tau_{link,2^n}$ is simply $\tau_{pur,j}$ but this is clearly a very crude estimate if the purification have a limited success probability. We therefore make another estimate of the average time by treating $\tau_{pur,j}$ as consisting of $2j$ independent binomial events with probabilities

$$P_1 = \frac{P_{pur}(F_0,F_0)\cdots P_{pur}(F_{j-1},F_0)}{\mathcal{Z}_{2;m}(P_0)} \tag{8.8}$$

$$P_2^{(i)} = P_{pur}(F_i,F_0)\cdots P_{pur}(F_{j-1},F_0) \tag{8.9}$$

$$P_3^{(i)} = \frac{P_{pur}(F_i,F_0)\cdots P_{pur}(F_{j-1},F_0)}{\mathcal{Z}_{1;m-1}(P_0)}. \tag{8.10}$$

We then estimate the average time, $\tau_{link,2^n}$ it takes to make 2^n purified pairs as

$$\begin{aligned}\tau_{link,2^n} = {} & \mathcal{Z}_{2^n;2^n}(P_1)(L_0/c+\tau_{local}) \\ & + \sum_{i=0}^{j-1} \mathcal{Z}_{2^n,2^n}(P_2^{(i)})\tau_{pur} \\ & + \sum_{i=1}^{j-1} \mathcal{Z}_{2^n,2^n}(P_3^{(i)})(L_0/c+\tau_{local}).\end{aligned} \tag{8.11}$$

Eq. (8.11) is a better estimate for the average time than $\tau_{pur,j}$ in the limit of small success probabilities. However, it overestimates the average distribution time when the purification has a large success probability. How much it overestimates depends on n and j. Comparing $\tau_{pur,j}$ to Eq. (8.11) we find that for $n \leq 5$ and $j \leq 2$ there is a factor $\lesssim 2$ between the two estimates, in the limit of large success probability for the purification operation. As we describe below we never consider more than 5 swap levels in our optimization and since we have a limited number of qubits pr. repeater station, we will never have to consider more than 2 rounds of purification. We can therefore use the estimate for $\tau_{link,2^n}$ given in Eq. (8.11).

To get the average time it takes to distribute one entangled pair over the total distance, L_{tot}, of the repeater, we need to add the time of the entanglement swapping, $\tau_{swap,nd}$ to $\tau_{link,2^n}$. We estimate $\tau_{swap,nd}$ as

$$\tau_{swap,nd} = (2^n-1)L_0/c + n\tau_c, \tag{8.12}$$

where the first term is the time of the classical communication and τ_c is the time of the CNOT operation involved in the swap procedure. The average distribution rate, of a parallel repeater with determinsitic gates, is thus $r_{p,d} = 1/(\tau_{link,2^n} + /\tau_{swap,nd})$.

For a sequential repeater with deterministic gates we estimate the time it takes to generate purified pairs in all 2^n pairs as

$$\tau^{(s)}_{link,2^n d} = \left(\tau_{link,2^{n-1}}\right)\Big|_{m\to 2m} + \left(\tau_{link,2^{n-1}}\right)\Big|_{m\to 2m-1}. \tag{8.13}$$

Here we have indicated that the number of qubits, which can be operated in parallel is $2m$ for the first 2^{n-1} pairs and $2m-1$ for the next 2^{n-1} pair compared to the parallel repeater, where only m qubits can be used in all 2^n pairs. Note, that we have assumed that first entanglement is established in half of the links and only when this is completed, entanglement is created in the remaning half of the links. This is clearly not the fastest way of operating the repeater but it gives an upper limit of the average distribution time. The entanglement swapping of the sequential repeater is exactly the same as for the parallel repeater and the average total rate, of the sequential repeater with deterministic gates, is thus $r_{s,d} = 1/(\tau^{(s)}_{link,2^n} + t_{swap,nd})$.

8.4.2 Probabilistic gates

To estimate the total, average distribution time of a parallel repeater with n swap levels and probabilistic gates, we will again treat $\tau_{pur,j}$ as consisting of $2j$ independent binomial events, as we did for the deterministic gates. The time it takes to make a single swap can be estimated as

$$\begin{aligned}\tau_{swap,1p} &= \frac{\mathcal{Z}_{2;2}(P_1)(L_0/c+\tau_{local})}{P_{swap}} + \frac{L_0/c}{P_{swap}} + \frac{\tau_c}{P_{swap}} \\ &\quad + \sum_{i=0}^{j-1} \frac{\mathcal{Z}_{2;2}(P_2^{(i)})\tau_{pur}}{P_{swap}} \\ &\quad + \sum_{i=1}^{j} \frac{\mathcal{Z}_{2;2}(P_3^{(i)})(L_0/c+\tau_{local})}{P_{swap}},\end{aligned} \tag{8.14}$$

where P_{swap} is the probability of the swap operation, i.e. the probability of the CNOT gate. Eq. (8.14) can be iterated such that the average time it takes to make n swap

levels is estimated as

$$\begin{aligned}\tau_{swap,np} &= \frac{\tilde{\mathcal{Z}}_{n;1}(P_{swap},P_1)(L_0/c+\tau_{local})}{P_{swap}} \\ &+\sum_{i=1}^{n}\frac{\tilde{\mathcal{Z}}'_{n;i}(P_{swap},P_{swap})(2^{i-1}L_0/c+\tau_c)}{P_{swap}} \\ &+\sum_{i=0}^{j-1}\frac{\tilde{\mathcal{Z}}_{n;1}(P_{swap},P_2^{(i)})\tau_{pur}}{P_{swap}} \\ &+\sum_{i=1}^{j-1}\frac{\tilde{\mathcal{Z}}_{n;1}(P_{swap},P_3^{(i)})(L_0/c+\tau_{local})}{P_{swap}},\end{aligned} \tag{8.15}$$

where

$$\tilde{\mathcal{Z}}^{(\prime)}_{n;i}(P_{swap},P) = \mathcal{Z}_{2;2}\left(\frac{P_{swap}}{\tilde{\mathcal{Z}}^{(\prime)}_{n-1;i}(P_{swap},P)}\right), \tag{8.16}$$

$$\tilde{\mathcal{Z}}_{i;i}(P_{swap},P) = \mathcal{Z}_{2;2}(P) \tag{8.17}$$

$$\tilde{\mathcal{Z}}'_{i;i}(P_{swap},P) = 1. \tag{8.18}$$

The average, rate of a parallel repeater with probabilistic gates and n swap levels is then $r_{p,p} = 1/\tau_{swap,np}$. Note that for $P_{swap} \approx 1$ and $P_0 \ll 1$, Eq. (8.15) underestimates the average distribution rate with a factor that increases with the number of swap levels, n. However, for $n \leq 5$, we find that this factor is $\lesssim 2$.

The operation of a sequential repeater with probabilistic gates is not straightforward since it is unclear how the sequential generation of entanglement should take place after a failed swap operation. We therefore choose to assume that initially, entanglement is generated in all 2^n links sequentially. When this is completed the first round of entanglement swapping is performed. If a swap fails, entanglement is restored in a parallel manner, i.e. the sequential operation is only employed in the initial generation of entanglement. Furthermore, we assume that the swap operations of a swap level is only initiated when all swap operations in the subsequent level have been successfull. The average time, it takes for all swap operations in the first level to succeed, is then

estimated as

$$\begin{aligned}\tau^{(s)}_{swap,1p} &= \sum_{i=0}^{2^{n-1}} P_{swap}^{2^{n-1}-i}(1-P_{swap})^i \Bigg[\\ &\mathcal{Z}_{i;i}\left(\frac{P_{swap}}{\mathcal{Z}_{2;2}(P_1)}\right)(L_0/c+\tau_{local}) \\ &+\mathcal{Z}_{i;i}(P_{swap})(L_0/c+\tau_c) \\ &+\sum_{k=0}^{j-1}\mathcal{Z}_{i;i}\left(\frac{P_{swap}}{\mathcal{Z}_{2;2}(P_2^{(i)})}\right)\tau_{pur} \\ &+\sum_{k=1}^{j-1}\mathcal{Z}_{i;i}\left(\frac{P_{swap}}{\mathcal{Z}_{2;2}(P_3^{(i)})}\right)(L_0/c+\tau_{local}) \\ &+(L_0/c+\tau_c)\delta_{i,0}\Bigg], \end{aligned} \tag{8.19}$$

where $\delta_{i,0}$ is a delta function. Eq. (8.19) can be generalized such that the time it takes to perform the l'th swap level is

$$\begin{aligned}\tau^{(s)}_{swap,lp} &= \sum_{i=0}^{2^{n-l}} P_{swap}^{2^{n-l}-i}(1-P_{swap})^i \Bigg[\\ &\mathcal{Z}_{i;i}\left(\frac{P_{swap}}{\tilde{\mathcal{Z}}_{l;1}(P_{swap},P_1)}\right)(L_0/c+\tau_{local}) \\ &+\sum_{k=1}^{l}\mathcal{Z}_{i;i}\left(\frac{P_{swap}}{\tilde{\mathcal{Z}}'_{l;k}(P_{swap},P_{swap})}\right)(2^{k-1}L_0/c+\tau_c) \\ &+\sum_{k=0}^{j-1}\mathcal{Z}_{i;i}\left(\frac{P_{swap}}{\tilde{\mathcal{Z}}_{l;1}(P_{swap},P_2^{(i)})}\right)\tau_{pur} \\ &+\sum_{k=1}^{j-1}\mathcal{Z}_{i;i}\left(\frac{P_{swap}}{\tilde{\mathcal{Z}}_{l;1}(P_{swap},P_3^{(i)})}\right)(L_0/c+\tau_{local}) \\ &+(2^{l-1}L_0/c+\tau_c)\delta_{i,0}\Bigg] \end{aligned} \tag{8.20}$$

The total rate of a sequential repeater with probabilistic gates and n swap levels can then be estimated as $r_{s,p} = 1/(\tau^{(s)}_{link,2^n} + \tau^{(s)}_{swap,1p} + \cdots + \tau^{(s)}_{swap,np})$.

8.5 Secret key rate

We imagine that the distributed entanglement is used to generate a secret key between two parties referred to as Alice and Bob. There exist various quantum key distribution schemes [8, 9, 13, 139] but the general idea is that Alice and Bob can elliminate the

information that an eavesdropper can contain about the key by measuring on their qubits and compairing results. We will assume that a six-state version of the BB84 protocol described in Ref. [139] is used to generate the secret key. This protocol consists of three steps:

1. Alice and Bob are assumed to have N qubit pairs, which have been distributed in a quantum channel. They can now choose to measure their qubits in one of three measurement bases. They pick a basis according to some probability distribution and measure the state of their qubits. This produces a binary string for both Alice and Bob, which is referred to as a *raw* key.

2. Alice and Bob now compares their choice of basis for all the measurements. If they had the same basis, they keep the information while they discard it if they measured in different bases. This step is referred to as the *shifting* of the raw key.

3. Finally Alice and Bob estimate the information that some eavesdropper could possible contain about their key. This is done by choosing a random sample of $2k$ bits from their raw key and compare the bits in order to estimate the error rate in the quantum channel. In the presence of errors, they seek to correct for them and erase the information that the eaves dropper could have obtained. This process is refereed to as *privacy amplification* [13]. By doing this they can end up with a completely secure key of smaller length ($< 2k$), if the errors are not to big.

For the six-state protocol, the secret key rate, r_{secret} can be defined as

$$r_{secret} = r_{dist} p_{shift} f_{secret}, \tag{8.21}$$

where r_{dist} is the distribution rate of the entangled pairs, p_{shift} is the probability that Alice and Bob chooses the same measurement basis and f_{secret} is the secret key fraction, which depends on the fidelity of the distributed pairs. Without loss of generality we can assume that the distributed pairs are Werner states of the form

$$\begin{aligned} \rho_{AB} &= F|\Phi^+\rangle\langle\Phi^+| + \frac{1-F}{3}\Big(|\Phi^-\rangle\langle\Phi^-| \\ &\quad +|\Psi^+\rangle\langle\Psi^+| + |\Psi^-\rangle\langle\Psi^-|\Big). \end{aligned} \tag{8.22}$$

For such states, it is shown in Ref. [13] that the secret key fraction in the six-state protocol can be estimated in the limit of inifinitely long raw keys to be

$$f_{secret} = 1 - h(\epsilon) - \epsilon + (1-\epsilon)h\left(\frac{1-3\epsilon/2}{1-\epsilon}\right), \tag{8.23}$$

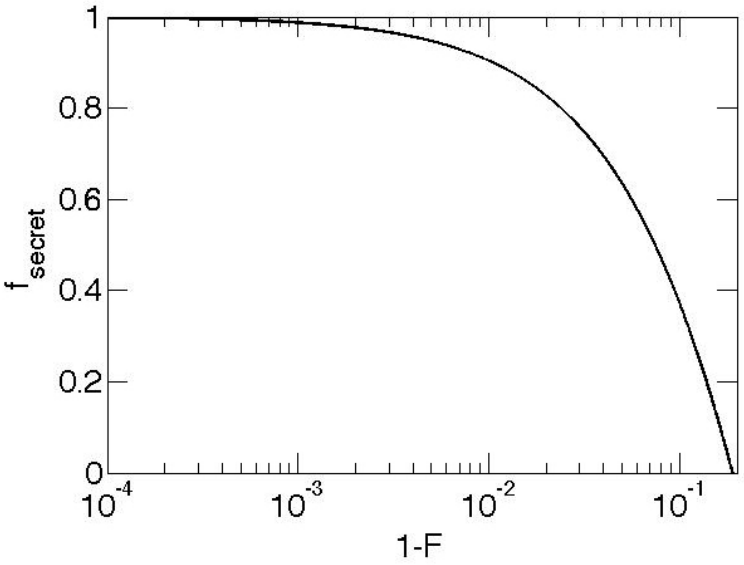

FIGURE 8.10: Secret key fraction (f_{secret}) as a function of the error $1-F$. For $1-F \gtrsim 13\%$ it is no longer possible to extract a secret key from the raw keys.

where $\epsilon = 2(1-F)/3$ and $h(p) = -p\log_2(p) - (1-p)\log_2(1-p)$ is the binary entropy. The expression for f_{secret} given in Eq. (8.23) is valid in the limit of perfect shifting and privacy amplification, which we assume is the case. Futhermore, we assume an assymmetric version of the six state protocol, where one basis is used almost all the time such that $p_{shift} \approx 1$ [13]. Fig. 8.10 shows how the secret key fraction depends on the fidelity of the distributed pairs. It is seen that high fidelity pairs are required in order to have a non-vanishing secret key fraction. On the other hand, the distribution rate r_{dist} will in general decrease in order to increase the fidelity of the distributed pair and the optimal secret key rate is thus obtained as a trade off between f_{secret} and r_{dist}.

8.6 Numerical optimization

We have numerical optimimized the secret key rate pr repeater station in order to find the optimal entanglement generation scheme, CNOT gate and repeater software for a given distance. The secret key rate depends on some experimental parameters such as the efficiency of single photon detectors, dark count rate etc. The values of these parameters are assumed fixed and are thus not part of the optimization. All the experimental parameters are shown in Table 8.3 togehter with the values assumed in the optimizations. The free parameters in the optimization are the number of swap levels, the number of purifications and whether is is a parallel or sequential repeater. In the optimizations, we calculate the secret key rate on a grid of all these parameters and pick the combination giving the highest rate. Fig. 8.11 shows a specific example where

Parameter	Value	Description
γ	$2\pi \cdot 6$ MHz	Spontaneous emission rate of atoms. This enters in the probability of emitting a photon in the entanglement generation schemes (see Eq. (8.2)) and in the gate time of gate 1 and 2.
η_d	50%	Detection efficiency of SPD detectors. This enters in the total detection efficiency η in the entanglement geneation schemes since $\eta = \eta_d \eta_f$. It also determines the fidelity of gate 1. Inefficient outcoupling of light from the cavities can be included in η_d.
L_{att}	22 km	Attenuation length of the fibers. The total transmission probability over a length L is assumed to be $\eta_f = e^{-L/L_{att}}$. We have assumed losses for telecom wavelengths.
τ_{local}	10 μs	Time of local qubit operations
r_{dark}	25 Hz	Dark count rate of SPD detectors. We include dark counts in the entanglement generation step but not in the gate operations since the gate operations are assumed to be fast.
c	$2 \cdot 10^5$ km/s	Reduced speed of light in the transmission fibers [18].

TABLE 8.3: Experimental parameters which influence the rate and fidelity of the repeaters. The second column gives the values used in all optimizations.

the combination of the single photon scheme with gate 2 is investigated for a parallel repeater and a cooperativity of 100. The number of swap levels and purifications, giving the highest rate for a specific distance, can be directly read off from the figure. The same calculations are then done for a sequential repeater with the same combination and finally the performance of the sequential repeater and the parallel repeater are compared in order to find the highest rate for this specific combination. This is done for all combinations of entanglement generation schemes and CNOT gates. The optimal measurement time, T, and excitation probability, ϵ, in the entanglement generation schemes are found for each grid point using a built-in numerical optimization in the program MATLAB[1]. The key parameter, determining the performance of the CNOT gates, is the cooperativity as described in Sec. 8.2. We therefore run optimizations for cooperativities $C \in [10; 1000]$ and distances between 100 km and 1000 km. Finally the optimizations are performed both for 2 qubits pr repeater station and 4 qubits pr. repeater station.

[1] see http://www.mathworks.se/help/matlab/ref/fminsearch.html

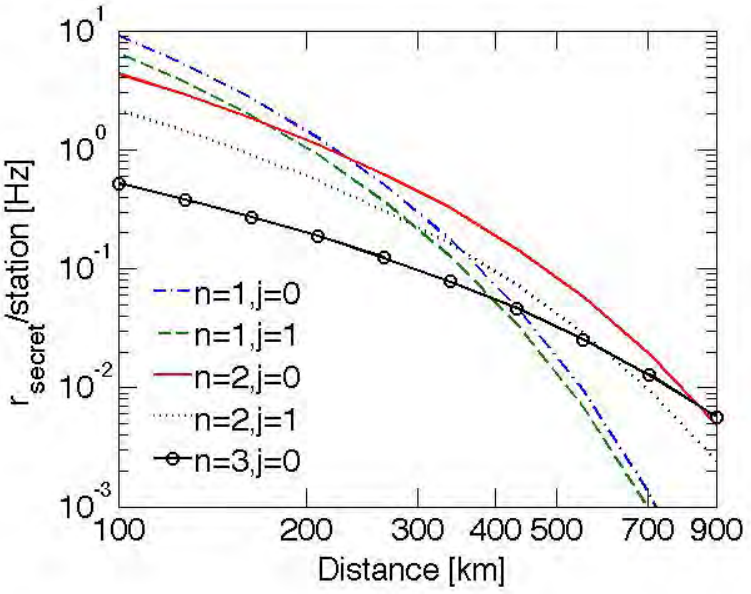

FIGURE 8.11: Secret key rate pr repeater station (r_{secret}/station) plotted against the distribution distance (Distance) for a parallel repeater based on the single photon generation scheme and gate 2. The cooperativity was assumed to be 100 and we assumed 4 qubits pr. repeater station. The optimal number of swap levels (n) and purification rounds (j) for a given distance can be directly read off the plot as the combination giving the highest rate. Note that because the gate fidelity is limited, situations with $j = 2$ and $n = 3, j = 1$ are shown since they result in to low a secret key rate.

We model the effect of non-perfect gates (gate 2 and 3), as depolarizing channels such that the output of a gate operation on a set $\mathcal{S}$ of two qubits is

$$\tilde{\rho} = FU_{\mathcal{S}}\rho U_{\mathcal{S}}^{\dagger} + \frac{1-F}{4}\left(\mathrm{Tr}\left\{\rho\right\}_{\mathcal{S}} \otimes \mathbb{1}_{\mathcal{S}}\right), \tag{8.24}$$

where F is the fidelity of the gate described by unitary $U_{\mathcal{S}}$, $\mathbb{1}_{\mathcal{S}}$ is the identity matrix of the set and $\mathrm{Tr}\{\ldots\}_{\mathcal{S}}$ is the trace over the set. ρ is the initial density matrix. We use Eq. (8.24) to propagate the density matrix from the entanglement generation (see App. F) through the steps of initial purification and entanglement swapping and calculate the average fidelity of the distributed pairs. To calculate the secret key fraction, we treat the distributed pairs as Werner states as described in Sec. 8.5.

The result of the optimizations are shown in Figs. 8.12-8.13.

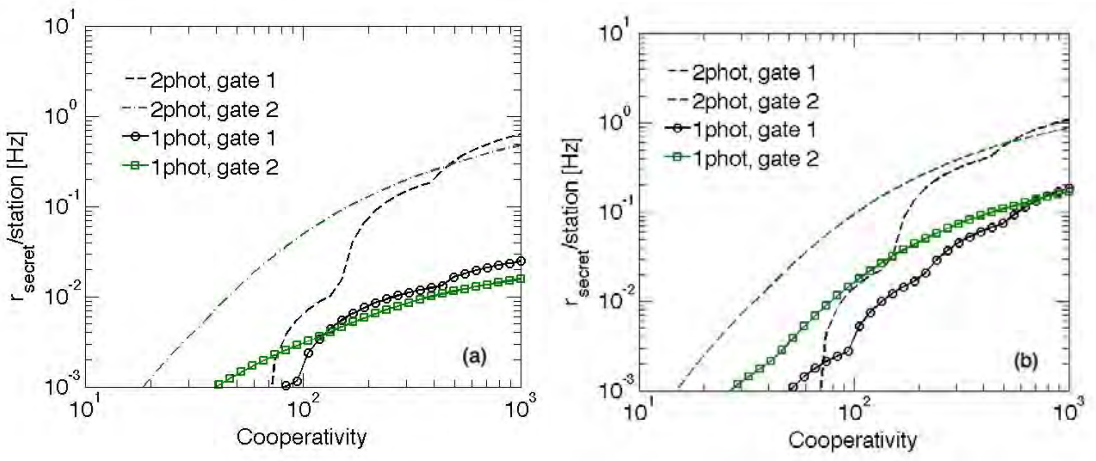

FIGURE 8.13: Optimal secret key rate pr. repeater station (r_{secret}) plotted against the cooperativity for various combinations of entanglement generation schemes and CNOT gates assuming a distribution distance of 1000 km. (a) is for 2 qubits pr repeater station while (b) is for 4 qubits pr repeater station.

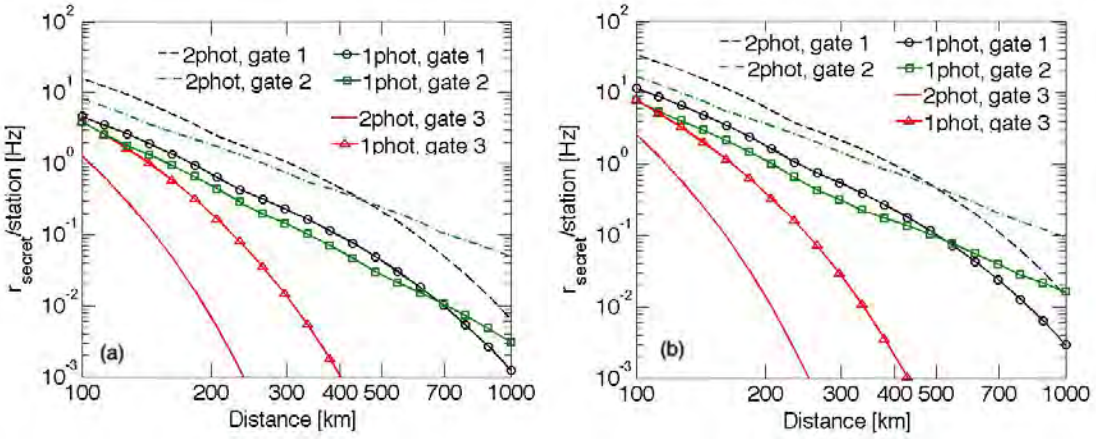

FIGURE 8.12: Optimal secret key rate pr. repeater station (r_{secret}) plotted against the distribution distance (Distance) for various combinations of entanglement generation schemes and CNOT gates assuming a cooperativity of 100. (a) is for 2 qubits pr repeater station while (b) is for 4 qubits pr repeater station.

It is clear from Fig 8.12, which assumed a cooperativity of 100, that a repeater based on gate 3 is simply not able to distribute entanglement over large distances for realisitc cooperativities. Repeaters based on gate 3 also does not show on Fig. 8.13, which assumes a distance of 1000 km since their distribution rate is to low. In general, a repeater based on the two-photon scheme and gate 1 achieves the highest distribution rate for a broad range of cooperativities and distances. This reflects the fact that the secret key rate favours distribution of high-fidelity pairs since these gives the highest secret fraction (see Fig. 8.10). It is also apparent from Fig 8.13 that while repeaters based on gate 2 need cooperativities above 100 for a distance of 1000 km, repeaters

based on gate 1 are able to function with much lower cooperativities around $30 - 40$. This is because the gate fidelity of gate 1 is unity, which allows for a higher number of swap levels.

It is important to stress that the rate plotted in Figs. 8.12-8.13, is the secret key rate pr repeater station. The true distribution rate can thus be obtained by multiplying with the number of repeater stations. The number of repeater stations should, however, not be lower than what is dictated by the optimal number of swap levels. For a repeater based on the two photon scheme and gate 2 we find a distribution rate of 20 Hz over 1000 km for 32 repeater stations and a cooperativity of 1000. For a more modest cooperativity of 100 the optimal combination is the two-photon scheme combined with gate 1, which achives a rate of 1.5 Hz over 1000 km using 32 repeater stations. Here we have assumed 2 qubits pr. repeater station.

8.7 Conclusion and discussion

In conclusion, we have performed a detailed analysis of quantum repeaters based on single emitters in optical cavitites. We have shown that the gate schemes described in Ref. [106] and Chap. 6 can enable fast secret key rates over large distances by improving the gate performance from the detrimental $1/\sqrt{C}$ scaling, which naively would be the case for cavity based quantum gates. Especially, the heralded gate described in Chap. 6 could fascilitate high secret key rates even for limited cooperativities ($<$ 100). Furthermore, we have performed a numerical optimization of the general repeater architecture for cooperativites $\in [10; 1000]$ and distances $\in [100; 1000]$ km allowing for initial purification and both parallel and sequentially operated repeaters. We optimized the secret key rate pr. repeater station to find the optimal number of swap levels and considered scenarios with both 2 and 4 qubits pr. repeater station. The secret key rate was calculated assuming a cryptograhy scheme based on the six state protocol decribed in Ref. [14]. Finally, we have compared the performance of entanglement generation schemes based on single photon detection and two photon detection. We found that the two photon scheme in general leads to higher secret key rates for realistic detection efficiencies. It should be noted that we have assumed fiber transmission losses for telecom wavelengths, which may require wavelength conversion techniques [140]. Any inefficeint conversion could be incorporated in the detection efficiency η_d.

For a cooperativity of 1000 and 2 qubits pr. repeater station, we found that a secret key rate of 20 Hz fo a distance of 1000 km using 32 repeater station. This was achieved for a repeater based on the two-photon detection scheme and the heralded gate described in Chap. 7. This should be compared to the rate obtainable with repeaters based

on atomic ensembles. In Ref. [17] an efficent repeater based on atomic ensembles are described, which achieves one of the highest distribution rates for repeaters based on atomic ensembles [18]. The fidelity of the distributed pair and the distribution rate are derived in Ref. [17] for a repeater with four swap levels corresponding to 16 repeater stations. Based on this we find that the secret key rate of this repeater at a distance of 1000 km assuming SPD efficiencies of 90% and otherwise similar assumptions about fiber losses etc., is ~ 0.03 Hz. We have assumed an optimistic, basic repetition rate of 100 MHz and memory efficiencies of 90%. This shows that repeaters based on single emitters in cavitites are very promising candidates for realizing efficent quantum repeaters with rates exceeding those obtainable with atomic ensembles. Note that this conclusion was also reached in Ref. [128], which considered quantum repeaters based on trapped ions. In Ref. [128], the entanglement swapping was, however assumed to work perfectly using techniques demonstrated with ion traps. Our work shows that the conclusions holds even for non-ideal, cavity based quantum gates.

Chapter 9

Summary and outlook

Quantum technology has the potential to revolutionize many aspects of todays high-technological society. It remains, however, a great challenge to find suitable quantum systems, which can be the basic building blocks of this new technology. Such quantum systems need to have an excellent level of control and to be robust against noise from the surrounding enviroment. Furthermore, they need to be scalable in order for quantum technology to be truely interesting.

In this thesis, I have presented the joint work of me and my collaborators on some of the problems in the development of quantum technology. Our hope is that our contributions to the field, described in this thesis, can help bringing quantum technology closer to reality and enable a better undstanding of the requirements for efficient quantum information processing. One of our main focus points has been quantum repeaters for long distance entanglement distribution. We have investigated both the basic constituents and the general architecture of quantum repeaters in order to describe the main limitations and possible ways of overcoming them. We have considered two types of generic repeaters, namely a hybrid repeater with fast local processing and a repeater based on single emitters in optical cavitites. Furthermore, we have considered the constituents of repeaters based on atomic ensembles.

The hybrid repeater tries to combine the best of two worlds using single photon detection to generate entanglement and storing the information in continous variables. Continous variables have shown promosing potential in quantum information processing [141, 142] and the distribution of entanglement in this form is thus of interest. Recently, there have been proposals for error-correcting codes implemented with cat states [143], which could be combined with, e.g. the swapping procedure described in our work, to facilitate fast entanglement distribution. In our work, we show that growing cat states locally enhances the distribution rate significantly but the growth procedure we describe is still

time consuming. Efficient and fast methods of growing cat states would be a powerful resource for quantum technology based on continous variabels. To this end, systems based on single atoms in nanocavities, similar to the system we considered for implementing heralded quantum gates, could be considered. The strong coupling of light obtainable with nanocavities, combined with efficient atomic detection, is an attractive system to consider. The possibility of heralded gates with error-detection could perhaps also enable the generation of high quality cat states by, e.g. employing error correction.

In our work on room temperature atomic memories and single photon sources, we have introduced the concept of motional averaging. We have shown how this can be applied to a specific system of microcells with Cs-atoms and the first proof-of-principle experiments towards realizing our scheme has already been conducted in the group of Eugene Polzik at the Niels Bohr Institute. The scalable nature of our scheme makes it interesting for applications such as DLCZ-like repeaters with spatial multiplexing [18] and photonic quantum simulators [125]. Repeaters based on atomic ensembles are limited by imperfections such as inefficient write and readout efficiencies but the relatively simple setups may lead to the first realizations of actual quantum repeaters.

Finally, we have considered quantum repeaters based on single emitters in optical cavities. Such repeaters have previously been considered and expected to obtain higher distribution rates than repeaters based on atomic ensembles [128]. While various entanglement generation schemes have been proposed, it has been unclear which scheme obtained the highest distribution rate under given experimental circumstances. We have presented a scheme for optimizing the secret key rate pr. repeater station, which finds the optimal repeater architecture for a given cooperativity of the optical cavitites, detection efficiency, distribution distance etc. Furthermore, we have implemented realistic gates for obtaining entanglement swapping and intial purification. Our work can thus be a guide for how to construct the optimal quantum repeater given a certain quality of the experimental constituents. Furthermore, our work shows that the heralded gates, that we have proposed, can enable fast entanglement distribution over large distances even for limited cooperativities.

Our work on heralded quantum gates could also be an important contribution to the field of fault-tolerant quantum computing. The fault tolerant threshold for such detectable errors may be much higher than for undetectable errors, which require more advanced error correcting procedures [144–146]. The gates, that we propose, show that it is possible to detect errors using highly efficient atomic detection but once an error is detected the qubit register has to be initialized. It would be interesting if our heralded gates could be combined with error correction such that the errors were not only detected but also corrected. Finally, the concept of heralded gate operations could be applied to

other systems in order to fascilitate high-fidelity gates even with non-ideal experimental systems.

A final focus point of our work, presented in this thesis, has been on enhancing the stability of atomic clocks. By developing an adaptive measurement strategy, we have shown that it is possible to obtain near-Heisenberg limited atomic clocks even under the assumption of a realistic source of decoherence. Our work thus establish that entanglement can be a useful resource for metrology in order to push beyond the standard quantum limit. There are, however, a number of more practical limitations to the stability of current experimental clocks for which our scheme would be relevant. These need to be adressed before one would benefit from our adaptive scheme. Currently many optical clocks are limited by the Dick noise, which needs to be surpressed below the quantum noise of the atoms before it makes sense to consider our scheme. Our work on operating atomic clocks based on several atomic ensembles could, however, be applied in e.g present ion clocks in order to increase the stability without having to increase the number of ions in the clocks.

Appendix A

Hybrid Repeater

In this appendix, we give the details of the growth procedure and the connection step of the altered repeater protocol described in Chap. 3. Furthermore, we present the details of the target state used to calculate the fidelity of the swapped state. Finally, we present the details of our numerical fidelity fits used in the optimization of the repeater.

A.1 Growth of cat states

In this section, we describe how the growth procedure transforms the Wigner function of the input states. In general, we write the Wigner function as

$$W_m(x,p) = \sum_{i=0}^{2^{m+1}} \sum_{j=0}^{2^{m+1}} w_{ij} x^i p^j e^{-(x^2+p^2)}. \tag{A.1}$$

For a one photon state we have $m = 0$ and the matrix containing w_{ij} is

$$\mathbf{w} = \begin{pmatrix} -\frac{1}{\pi} & 0 & \frac{2}{\pi} \\ 0 & 0 & 0 \\ \frac{2}{\pi} & 0 & 0 \end{pmatrix}. \tag{A.2}$$

The effect of the growth procedure in this representation is to change the size and elements of the matrix $\mathbf{w}$ along with the upper limit of the summations. The combination of two states of the form in Eq. (A.1) with variables x, p and x', p' on a balanced beam splitter is described by the transformations

$$\begin{aligned} x &\to \frac{1}{\sqrt{2}}\left(x + x'\right), \qquad p \to \frac{1}{\sqrt{2}}\left(p + p'\right) \\ x' &\to \frac{1}{\sqrt{2}}\left(x - x'\right), \qquad p' \to \frac{1}{\sqrt{2}}\left(p - p'\right). \end{aligned} \tag{A.3}$$

Thus, the state before the $\hat{X}$ measurement is

$$W'_{m+1}(x,p,x',p') = W_m\left(\frac{x+x'}{\sqrt{2}},\frac{p+p'}{\sqrt{2}}\right)\times W_m\left(\frac{x-x'}{\sqrt{2}},\frac{p-p'}{\sqrt{2}}\right). \tag{A.4}$$

Using the identity $(a+b)^i = \sum_s^i \binom{i}{s} a^s b^{i-s}$ and collecting powers of x and p, we can write W'_{m+1} in the form:

$$\begin{aligned} W'_{m+1}(x,p,x',p') = &\sum_{\{i,i'\}=0}^{2^{m+1}}\sum_{\{j,j'\}=0}^{2^{m+1}} \\ &\sum_{k=0}^{i+i'}\sum_{s'=s_{\min}}^{s_{\max}}\binom{i}{k-s'}\binom{i'}{s'}(-1)^{i'-s'}x'^{i+i'-k}x^k \\ &\sum_{l=0}^{j+j'}\sum_{t'=t_{\min}}^{t_{\max}}\binom{j}{l-t'}\binom{j'}{t'}(-1)^{j'-t'}p'^{j+j'-l}p^l \\ &e^{-(x^2+x'^2+p^2+p'^2)}w_{ij}w_{i'j'}, \end{aligned} \tag{A.5}$$

where

$$\begin{aligned} s_{\min} &= \max(0,k-i), \quad s_{\max} = \min(i',k), \\ t_{\min} &= \max(0,l-j), \quad t_{\max} = \min(j',l). \end{aligned} \tag{A.6}$$

The unnormalized average output after measuring $x' \in [-\Delta,\Delta]$ is found by integrating over momentum and position

$$\int_{-\infty}^{\infty}\mathrm{d}p'\int_{-\Delta}^{\Delta}\mathrm{d}x' W'_{m+1}(x,p,x',p'). \tag{A.7}$$

After carrying out the integrals, we can write the unnormalized state after the growth procedure as

$$\tilde{W}_{m+1}(x,p) = \sum_{k=0}^{2^{m+2}}\sum_{l=0}^{2^{m+2}}\tilde{w}_{kl}x^k p^l e^{-(x^2+p^2)}, \tag{A.8}$$

with

$$\begin{aligned} \tilde{w}_{kl} = &\sum_{\{i,i'\}=0}^{2^{m+1}}\sum_{\{j,j'\}=0}^{2^{m+1}} 2^{-(i+i'+j+j')/2}(-1)^{i+i'+j+j'-k-l} \\ &w_{ij}w_{i'j'}\kappa_k^{ii'}(\Delta)\kappa_l^{jj'}(\infty), \end{aligned} \tag{A.9}$$

and

$$\kappa_k^{ii'}(t) = \begin{cases} 0 & \text{if } r < 0, \\ \sum \binom{i}{k-s'} \binom{i'}{s'} \int_{-t}^{t} \mathrm{d}x e^{-x^2} x^r & \text{if } 0 < r, \end{cases} \tag{A.10}$$

where $r = i + i' - k$ and $\sum = \sum_{s'=s_{\min}}^{s'=s_{\max}}$. We have thus found a simple description for the Wigner function after a step of the growth procedure as function of the input Wigner function. To find the state after m steps, we start with the matrix in Eq. (A.2) and iterate (A.9) m times.

A.2 Connection of cat states

Here we describe the connection step in terms of Wigner functions. The state before the two asymmetric beam splitters with reflectivity r in the connection step is the product of the Wigner functions generated in step one of the repeater and two vacuum states

$$W_m(x,p)W_m(y,q)W_{vac}(x',p')W_{vac}(y',q'). \tag{A.11}$$

Here $W_m(-,-)$ has the form (A.1) and $W_{vac}(x,p) = \frac{1}{\pi} e^{-\frac{1}{2}(x^2+p^2)}$.

The modes described by (x, x', p, p') are on the left (location A) and the modes (y, y', q, q') on the right (location B), (see Fig. 3.2(ii)). Before the central station it is only necessary to focus on the modes described by (x, x', p, p'). Parameterizing $\sin(\theta_r) = \sqrt{r}$, the action of the first beam splitter is

$$\begin{aligned} x &\to \cos(\theta_r)x + \sin(\theta_r)x', \\ x' &\to \cos(\theta_r)x' - \sin(\theta_r)x, \end{aligned} \tag{A.12}$$

and the corresponding transformations on the momentum variables. This results in the state

$$\begin{aligned} &W_{a1}(x,x',p,p') = \\ &W_m(\cos(\theta_r)x + \sin(\theta_r)x', \cos(\theta_r)p + \sin(\theta_r)p') \times \\ &W_{vac}(\cos(\theta_r)x' - \sin(\theta_r)x, \cos(\theta_r)p' - \sin(\theta_r)p). \end{aligned} \tag{A.13}$$

An additional beam splitter describing losses in the optical fibers mixes x' and p' with the vacuum mode described by x'' and p''. We parameterize the loss by $\sqrt{\eta} = \cos(\theta_l)$.

$$\begin{aligned} x' &\to \cos(\theta_l)x' + \sin(\theta_l)x'', \\ x'' &\to \cos(\theta_l)x'' - \sin(\theta_l)x', \end{aligned} \tag{A.14}$$

and the corresponding transformations on the momentum variables. The number of photons, that are lost, is not known and consequently, we trace over x'' and y''. This produces the unnormalized state:

$$\begin{aligned} W_{a2}(x,x',p,p') = &\int_{-\infty}^{\infty} \mathrm{d}x'' \int_{-\infty}^{\infty} \mathrm{d}y'' \\ &W_{a1}(x, \cos(\theta_l)x' + \sin(\theta_l)x'', p, \cos(\theta_l)p' + \sin(\theta_l)p'') \times \\ &W_{vac}(\cos(\theta_l)x'' - \sin(\theta_l)x', \cos(\theta_l)p'' - \sin(\theta_l)p'). \end{aligned} \tag{A.15}$$

The modes described by (y, y', q, q') is brought to the central beam splitter in the same manner producing the state $W_{b2}(y, y', q, q')$. The action of the central beam splitter is

$$x' \to \frac{x'+y'}{\sqrt{2}}, \quad y' \to \frac{x'-y'}{\sqrt{2}}, \tag{A.16}$$

and the corresponding transformations on the momentum variables. Assuming that one output mode only contains vacuum and the other contains anything but vacuum, the subsequent state is projected onto

$$W_{vac}(y', q')(1 - W_{vac}(x', p')) \tag{A.17}$$

Consequently, the state in the quantum memories after the connection is

$$\begin{aligned} W_{ab}(x,y,p,q) = \frac{1}{N} &\int_{-\infty}^{\infty}\mathrm{d}x' \int_{-\infty}^{\infty}\mathrm{d}y' \int_{-\infty}^{\infty}\mathrm{d}p' \int_{-\infty}^{\infty}\mathrm{d}q' \\ &W_{vac}(y', q')(1 - W_{vac}(x', p')) \times \\ &W_{a2}(x, (x'+y')/\sqrt{2}, p, (p'+q')/\sqrt{2}) \times \\ &W_{b2}(y, (x'-y')/\sqrt{2}, q, (q'-p')/\sqrt{2}), \end{aligned} \tag{A.18}$$

where N is the normalization constant. After the integration, the resulting Wigner function can be written in the form

$$\begin{aligned} &W_{ab}(x,y,q,p) = \\ &\sum_{\{s,t,k,l\}=0}^{2^{m+1}} w_{stkl} x^k p^l y^s q^t e^{-x^2-p^2-y^2-q^2}. \end{aligned} \tag{A.19}$$

This can be seen by writing W_{a2} and W_{b2} in the form of (A.8) and evaluating the integrals using the identity $(a+b)^i = \sum_{s=0}^{i} \binom{i}{s} a^i b^{i-s}$ as in App. A.1. The expression for w_{stkl} is rather lengthy and we shall not reproduce it here. It can, however, be implemented numerically and thus provide an efficient description of the connection step.

A.3 Target state of swapping

Here we outline the calculations leading to Eq. (3.19) and give the expressions for the constants that appear in that equation.

We consider the swapping of two states of the type $|\Psi_m\rangle$ given in (3.14). The state before the swap is thus

$$\begin{aligned}|\Psi_m\rangle_{ab}|\Psi_m\rangle_{a'b'} \propto &(c_1|0_m\rangle|1_m\rangle + e_1|1_m\rangle|0_m\rangle)_{ab}\times \\ &(c_2|0_m\rangle|1_m\rangle + e_2|1_m\rangle|0_m\rangle)_{a'b'},\end{aligned} \tag{A.20}$$

where $c_1 = c_2 = e_1 = e_2 = 1$. For generality, we keep the coefficients named c_1, c_2 and e_1, e_2 since it will be important to consider $e_{1,2}, c_{1,2} \neq 1$ in order to describe later swapping stages. We imagine combining modes b and a' on a balanced beamsplitter. Using the approximations (3.16), (3.17), we have the following transformations up to constants of $1/N^{\pm}_{\mu_m}$ and $1/N^{\pm}_{\tilde{\mu}_m}$ on the right-hand side

$$\begin{aligned}|1_m\rangle_b|1_m\rangle_{a'} \rightarrow &(|\sqrt{2}\mu_m\rangle_b + |\text{-}\sqrt{2}\mu_m\rangle_b)|0\rangle_{a'} \\ &+ (|\sqrt{2}\mu_m\rangle_{a'} + |\text{-}\sqrt{2}\mu_m\rangle_{a'})|0\rangle_b \end{aligned} \tag{A.21}$$

$$\begin{aligned}|0_m\rangle_b|0_m\rangle_{a'} \rightarrow &(|\sqrt{2}\tilde{\mu}_m\rangle_b + |\text{-}\sqrt{2}\tilde{\mu}_m\rangle_b)|0\rangle_{a'} \\ &- (|\sqrt{2}\tilde{\mu}_m\rangle_{a'} + |\text{-}\sqrt{2}\tilde{\mu}_m\rangle_{a'})|0\rangle_b \end{aligned} \tag{A.22}$$

$$\begin{aligned}|1_m\rangle_b|0_m\rangle_{a'} \rightarrow &|(\tilde{\mu}_m + \mu_m)/\sqrt{2}\rangle_b|(\text{-}\tilde{\mu}_m + \mu_m)/\sqrt{2}\rangle_{a'} \\ &- |(\text{-}\tilde{\mu}_m + \mu_m)/\sqrt{2}\rangle_b|(\tilde{\mu}_m + \mu_m)/\sqrt{2}\rangle_{a'} \\ &+ |(\tilde{\mu}_m \text{-} \mu_m)/\sqrt{2}\rangle_b|(\text{-}\tilde{\mu}_m \text{-} \mu_m)/\sqrt{2}\rangle_{a'} \\ &- |(\text{-}\tilde{\mu}_m \text{-} \mu_m)/\sqrt{2}\rangle_b|(\text{-}\tilde{\mu}_m \text{-} \mu_m)/\sqrt{2}\rangle_{a'} \end{aligned} \tag{A.23}$$

$$\begin{aligned}|0_m\rangle_b|1_m\rangle_{a'} \rightarrow &|(\tilde{\mu}_m + \mu_m)/\sqrt{2}\rangle_b|(\text{-}\tilde{\mu}_m + \mu_m)/\sqrt{2}\rangle_{a'} \\ &+ |(\text{-}\tilde{\mu}_m + \mu_m)/\sqrt{2}\rangle_b|(\tilde{\mu}_m + \mu_m)/\sqrt{2}\rangle_{a'} \\ &- |(\tilde{\mu}_m \text{-} \mu_m)/\sqrt{2}\rangle_b|(\text{-}\tilde{\mu}_m \text{-} \mu_m)/\sqrt{2}\rangle_{a'} \\ &- |(\text{-}\tilde{\mu}_m \text{-} \mu_m)/\sqrt{2}\rangle_b|(\text{-}\tilde{\mu}_m \text{-} \mu_m)/\sqrt{2}\rangle_{a'}. \end{aligned} \tag{A.24}$$

The squeezing operators $\hat{S}(2)_b\hat{S}(2)_{a'}$ should multiply the expressions on the right-hand side but we omit these for simplicity. Going to the wave function picture, assuming that $\cos(\sqrt{2}\mu_m p') \approx \cos(\sqrt{2}\tilde{\mu}_m p')$, $\sin(\sqrt{2}\mu_m p') \approx \sin(\sqrt{2}\tilde{\mu}_m p')$, and that $(1 + e^{-2\mu_m^2}) \approx$

$(1-e^{-2\tilde{\mu}_m^2})$, we get the transformations

$$|1_m\rangle_b|1_m\rangle_{a'} \to -2\cos(\sqrt{2}\mu_m p')e^{-p'^2-x^2} \tag{A.25}$$

$$|0_m\rangle_b|0_m\rangle_{a'} \to 2\cos(\sqrt{2}\mu_m p')e^{-p'^2-x^2} \tag{A.26}$$

$$|1_m\rangle_b|0_m\rangle_{a'} \to -i(e^{-\sqrt{2}x(\mu_m-\tilde{\mu}_m)}+e^{\sqrt{2}x(\mu_m-\tilde{\mu}_m)})\times e^{-\frac{1}{2}(\mu_m-\tilde{\mu}_m)^2}\sin(\sqrt{2}\mu_m p')e^{-p'^2-x^2} \tag{A.27}$$

$$|0_m\rangle_b|1_m\rangle_{a'} \to i(e^{-\sqrt{2}x(\mu_m-\tilde{\mu}_m)}+e^{\sqrt{2}x(\mu_m-\tilde{\mu}_m)})\times e^{-\frac{1}{2}(\mu_m-\tilde{\mu}_m)^2}\sin(\sqrt{2}\mu_m p')e^{-p'^2-x^2}. \tag{A.28}$$

Here p' is the momentum variable of mode a' and x is the position variable of mode b. We now perform the $\hat{X}$ measurement on mode b and the $\hat{P}$ measurement on mode a' and assume that we get outcomes p'_0 and x_0. The unnormalized state after the swapping is

$$\begin{aligned} &e_1c_2A'|0_m\rangle_a|0_m\rangle_{b'} - e_2c_1A'|1_m\rangle_a|1_m\rangle_{b'} \\ &+ c_1c_2C|1_m\rangle_a|0_m\rangle_{b'} + e_1e_2C^*|0_m\rangle_a|1_m\rangle_{b'}, \end{aligned} \tag{A.29}$$

with

$$A' = 2\cos(\sqrt{2}\mu_m p'_0) \tag{A.30}$$

$$C' = i(e^{-\sqrt{2}x_0(\mu_m-\tilde{\mu}_m)}+e^{\sqrt{2}x_0(\mu_m-\tilde{\mu}_m)})\times e^{-\frac{1}{2}(\mu_m-\tilde{\mu}_m)^2}\sin(\sqrt{2}\mu_m p'_0). \tag{A.31}$$

Whenever $e_i = c_i^*$, this state contains one ebit of entanglement and can be written as:

$$\begin{aligned} &A|0_m\rangle_a|0_m\rangle_{b'} - A^*|1_m\rangle_a|1_m\rangle_{b'} + \\ &C|1_m\rangle_a|0_m\rangle_{b'} + C^*|0_m\rangle_a|1_m\rangle_{b'}, \end{aligned} \tag{A.32}$$

with

$$A = c_1^*c_2 2\cos(\sqrt{2}\mu_m p'_0) \tag{A.33}$$

$$C = c_1c_2 i(e^{-\sqrt{2}x_0(\mu_m-\tilde{\mu}_m)}+e^{\sqrt{2}x_0(\mu_m-\tilde{\mu}_m)})\times e^{-\frac{1}{2}(\mu_m-\tilde{\mu}_m)^2}\sin(\sqrt{2}\mu_m p'_0). \tag{A.34}$$

Swapping two states of the form in Eq.(A.32) with coefficients A_1, C_1 and A_2, C_2 respectively, it can be shown within the same approximations leading to Eq. (A.32) that the

swapped state will also be of the form:

$$\begin{aligned} &A|0_m\rangle|0_m\rangle - A^*|1_m\rangle|1_m\rangle + \\ &C|1_m\rangle|0_m\rangle + C^*|0_m\rangle|1_m\rangle, \end{aligned} \tag{A.35}$$

with coefficients

$$\begin{aligned} A &= \left[\mathbb{A}\cos(\sqrt{2}\mu_m p_0') + \mathbb{B}\sin(\sqrt{2}\mu_m p_0')\right] \\ C &= \left[\mathbb{C}\cos(\sqrt{2}\mu_m p_0') + \mathbb{D}\sin(\sqrt{2}\mu_m p_0')\right] \end{aligned} \tag{A.36}$$

with p_0' again being the outcome of the $\hat{P}$ measurement. The coefficients $\mathbb{A}, \mathbb{B}, \mathbb{C}$ and $\mathbb{D}$ depend on the measurement outcome of the $\hat{X}$ measurement in the relevant swap and in the previous swap levels as well as the $\hat{P}$ measurement in the previous swap levels (see Eq (A.33)). In the simulation of the repeater, we replace $\sqrt{2}\mu_m p_0' \to \theta_p$ and optimize the fidelity between the swapped state and the target state with respect to θ_p. Note that regardless of this, we always calculate the fidelity with a pure state containing one ebit of entanglement.

A.4 Parameters of fidelity fits

In this section, we list the parameters of the fidelity fits shown in Tab. 3.1 of the article. The matrices below contain the constants $\tilde{a}_{n,m}$-$\tilde{h}_{n,m}$. The first entry in a matrix is for

$n = 0, m = 1$ and so fourth.

$$\mathbf{a} = \begin{pmatrix} 0 & 0 & 0 \\ 0 & 0 & 0 \\ -2.19 & -5.39 & -6.81 \\ -9.75 & -14.6 & -20.1 \\ -15.6 & -26.1 & -39.9 \end{pmatrix} \qquad \mathbf{e} = \begin{pmatrix} - & - & - \\ -466 & -8.90 \cdot 10^{-7} & 0.993 \\ 0.969 & -2.71 \cdot 10^{-6} & 0.979 \\ 1.32 & -1.93 \cdot 10^{-5} & 0.954 \\ 0.824 & -1.74 \cdot 10^{-4} & 0.905 \end{pmatrix}$$

$$\mathbf{b} = \begin{pmatrix} 0.90 & 0.91 & 0.95 \\ 1.40 & 1.53 & 1.65 \\ 2.25 & 3.08 & 3.40 \\ 3.69 & 4.92 & 5.83 \\ 4.26 & 6.46 & 8.54 \end{pmatrix} \qquad \mathbf{f} = \begin{pmatrix} - & - & - \\ 0.351 & 5.39 & 0.411 \cdot 10^{-3} \\ 0.324 & 5.32 & 0.792 \cdot 10^{-3} \\ -0.592 & 4.58 & 3.81 \cdot 10^{-3} \\ -0.411 & 3.60 & 5.30 \cdot 10^{-3} \end{pmatrix}$$

$$\mathbf{c} = \begin{pmatrix} 0.0063 & 1.0 & 4.7 \\ 0.223 & 1.50 & 5.08 \\ 0.460 & 2.59 & 6.26 \\ 1.56 & 3.73 & 8.77 \\ 2.02 & 6.68 & 16.1 \end{pmatrix} \cdot 10^{-3} \qquad \mathbf{g} = \begin{pmatrix} - & - & - \\ 468 & 0.985 & - \\ -0.969 & 0.951 & - \\ -0.636 & 0.893 & - \\ -0.260 & 0.799 & - \end{pmatrix}$$

$$\mathbf{d} = \begin{pmatrix} 15.0 & 24.2 & 92.0 \\ 13.1 & 23.1 & 93.8 \\ 12.3 & 21.6 & 94.5 \\ 10.2 & 21.0 & 92.6 \\ 9.47 & 19.0 & 83.8 \end{pmatrix} \qquad \mathbf{h} = \begin{pmatrix} - & - & - \\ 0.350 & -2.80 \cdot 10^{-3} & - \\ 0.324 & 1.98 \cdot 10^{-3} & - \\ -2.45 & 3.78 \cdot 10^{-3} & - \\ -4.24 & 7.20 \cdot 10^{-3} & - \end{pmatrix}$$

Matrices $\mathbf{e} - \mathbf{h}$ show that the state's swap performance increases for large values of m and matrices $\mathbf{a} - \mathbf{d}$ show that the fidelity drops as a function of r and $\vec{\Delta}$. The fact that $\tilde{a}_{n,m} \leq 0$ reflects that the fits are made for $P_{connect} \ll 1$.

The numerical vectors of the constants $\tilde{i}_n$-$\tilde{k}_n$ and $\tilde{l}_m$ are

$$\begin{aligned} \mathbf{i} &= \begin{pmatrix} 1 & 0.938 & 0.811 & 0.618 & 0.413 \end{pmatrix} \\ \mathbf{j} &= \begin{pmatrix} 0 & -0.460 & -1.61 & -3.14 & -3.64 \end{pmatrix} \cdot 10^{-3} \\ \mathbf{k} &= \begin{pmatrix} 0 & 0.0323 & 0.104 & 0.207 & 0.275 \end{pmatrix} \\ \mathbf{l} &= \begin{pmatrix} 0.0112 & 0.0222 & 0.00542 \end{pmatrix}. \end{aligned}$$

Vectors $\mathbf{i} - \mathbf{k}$ show that the output fidelity drops as a function of n and vector $\mathbf{l}$ shows that as m increases, the states gets more robust to the swapping procedure.

Appendix B

Near Heisenberg limited atomic clocks

B.1 Limit of the Ramsey time

In this appendix, we describe the upper limit of the Ramsey time's dependence on the number of steps (l) in our numerical simulations of the atomic clocks. As described in the Sec. 4.4.3, this upper limit is due to the finite probability of a phase jump occuring that either results in a fringe hop or is large enough to spoil the measurement strategy.

For a simulation running for a time $\tau = lT$, we have l samples of the accumulated phase of the LO during the Ramsey time T. Assuming that these samples have an independent Gaussian probability distribution with zero mean [1], the probability of all of these phases to be less than a critical value (a) is

$$P(\leq a) = \left(1 - \text{erfc}\left(\frac{a}{\sqrt{2}\sigma}\right)\right)^l \tag{B.1}$$

where the variance of the distribution σ depends on γT. For large l, and as a function of σ, this probability will drop abruptly from ~ 1 to ~ 0 around a certain $\sigma = \sigma_{max}$. Defining σ_{max} to be the position where $P(\leq a) = 1/2$, we find that

$$1/2 = \left(1 - \text{erfc}\left(\frac{a}{\sqrt{2}\sigma_{max}}\right)\right)^l. \tag{B.2}$$

[1] This will be the case for white noise and is approximately true for $1/f$ noise when the LO is locked to the atoms

Solving this equation gives

$$\sigma_{max} \approx \frac{a}{\sqrt{\ln(2/\pi) + 2\ln(l) - 2\ln(\ln 2) - \ln(\ln(2/\pi) + 2\ln(l) - 2\ln(\ln 2))}}, \tag{B.3}$$

where we have expanded to first order in $z = (1 - 2^{-1/l}) \sim \ln(2)/l$. It is seen that the breakdown (σ_{max}) has a weak (logarithmic) dependence on l. Solving equation (B.2) with the lhs. being equal to 0.95 and 0.05 we find that $P(\leq a)$ drops from 0.95 to 0.05 within a window of $\sim 2\sigma_{max}/\ln(l)$. Hence for large l, the errors will appear very abruptly in the simulations.

Appendix C

Efficient atomic clocks

In this appendix, we describe the intermediate phase corrections, which allow our protocol of locking the LO to several ensembles, described in Chap. 5, to be effective for small N. Furthermore, we describe the final phase correction, which we apply in order to reduce the required time of our simulations. Finally, we discuss the upper limits of the Ramsey time for white and $1/f$ noise.

C.1 Phase corrections

The Ramsey sequence, and the subsequent estimate of the drifted phase of the LO relative to an ensemble of atoms, is described in the Sec. 5.2. Eqs. (5.1) - (5.3) describes the frequency offset of the LO ($\delta\omega(t)$) between time $t_{k-1} = (k-1)T$ and $t_k = kT$ when the LO is locked to two ensembles. We will now generalize this formalism to the case where the LO is locked to m ensembles. Assuming that the j'th ensemble is operated with Ramsey time $T_j = n^{j-1}T_1$, [1]the frequency offset of the LO between time $t_{k-1} = (k-1)T_1$ and $t_k = kT_1$ is

$$\delta\omega(t) = \delta\omega_0(t) + \Delta\omega_1(t_{s_1}) + \Delta\omega_2(t_{s_2 n}) + \ldots + \Delta\omega_m(t_{s_m n^{m-1}}), \tag{C.1}$$

where $\delta\omega_0(t_k)$ is the frequency fluctuations of the unlocked LO and $\Delta\omega_m(t_{s_j n^{j-1}})$ is the sum of the frequency corrections applied up to time $t_{s_j n^{j-1}}$ from the j'th ensemble[2]. Note that the index $s_j n^{j-1}$ should be read as s_j times n^{j-1}, describing the exponential increase in the Ramsey time each time an additional ensemble is used. The iterative

[1] n is an integer describing how many times the Ramsey time can be increased for each added ensemble
[2] s_j is found by rounding $(k-1)/n^{j-1}$ down to the nearest integer

equation for $\Delta\omega_j(t_{s_j n^{j-1}})$ is

$$\Delta\omega_j(t_{s_j n^{j-1}}) = \Delta\omega_j(t_{(s_j-1)n^{j-1}}) - \alpha\delta\phi^{e_j}(t_{s_j n^{j-1}})/T_j, \tag{C.2}$$

where $\delta\phi^{e_j}(t_{s_j n^{j-1}})$ is the estimated phase from the j'th ensemble at time $t_{s_j n^{j-1}}$ and α sets the strength of the feedback loop[3]. α determines how long time the clock needs to run before the LO is effectively locked by the feedbacks[4]. In Sec. 5.2, we assumed that $T_2 \gg T_1$ such that the feedback of the first ensemble had effectively locked the LO before the measurement of the second ensemble. In the general setup of locking the LO to m ensembles, this corresponds to assuming that $n \gg 1$. We will now show how we can apply a phase correction in the measurement of the j'th ensemble such that we can relax this assumption. The phase correction will compensate for the fact that the information from the last measurements on the first $(j-1)$ ensembles has not been fully exploited by the feedback loops before the measurement on the j'th ensemble. Note that we assume that the phase correction is only applied to the measurement and not to the LO.

The phase of the LO relative to the j'th ensemble, just before the measurement at time $t_{s_j n^{j-1}}$, is

$$\Phi^{j}_{s_j n^{j-1}} = \sum_{s=1}^{n^{j-1}} \phi_{s+(s_j-1)n^{j-1}} - \Phi^{\text{correct } j}_{s_j n^{j-1}}, \tag{C.3}$$

where $\phi_{s+(s_j-1)n^{j-1}} = \int_0^{T_1} \delta\omega(t_{s+(s_j-1)n^{j-1}} - t')\mathrm{d}t'$ and $\Phi^{\text{correct } j}_{s_j n^{j-1}}$ is the phase correction applied in the measurement of the j'th ensemble at time $t_{s_j n^{j-1}}$. Using Eq. (C.1)-(C.2) we can write

$$\begin{aligned}\Phi^{j}_{s_j n^{j-1}} \;=\; & \sum_{s=1}^{n^{j-1}} (\delta\phi_{s+(s_j-1)n^{j-1}} - \alpha \sum_{s'=1}^{s-1} \phi^{e_1}_{s'+(s_j-1)n^{j-1}}) - \alpha \sum_{s=2}^{n^{j-2}} \sum_{s'=1}^{s-1} \delta\phi^{e_2}_{s'n+(s_j-1)n^{j-1}} - \dots \\ & -\alpha \sum_{s=2}^{n} \sum_{s'=1}^{s-1} \delta\phi^{e_{j-1}}_{s'n^{j-1}+(s_j-1)n^{j-1}} - \Phi^{\text{correct } j}_{s_j n^{j-1}},\end{aligned} \tag{C.4}$$

where $\delta\phi_{s+(s_j-1)n^{j-1}}$ is the accumulated phase between time $t_{(s_j-1)n^{j-1}+s-1}$ and $t_{(s_j-1)n^{j-1}+s}$ due to the frequency fluctuations of the unlocked LO and the feedback corrections applied up to time $t_{(s_j-1)n^{j-1}}$. For simplicity, we have replaced the time dependence by an index such that $\delta\phi^{e_i}_{s'n^{i-1}+(s_j-1)n^{j-1}}$ is the phase estimate from the i'th ensemble at time $t_{s'n^{i-1}+(s_j-1)n^{j-1}}$. To fully exploit all information from the measurements on the first $(j-1)$ ensembles between time $t_{(s_j-1)n^{j-1}}$ and $t_{s_j n^{j-1}}$, we choose a phase correction of

[3] For now we assume equal strengths for all feedback loops

[4] The LO is locked after a time $\sim T_j/\alpha$

$\Phi^{\text{correct } j}_{s_j n^{j-1}} = \phi^{\text{correct}}_{j,1} + \phi^{\text{correct}}_{j,2} + \ldots + \phi^{\text{correct}}_{j,j-1}$, where

$$\begin{aligned}\phi^{\text{correct}}_{j,i} &= \sum_{s=1}^{n^{j-i}} \Bigg[(1-\alpha)^{n^{j-i}-s} \delta\phi^{e_i}_{sn^{i-1}+(s_j-1)n^{j-1}} \\ &\quad + \alpha \sum_{s'=1}^{s-1} (1-\alpha)^{n^{j-i}-s} \delta\phi^{e_i}_{s'n^{i-1}+(s_j-1)n^{j-1}} \Bigg]. \end{aligned} \tag{C.5}$$

Here we assume that when two or more ensembles are to be read out at the same instant in time, ensembles with a shorter Ramsey time are measured before the ones with longer Ramsey times such that the results from these measurements can be used as a correction for the ensembles with a longer Ramsey time. For this choice of $\Phi^{\text{correct } j}_{s_j n^{j-1}}$, the phase of the LO relative to ensemble j is

$$\begin{aligned}\Phi^{j}_{s_j n^{j-1}} &= \sum_{s=1}^{n^{j-1}} \phi_{s+(s_j-1)n^{j-1}} - \sum_{s=1}^{n^{j-1}} \delta\phi^{e_1}_{s+(s_j-1)n^{j-1}} - \sum_{s=1}^{n^{j-2}} \delta\phi^{e_2}_{sn+(s_j-1)n^{j-1}} - \ldots \\ &\quad - \sum_{s=1}^{n} \delta\phi^{e_{j-1}}_{sn^{j-1}+(s_j-1)n^{j-1}}, \end{aligned} \tag{C.6}$$

where $\phi_{s+(s_j-1)n^{j-1}} = \int_0^{T_1} \delta\omega(t_{s+(s_j-1)n^{j-1}} - t')\mathrm{d}t'$ is the accumulated phase of the LO relative to the atoms in the first ensemble between times $t_{s-1+(s_j-1)n^{j-1}}$ and $t_{s+(s_j-1)n^{j-1}}$. According to Eq. (C.6), $\Phi^{j}_{s_j n^{j-1}}$ is effectively the accumulated errors between the estimated phases and the actual phases for the $(j-1)$'th ensemble between times $t_{(s_j-1)n^{j-1}}$ and $t_{s_j n^{j-1}}$[5]. $\Phi^{j}_{s_j n^{j-1}}$ is thus the accumulated phase of the LO between time $t_{(s_j-1)n^{j-1}}$ and $t_{s_j n^{j-1}}$ minus the phase change already measured by the first $j-1$ ensembles, i.e. it does not require further running time to incorporate the information acquired in the first measurements. As opposed to the feedback loop, which corrects for e.g. frequency drifts by changing the frequency of the LO, the phase corrections directly correct the phase. This phase locking ensures a more rapid convergence, which is important when we want to apply the LO to the subsequent ensembles. With the phase corrections $\Phi^{\text{correct } j}_{s_j n^{j-1}}$, we can therefore relax the assumption of $n \gg 1$. Since the noise of the LO is white after stabilizing it to the first ensemble, the subsequent frequency corrections from the other ensembles could be replaced with merely phase corrections of the LO, which would simplify the above procedure by removing the need for phase corrections in the measurements. We have however chosen to consider frequency corrections to keep a consistent treatment of the feedback in all stages.

In our simulations, we are simulating a clock with a LO locked to m ensembles running for a long but finite time. Similar to our description of the phase corrections $\Phi^{\text{correct } j}_{s_j n^{j-1}}$

[5] this is seen by considering Eq. (C.6) for $j = 1, 2, \ldots$)

above, there will be some remaining information from the last measurements, which have not been fully exploited by the feedback loops when our simulation stops. In our simulations, we therefore include an additional phase correction $\Phi_{\text{final}}^{\text{correct}}$ to the LO after the final measurement. In principle, the influence of the last few measurements could also have been reduced by running the simulation for a longer time but by doing the phase correction, we reduce the required simulation time. With the phase correction the mean frequency offset of the LO ($\bar{\omega}(\tau)$), after running the clock for a total time of $\tau = lT_1$, is

$$\bar{\omega}(\tau) = \frac{1}{\tau}\sum_{s}^{l}\phi_s - \Phi_{\text{final}}^{\text{correct}}, \tag{C.7}$$

where $\phi_s = \int_0^{T_1}\delta\omega(t_s - t')\mathrm{d}t'$ is the phase of the LO relative to the atoms at time t_s and $\Phi_{\text{final}}^{\text{correct}}$ is the final phase correction of the LO. Using Eq. (C.1)-(C.2) and assuming that the j'th ensemble is operated with Ramsey time $T_j = n^{j-1}T_1$, we can write $\bar{\omega}(\tau)$ as:

$$\begin{aligned}\bar{\omega}(\tau) \;=\; & \frac{1}{\tau}\Bigg[\sum_{s=1}^{l}(\delta\phi_s^0 - \alpha\sum_{s'=1}^{s-1}\phi_{s'}^{e_1}) - \alpha\sum_{s=1}^{l/n}\sum_{s'=1}^{s-1}\delta\phi_{s'n}^{e_2} - \dots \\ & -\alpha\sum_{s=1}^{l/n^{m-1}}\sum_{s'=1}^{s-1}\delta\phi_{s'n^{m-1}}^{e_m} - \Phi_{\text{final}}^{\text{correct}}\Bigg]\end{aligned} \tag{C.8}$$

where $\delta\phi_s^0$ is the accumulated phase between time t_{s-1} and t_s due to the frequency fluctuations of the unlocked LO and $\delta\phi_{s'n^{j-1}}^{e_j}$ is the estimated phase from the j'th ensemble at time $t_{s'n^{j-1}}$. We find that the ideal performance is reached with $\Phi_{\text{final}}^{\text{correct}} = \phi_{\text{final},1}^{\text{correct}} + \phi_{\text{final},2}^{\text{correct}} + \dots + \phi_{\text{final},m}^{\text{correct}}$ where

$$\phi_{\text{final},j}^{\text{correct}} = \sum_{s=1}^{l/n^{j-1}}\left[(1-\alpha)^{l/n^{j-1}-s}\delta\phi_{sn^{j-1}}^{e_j} + \alpha\sum_{s'=1}^{s-1}(1-\alpha)^{l/n^{j-1}-s}\delta\phi_{s'n^{j-1}}^{e_j}\right]. \tag{C.9}$$

With this phase correction, the mean frequency offset is

$$\bar{\omega}(\tau) = \frac{1}{\tau}\left[\sum_{s=1}^{l/n^{m-1}}\tilde{\phi}_{sn^{m-1}} - \delta\tilde{\phi}_{sn^{m-1}}^{e_1} - \delta\tilde{\phi}_{sn^{m-1}}^{e_2} - \dots - \delta\tilde{\phi}_{sn^{m-1}}^{e_m}\right], \tag{C.10}$$

where $\tilde{\phi}_{sn^{m-1}} = \sum_{s'=1}^{n^{m-1}}\phi_{(s-1)n^{m-1}+s'} = \sum_{i=1}^{n^{m-1}}\int_0^{T_1}\delta\omega(t_{s'+(s_j-1)n^{m-1}} - t')\mathrm{d}t'$ is the sum of the accumulated phases of the LO relative to the first ensemble between time $t_{s'-1+(s_j-1)n^{m-1}}$ and $t_{s'+(s_j-1)n^{m-1}}$ and $\delta\tilde{\phi}_{sn^{m-1}}^{e_j} = \sum_{s'=1}^{n^{m-j}}\delta\phi_{s'n^{j-1}+(s-1)n^{m-j}}^{e_j}$ is the sum of the estimated phases from the j'th ensemble at times $t_{s'n^{j-1}+(s-1)n^{m-1}}$. Using Eq.

(C.6) we can write

$$\bar{\omega}(\tau) = \frac{1}{\tau}\left[\sum_{s=1}^{l/n^{m-1}} \tilde{\Phi}_s^m - \phi_s^{e_m}\right] \tag{C.11}$$

$$= \frac{1}{l/n^{m-1}}\left[\sum_{s=1}^{l/n^{m-1}} \frac{\tilde{\Phi}_s^m - \phi_s^{e_m}}{T_m}\right], \tag{C.12}$$

where T_m is the Ramsey time of the m'th ensemble, $\tilde{\Phi}_s^m$ is the accumulated phase of the stabilized LO relative to the atoms in the m'th ensemble at time $t_{sn^{m-1}}$ and $\phi_s^{e_m}$ is the estimate of that phase. Eq. (C.12) shows that the final phase correction effectively incorporate the remaining information from the measurements that has not yet been exploited by the feedback loop. Thus the mean frequency offset simply depends on how well we estimate the phase of the m'th ensemble and this last measurement is effectively a measurement of the accumulated errors of the phase estimates in the previous $(m-1)$ ensembles. We use Eq. (C.12) to determine the stability of the clock, which is given by $\sigma_\gamma(\tau) = \langle(\delta\bar{\omega}(\tau)/\omega)^2\rangle^{1/2}$.

C.2 Limit of the free evolution time

Here we discuss how to determine the upper limit of the Ramsey time for the scheme described in Chap. 5 and thereby the minimum number of atoms N_{min} required in each ensemble in order for the scheme to work. In Sec. 5.3, we show that the minimum number of atoms required in each ensemble, in order to increase the Ramsey time by a factor of a at each level of our protocol, is

$$N_{min} \sim a/\beta, \tag{C.13}$$

where β parameterize the maximal Ramsey time T_{max} for a LO subject to white noise. Note that, equivivalently, β is the maximal width of the distribution of phase jumps allowed, i.e. $\sigma^2_{\delta\phi,max} = \beta$. The requirement expressed in Eq. (C.13) ensures that when we increase the Ramsey time of the next ensemble by a factor of a compared to the Ramsey time of the previous ensemble we still keep $\sigma^2_{\delta\phi} \lesssim \sigma^2_{\delta\phi,max}$ for the noise seen by the next ensemble. Note that N_{min} is found by setting $a = 2$.

To determine β, we simulate an atomic clock with only a single ensemble of $N = 10^5$ atoms and a LO subject to white noise characterized by a strength γ. Furthermore, to determine β_1 (see Eq. 5.11) for a LO subject to $1/f$ noise, we do a similar simulation but with a $1/f$ noise spectrum of the LO i.e. $S(f) = \gamma^2/f$, where $S(f)$ denotes the noise spectrum and f is frequency. Note that we define the noise spectrum as $S(f)\delta(f+f') =$

$\langle \delta\omega(f)\delta\omega(f')\rangle$, where $\delta\omega(f)$ is the Fourier transform of the frequency fluctuations $\delta\omega(t)$ of the LO. $S(f)$ is thus the frequency noise spectrum. In the simulations, we do not simulate the full quantum evolution of the atomic state as we do for the simulations presented in Secs. 5.3 and 5.5. Instead, we approximate the probability distributions of $\hat{J}_{x,y,z}$ with Gaussian distributions as in Sec. 4.4.3. This Gaussian approximation is legitimate since $N \gg 1$. Furthermore, it is desirable for white noise in the unlocked LO to have a weak feedback strength α since a strong feedback increases the width of the phase noise for the locked LO. For white noise in the unlocked LO we therefore simulate the limit where $\alpha \ll 1$ such that the phases are uncorrelated. For $1/f$ noise, we use a feedback strength of $\alpha = 0.5$ since a stronger feedback is desirable to lock the LO more rapidly. The high number of atoms ensures that when we increase the Ramsey time T of the clock, we see the onset of the phase jumps as an abrupt break down, which is not blurred by the atomic noise in our phase estimates. In our simulations, the clock is running for a time $\tau = 10^6 T$, i.e. for $l = 10^6$ steps of T[6]. The onset of the break down will in principle have a weak (logarithmic) dependence on the number of steps that we simulate, which we do not expect to change our results significantly (see App.B.1). Fig. C.1 shows the result of our simulations.

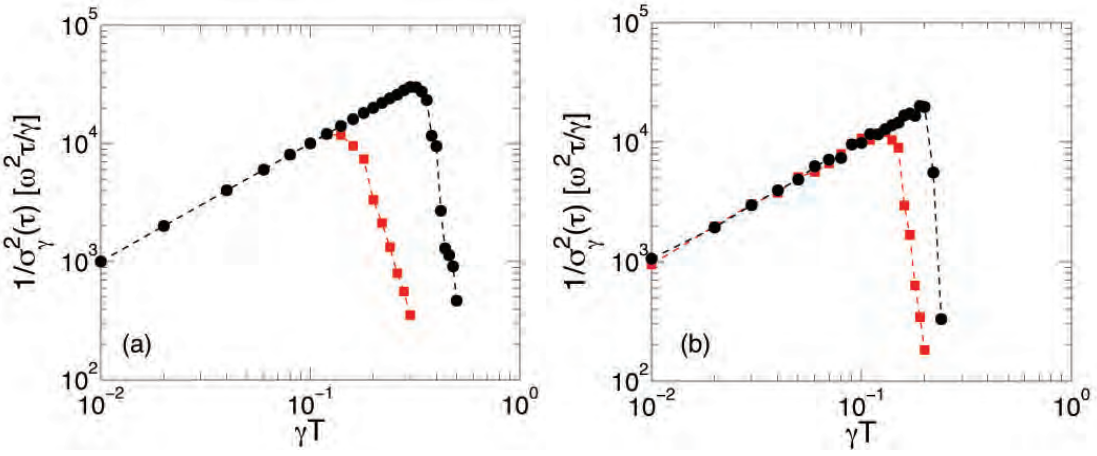

FIGURE C.1: Stability as a function of the Ramsey time (γT) for (a) white noise and (b) $1/f$ noise in the LO. The plots were made with $N = 10^5$. • is the adaptive protocol of described in Chap. 4 and ■ is the conventional Ramsey protocol. The adaptive protocol allows for $\gamma T \sim 0.3$ and 0.2 for white and $1/f$ - noise respectively while the conventional protocol only allows for $\gamma T \sim 0.1$ for both white and $1/f$ noise.

The adaptive protocol that we have used is that described in Chap. 4 since the modified adaptive protocol described in Sec. 5.4 will lead to similar results for large atom numbers, where the break down is most apparent, but is harder to simulate. Fig. C.1 shows that the conventional protocol allows for $\beta \sim 0.1$ for white noise and $\beta_1 \sim 0.1$ for $1/f$ noise in the unlocked LO while the adaptive protocol allows for $\beta \sim 0.3$ and $\beta_1 \sim 0.2$. With

[6]For $1/f$ noise we average over 100 independent runs with 10^4 steps of T.

$a = 2$ in Eq. (C.13), the minimum number of atoms required for the protocol of locking to several ensembles to work is thus $N_{min} = 20$ for conventional Ramsey strategy while the adaptive strategy can extend the applicability down to $N_{min} = 7$ atoms. We expect β of the modified adaptive protocol described in Sec. 5.4 to be identical since it also relies on the rotation of the atomic state to resolve phases between $\pm\pi$. In our numerical simulations of the modified protocol, we have therefore set $\beta \sim 0.3$ and $\beta_1 \sim 0.2$ for $1/f$ noise. Note that in our simulations of the full protocol of locking an atomic clock to several atomic ensembles, we still include the possibility of disruptive phase jumps. However, imposing the limits on β (β_1) identified from Fig. C.1 for all steps in the protocol ensures that we do not see any significant effect of them. The probability to have disruptive phase jumps for the duration of the simulations is simply negligible, i.e, the probability for phase jumps large enough to spoil the feedback strategy in a Ramsey sequence is well below 10^{-6}.

Appendix D

Heralded quantum gates

In order to confirm our results from perturbation theory described in Chap. 6, we have numerically integrated the full Master equation, defined by the Hamiltonian in Eq. (5.1) and the Lindblad operators, $\hat{L}_j \in \{\hat{L}_0, \hat{L}_g, \hat{L}_f, \hat{L}_1, \hat{L}_2\}$,

$$\frac{d}{dt}\rho(t) = -\frac{i}{\hbar}[\hat{H}, \rho(t)] + \sum_j \frac{1}{2}\left[2\hat{L}_j\rho(t)\hat{L}_j^\dagger - \rho(t)\hat{L}_j^\dagger\hat{L}_j - \hat{L}_j^\dagger\hat{L}_j\rho(t)\right] \tag{D.1}$$

We used the QuTiP 2 package [147], for Python, to set up the problem and used its 12th-order numerical integration algorithm to find the solution $\rho(t)$ as a time series. Then, we used the routines of the same package to analyze the results.

For each time series $\rho(t)$, we determined the gate time t_{gate}, the success probability P_{success}, and the fidelity F. We picked $|\psi_0\rangle_{12} = \frac{1}{\sqrt{2}}\big(|0\rangle + |1\rangle\big)_1 \otimes \frac{1}{\sqrt{2}}\big(|0\rangle + |1\rangle\big)_2$ as the initial state of the two qubits, $|g\rangle$ for the control atom, and zero photons in the cavity. Starting from here, we let the system evolve under the Master equation Eq.(D.1), and determined $P_g(t)$, the conditional state $\rho_g(t)$ and $F(t)$ as a function of time:

$$\begin{aligned} P_g(t) &= \text{Tr}\Big[\rho(t)|g\rangle\langle g|\Big], \\ \rho_g(t) &= \frac{|g\rangle\langle g|\rho(t)|g\rangle\langle g|}{P_g(t)}, \\ F(t) &= \max_{\phi_1,\phi_2}\Big\langle \psi_t^{\phi_1,\phi_2}\Big|\,\text{Tr}_{\text{c, c}}\big(\rho_g(t)\big)\,\Big|\psi_t^{\phi_1,\phi_2}\Big\rangle \end{aligned}$$

where $\text{Tr}_{\text{c, c}}$ is the partial trace operation over the control atom and the cavity, and $|\psi_t^{\phi_1,\phi 2}\rangle$ is the target state transformed with two single qubit z-rotations:

$$\Big|\psi_t^{\phi_1,\phi_2}\Big\rangle = \hat{U}_1(\phi_1)\hat{U}_2(\phi_2)\frac{1}{2}\Big(|00\rangle + |01\rangle + |10\rangle - |11\rangle\Big),$$

where $\hat{U}_k(\phi_k) = \exp\left[i|1\rangle_k\langle 1|_k\phi_k\right]$ is the z-rotation of qubit k $(= 1, 2)$ by the angle ϕ_k. From these time series, we determined the gate time t_{gate} by finding the timepoint where $F(t)$ is maximal,

$$t_{\text{gate}} = \underset{t}{\text{argmax}}\, F(t)$$

The fidelity and the success probability of the gate is then defined as $F = F(t_{\text{gate}})$, $P_{\text{success}} = P_g(t_{\text{gate}})$.

Plots of Fig. D.1 show the gate time (t_{gate}) and the success probability (P_{success}) as a function of C, for $\gamma_g = 0$, $\gamma = 0.1\kappa$, $\Omega \in \{0.1,\ 0.05,\ 0.025\}\kappa$. The detunings, Δ_E and Δ_e were choosen to be close to their optimal value, determined from the adiabatic theory, and numerically optimized to result in identical effective $|g\rangle \to |f\rangle$ transition rates $\Gamma_0 = \Gamma_1 = \Gamma_2$ for the qubit sectors $|00\rangle, |01\rangle, |11\rangle$. The rates Γ_j were found by numerically diagonalizing the master equation for the qubit sectors separately, and finding the eigenvalue with the smallest (but non-zero) absolute real part. This numerical optimization yielded the maximal fidelity. The symbols correspond to the numerical result, whereas the solid lines show the theoretical values. The agreement of the results confirm the validity of the adiabatic theory.

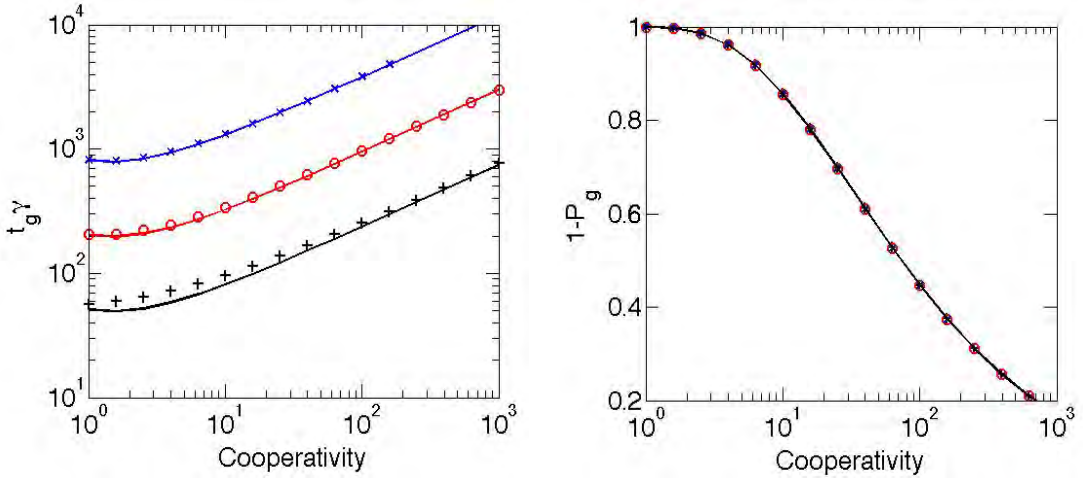

FIGURE D.1: Gate time (left) and failure probability (right) as a function of cooperativity (C) for $\gamma/\kappa = 0.1$, $\gamma_g = 0$, and $\Omega/\kappa = 0.1,\ 0.05,\ 0.025$ (denoted by the symbols "+", "o", "x" respectively. We used a gradual ramping up of $\Omega(t) = \Omega\left(1 - e^{-t/t_{\text{ramp}}}\right)$ with $t_{\text{ramp}} = 10/\gamma$.

Fig. D.2 shows the conditional *in*fidelity of the gate as a function of C for the same choice of parameters. The fidelity is limited by non-adiabatic effects, which can be surpressed by decreasing Ω. Adiabatically ramping down Ω at the end of the gate could also improve the adiabaticity but, for simplicity, we have not included this. The simulation confirms that using $\Omega/\kappa = 0.025$ is enough to push the (conditional) infidelity of the gate below 10^{-6} even for low cooperativity, such as $C = 5$.

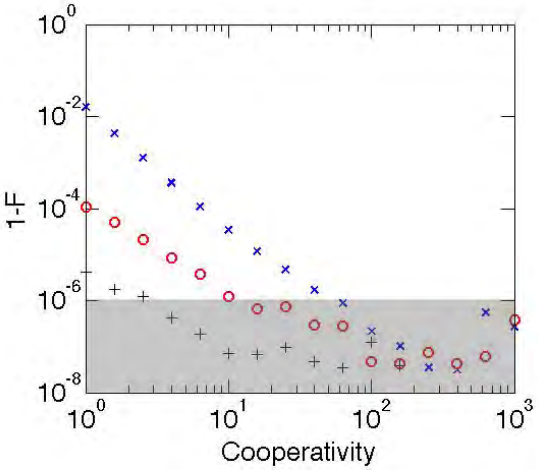

FIGURE D.2: Conditional infidelity of the gate as a function of cooperativity (C) for $\gamma/\kappa = 0.1$, $\gamma_g = 0$, and $\Omega/\kappa = 0.1,\ 0.05,\ 0.025$ (denoted by the symbols "x", "o", "+" respectively. The shaded region (at $\sim 10^{-6}$) shows the limit of numerical accuracy. We used a gradual ramping up of $\Omega(t) = \Omega\left(1 - e^{-t/t_{\rm ramp}}\right)$ with $t_{\rm ramp} = 10/\gamma$.

We repeated the above analysis for the two-photon-driving Hamiltonian in Eq. (6.23). We chose $\gamma = \gamma_g = \gamma_f = 0.1\,\kappa$, $\Omega = \frac{\Delta_{E2}}{8C^{1/4}}$, and $\Omega_{\rm MW} = 4\gamma C^{1/4}$, and choose Δ_E and Δ_e detunings again close to their adiabatic optimum, but numerically optimized them with the same procedure as previously. Plots of Fig. D.3 show the gate time and the success probability as a function of C for three different values of $\Delta_{E2} \in \{5, 10, 20\}\kappa$. Symbols indicate the numerical results while solid lines show the theoretical values. Fig. D.4

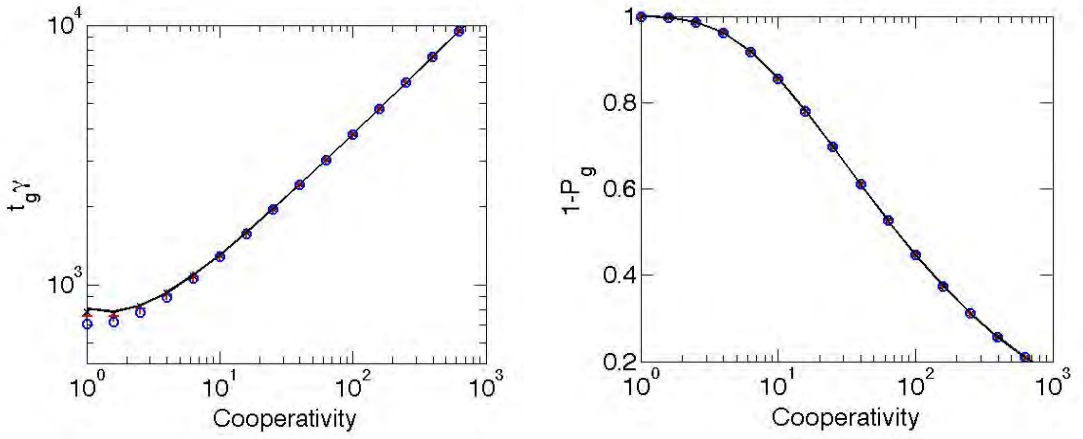

FIGURE D.3: Gate time (left) and failure probability (right) as a function of cooperativity (C) for $\gamma = \gamma_g = \gamma_f = 0.1$, $\Omega = \frac{\Delta_{E2}}{8C^{1/4}}$, $\Omega_{\rm MW} = 4\gamma C^{1/4}$, $\Delta_{E2}/\kappa = 5,\ 10,\ 20$ (denoted by the symbols "x", "+", "o" respectively.

shows the conditional *in*fidelity of the two-photon-driven gate as a function of C for the same choice of parameters. With this result, we confirm that by increasing Δ_{E2}, but keeping the effective driving strength $\Omega_{\rm eff} = \frac{\Omega_{\rm MW}\Omega}{2\Delta_{E2}}$ ($= 0.025\,\kappa$ here) constant, we can lower the infidelity error to an arbitrary small level. For high C, we do see some small

non-adiabatic effects, which we do not fully understand but they can be surpressed even further by decreasing Ω.

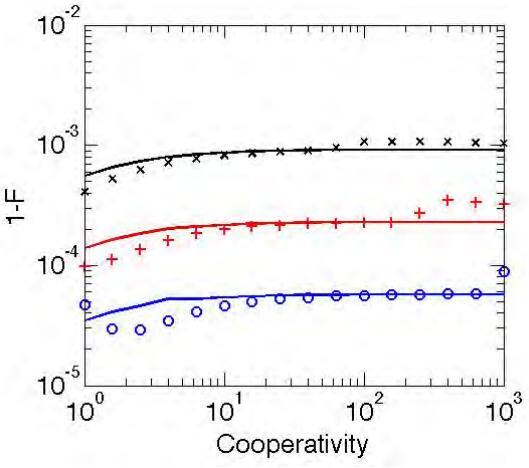

FIGURE D.4: Conditional infidelity of the gate as a function of cooperativity (C) for $\gamma = \gamma_g = \gamma_f = 0.1$, $\Omega = \frac{\Delta_{E2}}{8C^{1/4}}$, $\Omega_{\mathrm{MW}} = 4\gamma C^{1/4}$, $\Delta_{E2}/\kappa = 5,\ 10,\ 20$ (denoted by the symbols "x", "+", "o" respectively.

Appendix E

Room temperature single photon sources and quantum memories

In this appendix, we give the expressions for $\mathcal{A}(t)$, $\mathcal{B}_j(t)$, and $\mathcal{C}_j(t)$ with the extra couplings present for a realization with ^{133}Cs atoms (see Fig. E.1). We find that

$$\begin{aligned}
\mathcal{A}(t) &= -(\kappa_1/2 + i\Delta_{cav}) + \frac{1}{4}\sum_{j=1}^{N} \left|g_{43}^{(j)}(t)\right|^2 f_j(\Delta_3, k_q, t) + \left|g_{44}^{(j)}(t)\right|^2 f_j(\Delta_4, k_q, t) \\
&\quad + \left|g_{45}^{(j)}(t)\right|^2 f_j(\Delta_5, k_q, t) + \left|g_{45'}^{(j)}(t)\right|^2 f_j(\Delta_5, k_q, t) \qquad \text{(E.1)} \\
\mathcal{B}_j(t) &= \frac{1}{8}\Big(g_{43}^{(j)}(t)\Omega_{33}^{(j)}(t)\tilde{f}_j(\Delta_3, k_q, k_c, t) + g_{44}^{(j)}(t)\Omega_{34}^{(j)}(t)\tilde{f}_j(\Delta_4, k_q, k_c, t)\Big) \qquad \text{(E.2)} \\
\mathcal{C}_j(t) &= \frac{1}{16}\Big(\left|\Omega_{33}^{(j)}(t)\right|^2 f_j(\Delta_3, k_c, t) + \left|\Omega_{34}^{(j)}(t)\right|^2 f_j(\Delta_4, k_c, t) \\
&\quad + \left|\Omega_{45}^{(j)}(t)\right|^2 f_j(\tilde{\Delta}_5, k_c, t) + \left|\Omega_{44}^{(j)}(t)\right|^2 f_j(\tilde{\Delta}_4, k_c, t)\Big), \qquad \text{(E.3)}
\end{aligned}$$

where the detunings are defined in Fig. E.1 with $\tilde{\Delta} = \Delta + 2\pi \cdot 9.2$ GHz and we have defined the functions

$$\begin{aligned}
f_j(\Delta, k, t) &= \frac{e^{2ikz_j(t)} - 1}{\gamma/2 - i(\Delta - kv_z^{(j)}(t))} - \frac{1 - e^{-2ikz_j(t)}}{\gamma/2 - i(\Delta + kv_z^{(j)}(t))} \qquad \text{(E.4)} \\
\tilde{f}_j(\Delta, k_q, k_c, t) &= \frac{e^{i(k_q - k_c)z_j(t)} - e^{-i(k_c + k_q)z_j(t)}}{-\gamma/2 + i(\Delta + k_c v_z^{(j)}(t))} + \frac{e^{-i(k_q - k_c)z_j(t)} - e^{i(k_c + k_q)z_j(t)}}{-\gamma/2 + i(\Delta - k_c v_z^{(j)}(t))}. \qquad \text{(E.5)}
\end{aligned}$$

Here k_c (k_q) is the wavenumber of the classical (quantum) field. The couplings are defined such that

- $g_{4\alpha}^{(j)}(t)$ is the coupling between the states $|F = 4, m_F = 4\rangle$ and $|F' = \alpha, m_{F'} = 3\rangle$
- $g_{4\alpha'}^{(j)}(t)$ is the coupling between the states $|F = 4, m_F = 4\rangle$ and $|F' = \alpha, m_{F'} = 5\rangle$

- $\Omega^{(j)}_{3\alpha'}(t)$ is the coupling between the states $|F=3, m_F=3\rangle$ and $|F'=\alpha, m_{F'}=3\rangle$
- $\Omega^{(j)}_{4\alpha'}(t)$ is the coupling between the states $|F=4, m_F=4\rangle$ and $|F'=\alpha, m_{F'}=4\rangle$,

where the xy dependence of the couplings is implicit. Note that we have allowed for the cavity to be detuned from the the quantum field with a detuning of Δ_{cav} in Eq. (E.1). This detuning should be chosen such that it elliminates the phases from the coupling terms in Eq. (E.1), which would otherwise have a detrimental effect on the readout efficiency. We have assumed that this is case in all our numerical simulations.

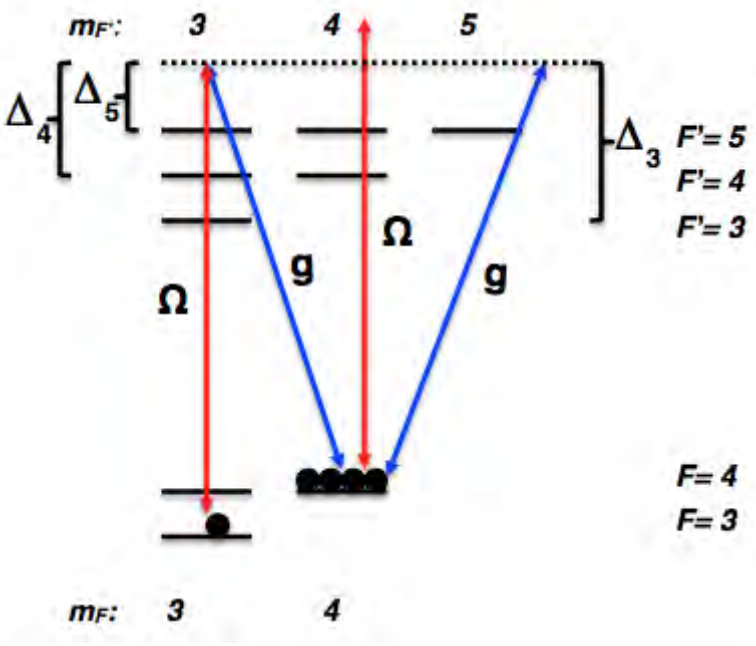

FIGURE E.1: The relevant level structure in ^{133}Cs for the readout process. The couplings of the classical (quantum) field are denoted Ω (g).

Appendix F

Optimization of repeater structures based on optical cavities

In this appendix, we present a detailed error analysis of both the single-photon and two-photon entanglement generation scheme, considered in Chap. 8. Furthermore, we present the details of the calculation of the factors $\mathcal{Z}_{l;m}$ introduced in Sec. 8.4

F.1 Error analysis of the single-photon scheme

The setup of the single-photon scheme is described in Sec. 8.1. The single photon detectors are assumed to have a dark count probability of P_{dark} and an efficiency of η_d while the transmission efficiency of the fibers is denoted η_f. As described in Sec. 8.1, the probability of an emitter to go from the excited state, $|e\rangle$ to the ground state $|1\rangle$ is P_{phot} while the excitation probability is ϵ^2. The scheme is conditioned on a single click at the central station and depending on which detector gave the click, a single qubit rotation can be employed such that ideally the state $|\Psi^+\rangle$ is created. Going through all the possibilities of obtaining a single click at the central station, we find that the density matrix following a single click, and possible subsequent single qubit rotations, is

$$\begin{aligned}\rho_{1click} &= F_1|\Psi^+\rangle\langle\Psi^+| + \alpha_1|\Phi^+\rangle\langle\Phi^+| + \alpha_1|\Phi^-\rangle\langle\Phi^-| + \beta_1|\Psi^-\rangle\langle\Psi^-| \\ &\quad +\tilde{\alpha}_1|00\rangle\langle 00| + \tilde{\beta}_1|11\rangle\langle 11|, \end{aligned} \tag{F.1}$$

with coefficients

$$
\begin{aligned}
F_1 &= \frac{1}{P_{1click}}\Big[2\eta_d\eta_f P_{phot}\epsilon^2(1-\epsilon^2)(1-P_{dark}) \\
&\quad +2\eta_f(1-\eta_d)P_{phot}\epsilon^2(1-\epsilon^2)P_{dark}(1-P_{dark}) \\
&\quad +\frac{1}{2}\eta_d\eta_f P_{phot}\epsilon^4(1-P_{phot}(1-P_{dark}) + \\
&\quad +2(1-\eta_f)P_{phot}\epsilon^2(1-\epsilon^2)P_{dark}(1-P_{dark}) \\
&\quad +(1-\eta_d\eta_f)P_{phot}\epsilon^4(1-P_{phot})P_{dark}(1-P_{dark}) \\
&\quad +(1-\epsilon^2)\epsilon^2(1-P_{phot})P_{dark}(1-P_{dark}) \\
&\quad +\frac{1}{2}\epsilon^2(1-P_{phot})^2P_{dark}(1-P_{dark})\Big] \\
\alpha_1 &= \frac{1}{P_{1click}}\Big[\frac{1}{2}\epsilon^2(1-P_{phot})^2P_{dark}(1-P_{dark})\Big] \\
\beta_1 &= \frac{1}{P_{1click}}\Big[\frac{1}{2}\eta_d\eta_f P_{phot}\epsilon^4(1-P_{phot})(1-P_{dark}) \\
&\quad +2(1-\eta_f)P_{phot}\epsilon^2(1-\epsilon^2)P_{dark}(1-P_{dark}) \\
&\quad +(1-\eta_d\eta_f)P_{phot}\epsilon^4(1-P_{phot})P_{dark}(1-P_{dark}) \\
&\quad +(1-\epsilon^2)\epsilon^2(1-P_{phot})P_{dark}(1-P_{dark}) \\
&\quad +\frac{1}{2}\epsilon^2(1-P_{phot})^2P_{dark}(1-P_{dark}) \\
&\quad +2\eta_f(1-\eta_d)P_{phot}\epsilon^2(1-\epsilon^2)P_{dark}(1-P_{dark})\Big] \\
\tilde{\alpha}_1 &= \frac{1}{P_{1click}}\Big[2(1-\epsilon^2)^2P_{dark}(1-P_{dark}) \\
&\quad +2(1-\epsilon^2)\epsilon^2(1-P_{phot1})P_{dark}(1-P_{dark})\Big] \\
\tilde{\beta}_1 &= \frac{1}{P_{1click}}\Big[\eta_d\eta_f P_{phot}\epsilon^4(1-P_{phot})(1-P_{dark}) \\
&\quad +2(1-\eta_d\eta_f)P_{phot}\epsilon^4(1-P_{phot})P_{dark}(1-P_{dark}) \\
&\quad +2(1-\eta_d\eta_f)^2P_{phot}^2\epsilon^4P_{dark}(1-P_{dark}) \\
&\quad +2(1-\eta_d\eta_f)\eta_d\eta_f P_{phot}^2\epsilon^4(1-P_{dark})^2\Big].
\end{aligned}
\tag{F.2}
$$

Here we have assumed that with probability $\epsilon^2(1-P_{phot})$, an emitter is excited but spontaneously decay to the ground states instead of emitting a cavity photon. Furthermore, we have assumed that the decay rates to the two ground states are equal such that the emitter ends up in $\frac{1}{2}(|0\rangle\langle 0| + |1\rangle\langle 1|)$. Note that the detectors are not assumed

to be number resolving. P_{1click} is the total success probability, which is

$$\begin{aligned} P_{1click} &= 2\eta_d\eta_f P_{phot}\epsilon^2(1-P_{phot}\epsilon^2)(1-P_{dark}) \\ &\quad +(2\eta_f\eta_d-\eta_f^2\eta_d^2)P_{phot}^2\epsilon^4 \\ &\quad +2(1-\epsilon^2P_{phot})^2P_{dark}(1-P_{dark}) \\ &\quad +2(1-\eta_d\eta_f)^2P_{phot}^2\epsilon^4P_{dark}(1-P_{dark}) \\ &\quad +4(1-\eta_d\eta_f)P_{phot}\epsilon^2(1-\epsilon^2P_{phot})P_{dark}(1-P_{dark}). \end{aligned} \tag{F.3}$$

Assuming $P_{dark} \ll 1$, the dominant error is where both qubits are excited but only a single click is detected at the central station. This leaves the qubits in the state $|11\rangle\langle 11|$ and this error is efficiently detected by the purification scheme described in Ref. [14].

F.2 Error analysis of the two-photon scheme

For the two photon scheme described in Sec. 8.1, we condition on a click in two detectors and once again we assume that appropriate single qubit rotations are employed depending on which detector combination clicked such that ideally the state $|\Psi^+\rangle$ is created. We find that the density matrix describing the qubit state after a successful event is

$$\rho_{2click} = F_2|\Psi^+\rangle\langle\Psi^+| + \alpha_2|\Phi^+\rangle\langle\Phi^+| + \alpha_2|\Phi^-\rangle\langle\Phi^-| + \beta_2|\Psi^-\rangle\langle\Psi^-|, \tag{F.4}$$

where we have defined

$$\begin{aligned}
F_2 &= \frac{(1-P_{dark})^2}{P_{2click}}\Big[\frac{1}{2}eta_d^2\eta_f^2P_{phot}^2 \\
&\quad +\eta_d(1-\eta_d)\eta_f^2P_{dark}P_{phot}^2 \\
&\quad +\eta_f^2(1-\eta_d)^2P_{phot}^2P_{dark}^2 \\
&\quad +P_{dark}^2(1-P_{phot})^2+\eta_d(1-\eta_f)\eta_fP_{dark}P_{phot}^2 \\
&\quad +\eta_d\eta_fP_{dark}P_{phot}(1-P_{phot}) \\
&\quad +(1-\eta_f)^2P_{phot}^2P_{dark}^2 \\
&\quad +2\eta_f(1-\eta_d)(1-\eta_f)P_{phot}^2P_{dark}^2 \\
&\quad +2(1-\eta_d\eta_f)P_{phot}(1-P_{phot})P_{dark}^2\Big] \\
\alpha_2 &= \frac{(1-P_{dark})^2}{P_{2click}}\Big[-eta_d(1-\eta_f)\eta_fP_{dark}P_{phot}^2 \\
&\quad +P_{dark}^2(1-P_{phot})^2+\eta_d\eta_fP_{dark}P_{phot}(1-P_{phot}) \\
&\quad +(1-\eta_f)^2P_{phot}^2P_{dark}^2 \\
&\quad +2\eta_f(1-\eta_d)(1-\eta_f)P_{phot}^2P_{dark}^2 \\
&\quad +2(1-\eta_d\eta_f)P_{phot}(1-P_{phot})P_{dark}^2 \\
&\quad +\eta_d(1-\eta_d)\eta_f^2P_{dark}P_{phot}^2 \\
&\quad +\eta_f^2(1-\eta_d)^2P_{phot}^2P_{dark}^2\Big] \\
\beta_2 &= \alpha_2+\frac{(1-P_{dark})^2}{P_{2click}}\Big[\eta_d(1-\eta_d)\eta_f^2P_{dark}P_{phot}^2 \\
&\quad +\eta_f^2(1-\eta_d)^2P_{phot}^2P_{dark}^2\Big].
\end{aligned} \tag{F.5}$$

The success probability P_{2click} is

$$\begin{aligned}
P_{2click} &= (1-P_{dark})^2\Big[\frac{1}{2}\eta_d^2\eta_f^2P_{phot}^2 \\
&\quad +4\eta_d\eta_f(1-\eta_d\eta_f)P_{dark}P_{phot}^2 \\
&\quad +4P_{dark}^2(1-P_{dark})^2 \\
&\quad +4\eta_d\eta_fP_{dark}P_{phot}(1-P_{phot}) \\
&\quad +4(1-\eta_d\eta_f)^2P_{phot}^2P_{dark}^2 \\
&\quad +8(1-\eta_d\eta_f)P_{phot}(1-P_{phot})P_{dark}^2\Big]
\end{aligned} \tag{F.6}$$

As in the single-photon scheme, we have not assumed number resolving detectors and we have assumed that with probability $(1-P_{phot})$, an emitter spontaneously decay to one of the ground states resulting in the state $\frac{1}{2}(|0\rangle\langle 0|+|1\rangle\langle 1|)$.

F.3 Coin tosses

In this section, we outline how to calculate the factors $\mathcal{Z}_{l;m}(p)$ introduced in Sec. 8.4. We follow the lines of Ref. [138] where similar factors are derived. Assuming that we toss m coins simultaneously in every attempt, we ask how many attempts we need in order to get at least l tails, assuming that each coin have a probability of p to show tails. Coins showing tail after a toss are kept and only the coins showing head are tossed again until l tails are obtained. The expression for $\mathcal{Z}_{m;m}(p)$ is already derived in Ref. [138] and their result is stated below

$$\mathcal{Z}_{m;m} = \sum_{k=1}^{m} \binom{m}{k} \frac{(-1)^{k+1}}{1-(1-p)^k}. \tag{F.7}$$

For $\mathcal{Z}_{l;m}$ where $l \neq m$, we only need to find expressions for $\mathcal{Z}_{1;m}$ with $m = 1, 2, 3, 4$, $\mathcal{Z}_{2;m}$ with $m = 3, 4$ and $\mathcal{Z}_{3;4}$ since we have a maximum of 4 qubits pr. repeater station. For $\mathcal{Z}_{2;3}$, we have that

$$\begin{aligned}
\mathcal{Z}_{2:3} \quad = \quad & \binom{3}{3} \sum_{k=1}^{\infty} k(q^3)^{k-1}p^3 + \binom{3}{2} \sum_{k=1}^{\infty} k(q^3)^{k-1}p^2 q \\
& + \binom{3}{1}\binom{2}{1} \sum_{k=1}^{\infty} \sum_{l}^{\infty} (k+l)[q^3)^{k-1}pq^2][(q^2)^{l-1}pq] \\
& + \binom{3}{1}\binom{2}{2} \sum_{k=1}^{\infty} \sum_{l}^{\infty} (k+l)[q^3)^{k-1}pq^2][(q^2)^{l-1}p^2],
\end{aligned} \tag{F.8}$$

where $q = 1 - p$. The first term in Eq. (F.8) describes the situations where three tails are obtained in a single toss after a given number of tosses, where all coins showed head. We will refer tosses where all coins show tail as failed tosses. The second term describes the situation where we get two tails in the same toss after a given number of failed tosses. The third and fourth terms are where we get a single tail after a given number of failed tosses. The coin showing tail is then kept and the two remaning coins are tossed until we obtain another tail (third term) or two tails simultaneously (fourth term). The geometric series in Eq. (F.8) can be solved to give

$$\mathcal{Z}_{2;3} = \frac{5-(7-3p)}{(2-p)p(3+(p-3)p)} \approx \frac{5}{6}\frac{1}{p}, \tag{F.9}$$

where the approximate expression is for $p \ll 1$. Note that the factor of $\frac{5}{6}$ corresponds to a simple picture where it on average takes $\frac{1}{3}\frac{1}{p}$ attempts to get the first 'tail' using 3 coins and $\frac{1}{2}\frac{1}{p}$ attempts to get the second using the remaining 2 coins. In a similar

manner, we find that

$$\mathcal{Z}_{1;2} = \frac{1}{2p-p^2} \approx \frac{1}{2p} \tag{F.10}$$

$$\mathcal{Z}_{1;3} = \frac{1}{3p-3p^2+p^3} \approx \frac{1}{3p} \tag{F.11}$$

$$\mathcal{Z}_{1;4} = \frac{1}{4p-6p^2+4p^3-p^4} \approx \frac{1}{4p} \tag{F.12}$$

$$\mathcal{Z}_{2;4} = \frac{-7+p(15+p(4p-13))}{(p-2)p(3+(p-3)p)(2+(p-2)p)} \approx \frac{7}{12p} \tag{F.13}$$

$$\mathcal{Z}_{3;4} = \frac{-13+p(33+p(22p-6p^2-37))}{(p-2)p(3+(p-3)p)(2+(p-2)p)} \approx \frac{13}{12p}. \tag{F.14}$$

Here the approximate expressions are all for $p \ll 1$ and they correspond to the expressions one would get using simple pictures similar to the one described above in the discussion of $\mathcal{Z}_{2;3}$.

Bibliography

[1] Niels Bohr. On the constitution of atoms and molecules. *Philosophical Magazine*, 26:476–502, 1913. doi: 10.1080/14786441308634955.

[2] Albert Einstein. Über einen die erzeugung und verwandlung des lichtes betreffenden heuristichen gesichtspunkt. *Annalen der Physik*, 17:132–148, 1905. doi: 10.1002/andp.19053220607.

[3] W. Heisenberg. Über den anschaulichen inhalt der quantentheoretischen kinematik und mechanik. *Zeitschrift für Physik*, 43:172–198, 1927. doi: 10.1007/BF01397280.

[4] G. Kucsko, P. C. Maurer, N. Y. Yao, M. Kubo, H. J. Noh, P. K. Lo, H. Park, and M. D. Lukin. Nanometre-scale thermoetry in a living cell. *Nature*, 500:54–58, 2013. doi: doi:10.1038/nature12373.

[5] D. J. Wineland, J. J. Bollinger, W. M. Itano, and D. J. Heinzen. Squeezed atomic states and projection noise in spectroscopy. *Phys Rev. A*, 50:67–88, 1994. doi: 10.1103/PhysRevA.50.67.

[6] P. W. Shor. Polynomial-time algorithms for prime factorization and discrete logarithms on a quantum computer. *SIAM J. Comput.*, 26:1484–1509, 1997. doi: 10.1137/S0097539795293172.

[7] R. P. Feynman. Simulating physics with computers. *Int. J. Theor. Phys.*, 21: 467–488, 1982. doi: 10.1007/BF02650179.

[8] *Quantum cryptography: Public key distribution and coin tossing*, 1984.

[9] Artur K. Ekert. Quantum cryptography based on bell's theorem. *Phys. Rev. Lett.*, 67:661–663, 1991. doi: 10.1103/PhysRevLett.67.661.

[10] T. D. Ladd, F. Jelezko, R. Laflamme, Y. Nakamura, C. Monroe, and J. L. O'Brien. Quantum computers. *Nature*, 464:45–53, 2010. doi: 10.1038/nature08812.

[11] J. Benhelm, Gerhard Kirchmair, Christian F. Roos, and R. Blatt. Towards fault-tolerant quantum computing with trapped ions. *Nature Physics*, 4:463–466, 2008. doi: 10.1038/nphys961.

[12] D. Kielpinski, C. Monroe, and D. J. Wineland. Architecture for a large-scale ion-trap quantum computer. *Nature*, 417:709–711, 2002. doi: doi:10.1038/nature00784.

[13] Valerio Scarani, Helle Bechmann-Pasquinucci, Nicolas J. Cerf, Miloslav Dušek, Norbert Lütkenhaus, and Momtchil Peev. The security of practical quantum key distribution. *Rev. Mod. Phys.*, 81:1301–1350, 2009. doi: 10.1103/RevModPhys.81.1301.

[14] Charles H. Bennett, Gilles Brassard, Sandu Popescu, Benjamin Schumacher, John A. Smolin, and William K. Wootters. Purification of noisy entanglement and faithful teleportation via noisy channels. *Phys. Rev. Lett.*, 76:722–725, 1996. doi: 10.1103/PhysRevLett.76.722.

[15] H.-J. Briegel, W. Dür, J. I. Cirac, and P. Zoller. Quantum repeaters: The role of imperfect local operations in quantum communication. *Phys. Rev. Lett.*, 81:5932–5935, 1998. doi: 10.1103/PhysRevLett.81.5932.

[16] L.-M. Duan, M. D. Lukin, J. I. Cirac, and P. Zoller. Long-distance quantum communication with atomic ensembles and linear optics. *Nature*, 414:413–418, 2001. doi: 10.1038/35106500.

[17] Nicolas Sangouard, Christoph Simon, Bo Zhao, Yu-Ao Chen, Hugues de Riedmatten, Jian-Wei Pan, and Nicolas Gisin. Robust and efficient quantum repeaters with atomic ensembles and linear optics. *Phys. Rev. A*, 77:062301, 2008. doi: 10.1103/PhysRevA.77.062301.

[18] Nicolas Sangouard, Christoph Simon, Hugues de Riedmatten, and Nicolas Gisin. Quantum repeaters based on atomic ensembles and linear optics. *Rev. Mod. Phys.*, 83:33–80, 2011. doi: 10.1103/RevModPhys.83.33.

[19] P. van Loock, T. D. Ladd, K. Sanaka, F. Yamaguchi, Kae Nemoto, W. J. Munro, and Y. Yamamoto. Hybrid quantum repeater using bright coherent light. *Phys. Rev. Lett.*, 96:240501, 2006. doi: 10.1103/PhysRevLett.96.240501.

[20] Z.-S. Yuan, Yu-Ao Chen, Bo Zhao, Shuai Chen, Jorg Schmiedmayer, and Jian-Wei Pan. Experimental demonstration of a bdcz quantum repeater node. *Nature*, 454:1098–1101, 2008.

[21] I Usmani, C. Clausen, Bussiéres, N. Sangouard, M. Afzelius, and N. Gisin. Heralded quantum entanglement between two crystals. *Nature photonics*, 6:234–237, 2011. doi: doi:10.1038/nphoton.2012.34.

[22] J. F. Sherson, H. Krauter, R. K. Olsson, B. Julsgaard, K. Hammerer, I. Cirac, and E. S. Polzik. Quantum teleportation between light and matter. *Nature*, 443: 557–560, 2006. doi: doi:10.1038/nature05136.

[23] S. Barz, G. Cronenberg, A. Zeilinger, and P. Walther. Heralded generation of entangled photon pairs. *Nature photonics*, 4:553–556, 2010. doi: doi:10.1038/nphoton.2010.156.

[24] J. B. Brask, I. Rigas, E. S. Polzik, U. L. Andersen, and A. S. Sørensen. Hybrid long-distance entanglement distribution protocol. *Phys. Rev. Lett.*, 105:160501, 2010. doi: 10.1103/PhysRevLett.105.160501.

[25] J. D. Thompson, T. G. Tiecke, N. P. de Leon, J. Feist, A. V. Akimov, M. Gullans, A. S. Zibrov, V. Vuletić, and M. D. Lukin. Coupling a single trapped atom to a nanoscale optical cavity. *Science*, 340:1202–1205, 2013. doi: 10.1126/science.1237125.

[26] C. C. Gerry and P. L. Knight. *Introductory Quantum Optics*. Cambridge University Press, 2008.

[27] M. Nielsen and I. Chuang. *Quantum Computation and Quantum Information*. Cambridge University Press, 2010.

[28] Charles H. Bennett, Gilles Brassard, Claude Crépeau, Richard Jozsa, Asher Peres, and William K. Wootters. Teleporting an unknown quantum state via dual classical and einstein-podolsky-rosen channels. *Phys. Rev. Lett.*, 70:1895–1899, 1993. doi: 10.1103/PhysRevLett.70.1895.

[29] D. Dieks. Communication by epr devices. *Physics Letters A*, 92:271 – 272, 1982. doi: DOI:10.1016/0375-9601(82)90084-6.

[30] W. K. Wootters and W. H. Zurek. A single quantum cannot be cloned. *Nature*, 299:802, 1982. URL http://dx.doi.org/10.1038/299802a0.

[31] S. Ritter, C. Nölleke, C. Hahn, A. Reiserer, A. Neuzner, M. Uphoff, M. Mücke, E. Figueroa, J. Bochmann, and G. Rempe. An elementary quantum network of single atoms in optical cavities. *Nature*, 484:195–200, 2012. doi: 10.1038/nature11023.

[32] V. V. Dobrovitski, G. D. Fuchs, A. L. Falk, C. Santori, and D. D. Awschalom. Quantum control over single spins in diamond. *Annual Review of Condensed Matter Physics*, 4:23–50, 2013. doi: 10.1146/annurev-conmatphys-030212-184238.

[33] A. Imamoglu, D. D. Awschalom, G. Burkard, D. P. DiVincenzo, D. Loss, M. Sherwin, and A. Small. Quantum information processing using quantum dot spins and cavity qed. *Phys. Rev. Lett.*, 83:4204–4207, 1999. doi: 10.1103/PhysRevLett.83.4204.

[34] M. Hochberg, T. Baehr-Jones, C. Walker, J. Witzens, L. C. Gunn, and A. Scherer. Segmented waveguides in thin silicon-on-insulator. *J. Opt. Soc. Am. B*, 22:1493–1497, 2005. doi: 10.1364/JOSAB.22.001493.

[35] S. Y. Lin, E. Chow, S. G. Johnson, and J. D. Joannopoulos. Demonstration of highly efficient waveguiding in a photonic crystal slab at the 1.5 μm wavelength. *Optics Letters*, 25:1297–1299, 2000. doi: 10.1364/OL.25.001297.

[36] T. G. Tiecke, J. D. Thompson, N. P. de Leon, L. R Liu, Vuletić, and M. D. Lukin. Nanophotonic quantum phase switch with a single atom. *Nature*, 508:241–244, 2014. doi: 10.1038/nature13188.

[37] Q. A. Turchette, C. J. Hood, W. Lange, H. Mabuchi, and H. J. Kimble. Measurement of conditional phase shifts for quantum logic. *Phys. Rev. Lett.*, 75:4710–4713, 1995. doi: 10.1103/PhysRevLett.75.4710.

[38] P. Lodahl, S. Mahmoodian, and S. Stobbe. Intefacing single photons and single quantum dots with photonic nanostructures. *arXiv:1312.1079*, 2013.

[39] P. Lodahl. Highly-efficient quantum dot single-photon sources and giant-photon nonlinearitites for quantum-information processing. *Optics InfoBase*, 2014. doi: 10.1364/QIM.2014.QW5A.6.

[40] Klemens Hammerer, Anders S. Sørensen, and Eugene S. Polzik. Quantum interface between light and atomic ensembles. *Rev. Mod. Phys.*, 82:1041–1093, 2010. doi: 10.1103/RevModPhys.82.1041.

[41] G. Santarelli, Ph. Laurent, P. Lemonde, A. Clairon, A. G. Mann, S. Chang, A. N. Luiten, and C. Salomon. Quantum projection noise in an atomic fountain: A high stability cesium frequency standard. *Phys. Rev. Lett.*, 82:4619–4622, Jun 1999. doi: 10.1103/PhysRevLett.82.4619.

[42] W. M. Itano, J. C. Bergquist, J. J. Bollinger, J. M. Gilligan, D. J. Heinzen, F. L. Moore, M. G. Raizen, and D. J. Wineland. Quantum projection noise: Population fluctuations in two-level systems. *Phys Rev. A*, 47:3554–3570, 1993. doi: 10.1103/PhysRevA.47.3554.

[43] S. A. Diddams, Th. Udem, J. C. Bergquist, E. A. Curtis, R. E. Drullinger, L. Hollberg, W. M. Itano, W. D. Lee, C. W. Oates, K. R. Vogel, and D. J. Wineland.

An optical clock based on a single trapped $^{199}hg^{+}$ ion. *Science*, 293:825–828, July 2001. doi: 10.1126/science.1061171.

[44] D. J. Berkeland, J. D. Miller, J. C. Bergquist, W. M. Itano, and D. J. Wineland. Laser-cooled mercury ion frequency standard. *Phys. Rev. Lett.*, 80:2089–2092, Mar 1998. doi: 10.1103/PhysRevLett.80.2089.

[45] N. Hinkley, J. A. Sherman, N. B. Phillips, M. Schioppo, N. D. Lemke, K. Beloy, M. Pizzocaro, C. W. Oates, and A. D. Ludlow. An atomic clock with 10^{-18} instability. *arXiv:1305.5869 [physics.atom-ph]*, 2013.

[46] Feng-Lei Takamoto, Feng-Lei Hong, Ryoichi Higashi, and Hidetoshi Katori. An optical lattice clock. *Nature*, 435:321–324, 2005. doi: doi:10.1038/nature03541.

[47] N. F. Ramsey. *Molecular Beams*. Oxford University Press, London, 1956.

[48] A. S. Sørensen. Lecture notes for the course Quantum Optics 2 at the Niels Bohr Institute.

[49] A. André, A. S. Sørensen, and M. D. Lukin. Stability of atomic clocks based on entangled atoms. *Phys. Rev. Lett.*, 92:230801, 2004. doi: 10.1103/PhysRevLett.92.230801.

[50] R. H. Hadfield. Single-photon detectors for optical quantum information applications. *Nature Photonics*, 3:696, 2009. URL http://dx.doi.org/10.1038/nphoton.2009.230.

[51] L.-M. Duan, M. D. Lukin, J. I. Cirac, and P. Zoller. Long-distance quantum communication with atomic ensembles and linear optics. *Nature*, 414:413, 2001. doi: 10.1038/35106500.

[52] N. Sangouard, C. Simon, N. Gisin, J. Laurat, R. Tualle-Brouri, and P. Grangier. Quantum repeaters with entangled coherent states. *J. Opt. Soc. Am. B*, 27:A137–A145, 2010. URL http://josab.osa.org/abstract.cfm?URI=josab-27-6-A137.

[53] J. Borregaard, J. B. Brask, and A. S. Sørensen. Hybrid quantum repeater protocol with fast local processing. *Phys. Rev. A*, 86:012330, 2012. doi: 10.1103/PhysRevA.86.012330.

[54] Christoph Simon, Hugues de Riedmatten, Mikael Afzelius, Nicolas Sangouard, Hugo Zbinden, and Nicolas Gisin. Quantum repeaters with photon pair sources and multimode memories. *Phys. Rev. Lett.*, 98(190503), May 2007. doi: 10.1103/PhysRevLett.98.190503.

[55] Daniel E. Browne, Jens Eisert, Stefan Scheel, and Martin B. Plenio. Driving non-gaussian to gaussian states with linear optics. *Phys. Rev. A*, 67:062320, 2003.

[56] J. Eisert, D.E. Browne, S. Scheel, and M. B. Plenio. Distillation of continous-variable entanglement with optical means. *Annals of Physics*, 311:431–458, 2004.

[57] J. B. Brask. *Long-distance distribution of discrete and continuous variable entanglement with atomic ensembles.* PhD thesis, University of Copenhagen, April 2010.

[58] J. B. Brask, L. Jiang, A. V. Gorshkov, V. Vuletic, A. S. Sørensen, and M. D. Lukin. Fast entanglement distribution with atomic ensembles and fluorescent detection. *Phys. Rev. A*, 81(020303), Feb 2010. doi: 10.1103/PhysRevA.81.020303.

[59] Alexey V. Gorshkov, Axel André, Michael Fleischhauer, Anders S. Sørensen, and Mikhail D. Lukin. Universal approach to optimal photon storage in atomic media. *Phys. Rev. Lett.*, 98:123601, 2007. doi: 10.1103/PhysRevLett.98.123601.

[60] K. F. Reim et al. Towards high-speed optical quantum memories. *Nature Photonics*, 4:218–221, 2010.

[61] K. Jensen et al. Quantum memory for entangled continuous-variable states. *Nature Physics*, 7:13–16, 2011. doi: 10.1038/nphys1819.

[62] C. Simon et al. Quantum memories. *European Physical Journal D*, 58:1–22, 2010. doi: 10.1140/epjd/e2010-00103-y.

[63] O. A. Collins, S. D. Jenkins, A. Kuzmich, and T. A. B. Kennedy. Multiplexed memory-insensitive quantum repeaters. *Physical Review Letters*, 98(060502), Feb 2007. doi: 10.1103/PhysRevLett.98.060502.

[64] J. J. Bollinger, Wayne M. Itano, D. J. Wineland, and D. J. Heinzen. Optimal frequency measurements with maximally correlated states. *Phys Rev. A*, 54:R4649–R4652, 1996. doi: 10.1103/PhysRevA.54.R4649.

[65] Till Rosenband. Numerical test of few-qubit clock protocols. *arXiv:1203.0288v2 [quant-ph]*, 2012.

[66] Vittorio Giovanetti, Seth Lloyd, and Lorenzo Maccone. Advances in quantum metrology. *nature photonics*, 5(222–229), march 2011. doi: 10.1038/nphoton.2011.35.

[67] D. Leibfried, M. D. Barrett, T. Schaetz, J. Britton, J. Chiaverini, W. M. Itano, J. D. Jost, C. Langer, and D. J. Wineland. Toward heisenberg-limited spectroscopy with multiparticle entangled states. *Science*, 304:1476–1478, 2004. doi: 10.1126/science.1097576.

[68] Ian D. Leroux, Monika H. Schleier-Smith, and Vladan Vuletić. Implementation of cavity squeezing of a collective atomic spin. *Phys. Rev. Lett.*, 104:073602, Feb 2010. doi: 10.1103/PhysRevLett.104.073602. URL http://link.aps.org/doi/10.1103/PhysRevLett.104.073602.

[69] J. Appel, P. J. Windpassinger, D. Oblak, U. B. Hoff, N. Kjærgaard, and E. S. Polzik. Mesoscopic atomic entanglement for precision measurements beyond the standard quantum limit. *Proceedings of the National Academy of Sciences*, 106 (27):10960–10965, 2009. doi: 10.1073/pnas.0901550106. URL http://www.pnas.org/content/106/27/10960.abstract.

[70] Anne Louchet-Chauvet, Jürgen Appel, Jelmer J Renema, Daniel Oblak, Niels Kjaergaard, and Eugene S Polzik. Entanglement-assisted atomic clock beyond the projection noise limit. *New Journal of Physics*, 12(6):065032, 2010. URL http://stacks.iop.org/1367-2630/12/i=6/a=065032.

[71] Max F Riedel, Pascal Böhi, Yun Li, Theodor W Hänsch, Alice Sinatra, and Philipp Treutlein. Atom-chip-based generation of entanglement for quantum metrology. *Nature*, 464(7292):1170–1173, 2010.

[72] Christian Gross, Tilman Zibold, Eike Nicklas, Jerome Esteve, and Markus K Oberthaler. Nonlinear atom interferometer surpasses classical precision limit. *Nature*, 464(7292):1165–1169, 2010.

[73] S. F. Huelga, C. Macchiavello, T. Pellizzari, A. K. Ekert, M. B. Plenio, and J. I. Cirac. Improvement of frequency standards with quantum entanglement. *Phys. Rev. Lett.*, 79:3865–3868, 1997. doi: 10.1103/PhysRevLett.79.3865.

[74] D. W. Berry and H. M. Wiseman. Optimal states and almost optimal adaptive measurements for quantum interferometry. *Phys. Rev. Lett.*, 85:5098–5101, 2000. doi: 10.1103/PhysRevLett.85.5098.

[75] B. L. Higgins, D. W. Berry, S. D. Bartlett, H. M. Wiseman, and G. J. Pryde. Entanglement-free heisenberg-limited phase estimation. *Nature*, 450:393–396, 2007. doi: 10.1038/nature06257.

[76] J. Borregaard and A. S. Sørensen. Near heisenberg limited atomic clocks in the presence of decoherence. *Phys. Rev. Lett.*, 111:090801, 2013. doi: 10.1103/PhysRevLett.111.090801.

[77] C. W. Chou, D. B. Hume, J. C. J. Koelemeij, D. J. Wineland, and T. Rosenband. Frequency comparison of two high-accuracy al$^+$ optical clocks. *Phys. Rev. Lett.*, 104:070802, Feb 2010. doi: 10.1103/PhysRevLett.104.070802.

[78] Ekkehard Peik, Tobias Schneider, and Christian Tamm. Laser frequency stabilization to a single ion. *J. Phys. B: At. Mol. Opt. Phys*, 39:145–158, Dec 2006. doi: doi:10.1088/0953-4075/39/1/012.

[79] T. L. Nicholson, M. J. Martin, J. R. Williams, B. J. Bloom, M. Bishof, M. D. Swallows, S. L. Campbell, and J. Ye. Comparison of two independent sr optical clocks with 1×10^{-17} stability at 10^3 **s**. *Phys. Rev. Lett.*, 109:230801, Dec 2012. doi: 10.1103/PhysRevLett.109.230801.

[80] Alex W. Chin, Susana F. Huelga, and Martin B. Plenio. Quantum metrology in non-markovian environments. *Phys. Rev. Lett.*, 109:233601, 2012. doi: 10.1103/PhysRevLett.109.233601.

[81] Yuichiro Matsuzaki, Simon C. Benjamin, and Joseph Fitzsimons. Magnetic field sensing beyond the standard quantum limit under the effect of decoherence. *Phys Rev. A*, 84:012103, 2011. doi: 10.1103/PhysRevA.84.012103.

[82] D. J. Wineland, C. Monroe, W. M. Itano, D. Leibfried, B. E King, and D. M. Meekhof. Experimental issues in coherent quantum-state manipulation of trapped atomic ions. *J. Res. Natl. Inst. Stand. Technol.*, 103:259–328, 1998. doi: 10.6028/jres.103.019.

[83] T. Rosenband and D. R. Leibrandt. Exponential scaling of clock stability with atom number. *arXiv:1303.6357 [quant-ph]*, 2013.

[84] J. Borregaard and A. S. Sørensen. Efficient atomic clocks operated with several atomic ensembels. *Phys. Rev. Lett.*, 111:090802, 2013. doi: 10.1103/PhysRevLett.111.090802.

[85] N. Shiga and M. Takeuchi. Locking the local oscillator phase to the atomic phase via weak measurement. *New Journal of Physics*, 14:023034, 2012. doi: 10.1088/1367-2630/14/2/023034.

[86] Masahiro Kitagawa and Masahito Ueda. Squeezed spin states. *Phys. Rev. A*, 47:5138–5143, Jun 1993. doi: 10.1103/PhysRevA.47.5138. URL http://link.aps.org/doi/10.1103/PhysRevA.47.5138.

[87] G. Dick. Local oscillator induced instabilities in trapped ion frequency standards. *Proceedings of the Nineteenth Annual Precise Time and Time Interval (PTTI) Applications and Planning Proceedings of the Nineteenth Annual Precise Time and Time Interval (PTTI) Applications and Planning Meeting*, pages 133–147, 1987.

[88] Monika H. Schleier-Smith, Ian D. Leroux, and Vladan Vuletić. States of an ensemble of two-level atoms with reduced quantum uncertainty. *Phys. Rev. Lett.*, 104:073604, Feb 2010. doi: 10.1103/PhysRevLett.104.073604.

[89] J. L. Sørensen, J. Hald, and E. S. Polzik. Quantum noise of an atomic spin polarization measurement. *Phys. Rev. Lett.*, 80:13487–3490, 1998. doi: 10.1103/PhysRevLett.80.3487.

[90] K. Hammerer, K. Mølmer, E. S. Polzik, and J. I. Cirac. Light-matter quantum interface. *Phys. Rev. A*, 70:044304, 2004. doi: 10.1103/PhysRevA.70.044304.

[91] Lu-Ming Duan, J. I. Cirac, P. Zoller, and E. S. Polzik. Quantum communication between atomic ensembles using coherent light. *Phys. Rev. Lett.*, 85:5643–5646, 2000. doi: 10.1103/PhysRevLett.85.5643.

[92] A. Kuzmich, L. Mandel, and N. P. Bigelow. Generation of spin squeezing via continuous quantum nondemolition measurement. *Phys. Rev. Lett.*, 85:1594–1597, 2000. doi: 10.1103/PhysRevLett.85.1594.

[93] Anders S. Sørensen and Klaus Mølmer. Entanglement and extreme spin squeezing. *Phys. Rev. Lett.*, 86:4431–4434, May 2000. doi: 10.1103/PhysRevLett.86.4431.

[94] E. M. Kessler, P. Kómár, M. Bishof, L. Jiang, A. S. Sørensen, J. Ye, and M. D. Lukin. Heisenberg-limited atom clocks based on entangled qubits. *Phys. Rev. Lett.*, 112:190403, 2014. doi: 10.1103/PhysRevLett.112.190403.

[95] Jerome Lodewyck, Phillip G. Westergaard, Arnaud Lecallier, Luca Lorini, and Pierre Lemonde. Frequency stability of optical lattice clocks. *New Journal of Physics*, 12:065026, 2010. doi: 10.1088/1367-2630/12/6/065026.

[96] Masao Takamoto, Tetsushi Takano, and Hidetoshi Katori. Frequency comparison of optical lattice clocks. *nature photonics*, 5:288–292, 2011. doi: doi:10.1038/nphoton.2011.34.

[97] P. Laurent, P. Lemonde, E. Simon, G. Santarelli, A. Clairon, N. Dimarcq, P. Petit, C. Audoin, and C. Salomon. A cold atom clock in absence of gravity. *The European Physical Journal D*, 3:201–204, September 1998. doi: 10.1007/PL00021584.

[98] A. André. *Nonclassical states of light and atomic ensembles: Generation and New Applications*. PhD thesis, Harvard Univeristy, Cambridge Massachusetts, May 2005.

[99] M. Mullan and E. Knill. Optimizing passive quantum clocks. *arXiv:1404.3810 [physics.atom-ph]*, 2014.

[100] E. Knill, R. Laflamme, and G. J. Milburn. A scheme for efficient quantum computation with linear optics. *Nature*, 409:46–52, 2000. doi: 10.1038/35051009'.

[101] J. Borregaard, P Kómár, E. M. Kessler, A. S. Sørensen, and M. D. Lukin. Heralded quantum gates with integrated error detection in optical cavities. *in preparation...*, .

[102] P. Kómár, E. M. Kessler, M. Bishof, L. Jiang, A. S. Sørensen, J. Ye, and M. D. Lukin. A quantum network of clocks. *Nature Physics*, 2014. doi: doi:10.1038/nphys3000.

[103] S. Perseguers, G. J. Lapeyre Jr, D. Cavalcanti, M. Lewenstein, and A. Acín. Distribution of entanglement in large-scale quantum networks. *Rep. Prog. Phys*, 76:096001, 2013. doi: doi:10.1088/0034-4885/76/9/096001.

[104] T. Pellizzari, S. A. Gardiner, J. I. Cirac, and P Zoller. Decoherence, continuous observation, and quantum computing: A cavity qed model. *Phys. Rev. Lett.*, 75: 3788–3791, 1995. doi: 10.1103/PhysRevLett.75.3788.

[105] M. J. Kastoryano, F. Reiter, and A. S. Sørensen. Dissipative preparation of entanglement in optical cavities. *Phys. Rev. Lett.*, 106:090502, 2011. doi: 10.1103/PhysRevLett.106.090502.

[106] Anders S. Sørensen and Klaus Mølmer. Measurement induced entanglement and quantum computation with atoms in optical cavities. *Phys. Rev. Lett.*, 91:097905, Aug 2003. doi: 10.1103/PhysRevLett.91.097905.

[107] L.-M. Duan, B. Wang, and H. J. Kimble. Robust quantum gates on neutral atoms with cavity-assisted photon scattering. *Phys. Rev. A*, 72:032333, 2005. doi: 10.1103/PhysRevA.72.032333.

[108] L.-M. Duan and H. J. Kimble. Scalable photonic quantum computation through cavity-assisted interactions. *Phys. Rev. Lett.*, page 127902, 2004. doi: 10.1103/PhysRevLett.92.127902.

[109] Anders S. Sørensen and Klaus Mølmer. Probabilistic generation of entanglement in optical cavities. *Phys. Rev. Lett.*, 90:127903, Mar 2003. doi: 10.1103/PhysRevLett.90.127903.

[110] A. Reiserer, N. Kalb, G. Rempe, and S. Ritter. A quantum gate between a flying optical photon and a single trapped atom. *Nature*, 508:237–240, 2014. doi: 10.1038/nature13177.

[111] Jiannis Pachos and Herbert Walther. Quantum computation with trapped ions in an optical cavity. *Phys. Rev. Lett.*, 89:187903, 2002. doi: 10.1103/PhysRevLett.89.187903.

[112] Almut Beige, Daniel Braun, Ben Tregenna, and Peter L Knight. Quantum computing using dissipation to remain in a decoherence-free subspace. *Phys. Rev. Lett.*, 85:1762–1765, 2000. doi: 10.1103/PhysRevLett.85.1762.

[113] V. Giovannetti, D. Vitali, P. Tombesi, and A Ekert. Scalable quantum computation with cavity qed systems. *Phys. Rev. Lett.*, 62:032306, 2000. doi: 10.1103/PhysRevA.62.032306.

[114] Florentin Reiter and Anders S. Sørensen. Effective operator formalism for open quantum systems. *Phys. Rev. A*, 85:032111, 2012. doi: 10.1103/PhysRevA.85.032111.

[115] Jonathan Simon, Haruka Tanji, James K. Thompson, and Vladan Vuletić. Interfacing collective atomic excitations and single photons. *Phys. Rev. Lett.*, 98:183601, 2007. doi: 10.1103/PhysRevLett.98.183601.

[116] C.-W. Chou, L. Laurat, H. Deng, K. S. Choi, H. de Riedmatten, D. Felinto, and H. J. Kimble. Functional quantum nodes for entanglement distribution over scalable quantum networks. *Science*, 316:1316–1320, 2007. doi: 10.1126/science.1140300.

[117] Yu-Ao Chen, S. Chen, Z. S. Yuan, B. Zhao, C. S. Chuu, J. Schmiedmayer, and Jian-Wei Pan. Memory-built-in quantum teleportaion with photonic and atomic qubits. *Nature Physics*, 4:103–107, 2008. doi: 10.1038/nphys832.

[118] J. Borregaard, J. M. Petersen, M. Zugenmaier, H. Shen, G. Vasilakis, E. S. Polzik, and A. S. Sørensen. Scalable room-temperature single photon soruces and quantum memories. *in preparation...*, .

[119] M. V. Balabas, T. Karaulanov, M. P. Ledbetter, and D. Budker. Polarized alkali-metal vapor with minute-long transverse spin-relaxation time. *Phys. Rev. Lett.*, 105:070801, 2010. doi: 10.1103/PhysRevLett.105.070801.

[120] Alexey V. Gorshkov, Axel André, Mikhail D. Lukin, and Anders S. Sørensen. Photon storage in λ-type optically dense atomic media. i. cavity model. *Phys. Rev. A*, 76:033804, 2007. doi: 10.1103/PhysRevA.76.033804.

[121] Jonas Meyer Petersen. An ion crystal quantum repeater. Master's thesis, The Niels Bohr Institute, University of Copenhagen, May 2010.

[122] John David Jackson. *Classical Electrodynamics*. John Wiley and Sons, Inc., 1975.

[123] Kasper Jensen. *Quantum Information, Entanglement and Magnetometry with macroscopic Gas Samples and Non-Classical Light*. PhD thesis, The Niels Bohr Institute, University of Copenhagen, February 2011.

[124] C. K. Hong, Z. Y. Ou, and L. Mandel. Measurement of subpicosecond time intervals between two photons by interference. *Phys. Rev. Lett.*, 59:2044–2046, 1987. doi: 10.1103/PhysRevLett.59.2044.

[125] A. Aspuru-Guzik and P. Walther. Photonic quantum simulators. *Nature Physics*, 8:285–291, 2011. doi: 10.1038/nphys2253.

[126] M. Tillmann, B. Dakić, R. Heilmann, S. Nolte, A. Szameit, and P. Walther. Experimental boson sampling. *Nature photonics*, 7:540–544, 2011. doi: 10.1038/nphoton.2013.102.

[127] L. Childress, J. M. Taylor, A. S. Sørensen, and M. D. Lukin. Fault-tolerant quantum communication based on solid-state photon emitters. *Phys. Rev. Lett.*, 96: 070504, 2006. doi: 10.1103/PhysRevLett.96.070504.

[128] Nicolas Sangouard, Romain Dubessy, and Christoph Simon. Quantum repeaters based on single trapped ions. *Phys. Rev. A*, 79:042340, 2009. doi: 10.1103/PhysRevA.79.042340.

[129] C. A. Ryan, M. Laforest, and R. Laflamme. Randomized benchmarking of single- and multi-qubit control in liquid-state nmr quantum information processing. *New Journal of Physics*, 11:013034, 2009. doi: 10.1088/1367-2630/11/1/013034.

[130] R. Barends, J. Kelly, A. Veitia, D. Sank, E. Jeffrey, T. C. White, J. Mutus, A. G. Fowler, B. Campbell, Y. Chen, Z. Chen, B. Chiaro, A. Dunsworth, C. Neill, P. O'Malley, P. Roushan, A. Vainsencher, J. Wenner, A. N. Korotkov, A. N. Cleland, and J. M. Martinis. Superconducting quantum circuits at the surface code threshold for fault tolerance. *Nature*, 508:500–503, 2014. doi: 10.1038/nature13171.

[131] David Deutsch, Artur Ekert, Richard Jozsa, Chiara Macchiavello, Sandu Popescu, and Anna Sanpera. Quantum privacy amplification and the security of quantum cryptography over noisy channels. *Phys. Rev. Lett.*, 77:2818–2821, 1996. doi: 10.1103/PhysRevLett.77.2818.

[132] Lu-Ming Duan, G. Giedke, J. I. Cirac, and P. Zoller. Entanglement purification of gaussian continuous variable quantum states. *Phys. Rev. Lett.*, 84:4002–4005, 2000. doi: 10.1103/PhysRevLett.84.4002.

[133] Jian-Wei Pan, Christoph Simon, C. Brukner, and A. Zeilinger. Entanglement purification for quantum communication. *Nature*, 410:1067–1070, 2001. doi: 10.1038/35074041.

[134] J. Borregaard, P Kómár, E. M. Kessler, A. S. Sørensen, and M. D. Lukin. Heralded quantum gates with itegrated error detection in optical cavities. *in preparation...*, .

[135] Daniel E. Browne, Martin B. Plenio, and Susana F. Huelga. Robust creation of entanglement between ions in spatially separate cavities. *Phys. Rev. Lett.*, 91: 067901, 2003. doi: 10.1103/PhysRevLett.91.067901.

[136] L.-M. Duan and H. J. Kimble. Efficient engineering of multiatom entanglement through single-photon detections. *Phys. Rev. Lett.*, 90:253601, 2003. doi: 10.1103/PhysRevLett.90.253601.

[137] C. Cabrillo, J. I. Cirac, P. García-Fernández, and P. Zoller. Creation of entangled states of distant atoms by interference. *Phys. Rev. A*, 59:1025–1033, 1999. doi: 10.1103/PhysRevA.59.1025.

[138] Nadja K. Bernardes, Ludmiła Praxmeyer, and Peter van Loock. Rate analysis for a hybrid quantum repeater. *Phys. Rev. A*, 83:012323, 2011. doi: 10.1103/PhysRevA.83.012323.

[139] Dagmar Bruss. Optimal eavesdropping in quantum cryptography with six states. *Phys. Rev. Lett.*, 81:3018–3021, 1998. doi: 10.1103/PhysRevLett.81.3018.

[140] B. Albrecht, P. Farrera, X. Fernandez-Gonzalvo, M. Christiani, and H. de Riedmatten. A waveguide frequency converter connecting rubidium-based quantum memories to the telecom c-band. *Nature Communications*, 5(3376), 2014. doi: 10.1038/ncomms4376.

[141] U. L. Andersen, G. Leuchs, and C. Silberhorn. Continous variable quantum information processing. *Laser and Photonics Review*, 4:337–354, 2010. doi: 10.1002/lpor.200910010.

[142] G. Adesso, S. Ragy, and A. R. Lee. Continous variable quantum information: Gaussian states and beyond. *Open Syst. Inf. Dyn.*, 21:1440001, 2014. doi: 10.1142/S1230161214400010.

[143] M. Mirrahimi, Z. Leghtas, V. V. Albert, S. Touzard, R. J. Schoelkopf, L. Jiang, and M. H. Devoret. Dynamically protected cat-qubits: a new paradigm for universal quantum computation. *New J. Phys.*, 16:045014, 2014. doi: 10.1088/1367-2630/16/4/045014.

[144] M. Grassl, Th. Beth, and T. Pellizzari. Codes for the quantum erasure channel. *Phys. Rev. A*, 56:33–38, 1997. doi: 10.1103/PhysRevA.56.33.

[145] T. C. Ralph, A. J. F. Hayes, and Alexei Gilchrist. Loss-tolerant optical qubits. *Phys. Rev. Lett.*, 95:100501, 2005. doi: 10.1103/PhysRevLett.95.100501.

[146] Michael Varnava, Daniel E. Browne, and Terry Rudolph. Loss tolerance in one-way quantum computation via counterfactual error correction. *Phys. Rev. Lett.*, 97:120501, 2006. doi: 10.1103/PhysRevLett.97.120501.

[147] J.R. Johansson, P.D. Nation, and Franco Nori. Qutip 2: A python framework for the dynamics of open quantum systems. *Computer Physics Communications*, 184(4):1234 – 1240, 2013. ISSN 0010-4655. doi: 10.1016/j.cpc.2012.11.019. URL http://www.sciencedirect.com/science/article/pii/S0010465512003955.